Exploring the role of LRRK2 mutations on macrophage function in Parkinson's disease

Rebecca Morrison

University College London

and

The Francis Crick Institute

PhD Supervisor: Dr Maximiliano Gutierrez

A thesis submitted for the degree of

Doctor of Philosophy

University College London (UCL)

Declaration

I Rebecca Morrison confirm that the work presented in this thesis is my own. Where information has been derived from other sources, I confirm that this has been indicated in the thesis.

Abstract

LRRK2 is commonly mutated in Parkinson's disease and has cell type-specific mechanisms of activation and function. LRRK2 is expressed by immune cells, and while there is evidence of an inflammatory component to PD, the activity of LRRK2 pathogenic mutations in immune cells is not well characterised. In macrophages, LRRK2 is associated with lysosomes and is activated following lysosomal damage. However, the functional outcomes of clinically relevant pathogenic mutations in macrophages are unknown. Here, using primary mouse and patient-derived iPSC-derived macrophage (iPSDM) models of LRRK2-G2019S, I defined the substrates of LRRK2 after lysosomal damage. A phosphoproteomics-based comparison between wild-type macrophages and macrophages lacking LRRK2 kinase activity revealed a subset of Rab GTPases, common to those identified in previous studies, as LRRK2 kinase substrates in macrophages. Comparison of LRRK2-G2019S and wild-type macrophages demonstrated a remarkably similar level of Rab GTPase phosphorylation at baseline and after lysosomal damage. Only two Rab phosphorylations differed after lysosomal damage in LRRK2-G2019S macrophages: phosphorylated Rab12 was increased, while phosphorylated Rab35 was decreased compared to wild-type cells. Live cell snapshot imaging revealed a deficit in the repair of lysosomal damage in LRRK2-G2019S macrophages. However, lysosomal repair via the endosomal sorting complex required for transport (ESCRT) machinery was not dependent on LRRK2 kinase activity in mouse primary macrophages. Functionally, LRRK2-G2019S macrophages showed more cell death and increased markers of apoptosis after lysosomal membrane damage. This increase in lysosomal damage-induced cell death was recapitulated in iPSDM from patients carrying the G2019S mutation, but not in isogenic control iPSDM. Altogether, this work defines the signaling downstream of G2019S in macrophages and identifies susceptibility to cell death after lysosomal damage as an important phenotype of this mutation.

Impact statement

More than 10 million people are living with Parkinson's disease (PD) worldwide, but current treatment options provide limited relief of symptoms, and there is no treatment that can halt disease progression. Mutations in the *leucine rich repeat kinase 2* (*LRRK2*) gene are a major cause of PD, and understanding the pathways in which LRRK2 acts could uncover new disease-modifying treatments in PD. LRRK2 is a large and complex protein and has a multitude of reported functions which vary markedly by cell type.

Parkinson's disease research has focused on the brain as instigator and perpetrator of disease for many decades. However, recent work has highlighted that immune cell dysfunction is also important for disease onset and progression. There is inflammation and immune cell activation in PD, and patients often show a significant deterioration in their symptoms during systemic infections. LRRK2 is closely linked to immune function as it is highly expressed by immune cells, tightly regulated by immune stimuli, and associated with other inflammatory disease including Crohn's disease, leprosy, and tuberculosis. This thesis sheds light on how LRRK2 mutations in immune cells can impact on the function of these cells, contributing to the inflammation that is present in PD. I discuss the generation of a large dataset demonstrating the LRRK2 kinase substrates that are relevant to immune cell biology. This dataset will undoubtedly be useful in future studies of the role of LRRK2 specific to these cells. Further, I have characterised two independent cellular systems in which LRRK2 mutations can be studied, and identified pathways that are disturbed in LRRK2-mutant cells from both biological systems. This data can form a basis for future studies that aim to pinpoint underlying mechanisms behind inflammation in PD and ultimately will aid in the development of disease-modifying targets for LRRK2-PD.

Finally, the normal function of LRRK2, and how mutant LRRK2 differs in function, is still not completely understood. Without this understanding, we risk developing LRRK2-based treatments, such as LRRK2 kinase inhibitors, that have unpredictable side-effects, thus wasting time, resources, and money. My data provides further insight into the mechanism of action of LRRK2 in macrophages. Through greater

understanding, we can work closer towards the delivery of a safe and effective treatment for PD.

Acknowledgement

Firstly, I'd like to thank my supervisor Dr Max Gutierrez for giving me the opportunity to carry out a PhD in his lab. Over the past three years, Max has provided me with guidance and support to develop scientific skills that I will now be able to put to good use in my clinical role. On a personal level Max's encouragement and trust in me throughout, and especially when I faced challenges, has given me a sense of confidence and self-belief that I will take forward in life. I am very glad that Max's studies of *Mycobacterium tuberculosis* led him to LRRK2. I would also like to thank all the members of the Gutierrez lab for their support both practically in the lab and through academic discussions. Enrica Pellegrino and Natalia Athanasiadi generated the isogenic control iPSC that were invaluable to this project. Natalia Athanasiadi also worked tirelessly, often coming in over weekends, to generate enough iPSDM so that I could do experiments. Angela Rodgers carried out all animal work and without her I would not have the murine cells I needed for experiments. Sila Ultanir and Simeon Mihaylov carried out the phosphoproteomics, which proved to be a key part of this thesis. I am very grateful for the opportunity to carry out my PhD at the Crick, it is an outstanding research institute with incredible facilities and people.

To my parents Margaret and Paul, thank you for travelling from Scotland to London to support me whenever I needed you, for being there on the phone, and for always believing in me. I could not have done this without your support. To my husband Harry who has been on this journey with me every step of the way, thank you for lifting me up and keeping me going when things were tough, for your patience, for the financial and time sacrifices, and for the many, many hours of solo parenting you have done. Finally, to my son Leo, who was just 4 months old when I started and is now a joyous three-year-old, I want to show you that you can do anything you put your mind to in life, and I hope this proves that to you.

Table of Contents

Table of Figures

List of Tables

Abbreviations

AMP	Adenosine monophosphate
ANK	Ankyrin repeat
ANOVA	Analysis of variance
ANX	Annexins
ARM	Armadillo repeat motif
Arm	Armadillo repeat containing protein
ASC	Apoptosis-associated speck-like protein containing a CARD
ATP	Adenosine triphosphate
BMDM	Bone marrow derived macrophages
Cas	Caspase
Cas9	CRISPR-associated protein-9
CD	Cluster of differentiation
CHMP	Charged multivesicular body protein
CNS	Central nervous system
COR	C-terminal of ROC
CRISPR	Clustered regularly interspaced short palindromic repeats
Cryo-EM	Cryogenic electron microscopy
Cts	Cathepsin
DAMP	Damage associated molecular pattern
DAPK1	Death associated protein kinase 1
DC_{50}	Half-maximal degradation concentration
Dennd	DENN/MADD domain containing
DMSO	Dimethylsulfoxide
Dmxl	DmX-like protein
DNA	Deoxyribonucleic acid
DTT	Dithiothreitol
EB	Embryoid bodies
ERK	Extracellular signal-regulated kinase
ESCRT	Endosomal sorting complex required for transport
FAS	Fas ligand
FBS	Fetal bovine serum

FGF	Fibroblast growth factor
Fv4	Retrovirus-related Env polyprotein from Fv-4 locus
G-CSF	Granulocyte colony stimulating factor
G3BP	Ras GTPase-activating protein-binding protein
GAD	G-protein activated by nucleotide-dependent dimerisation
Gal	Galectin
GAP	GTPase activating protein
GDI	GDP dissociation inhibitor
GDP	Guanosine diphosphate
GEF	Guanine nucleotide exchange factor
GFP	Green fluorescent protein
GM-CSF	Granulocyte-macrophage colony-stimulating factor
GSDMD	Gasdermin D
GTP	Guanosine triphosphate
GWAS	Genome-wide association studies
HCD	Higher-energy collisional dissociation
HEK 293	Human embryonic kidney 293 cells
Herpud	Homocysteine-responsive ER-resident ubiquitin-like domain member
HKLM	Heat killed listeria monocytogenes
HMC3	Human microglial clone 3
Hp1bp	Heterochromatin protein 1-binding protein
HRP	Horseradish peroxidase
HSP90	Heat shock protein 90
IC_{50}	Half-maximal inhibitory concentration
IFN	Interferon
Igf2bp1	Insulin-like growth factor 2 mRNA-binding protein
IL	Interleukin
Il1rn	Interleukin-1 receptor antagonist protein
InDel	Insertions/deletions
IP-10	Interferon gamma-induced protein 10
iPSC	Induced pluripotent stem cell
iPSDM	Induced pluripotent stem cell-derived macrophage
IRF	Interferon regulatory factor

JIP	JNK-interacting protein
JNK	c-Jun N-terminal kinase
KO	Knock out
LAMP	Lysosomal-associated membrane protein
LC-MS/MS	Liquid Chromatography with tandem mass spectrometry
LC3	Microtubule-associated protein 1A/1B-light chain 3
LFA	Lymphocyte function-associated antigen
LLOMe	L-leucyl-L-leucine methyl ester
LPS	Lipopolysaccharide
LRR	Leucine-rich repeat
LRRK	Leucine rich repeat kinase
LTR	LysoTracker DND-99
LYTL	Lysosomal tubulation/sorting driven by LRRK2
M-CSF	Macrophage colony-stimulating factor
M6PR	Mannose 6-phosphate receptor
MAPK	Mitogen activated protein kinase
MASL	Malignant fibrous histiocytoma amplified sequence
MCP	Monocyte chemoattractant protein
MEF	Mouse embryonic fibroblast
MHC	Major histocompatibility complex
MIP	Macrophage inflammatory protein
MJFF	Michael J Fox Foundation
MLKL	Mixed lineage kinase domain like pseudokinase
MOMP	Mitochondrial outer membrane permeabilisation
MPP	Microtubule-associated protein 1A/1B-light chain 3
mRNA	Messenger RNA
Mrpl51	39S ribosomal protein L51
Mt2	Metallothionein-2
Mtb	Mycobacterium tuberculosis
mTORC1	Mammalian/mechanistic target of rapamycin complex 1
Mucl1	Mucin-like 1
MyD88	Myeloid differentiation primary response gene-88
NF-kB	Nuclear factor kappa B

NFAT	Nuclear factor of activated T cells
NK cell	Natural killer cell
NLRP3	Nucleotide-binding domain, leucine-rich repeat-containing family, pyrin domain containing 3
ORCL	Oculocerebrorenal syndrome of Lowe
ORP	OSBP-related proteins
OSBP	Oxysterol-binding protein
p53	Tumour protein 53
PAM	Protospacer adjacent motif
PAM3CSK4	Pam3-Cys-Ser-Lys4
PAMP	Pathogen associated molecular pattern
PARP	Poly (ADP-ribose) polymerase
PAT4	Proton-dependent amino acid transporter 4
PBMC	Peripheral blood mononuclear cell
PBS	Phosphate buffered saline
PD	Parkinson's disease
PDGF	Platelet derived growth factor
PE	Phosphatidylethanolamine
PI	Propidium iodide
PI3K	Phosphatidylinositol-3-kinase
PI4K	Phosphatidylinositol-4-kinase
PKA	Protein kinase A
Poly(I:C)	Polyinosinic:polycytidylic acid
PPARγ	Peroxisome proliferator-activated receptor-gamma
PPMI	Parkinson's progression markers initiative
PROTAC	Proteolysis targeting chimera
PVDF	Polyvinylidene fluoride
Rab	Rab GTPase
RANTES	Regulated on activation, normal T cell expressed and secreted
RILPL	Rab interacting lysosomal protein-like
RIPK	Receptor interacting protein kinase
RNA	Ribonucleic acid
Roc	Ras-of-complex

ROS	Reactive oxygen species
Rpl	60S ribosomal protein
SD	Standard deviation
SEM	Standard error of the mean
sgRNA	Single guide RNA
SMOAC	Sequential enrichment of metal oxide affinity chromatography
SNP	Single nucleotide polymorphism
ssODN	Single stranded oligodeoxyribonucleotide
STAT	Signal transducer and activator of transcription
TB	Tuberculosis
TDP-43	Transactive response DNA binding protein of 43 kDa
TFEB	Transcription factor EB
TfR	Transferrin receptor
Th2	T helper 2
TLR	Toll-like receptor
TMT	Tandem mass tag
TNF	Tumour necrosis factor
TRIF	TIR-domain-containing adapter-inducing interferon-beta
TRIM	Tripartite motif
Trp53i11	Tumour protein p53-inducible protein 11
ULK	Unc-51-like kinase 1
VEGF	Vascular endothelial growth factor
VPS	Vacuolar protein sorting
WAVE2	Wiskott-Aldrich syndrome protein family verprolin-homologous protein-2

Chapter 1. Introduction

1.1 The *LRRK2* gene and Parkinson's disease

In 2002, a novel locus for Parkinson's disease (PD) on chromosome 12p11.2-q13.1, designated *PARK8*, was reported in a Japanese family with autosomal dominant PD (Funayama et al., 2002). Two years later, mutations in *Leucine rich repeat kinase 2* (*LRRK2*) were uncovered as the cause of *PARK8*-PD by two independent groups (Paisan-Ruiz et al., 2004; Zimprich et al., 2004). The *LRRK2* gene on chromosome 12 comprises 51 exons that encode a large, multidomain protein (Paisan-Ruiz et al., 2004; UniProt, 2023). To date, there are seven mutations in *LRRK2* that are proven causative for PD through segregation analysis in multiple independent families: G2019S (Di Fonzo et al., 2006; Infante et al., 2006; Lesage et al., 2005; Nichols et al., 2005; Williams-Gray et al., 2006; Zabetian et al., 2006), I2020T (Tomiyama et al., 2006; Zimprich et al., 2004), N1437H (Aasly et al., 2010; Johansen et al., 2011), R1441C (Di Fonzo et al., 2006; Mata et al., 2005a; Zimprich et al., 2004), R1441G (Mata et al., 2005b; Paisan-Ruiz et al., 2004) , R1441H (Mata et al., 2005a; Zabetian et al., 2005), and Y1699C (Khan et al., 2005; Zimprich et al., 2004). Pathogenic mutations in *LRRK2* cause autosomal dominant PD with variable, age-related penetrance. An analysis of over 100 families worldwide reported that 74% of LRRK2-G2019S carriers will develop PD by the age of 79 years (Healy et al., 2008). It remains unknown why some patients go on to develop disease over others, but it is likely that there are other genetic and environmental contributors. Indeed, there are reports of tobacco usage, black tea drinking, and caffeine consumption having protective effects in carriers of *LRRK2* mutations (Crotty et al., 2020; Luth et al., 2020).

The most common pathogenic mutation is LRRK2-G2019S: an adenine (A) to guanine (G) substitution in exon 41 that results in a glycine to serine amino acid substitution in the protein (Correia Guedes et al., 2010). The frequency of LRRK2-G2019S differs significantly by geographical location: it is detected in around 40% of cases in North African populations (Lesage et al., 2005), 10-20% in the Ashkenazi Jewish population (Ozelius et al., 2006), 5-10% of cases in European populations

(Bras et al., 2005; Di Fonzo et al., 2006; Healy et al., 2008), and < 1% of cases in Asian populations (Zabetian et al., 2009).

In addition, genome-wide association studies (GWAS) have identified 90 variants in the *LRRK2* gene and its promoter which are associated with risk of sporadic PD (Blauwendraat et al., 2020). A few of these variants are found within the coding region of *LRRK2* and correlate strongly with one's lifetime risk of PD: G2385R, R1628P and M1646T increase risk (Funayama et al., 2007; Ross et al., 2011; Wang et al., 2016); while N551K, R1398H and N551K-R1398H reduce risk (Ross et al., 2011). There are also several non-coding variants in *LRRK2* which have a small effect on PD risk including the canonical rs76904798 variant (Blauwendraat et al., 2020; Bryant et al., 2021; Chen et al., 2011; Tan et al., 2010). The functional consequences of such non-coding variants are unknown but could alter gene expression levels or lead to mRNA changes. Importantly, the presence of *LRRK2* variants in cases of sporadic PD implicates LRRK2 function in a pathway common to sporadic and genetic PD. This means that targeted therapies against LRRK2 could potentially benefit patients with both forms of disease.

1.2 The clinical and pathological features of *LRRK2*-PD

PD is largely a disease of the elderly, affecting around 2% of the population aged over 65 years (de Rijk et al., 2000). *LRRK2*-PD shows a similar age of onset to sporadic PD at around 67 years of age (Healy et al., 2008). *LRRK2*-PD patients show the characteristic motor features of PD including resting tremor, bradykinesia, rigidity, and postural instability, and the disease is generally regarded to be clinically indistinguishable from sporadic PD (Healy et al., 2008; Li et al., 2014). *LRRK2*-PD patients also suffer from non-motor symptoms such as cognitive decline, depression, anxiety, constipation, and loss of sense of smell (Healy et al., 2008; Saunders-Pullman et al., 2022). Although it is not possible to distinguish the clinical features of *LRRK2*-PD from sporadic PD on an individual basis, longitudinal studies have reported slower progression rates and a favourable prognosis in *LRRK2*-PD in comparison to sporadic PD (Ahamadi et al., 2021; Saunders-Pullman et al., 2018).

The classical neuropathological findings in sporadic PD are the loss of dopaminergic neurons in the substantia nigra *pars compacta* of the midbrain and the accumulation of α-synuclein-containing Lewy bodies in surviving neurons (Braak et al., 2004; Spillantini et al., 1997). While these pathological findings have been reported in *LRRK2*-mutant PD (Giasson et al., 2006; Ross et al., 2006), there are also reports of neuronal loss in the absence of Lewy body accumulation (Funayama et al., 2005; Giasson et al., 2006; Kalia et al., 2015), and the presence of Tau pathology (Rajput et al., 2006; Ujiie et al., 2012) and TDP-43 pathology (Agin-Liebes et al., 2023; Wider et al., 2010). Taken together, it appears that *LRRK2*-mutant PD is associated with heterogenous neuropathological findings, distinct from the pathology present in sporadic PD.

1.3 *LRRK2* expression and alternative splicing

LRRK2 is widely expressed at both the cellular level and tissue level (LRRK2, Human Protein Atlas, available from: https://www.proteinatlas.org/ENSG00000188906-LRRK2, accessed 28th April 2024) (Biskup et al., 2007). The highest *LRRK2* expression levels are found in blood-derived immune cells: specifically, B cells, monocytes, and neutrophils (Atashrazm et al., 2019; Fan et al., 2018; Gardet et al., 2010). *LRRK2* is also highly expressed in tissue macrophages and dendritic cells including microglia, the tissue resident macrophage of the central nervous system (CNS) (Hakimi et al., 2011; Lee et al., 2020). Comparatively, *LRRK2* expression levels are low in neurons of the CNS (Gardet et al., 2010).

Alternative splicing is the process whereby a single gene gives rise to multiple mRNA transcripts through different combinations of exons. These mRNA transcripts can show different subcellular localisations, stability, and expression levels. Alternative splicing produces multiple protein isoforms which can behave differently in terms of protein-protein interactions, subcellular localisation, protein signalling and enzymatic activities (La Cognata et al., 2015). Giesert *et al.* reported two *LRRK2* splice variants in the brain of adult mice: one *LRRK2* variant missing exon 5 and found in astrocytes, and one shorter *LRRK2* variant terminating at exon 41a found in neurons and astrocytes (Giesert et al., 2013). Another study reported a LRRK2 splicing variant

missing exons 32-33 in the substantia nigra of brain tissue from PD patients (Trabzuni et al., 2013). The consequences of such splicing variants for PD pathogenesis remains to be elucidated (La Cognata et al., 2015). In addition, one study reported that overexpression of mutant *LRRK2* in cell lines resulted in alternative splicing of other PD-associated genes such as α-synuclein (*SNCA*), postulating that mutant *LRRK2* may affect alternative splicing of other genes linked to neurodegeneration.

Although LRRK2 is expressed at low levels in the brain, there are reports of increased LRRK2 expression in PD brain compared to age-matched controls (Cho et al., 2013; Guerreiro et al., 2013). LRRK2 expression in the brain has been found to correlate with levels of α-synuclein, suggesting that the expression of these proteins is interlinked (Guerreiro et al., 2013). These studies are limited by the small number of cases and difficulties around measuring LRRK2 in formalin fixed and paraffin-embedded tissue. Dzamko and colleagues found increased LRRK2 expression in post-mortem brain tissue of asymptomatic patients with incidental Lewy body pathology, with no difference in LRRK2 expression in patients with clinically apparent PD compared to age-matched controls (Dzamko et al., 2017). This group subsequently studied LRRK2 expression in *LRRK2*-PD and found that LRRK2 expression levels were reduced in *LRRK*2-PD compared to age-matched controls and cases of sporadic PD (Zhao et al., 2018).

In a small study of 40 patients, LRRK2 protein expression in B cells, T cells and monocytes was higher in PD patients compared to age-matched controls (Cook et al., 2017). A similar study of 26 PD patients found higher levels of LRRK2 protein in monocytes, but not B cells, compared to age-matched controls (Bliederhaeuser et al., 2016). The underlying mechanism behind increased LRRK2 expression in immune cells in PD is unknown, however one study reported that α-synuclein fibrils induced LRRK2 expression in human peripheral blood mononuclear cells (Xu et al., 2022a). Taken together, it appears that LRRK2 expression in PD is cell-type dependent, possibly reflecting the different cellular functions of LRRK2 and the different pathways involved in PD pathogenesis.

1.4 *LRRK2* is implicated in disease other than PD

1.4.1 Mycobacterial disease

In 2009, a single nucleotide polymorphism (SNP) in *LRRK2* was associated with susceptibility to multibacillary leprosy by GWAS (Zhang et al., 2009). Multibacillary leprosy, caused by the bacterium *Mycobacterium leprae*, is a severe form of leprosy associated with an exaggerated Th2 cell immune response, type 1 interferon secretion and suppression of macrophage activity (Froes et al., 2022). A later study identified several other SNPs in *LRRK2* linked to leprosy in the Chinese population (Wang et al., 2015). While the underlying mechanism linking *LRRK2* to *Mycobacterium leprae* infection is unknown, experimental studies revealed that *LRRK2* variants associated with leprosy altered autophagy and nuclear factor of activated T cells (NFAT) pathways in cell lines (Wang et al., 2015).

In addition, a large meta-analysis identified *LRRK2* as one of the top hits upregulated in patients with pulmonary tuberculosis (TB), caused by the bacterium *Mycobacterium tuberculosis* (*Mtb*) (Wang et al., 2018b). *LRRK2* upregulation in *Mtb* infection was further confirmed in samples from peripheral blood mononuclear cells (Xie et al., 2020). Using a single cell sequencing approach, Lin *et al*. identified LRRK2 as a potential drug target for *Mtb* infection and showed that a SNP in the LRRK2 promoter resulted in increased LRRK2 expression during *Mtb* infection in cells (Lin et al., 2022). Intriguingly, a large retrospective observational Taiwanese study identified a small increased risk (1.38-fold) of PD in patients infected with TB (Shen et al., 2016). *Mtb* is a respiratory pathogen that is spread via the inhalation of infected droplets that reach the alveoli of the lung. *Mtb* infection is established in alveolar macrophages where it evades immune responses and replicates in the intracellular environment (Bussi and Gutierrez, 2019). In mouse primary macrophages, LRRK2 is a negative regulator of the phagosomal maturation pathway during *Mtb* infection: LRRK2 KO macrophages and macrophages treated with LRRK2 kinase inhibitors showed better control of *Mtb* infection compared to wild-type and LRRK2-mutant macrophages (Hartlova et al., 2018).

1.4.2 Crohn's disease

Crohn's disease is a type of inflammatory bowel disease which causes inflammation throughout the entire gastrointestinal tract, leading to ulceration, fistula formation and bowel obstruction (Roda et al., 2020). The *LRRK2* gene is a major susceptibility locus in Crohn's disease, as identified by multiple independent GWAS (Barrett et al., 2008; Franke et al., 2010). Interestingly, the *LRRK2* N551K and N551K-R1398H coding variants, which are protective against the development of PD, are also protective against the development of Crohn's disease (Hui et al., 2018). In contrast, the N2081D mutation increased the risk of both PD and Crohn's disease (Hui et al., 2018).

1.4.3 Cancer

It is widely accepted that there is a reduced incidence of non-skin cancers in PD compared to the general population (Feng et al., 2015). Some studies have reported an association between LRRK2-G2019S and non-skin cancers including renal, breast, lung, and prostate cancer (Agalliu et al., 2015; Inzelberg et al., 2012; Saunders-Pullman et al., 2010). Notably, the overall incidence of cancer in these studies was low with only a few cases in the LRRK2-G2019S groups. In contrast to this, LRRK2 overexpression was shown to be associated with a better prognosis in renal cancer (Yang et al., 2021). There are also studies reporting no differences in cancer incidence between LRRK2-G2019S and sporadic PD cases (Allegra et al., 2014; Ruiz-Martinez et al., 2014). Thus, it remains to be clarified whether LRRK2 mutations have a definite role in carcinogenesis, although it is possible that they contribute to a subset of cancers.

1.5 LRRK2 and inflammation in PD

1.5.1 LRRK2 regulation by immune stimuli

The link between LRRK2 variants and inflammatory disease, along with high expression of LRRK2 in immune cells, points to a role for LRRK2 in inflammation (Herbst and Gutierrez, 2019; Wallings and Tansey, 2019). Indeed, LRRK2 activity is

closely regulated by immune receptors and stimuli including Toll-like receptors (TLR) and interferon gamma (IFN-γ). However, the role of LRRK2 in inflammation is complex and appears to be cell type-dependent (Wallings and Tansey, 2019).

TLRs are a type of pattern recognition receptor found on the surface of innate immune cells including macrophages (Vijay, 2018). These receptors are designed to recognise common structural motifs that are present on different pathogens, known as pathogen-associated molecular patterns (PAMPs). There are 10 human TLRs which signal by the myeloid differentiation primary response gene-88 (MyD88) or TIR-domain-containing adapter-inducing interferon-β (TRIF) pathways, leading to phosphorylation and activation of nuclear factor kappa B (NF-κβ) and/or interferon regulatory factors (IRFs) (Vijay, 2018). Ultimately, this results in the transcription and translation of genes encoding pro-inflammatory cytokines and/or type 1 IFNs. Treatment of mouse primary macrophages with bacterial lipopolysaccharide (LPS) (TLR4 agonist), bacterial lipopeptide Pam3-Cys-Ser-Lys4 (Pam3CSK4) (TLR2/1 agonist), Flagellin (TLR5 agonist) and Heat Killed Listeria monocytogenes (HKLM) (TLR2 agonist) resulted in phosphorylation of LRRK2 at the serine 935 residue (Dzamko et al., 2012). This phosphorylation site is important for LRRK2 binding to 14-3-3 proteins (discussed later). However, while this study and a study using the macrophage-like cell line RAW 264.7 cells (Oun et al., 2023) found no differences in LRRK2 expression in response to LPS treatment, other groups have reported increased LRRK2 expression in LPS-treated mouse primary macrophages (Hakimi et al., 2011). A similar increase in LRRK2 expression, alongside increased LRRK2 kinase activity, has been reported in LPS-treated rat primary microglia (Moehle et al., 2012).

The effect of LRRK2 on the inflammatory response to LPS treatment appears to be cell-type dependent: LRRK2 KO dendritic cells produce more pro-inflammatory cytokines (Kubo et al., 2020); LRRK2 KO RAW 264.7 cells (Oun et al., 2023) and LRRK2 KO rat primary microglia (Moehle et al., 2012) produce less pro-inflammatory cytokines; and LRRK2 KO mouse primary macrophages show no differences in cytokine secretion (Dzamko et al., 2012; Hakimi et al., 2011). Ahmadi Rastegar and colleagues performed a Luminex bead-based assay to detect a panel of 27 cytokines in human iPSC-derived monocytes treated with different immune stimuli (Ahmadi

Rastegar et al., 2019). They found no differences in cytokine secretion between LRRK2 KO and LRRK2 wild-type cells treated with LPS and PAM3CSK4 but increased pro-inflammatory cytokine secretion in cells with the LRRK2-G2019S mutation.

IFN-γ is a type 2 interferon produced mainly by T-cells and NK cells in the adaptive immune response, functioning to activate other immune cells and pathways (Schroder et al., 2004). IFN-γ is also linked to PD pathophysiology: PD patients show high levels of IFN-γ in the blood and CNS (Kustrimovic et al., 2018; Mogi et al., 2007), and IFN-γ is required for neurodegeneration in animal models of PD (Chakrabarty et al., 2011; Mount et al., 2007). In cell culture, IFN-γ results in a robust increase in LRRK2 expression across many different immune cell types and in neurons (Gardet et al., 2010; Kuss et al., 2014; Lee et al., 2020; Panagiotakopoulou et al., 2020). Bioinformatics analysis identified a consensus sequence within the LRRK2 promoter that binds to IFN response factors and is highly conserved across 28 difference species; indicating that the binding of IFN-γ response factors to this region leads to increased LRRK2 expression (Gardet et al., 2010).

Finally, LRRK2 has been linked to phagocytosis in macrophages: Kim *et al*. reported that LRRK2, via its interaction with the actin cytoskeletal component WAVE2, is important for phagocytic uptake of latex beads and *Escherichia coli* particles (Kim et al., 2018). However, this finding has not been reproduced by other groups, who have reported no effect of LRRK2 on internalisation of *Mtb* (Hartlova et al., 2018) or beads (Lee et al., 2020; Schapansky et al., 2014). In human iPSC-derived macrophages and microglia, LRRK2 has been identified on the late phagosomal membrane alongside Rab8 and Rab10, although its exact role on this membrane is yet to be elucidated (Lee et al., 2020).

1.5.2 The role of inflammation in PD

PD has historically been regarded as a disease of the brain and the majority of LRRK2 research has focussed on neuronal-mediated mechanisms of disease. In more recent years there has been a paradigm shift in our understanding of PD with

growing evidence that immune dysfunction and inflammation is central to its pathogenesis (Herbst and Gutierrez, 2019; Tansey et al., 2022; Wallings et al., 2020). Clinical studies in PD patients consistently report raised pro-inflammatory peripheral and CSF cytokines (Brodacki et al., 2008; Rentzos et al., 2007; Schroder et al., 2018; Xu et al., 2022b), disturbances in immune cell function (Grozdanov et al., 2014; Thome et al., 2021) and altered gut microbiome associated with intestinal inflammation (Perez-Pardo et al., 2019), with these changes being present at very early stages of disease (Forsyth et al., 2011). Another clinical study reported high levels of bacterial endotoxin associated with distinct monocyte subsets in PD patients which closely correlated to progression to dementia (Wijeyekoon et al., 2020). Accordingly, several groups now argue that inflammation could be the driving factor for disease onset and progression in some PD patients (Cabezudo et al., 2020; Kozina et al., 2022).

LRRK2 expression in immune cells is higher in PD patients than age-matched controls (Cook et al., 2017). Proinflammatory cytokines are highest in LRRK2-mutant PD patients with severe symptoms (Brodacki et al., 2008). Intriguingly, LRRK2-G2019S is associated with increased proinflammatory cytokines in the blood of asymptomatic carriers (Dzamko et al., 2016), suggesting it could contribute to the prodromal stage of PD. In animal models, high-dose LPS stimulation results in selective dopaminergic neuronal cell death only in mice with LRRK2 mutations, and this phenotype is rescued by bone marrow transplant to replace mutant LRRK2 for wild-type LRRK2 in immune cells, further indicating the importance of the immune system in the onset of PD (Kozina et al., 2022; Kozina et al., 2018) .

1.6 LRRK2 protein structure

LRRK2 is a large protein comprising 2527 amino acids with four protein-protein interacting domains and two enzymatic domains. The domains of LRRK2 and location of the pathogenic mutations are shown in **Figure** 1.6.1. The protein-protein interacting domains are an armadillo repeat motif (ARM), ankyrin repeat (ANK), and leucine-rich repeat (LRR) towards the amino-terminal, and a WD-40 domain near the carboxy-terminal. The enzymatic core comprises a Ras-of-complex (Roc), C-

terminal of ROC (COR) tandem domain with GTPase activity and a serine-threonine kinase domain with phosphotransfer activity. Recent Cryo-EM studies have shed light on the structure of LRRK2 including domain positioning and interactions. Deniston and colleagues showed that the catalytic half of LRRK2 comprising the Roc, COR, kinase, and WD-40 domains (LRRK2^{RCKW}) is J-shaped, with the kinase and GTPase domains very close to one another (Deniston et al., 2020). Myasnikov *et al*. modelled full-length LRRK2 in its inactive state and found that the ARM, ANK and LRR domains wrap around the LRRK2^{RCKW} domains, with the LRR domain blocking the kinase binding site (Myasnikov et al., 2021). A third group modelled kinase-active LRRK2^{RCKW} interactions with microtubules and found that the Roc domain was essential for microtubule binding (Snead et al., 2022).

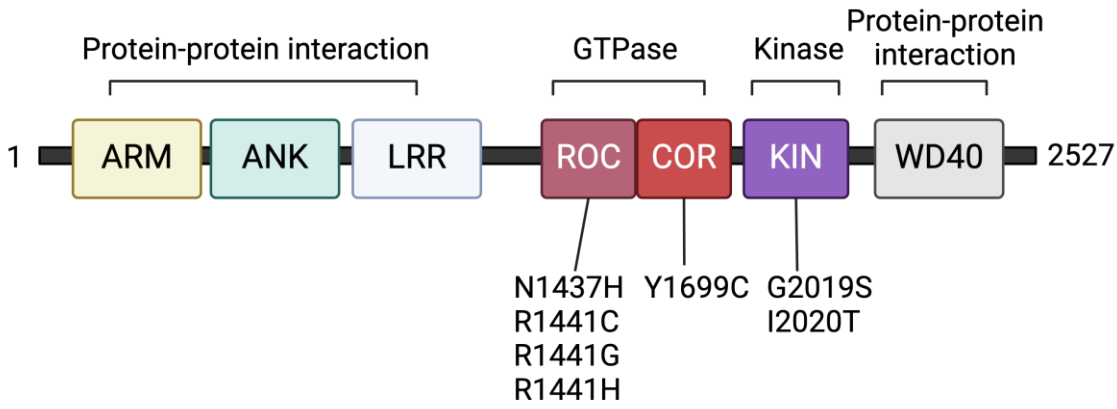

Figure 1.6.1. The structure of LRRK2 protein and location of pathogenic LRRK2 mutations that cause PD.

The predicted functions of each LRRK2 domain are indicated above and the pathogenic mutations causative of PD are indicated below the involved domain. Abbreviations: ARM, armadillo repeats; ANK, ankyrin repeats; LRR, leucine-rich repeats; ROC, Ras of complex; COR, C-terminal of Roc; KIN, kinase; WD40, WD40 repeats.

1.6.1 The Roc-COR GTPase domain

The basic functioning of a GTPase cycles between an active guanosine triphosphate (GTP)-bound state and an inactive guanosine diphosphate (GDP)-bound state (Figure 1.6.2). The length of time that a GTPase is in its active state is therefore dependent on the rate of GTPase activity. The Roc-COR tandem domain of LRRK2 makes it a member of the Roco protein family where the Roc domain, which contains

the GTP/GDP binding site, is present next to a COR domain (Lewis, 2009). A proposed model for the activation of this tandem domain is the G-protein activated by nucleotide-dependent dimerisation (GAD) model, where the COR-domain mediates dimerisation of LRRK2, resulting in Roc-domain GTPase activity (Gotthardt et al., 2008; Guaitoli et al., 2016) (Figure 1.6.2). This is supported by recent atomic resolution structural data of LRRK2, where COR-COR domain interface between two LRRK2 molecules was associated with LRRK2 complex formation (Deniston et al., 2020). In humans, only four Roco proteins exist: leucine rich repeat kinase 1 (LRRK1), LRRK2, death associated protein kinase 1 (DAPK1) and malignant fibrous histiocytoma amplified sequence 1 (MASL1) (Lewis, 2009). LRRK1 shows a remarkably similar structure to LRRK2, missing only the ARM domain, but is functionally distinct with its own set of substrates and, unlike LRRK2, plays an important role in bone development (Metcalfe et al., 2023). DAPK1 is required for apoptosis and is linked to certain cancers (Lewis, 2009). MASL1 differs from the other Roco proteins as it does not contain a kinase domain but has also been linked to cancer development (Dihanich, 2012).

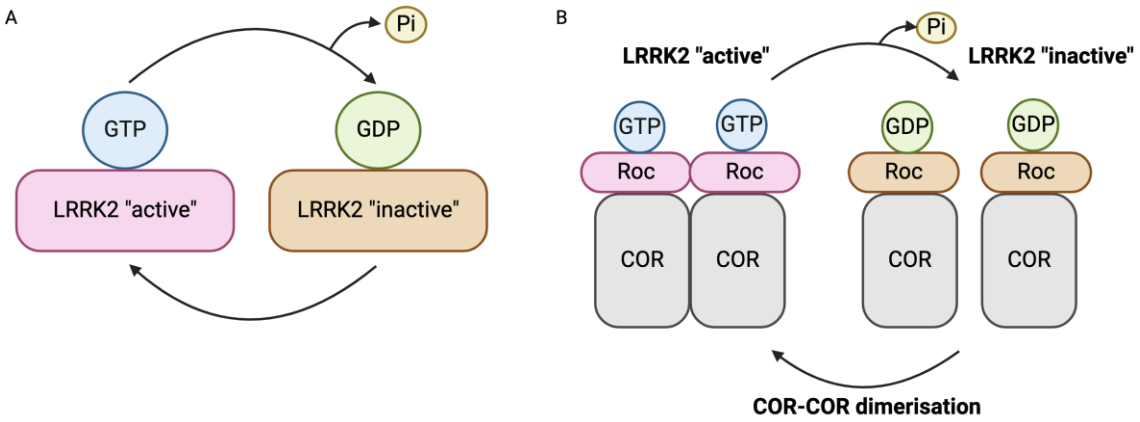

Figure 1.6.2. A summary of the cycle of GTPase activity and proposed mechanism of GTPase activation in LRRK2

A. GTPase enzymes function by cycling between a GTP-bound and GDP-bound state. The enzyme is active when GTP-bound and hydrolyses GTP to GDP + Pi. The enzyme is inactive when bound to GDP. B. In the G-protein activated by nucleotide-dependent dimerisation model for LRRK2 GTPase activation, COR-COR mediated dimerisation of two LRRK2 monomers results in GTPase activity. Abbreviations: GTP, guanosine triphosphate; GDP, guanosine diphosphate; Pi, inorganic phosphate.

Five of the seven pathogenic mutations that cause PD locate in the Roc-COR GTPase domain of LRRK2 (see **Figure** 1.6.1). Using a sensitive *in vitro* GTPase assay, Lewis *et al*. showed that the R1441C mutation was associated with reduced GTPase activity (Lewis et al., 2007) and later confirmed reduced GTPase activity in the Y1699C mutation, possibly due to reduced dimerisation of mutant LRRK2 (Daniels et al., 2011). Reduced GTPase activity in LRRK2 R1441C and R1441G mutations has also been reported by other groups (Deng et al., 2008; Guo et al., 2007; Xiong et al., 2010). In addition, there is a report of increased GTP binding in the R1441C, R1441G, and Y1699C mutations (West et al., 2007). The N1347H mutation was shown to have reduced GTPase activity and reduced affinity for GTP binding (Huang et al., 2019; Puschmann et al., 2012). These findings all point to pathogenic mutations leading to an increase in active LRRK2 GTPase, expected to increase the duration of LRRK2 signalling activity.

1.6.2 Serine-threonine kinase domain

The serine-threonine kinase domain of LRRK2 shares features with the Receptor Interacting Protein Kinase (RIPK) family (Greggio and Cookson, 2009), linked to cell death and inflammatory signalling (Rideout and Re, 2017). The kinase activity of LRRK2 results in the transfer of a phosphate group from ATP to a serine or threonine amino acid residue within a substrate. The kinase domain is composed of an N-lobe and a C-lobe, with an activation segment in the C-lobe. The activation segment, which binds to the substrate and ATP, contains a DFGψ motif that is critical for kinase activation (Zhang and Kortholt, 2023). Two of the seven pathogenic mutations that cause PD are in the DFGψ motif of the kinase domain: G2019S and I2020T (see **Figure** 1.6.1) (Schmidt et al., 2019). The G2019S mutation is reported to increase kinase activity 1.4 to 3-fold *in vitro* (Greggio et al., 2006; Myasnikov et al., 2021; Smith et al., 2006; West et al., 2005), and 1.9-fold in neutrophils (Karayel et al., 2020). There is no consensus on the effects of the I2020T mutation on kinase activity *in vitro* as studies report conflicting findings (Funayama et al., 2005; Greggio and Cookson, 2009; Jaleel et al., 2007; Nichols et al., 2010). However, LRRK2 kinase activity is required for its pathogenic effects in cell models (Greggio et al., 2006; Smith et al., 2006). These findings led to the development of LRRK2 kinase inhibitors

as a treatment strategy for PD (Deng et al., 2011). It has since been shown that LRRK2 kinase activity is increased in the brain of patients with sporadic PD (Di Maio et al., 2018), suggesting that LRRK2 kinase inhibitors may be of use in both forms of disease. The substrates of the kinase domain and regulation of kinase activity will be discussed later.

1.6.3 Protein-protein interaction domains

The presence of four protein-protein interacting domains points to LRRK2 as a signalling hub within the cell (Price et al., 2018). Identification of protein-protein interactions with LRRK2 is challenging because these interactions may be transient and are likely to be cell type-dependent and context-dependent, for example only triggered by specific intracellular events or stresses within a single cell type. There are thousands of reported LRRK2 interacting proteins although many are not independently verified. Zhao *et al*. performed a computational analysis of the human LRRK2 interactome using three independent repositories and identified a total of 1871 interacting partners (Zhao et al., 2023). After removing interactors that had not been independently verified, there were still 407 proteins remaining, including LRRK2 itself, many cytoskeletal proteins, other protein kinases, and Rab GTPases.

One well characterised LRRK2 interactor is the 14-3-3 protein group, a family of adaptor proteins that upon binding to a partner, alter its enzymatic activities and subcellular localisation (Abdi et al., 2024). The binding of 14-3-3 isoforms to LRRK2 is dependent on phosphorylation of sites on LRRK2 including serine (S) residues that are located between the ANK and LRR domains: S910 and S935 (Dzamko et al., 2010; Li et al., 2011; Nichols et al., 2010). This phosphorylation and the effects of 14-3-3 binding on the subcellular localisation and activity of LRRK2 will be discussed below. Another well-known LRRK2 interactor is heat shock protein 90 (HSP90), a ubiquitously expressed protein whose levels rise dramatically in response to cellular stress (Mansour et al., 2024). LRRK2 and HSP90 form a complex that prevents the ubiquitination and proteasomal degradation of LRRK2 (Ko et al., 2009); treatment with a HSP90 inhibitor resulted in LRRK2 degradation in

multiple independent studies (Narayan et al., 2015; Rudenko et al., 2012; Wang et al., 2008).

1.7 Rab GTPases are bona fide substrates of LRRK2 kinase

In 2016, Steger and colleagues provided a breakthrough in the LRRK2 field by identifying a subset of Rab GTPases (Rabs) as the bona fide substrates of LRRK2 kinase: Rab3A/B/C/D, Rab8A/B, Rab10, Rab12, Rab35 and Rab43 (Steger et al., 2017; Steger et al., 2016). This body of work required multiple phosphoproteomic screens using different LRRK2 inhibitors and LRRK2 mutant cells, followed by validation with phospho-specific antibodies against Rab GTPases (Steger et al., 2017). To date, Rab GTPases are the only LRRK2 kinase substrates that show reproducible results across multiple independent groups (Jeong et al., 2018; Purlyte et al., 2018; Thirstrup et al., 2017).

1.7.1 The Rab GTPase cycle

Rab GTPases cycle between an inactive GDP-bound state and an active GTP-bound state (Gutierrez, 2013; Pfeffer, 2018). In the active GTP-bound state, Rab proteins localise to intracellular membranes and bind to effector proteins, mediating downstream pathways such as membrane vesicle budding, docking and fusion events (Prashar et al., 2017). In the inactive GDP-bound state, Rab GTPases are primarily cytosolic. The intrinsic hydrolysis rate of the GTP $\rightarrow$ GDP + Pi reaction is low but is accelerated by GTPase activating proteins (GAPs), which promote more inactive GDP-bound Rabs. In contrast, guanine nucleotide exchange factors (GEFs) foster the binding of GTP and thus increase the amount of active GTP-bound Rab. Another Rab regulatory family is the GDP dissociation inhibitors (GDI), which stabilise GDP-bound inactive Rab in the cytosol and prevent the formation of GTP-bound active Rabs (Muller and Goody, 2018). In addition, Rab activity is modulated by post-translational modifications including prenylation (the irreversible addition of farnesyl or geranylgeranyl, important for membrane tagging) (Pereira-Leal et al., 2001), phosphorylation and AMPylation (the addition of adenosine monophosphate (AMP) by pathogens during intracellular infection) (Shinde and Maddika, 2018).

Endogenous LRRK2 kinase phosphorylates the effector-binding Switch-II motif of 10 Rabs in HEK293 cells and MEFs: Rab3A/B/C/B, Rab8A/B, Rab10, Rab12, Rab35 and Rab43 (Steger et al., 2016). The effects of LRRK2-mediated phosphorylation on Rab GTPase function remain incompletely understood. However, rather than altering GTP/GDP binding or GTPase activity, phosphorylation is thought to affect Rab GTPase to effector and Rab regulatory protein binding (Pfeffer, 2018). In the next section I will summarise the main functions of the Rab substrates that are phosphorylated by LRRK2 kinase.

1.7.2 Rab3A/B/C/D

The characteristics and LRRK2 phosphorylation sites of the Rab3A/B/C/D proteins are shown in Table 1.7.1. Rab3A/B/C/D protein expression is enriched in the central nervous system (Schluter et al., 2002), where they regulate the dynamics of neurotransmitter vesicle exocytosis at the synapse (Fischer von Mollard et al., 1991; Geppert et al., 1997). Rab3A/B/C/D isoforms are differentially expressed but functionally redundant meaning if one isoform is knocked out there is compensation by another isoform: only quadruple knock-out mice for Rab3A/B/C/D are lethal (Schluter et al., 2004). Rab3 proteins are also highly expressed in endocrine organs such as the adrenal and pituitary gland, and exocrine tissues such as the parotid gland (Schluter et al., 2002). At the subcellular level, Rab3 proteins localise predominantly to the membrane of exocytic vesicles (Matsui et al., 1988; Touchot et al., 1987; Zahraoui et al., 1989) and act here as mediators of exocytosis.

Isoform	Molecular weight	Amino acids	LRRK2 phosphorylation site
Rab3A	24 kDa	220	Threonine 86
Rab3B	25 kDa	219	Threonine 86
Rab3C	26 kDa	227	Threonine 94
Rab3D	26 kDa	219	Threonine 86

Table 1.7.1. The molecular characteristics and LRRK2 phosphorylation sites of the Rab3 protein family.

Data derived from Steger et al. 2016, Steger et al. 2017 and https://www.uniprot.org/, (accessed 7th April 2024).

The Rab3-specific GEF is essential for the exocytic activities of Rab3A/B/C/D, as neurotransmitter release was significantly reduced in Rab3 GEP knock-out neurons in culture (Yamaguchi et al., 2002). A GAP for Rab3 has also been reported (Fukui et al., 1997). There are two Rab3 effectors whose function is linked to neurotransmitter release: Rabphilin (Schluter et al., 1999) and RIM1α (Calakos et al., 2004). LRRK2 mutations have been shown to increase the amount of phosphorylated Rab3A/B isoforms in cells (Steger et al., 2017); however, the downstream consequences of Rab3 hyperphosphorylation are not yet characterised. In a Rab3A overexpression model in cell lines, Rab3A was found to localise on lysosomes and regulated lysosomal positioning and exocytosis; indicating that its function may not be limited to exocytic vesicles (Vieira, 2018). Finally, Rab3 proteins may have a function in immune cells: Rab3 isoforms have been detected in phagosomes isolated from cells treated with IFN-γ, and may play a role in antigenic cross-presentation in dendritic cells (Gutierrez, 2013; Trost et al., 2009; Zou et al., 2009).

1.7.3 Rab8A/B

Rab8A and Rab8B are 24 kDa Rab GTPases comprising 207 amino acids (https://www.uniprot.org/, accessed 7th April 2024) and undergo phosphorylation by LRRK2 at the threonine 72 residue (Steger et al., 2016). Rab8A and Rab8B are ubiquitously expressed, with highest levels detected in the brain, gut, and lymphoid tissues (https://www.proteinatlas.org/, accessed 7th May 2024). In cell models, knock-out of Rab8A or Rab8B affects cell shape (Peranen, 2011), lysosomal positioning and lysosomal protein composition (Mamais et al., 2024), trafficking of neurotransmitter receptors (Gerges et al., 2004), and ciliogenesis (Dhekne et al., 2018; Yoshimura et al., 2007), suggesting Rab8 has pleiotropic effects dependent on cell type. In macrophages, Rab8A was shown to interact with PI3 kinase (PI3K) at the plasma membrane during TLR4 signalling, leading to altered cytokine secretion (Luo et al., 2014).

The consequences of LRRK2-dependent phosphorylation of Rab8A have been described. Rabin8 is a Rab8-specific GEF (Homma and Fukuda, 2016) and binds to Rab8A in the switch II domain; Rab8A pT72 phosphorylation blocks binding with Rabin8 and thus prevents the exchange of GDP to GTP (Steger et al., 2016). In addition, phosphorylated Rab8 was unable to bind to GDI in the cytosol which would be expected to alter its ability to recycle from one intracellular membrane, via the cytosol, to other intracellular membranes (Steger et al., 2016). Further, phosphorylated Rab8 is unable to bind to its usual effector proteins such as oculocerebrorenal syndrome of Lowe (ORCL), and instead binds to alternate effectors such as Rab interacting lysosomal protein-like 1 (RILPL1), Rab interacting lysosomal protein-like 2 (RILPL2), JNK-interacting protein 1 (JIP1) and JNK-interacting protein 2 (JIP2) (Steger et al., 2017; Steger et al., 2016; Waschbusch et al., 2020). Through these interactions, phosphorylated Rab8 is linked to ciliogenesis and organelle transport (Pfeffer, 2022). An important caveat to these studies is that the use of phosphomutant Rabs in cells may be invalid: Dhekne and colleagues found that Rab8A and Rab10 phosphomutants were non-functioning: they show non-physiological accumulation on Golgi and cannot bind to Rab regulatory proteins (Dhekne et al., 2018).

1.7.4 Rab10

Rab10 is a 23 kDa Rab GTPase comprising 200 amino acids (https://www.uniprot.org/, accessed 7th April 2024) and undergoes phosphorylation by LRRK2 at its threonine 73 residue (Steger et al., 2016). Rab10 protein expression is ubiquitous at the tissue level and is localised to Golgi, endoplasmic reticulum, endosomes, lysosomes and cilia at the subcellular level (https://www.proteinatlas.org, accessed 9th May 2024) (Singh et al., 2023). The importance of Rab10 in a plethora of functions is demonstrated by the finding that Rab10 KO mice are not viable (Lv et al., 2015). In neurons, Rab10 is required for axonal growth, transport of vesicles through axons, and recycling of neurotransmitters at the synapse (Deng et al., 2014; Glodowski et al., 2007; Xu et al., 2014). Rab10 is also involved in the recycling endosome pathway whereby endocytosed cargo are transported back to the plasma membrane for reuse (Khan

et al., 2022; Liu and Grant, 2015; Singh et al., 2023; Wang et al., 2010). In addition, Rab10 is linked to autophagy - where defective or aged cellular components are bound by a double layer membrane forming autophagosomes and reach lysosomes for degradation. Rab10 deficient cells show accumulation of autophagosomes and autophagic cargo in basal conditions, indicating that Rab10 is required for normal autophagic flux (Palmisano et al., 2017). Rab10 has also been linked to initial steps of autophagosome formation (Li et al., 2016).

Rab10 is arguably the best characterised LRRK2 substrate – one reason for this is the availability of a commercially available anti-phospho Rab10 antibody that is reliable and robust across different experimental approaches (Lis et al., 2018). Phosphorylated Rab10 binds with high affinity to RILPL1, RILPL2 and Myosin Va proteins and Rab10, like Rab8, is linked to ciliogenesis (Dhekne et al., 2018; Dhekne et al., 2021; Waschbusch et al., 2020). Cilia are found on almost every cell of the human body and are thought to function both as cell sensors for a variety of signals and motility organelles, creating flow for fluids such as CSF and mucus (Ishikawa and Marshall, 2011). Rab10, in contrast to Rab8, has an inhibitory effect on ciliogenesis, and Dhekne and colleagues showed that this inhibitory effect is dependent on binding of phosphorylated Rab10 to RILPL1 and Myosin Va proteins (Dhekne et al., 2021). In immune cells, LRRK2-mediated phosphorylation of Rab10 interferes with the maturation and recycling of cargo that are internalised by macropinocytosis, leading to altered immune signalling pathways (Liu et al., 2020). Finally, phosphorylated Rab10 is present at damaged lysosomal membranes and is linked to LRRK2-mediated response to lysosomal damage (discussed later) (Bonet-Ponce et al., 2020).

1.7.5 Rab12

Rab12 is a 27 kDa Rab GTPase comprising 244 amino acids in humans and 243 amino acids in mice (https://www.uniprot.org/, accessed 7th April 2024). It undergoes phosphorylation by LRRK2 at the serine 106 residue in humans and the serine 105 residue in mice (https://www.phosphosite.org/, accessed 7th April 2024). The earliest studies of Rab12 GTPase showed mRNA expression was highest in the heart, lung,

and endocrine glands of mouse tissue (Elferink et al., 1992; Iida et al., 1996; Olkkonen et al., 1993). Overexpression of Rab12 GTPase in various cell lines co-localised with the Golgi apparatus (Olkkonen et al., 1993; Rydell et al., 2014), endosomal compartment (Iida et al., 2005; Rydell et al., 2014), and secretory granules in atrial myocytes (Iida et al., 1996). Using a GDP release assay, Yoshimura *et al*. reported that DENN/MADD domain containing 3 (Dennd3) is a Rab12 GEF *in vitro (*Yoshimura et al., 2010*)*, later confirmed *in cellulo* by Fukuda and colleagues (Matsui et al., 2014). In 2011, Matsui *et al*. described a Rab12-dependent pathway mediating the delivery of transferrin-containing recycling endosomes directly to lysosomes (Matsui et al., 2011). Matsui and colleagues have also shown that Rab12 modulates the lysosomal degradation of the amino acid transporter PAT4, leading to inhibition of the autophagy protein mammalian/mechanistic target of rapamycin complex 1 (mTORC1), resulting in the initiation of autophagy (Matsui and Fukuda, 2013). This was confirmed independently by another group, who also showed that Dennd3-activated Rab12 co-localised with LC3 on recycling endosomes and autophagosomes, postulating that Rab12 is involved in autophagosome trafficking (Xu et al., 2015). In retinol ganglion cells, a mutation in the autophagy receptor optineurin resulted in increased colocalisation of optineurin with Rab12 and increased autophagic cell death (Sirohi et al., 2013). Our current understanding of the functions of Rab12 GTPase is summarised in Figure 1.7.1.

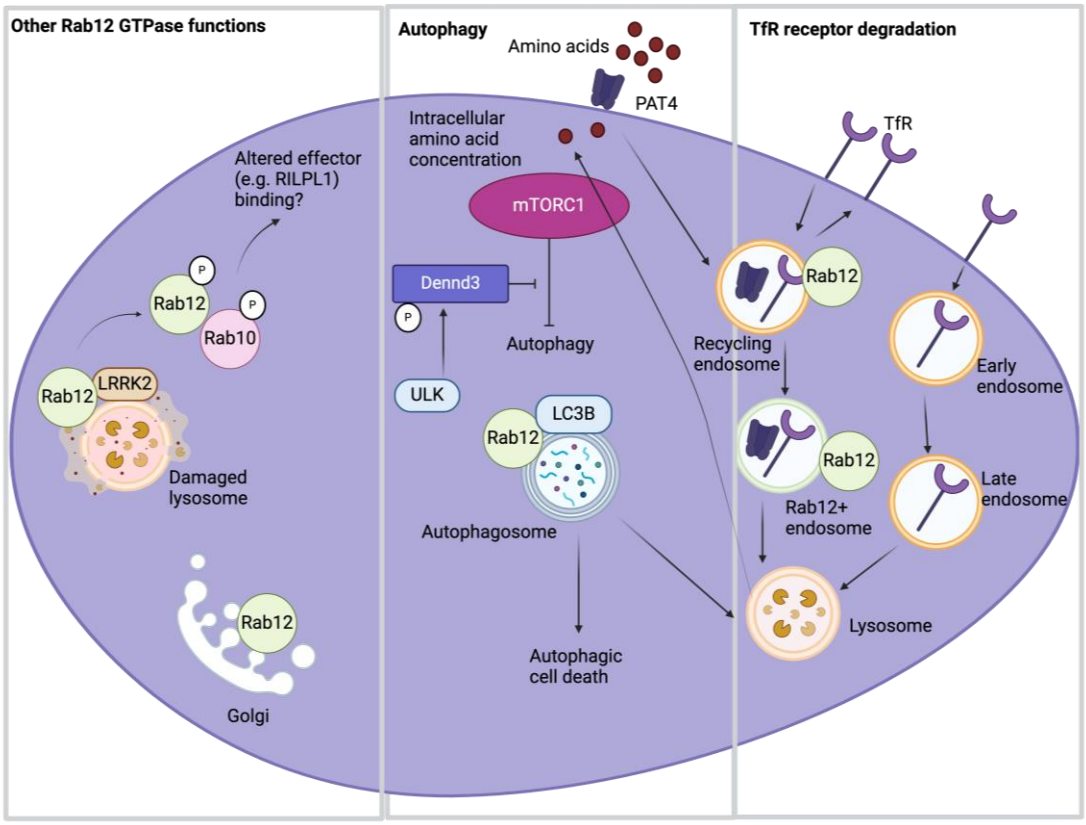

Figure 1.7.1. Current understanding of functions of Rab12 GTPase

Rab12 GTPase is reported to colocalise with recycling endosomes and is required for transferrin receptor (TfR) and PAT4 delivery to lysosomes for degradation (Matsui and Fukuda, 2013; Matsui et al., 2011). By modulating the amount of PAT4 present in the plasma membrane and thus intracellular amino acid levels, Rab12 is linked to the inhibition of mTORC1 and induction of autophagy (Matsui and Fukuda, 2013). Rab12 activation is controlled by the GEF Dennd3, which is in turn activated and phosphorylated by the autophagy protein ULK (Xu et al., 2015; Xu and McPherson, 2017). In retinal ganglion cells, Rab12 function in autophagy was also linked to autophagic cell death (Sirohi et al., 2013). Rab12 has been reported to co-localise with Golgi markers by multiple groups (Elferink et al., 1992; Rydell et al., 2014). Recent work has shown that Rab12 is required for LRRK2 recruitment to damage lysosomes, leading to phosphorylation of Rab10 pT73 and Rab12 pS106 (Dhekne et al., 2023; Wang et al., 2023). The downstream consequences of Rab phosphorylation by LRRK2 are thought to involve altered binding of the phosphorylated Rab to Rab effector proteins such as RILPL1 (Pfeffer, 2022). Image created with BioRender.com.

1.7.6 Rab35

Rab 35 is a 23 kDa Rab GTPase comprising 201 amino acids (https://www.uniprot.org/, accessed 7th April 2024) and undergoes phosphorylation

by LRRK2 at its threonine 72 site (Steger et al., 2016). Rab35 is ubiquitously expressed at the tissue level (Zhu et al., 1994). At the subcellular level, Rab35 is found on endosomes and on the plasma membrane (Kouranti et al., 2006). Rab35 is strongly linked to the recycling endosomal pathway; Rab35 deficient cells accumulate cargo-containing large intracellular vacuoles (Dikshit et al., 2015; Kouranti et al., 2006; Patino-Lopez et al., 2008). In immune cells, Rab35 is required for endocytic recycling of the MHC II receptor (Walseng et al., 2008), and initial steps of phagocytosis (Egami et al., 2015; Egami et al., 2011). Finally, Rab 35 was identified as a potential serum biomarker for PD through the analysis of proteomic profiles of PD patients (Chiu et al., 2016).

Jeong *et al*. investigated Rab35 phosphorylation by LRRK2 kinase in neuronal cell cultures and in mice (Jeong et al., 2018). They found that phosphorylated Rab35 and a phosphomimetic Rab35 mutant was associated with neuronal cell death. They also identified increased GTP binding associated with LRRK2-mediated Rab35 phosphorylation and postulated this might result in Rab35 pT72 becoming “trapped” on intracellular membranes, although they did not investigate Rab35 GEF, GAP, GDI or effector interactions (Jeong et al., 2018). LRRK2-dependent phosphorylation of Rab35 has also been identified at lysosomal membranes during lysosomal membrane damage – this will be discussed further later (Bonet-Ponce et al., 2020).

1.7.7 Rab43

Rab43 is a 23 kDa Rab GTPase comprising 212 amino acids (https://www.uniprot.org/, accessed 7th April 2024) and undergoes phosphorylation by LRRK2 at its threonine 83 site (Steger et al., 2016). Rab43 protein expression is highest in the brain, endocrine organs, and testis (https://www.proteinatlas.org, accessed 9th May 2024). At the subcellular level, Rab43 is almost exclusively located on the Golgi apparatus, where it regulates cargo transport through the Golgi or between Golgi and endoplasmic reticulum (Cox et al., 2016; Dejgaard et al., 2008; Li et al., 2017). In a subset of dendritic cells, Rab43 knock-out led to impairment of antigen cross-presentation (Kretzer et al., 2016). In RAW 264.7 cells, overexpressed Rab43 was detected on Staphylococcus aureus and Mtb-containing phagosomes

(Seto et al., 2011). Although Rab43 is an endogenous LRRK2 substrate, the effects of LRRK2-mediated phosphorylation of Rab43 on its function have not yet been explored.

1.7.8 Other putative LRRK2 kinase substrates

There are many other reported substrates of LRRK2 kinase, however most are based on *in vitro* kinase assays and are not independently verified – such as α-synuclein at serine 129 (Qing et al., 2009), and the cytoskeletal protein moesin at threonine 558 (Jaleel et al., 2007). The tumour suppressor protein p53 was reported to be phosphorylated by LRRK2 at the T304 and T377 sites by *in vitro* assay (Ho et al., 2015), and this was confirmed by the same group in a microglial cell line (Ho et al., 2017). It remains to be determined whether other non-Rab LRRK2 kinase substrates are authentic in cells, and perhaps related to cell type or context-specific phosphorylation.

Cell type- and context-specific effects of LRRK2 kinase could be particularly relevant in neurons, highly specialised cells that conduct electrical impulses at nerve synapses. Mice treated with LRRK2 kinase inhibitors show changes in dopaminergic and glutaminergic signalling, indicating that LRRK2 kinase has an effect at the synapse. Studies have suggested that LRRK2 phosphorylates proteins such as ATPase N-ethylmaleimide sensitive factor (NSF), endophilinA, dynamin, synaptojanin1, auxilin, snapin and syanpsin I within neurons (Kuhlmann and Milnerwood, 2020; Pischedda and Piccoli, 2021). However, identification of the precise LRRK2 kinase substrates during synaptic signalling is technically challenging given that such events are transient (duration is less than 1 ms) and involve only a small proportion of synaptic vesicles, thus showing low stoichiometry (Rizo and Xu, 2015).

1.8 Regulation of the kinase activity of LRRK2

Several mechanisms have been proposed for the regulation of kinase activity: dimerisation phosphorylation, protein-protein interactions, allosteric interdomain

interactions and Redox regulation. In the next section I will discuss these mechanisms in further detail.

1.8.1 Dimerisation and subcellular localisation

In resting conditions, the majority of intracellular LRRK2 is present as monomers in the cytosol with low intrinsic kinase activity (Berger et al., 2010; James et al., 2012). However, a proportion of intracellular LRRK2 is dimerised, and this dimeric form is associated with significantly higher kinase activity as detected by LRRK2 autophosphorylation (Greggio et al., 2008; Sen et al., 2009) and phosphorylation of Rab10 (Leandrou et al., 2019). In cells which are heterozygous for a LRRK2 mutation, LRRK2 dimers can be formed of one wild-type LRRK2 molecule and one mutant-LRRK2 molecule, two wild-type LRRK2 molecules, or two mutant-LRRK2 molecules (Leandrou et al., 2019). Intriguingly, the presence of only one mutant LRRK2 molecule within a dimer does not increase LRRK2 kinase activity beyond a dimer composed of two wild type LRRK2 molecules (Leandrou et al., 2019). More recently, Rab29-depedent LRRK2 tetramers have been detected, and are also linked to increased LRRK2 kinase activity (Zhu et al., 2023).

The recruitment of LRRK2 to intracellular membranes is closely linked to its dimerisation (Berger et al., 2010), likely due to the higher concentration of LRRK2 molecules present at membranes (Zhang and Kortholt, 2023). A small fraction of endogenous LRRK2 is detected on intracellular membranes in basal conditions including Golgi apparatus, early endosomes, lysosomes and mitochondria (Biskup et al., 2006; Hatano et al., 2007), and in a subset of dysfunctional lysosomes in endogenous resting astrocytes (Bonet-Ponce et al., 2020). There is strong evidence of LRRK2 recruitment to membranes during lysosomal stress and lysosomal damage (Bonet-Ponce et al., 2020; Eguchi et al., 2018; Herbst et al., 2020), possibly induced via changes in calcium concentration (Herbst et al., 2020). However, damage is not a prerequisite for LRRK2 activation, as increased LRRK2 kinase activity was detected by Kluss *et al*. upon transfection with a plasmid that targeted LRRK2 to different intracellular membranes, indicating that its presence on the membrane is enough for activation (Kluss et al., 2022b).

In its cytosolic monomeric form, LRRK2 is tightly bound to and regulated by the 14-3-3 protein family. There are seven 14-3-3 isoforms, each encoded by its own gene and differing in expression and function (Giusto et al., 2021). LRRK2 shows strongest affinity for the 14-3-3-γ and 14-3-3-η isoforms (Manschwetus et al., 2020). There are four reported phosphorylation sites on LRRK2 that are pre-requisite for LRRK2 and 14-3-3 binding: serine 910, serine 935, serine 1444, and threonine 2524 (Li et al., 2011; Manschwetus et al., 2020; Muda et al., 2014; Nichols et al., 2010). The phosphorylation of these sites appears to be closely linked to the conformational status of LRRK2, with significant dephosphorylation of the serine 910 and serine 935 sites when LRRK2 is in its closed (active) conformation (Kalogeropulou et al., 2022). Reduced binding of LRRK2 and 14-3-3 proteins results in increased LRRK2 kinase activity (Lavalley et al., 2016; Muda et al., 2014) and disturbed localisation of LRRK2 into large cytoplasmic aggregates (Nichols et al., 2010). Additionally, a proximity ligation assay that detected LRRK2-14-3-3 interactions found a significant loss of 14-3-3 signal along with increased pS1292 and pRab10 signal in the post-mortem brain tissue of patients with sporadic PD, further linking 14-3-3 regulation of LRRK2 to the pathobiology of PD (Di Maio et al., 2018).

Microtubules are hollow tubular structures, composed of the protein tubulin, found in the cytoskeleton of almost all human cells. They function to organise the cytoskeleton and can transport vesicles and organelles throughout the cytosol via interaction with motor proteins such as dynein and kinesin (Gudimchuk and McIntosh, 2021). Overexpressed LRRK2 is detected on microtubules, where it forms filamentous structures (i.e. a long chain of LRRK2 molecules) (Kett et al., 2012; Schmidt et al., 2021; Snead et al., 2022; Watanabe et al., 2020). The amount of LRRK2 bound to microtubules is increased by treatment with type 1 LRRK2 kinase inhibitors (Caesar et al., 2013; Kalogeropulou et al., 2022), and by some pathogenic LRRK2 mutations (Kett et al., 2012; Watanabe et al., 2020); dependent upon LRRK2 being in a closed (active) conformation. LRRK2 binding to microtubules does not seem to alter substrate phosphorylation but instead inhibits the action of motor proteins dynein and kinesin on microtubules, suggesting that LRRK2 could block vesicle trafficking along microtubules (Snead et al., 2022). Notably, LRRK2-microtubule colocalisation has

only been identified in overexpression studies and it remains unclear whether this interaction is present under endogenous conditions.

1.8.2 Phosphorylation

Phosphorylation of a kinase is a common event in kinase regulation and has been shown to be important in the regulation of LRRK2 activity. There are many phosphorylation sites on LRRK2 itself including sites of autophosphorylation and sites of phosphorylation by another kinase. The serine 1292 autophosphorylation site is a proposed marker of LRRK2 kinase activity: this site is not phosphorylated in LRRK2 kinase-dead mutants, dephosphorylated in response to LRRK2 kinase inhibitors, and shows increased phosphorylation in some pathogenic mutations (Kluss et al., 2018; Sheng et al., 2012; Wang et al., 2017). However, phosphorylated LRRK2 serine 1292 levels do not always correlate with LRRK2 kinase activity: Kalogeropulou and colleagues analysed 100 LRRK2 variants linked to PD and found that phosphorylation of Rab10 showed greater correlation with kinase activity than phosphorylation of LRRK2 serine 1292 (Kalogeropulou et al., 2022); similarly Iannotta *et al*. found a discrepancy between LRRK2 kinase activity, Rab10 phosphorylation and serine 1292 phosphorylation in mouse tissues and between different LRRK2 mutations (Iannotta et al., 2020).

The serine 935 phosphorylation site, in contrast, is not a LRRK2 autophosphorylation site – LRRK2 kinase dead molecules do not show complete dephosphorylation of this residue (Dzamko et al., 2010) - thus this site cannot be a direct indicator of LRRK2 kinase activity. Kinases such as casein kinase 1, protein kinase A and tank binding kinase 1 (TBK1) have been reported to phosphorylate this site on LRRK2 (Chia et al., 2014; Dzamko et al., 2012; Li et al., 2011). Interestingly, this site is dephosphorylated in response to LRRK2 kinase inhibitor treatment, thus may be an indirect measure of LRRK2 kinase activity (Deng et al., 2011). Notably, serine 935 phosphorylation is unaltered or significantly decreased in some LRRK2 pathogenic mutations (Kalogeropulou et al., 2022; Padmanabhan et al., 2020). As discussed above, the serine 935 phosphorylation site is one of the important modulators of 14-3-3 protein binding.

1.8.3 Protein-protein interactions

For several years, Rab29 (also known as Rab7L1) was considered a major upstream regulator of LRRK2 kinase activity, as independent groups reported that overexpression of Rab29 led to LRRK2 recruitment and activation at the Golgi apparatus (Liu et al., 2018; Madero-Perez et al., 2018; Purlyte et al., 2018). However, a later study found no effect of Rab29 KO on Rab phosphorylation in LRRK2 wild-type and LRRK2-mutant mice, indicating that the Rab29 activating effect on LRRK2 was secondary to overexpression rather than a physiological event (Kalogeropulou et al., 2020). However, Rab29 has also been captured binding to the ARM domain of LRRK2 in its the tetrameric form, suggesting it could still activate LRRK2 by inducing conformational changes (Zhu et al., 2023).

More recently an effort by two independent groups to identify genes that positively regulate Rab10 phosphorylation by RNA-based screens has revealed Rab12 as a master regulator of LRRK2. Wang *et al.* performed a targeted siRNA screen on 14 Rab genes in human A549 cells, while Dhekne *et al.* performed a pooled CRISPR screen targeting 19,674 genes in mouse NIH-3T3 cells (Dhekne et al., 2023; Wang et al., 2023). Remarkably, excluding LRRK2 and Rab10, Rab12 was the strongest validated hit in both studies. Wang *et al*. reported that Rab12 regulation of LRRK2 is required during lysosomal damage, as LRRK2 recruitment and Rab10 phosphorylation was abolished in Rab12 KO cells treated with the lysosomal damaging agent LLOMe (Wang et al., 2023). Dhekne *et al*. also identified a Rab12-specific binding site on the ARM domain of LRRK2 and altered ciliogenesis in Rab12 KO and Rab12-overexpressing cells (Dhekne et al., 2023).

1.8.4 Allosteric interdomain interactions

Allosteric regulation is defined as a change in enzyme activity through modulation of a site other than the active site of the enzyme. For LRRK2, this relates to modulation of kinase activity via conformational change induced by other domains of LRRK2. Indeed, the GTPase and kinase functions of LRRK2 are closely related: GTPase

domain-mediated dimerisation is postulated to be a pre-requisite for LRRK2 kinase activity (Berger et al., 2010; Deyaert et al., 2017; Sen et al., 2009). LRRK2 dimerisation is also thought to be stabilised by other domains such as the Roc and LRR domains (Greggio et al., 2008) and WD40 domains (Jorgensen et al., 2009).

1.8.5 Other mechanisms of LRRK2 regulation

LRRK2 kinase activity is sensitive to oxidation and reduction (redox) regulation due to the presence of a unique “CC” motif (positions C2024 and C2025) in the kinase domain (Trilling et al., 2024). This motif comprises two cysteine amino acids which are highly sensitive to redox reactions: mutation of the cysteine residues to redox-resistant serine residues resulted in reduced kinase activity *in vitro*, associated with reduced docking onto microtubules in HEK293 cells (Trilling et al., 2024). Oxidising agents have also been linked to LRRK2 kinase activity by other studies (Di Maio et al., 2018; Mamais et al., 2014), and redox-based treatments could represent a novel strategy for LRRK2-PD.

Finally, the D620N mutation in the *vacuolar protein sorting 35* (*VPS35*) gene, also a cause of autosomal dominant PD, results in a robust increase in LRRK2 kinase activity across multiple cell lines from animal models and PD patients (Mir et al., 2018). The *VPS35* gene encodes the retromer complex which transports cargo from late endosomes to the Golgi, and from endosomes to the plasma membrane (Williams et al., 2017). The exact mechanism by which this mutation in the retromer complex regulates LRRK2 activity remains unknown, although it likely acts via an intermediary step as LRRK2 and the retromer are not known to directly interact. Indeed, Pal *et al*. report that the *VPS35* D620N mutation results in altered lysosomal protein composition, creating dysfunctional lysosomes that accumulate LRRK2 and phosphorylated Rab proteins by an as yet unknown mechanism. (Pal et al., 2023)

1.9 Targeting LRRK2 as a treatment strategy for PD

1.9.1 LRRK2 kinase inhibitors

There are two types of LRRK2 kinase inhibitors: type 1 and type 2 which bind to LRRK2 in a closed (active) conformation and an open (inactive) conformation, respectively. LRRK2 kinase inhibitors remain an exciting prospect in the treatment of PD. The type 1 LRRK2 kinase inhibitor BIIB122, developed jointly by Denali Therapeutics and Biogen, reached phase 2b clinical trials in April 2022 and is due to complete by December 2025 (https://clinicaltrials.gov/study/NCT05348785, accessed 11th May 2024). In addition to their clinical relevance, LRRK2 kinase inhibitors are an important experimental tool when studying LRRK2 kinase activity; the type 1 LRRK2 kinase inhibitor MLi-2 was key in identification of bona fide LRRK2 kinase substrates by phosphoproteomics (Steger et al., 2016).

MLi-2 is a highly potent LRRK2 kinase inhibitor, demonstrating a half-maximal inhibitory concentration (IC_{50}) value of 0.8 nM in an *in vitro* LRRK2 kinase assay (Fell et al., 2015). Although MLi-2 is sensitive for LRRK2 kinase, at higher concentrations *in vitro* it inhibits other intracellular kinases including CDC like kinase 2, CDC like kinase 4, mitogen-activated protein kinase kinase kinase 5, mitogen-activated protein kinase kinase kinase 14, and dual specificity protein kinase TTK (Fell et al., 2015). In addition, it inhibits some non-kinase proteins: serotonin, norepinephrine transporter, muscarinic M2, PPARγ and adenosine transporter (Fell et al., 2015). An important caveat to the use of type 1 LRRK2 kinase inhibitors is that they bind to and stabilise LRRK2 in a closed, active conformation, promoting the formation of LRRK2 on microtubules (Obergasteiger et al., 2020; Sanz Murillo et al., 2023). Given that the presence of LRRK2 on microtubules is associated with inhibition of dynein and kinesin movement across microtubules (Snead et al., 2022), possible side effects secondary to this should be considered. Finally, there is *in vivo* evidence that LRRK2-G2019S knock-in mice are resistant to the effects of MLi-2 compared to wild-type controls (Kelly et al., 2018). The underlying mechanism behind this resistance is unknown but could be linked to differences in the conformation of LRRK2-G2019S that are not captured by *in vitro* assays.

GZD-824 is an example of a type 2 LRRK2 kinase inhibitor, originally developed to treat chronic myelogenous leukaemia by inhibiting the breakpoint cluster region-Abelson kinase (Ren et al., 2013; Tasegian et al., 2021). Type 2 kinase inhibitors do not promote the docking of LRRK2 onto microtubules. However, type 2 inhibitors show a preference for binding with wild-type LRRK2 over LRRK2-G2019S *in vitro* and in cells: GZD-824 IC_{50} value for wild-type LRRK2 is 17 nM and for G2019S-LRRK2 is 80 nM (Tasegian et al., 2021). Further, type 2 LRRK2 kinase inhibitors are less specific for LRRK2 than type 1 kinase inhibitors, and the likelihood of off-target effects are higher when using these inhibitors (Zhao et al., 2014).

1.9.2 LRRK2 proteolysis targeting chimeras

The proteasome forms the major pathway of protein degradation in cells. Proteasome composition differs by cell type and activity, but in simple terms it is formed from a combination of ring-shaped subunits into a hollow cylindrical configuration, with protease activity present interiorly in the central portion (Bi et al., 2021). Proteins are recognised by the proteasome when bound to polyubiquitin chains, which are added onto the target by the ubiquitin ligases E1, E2 and E3 (Rousseau and Bertolotti, 2018). An emerging potential treatment strategy for LRRK2-PD is the LRRK2 Proteolysis Targeting Chimeras (PROTACs). PROTACs consist of a protein-of-interest binding ligand connected to an E3-recruiting ligand by a linker (Zhao et al., 2022). Upon binding to the protein-of-interest, the PROTAC induces its ubiquitination and degradation by the proteasome. Thus, PROTAC treatment is also highly useful experimentally in the identification of kinase-independent effects of LRRK2. XL01126 is a commercially available LRRK2 PROTAC with a half-maximal degradation concentration (DC_{50}) of 32 nM for wild-type LRRK2 and 14 nM for LRRK2-G2019S (Liu et al., 2022). XL01126 was able to degrade a maximum of 86% total LRRK2 in mouse bone marrow-derived macrophages after 4h treatment, albeit at relatively high concentrations above 1 μM (Liu et al., 2022).

1.10 Lysosomes

1.10.1 Lysosomal composition and biogenesis

Late endocytic organelles (hereinafter “lysosomes”) are acidic membrane-bound organelles containing around 60 enzymes capable of degrading proteins, lipids, sugars, DNA and RNA. These enzymes are known as acid hydrolases because they show optimal activity at low pH, maintained inside the lysosome by a proton pump system that transports hydrogen ions from the cytosol (pH ~ 7.2) to the lumen (pH ~ 5.4) in exchange for ATP. Most luminal enzymes require cleavage from pre-pro-peptide to pro-peptide to active peptide. For example, newly synthesised cathepsins are delivered to lysosomes in the “pro” form and then are cleaved to their active form within the lysosomal lumen (Alberts, 2022). The transcription factor EB (TFEB) is the master regulator of lysosomal biogenesis (Sardiello et al., 2009). The translocation of TFEB from the cytosol to the nucleus, induced by changes in intracellular nutrient sensing or impaired lysosomal storage, results in the expression of genes encoding lysosomal membrane proteins, lysosomal hydrolases, and autophagy proteins (Settembre et al., 2011).

The lysosomal membrane forms the interface between the cytosol and the acidic lysosomal lumen. It is composed of a lipid bilayer containing > 700 proteins however its main components are the carbohydrate-rich (glycosylated) lysosomal-associated membrane protein 1 (LAMP-1) and lysosomal-associated membrane protein 2 (LAMP-2) (Rudnik and Damme, 2021). LAMP-1 and LAMP-2 proteins form a shield on the luminal aspect of the lysosomal membrane, protecting other membrane components from degradation (Alberts, 2022).

1.10.2 The endolysosomal system

Lysosomes form one part of the endolysosomal system, which also includes early endosomes, late endosomes, and recycling endosomes. Each of these organelles are single membrane bound and are defined by specific markers, for example Rab5 is an early endosomal marker while Rab7 is a late endosome marker. Cargo molecules can enter the endolysosomal system by endocytosis, phagocytosis, or

autophagy. A simplified overview of the endolysosomal system is demonstrated in Figure 1.10.1.

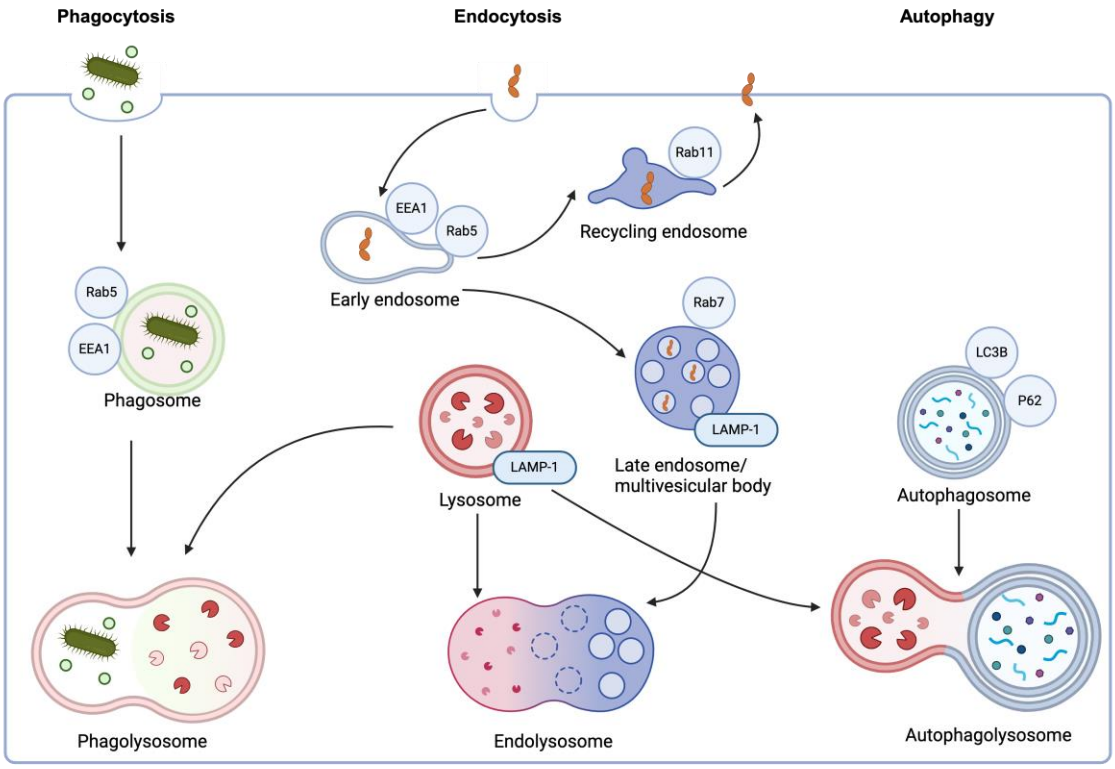

Figure 1.10.1. An overview of the endolysosomal system.

There are three main entry routes into the endolysosomal system: phagocytosis, endocytosis, and autophagy. Phagocytosis is the engulfment of large particles such as pathogens and dead cells into a phagosome. Phagosomes undergo a series of maturation steps before fusing with lysosomes to form phagolysosomes. Endocytosis is the uptake of small particles into the cell via an early endosome. Cargos are sorted at the early endosome: some will recycle back to the plasma membrane via recycling endosomes, while others are degraded via a series of maturation steps to late endosomes/multivesicular bodies and fusion with lysosomes. Intracellular proteins, organelles and pathogens can also enter the endolysosomal system by autophagy, where the cargo is bound by the double-membrane autophagosome. The figure and legend are adapted from information from (Alberts, 2022). Image created on biorender.com.

1.10.3 Lysosomal heterogeneity

In addition to its role in the endolysosomal system, the lysosome functions in cell signalling, energy metabolism, plasma membrane repair, and orchestration of cell death pathways, to name a few (Alberts, 2022). Indeed, lysosomes are present in all

eukaryotic cells except for red blood cells, and they vary in shape, size and number depending on cell type (Bussi and Gutierrez, 2024; de Araujo et al., 2020). From an experimental standpoint, it is important to consider differences in lysosomal heterogeneity between cells. Different cell models show vast disparities in lysosomal number, area and proteolytic activity – for example cell lines such as HeLa and HEK-293T cells show much less lysosomal content and activity than human iPSC-derived macrophages (Bussi and Gutierrez, 2024).

Single organelle resolution-based imaging has revealed that even within a single cell there are lysosomal subpopulations which vary in subcellular location, content, and function. This has led to a recent proposal to introduce a “lysosome states” framework whereby each lysosome within a cell has its own distinct molecular signature and forms one part of a large, interconnected network (Bussi and Gutierrez, 2024). Johnson *et al*. used quantitative ratiometric fluorescence microscopy to show that lysosomes at the cell periphery are more alkaline and less proteolytically active compared to juxta-nuclear lysosomes (Johnson et al., 2016). Lysosomes can also take on different shapes: lysosomal tubulation was first described in murine bone marrow derived macrophages (Phaire-Washington et al., 1980) where they form in response to macrophage activation, creating an expanded reticular lysosomal network (Hipolito et al., 2019). Tubular lysosomes, defined as ≥ 4 μm in length (Saric et al., 2016), also function in phagocytosis and antigen presentation in macrophages (Saric et al., 2016; Suresh et al., 2021). Finally, lysosomal size influence’s function: Bandyopadhyay et al. compared transport of enlarged lysosomes by live cell imaging and found overall slower intracellular movement of larger lysosomes (Bandyopadhyay et al., 2014).

1.11 The role of LRRK2 in the endolysosomal system

1.11.1 Loss of LRRK2 alters lysosomal homeostasis

An important observation in LRRK2 KO animal models is the appearance of enlarged vacuoles, lipofuscin granules and protein aggregates in the renal tubular cells of the kidney (Baptista et al., 2013; Eguchi et al., 2018; Tong et al., 2010). LRRK2 KO does not, however, result in any brain pathology, leading to the suggestion that LRRK1

can compensate for LRRK2 activity in the brain of these animals (Tong et al., 2010). In addition, animals treated with a LRRK2 kinase inhibitor show an accumulation of lamellar bodies (surfactant-containing secretory vesicles) and enlarged vacuoles in type II pneumocytes of the lung (Baptista et al., 2020). These findings point to a role for LRRK2 in the endolysosomal system of the kidney and lung.

In LRRK2 KO mouse primary astrocytes, transduction with the insect virus baculovirus containing a GFP-labelled LAMP-1 construct results in labelling of a significantly higher number of late endosomes/lysosomes compared to wild-type astrocytes, and higher levels of LAMP-1 and LAMP-2 are present in LRRK2 KO cells by Western blot (Henry et al., 2015). Despite these changes, overall lysosomal proteolytic activity does not differ in LRRK2 KO astrocytes. (Henry et al., 2015). In contrast, LRRK2 KO mouse primary macrophages show increased proteolytic activity in phagosomes containing fluorescently-labelled latex beads, and proteomics from isolated phagosomes demonstrates upregulation of hydrolytic enzymes and late endosomal/lysosomal proteins (Hartlova et al., 2018). A similar report of increased proteolytic activity in in LRRK2 KO human iPSC-derived macrophages and mouse primary macrophages alongside increased LAMP-1 and cathepsin levels by Western blot analysis was described (Yadavalli and Ferguson, 2023). These changes were associated with increased nuclear translocation of TFEB, indicating that there is increased lysosomal biogenesis in LRRK2 KO cells (Yadavalli and Ferguson, 2023).

1.11.2 Mutant LRRK2 alters lysosomal biology

in human iPSC-derived macrophages and mouse primary macrophages, the LRRK2-G2019S mutation results in a LRRK2 kinase-dependent reduction in proteolytic activity as detected by immunofluorescence, and reduced levels of LAMP-1 and Cathepsins by Western blot analysis (Yadavalli and Ferguson, 2023). Basal LRRK2 kinase activity appears to be a negative regulator of proteolytic activity: LRRK2 wild-type cells treated with a LRRK2 kinase inhibitor show increased proteolytic activity (Yadavalli and Ferguson, 2023). Whether such defects in lysosomal proteolysis are present in healthy carriers of LRRK2 mutations, as such

significant defects could have deleterious effects on normal immune cell functioning remains to be defined. A small reduction in proteolytic activity is present in phagosomes isolated from LRRK2-G2019S mouse primary macrophages, and high concentrations of LRRK2 kinase inhibitor can reverse this defect (Hartlova et al., 2018).

Mouse primary astrocytes overexpressing LRRK2-G2019S accumulate enlarged juxta-nuclear late endosomes/lysosomes by LAMP-2 immunofluorescence and live cell imaging with LysoTracker dye (Henry et al., 2015). However, overall lysosome number is markedly less in LRRK2-G2019S astrocytes following transduction with the insect virus baculovirus containing a GFP-labelled LAMP-1 construct, and there is reduced LAMP-1 and LAMP-2 expression by Western blot analysis. Further, lysosomal pH and proteolytic activity are also reduced in LRRK2-G2019S astrocytes (Henry et al., 2015). Mouse primary astrocytes homozygous for LRRK2-G2019S show significantly reduced number of lysosomes and reduced lysosomal volume by electron microscopy, associated with reduced LAMP-2A-positive late endosomes/lysosomes by immunofluorescence (Streubel-Gallasch et al., 2021). However lysosomal pH did not differ in LRRK2-G2019S astrocytes in the study, suggesting that use of different mouse models results in changes to lysosomal pH (Streubel-Gallasch et al., 2021). Finally, mouse primary neurons homozygous for LRRK2-G2019S show reduced levels of LAMP-1 and LAMP-2, a larger number of lysosomes that are smaller in size, and increased lysosomal pH (Schapansky et al., 2018).

1.11.3 Late endosomes and lysosomes are reduced in dopaminergic neurons in PD

A commonly used drug in animal models of PD is rotenone, a toxic pesticide that induces LRRK2-dependent oxidative stress (Quintero-Espinosa et al., 2023) leading to dopaminergic neurodegeneration and aggregation of α-synuclein (Miyazaki et al., 2020). Rotenone-treated rats show a LRRK2 kinase-dependent reduction in the late endosomal/lysosomal marker LAMP-1 and the chaperone-mediated autophagy marker LAMP-2a by immunofluorescence (Di Maio et al., 2018). Increased early

endosomes and decreased late endosomes/lysosomes in post-mortem brain tissue from PD patients is also described (Rocha et al., 2020). Additionally, PD post-mortem brain tissue shows a reduction in degradative lysosomal enzymes such as cathepsin D and aspartyl protease (Rocha et al., 2020). As such, a current hypothesis in PD pathogenesis is that there is impaired endosomal and lysosomal maturation induced by LRRK2 kinase overactivity, resulting in a defect in cellular degradative capacity.

1.12 Lysosomal damage in health and disease

Since their discovery in 1955, lysosomal hydrolases were considered a potential threat to cell survival due to their high degradative capacity; harmful effects would surely result from their leakage into the cytosol (De Duve et al., 1955). In recent years, this perspective has shifted and it has been proposed that low levels of lysosomal damage are in fact essential for cell division, genetic integrity, cell movement, and cell signalling (Reinheckel and Tholen, 2022; Stahl-Meyer et al., 2021). However, the process of lysosomal damage is utilised by some pathogens as a mechanism to evade immune responses, and excessive lysosomal damage is thought to contribute to the pathology of neurodegenerative disease such as PD.

1.12.1 Physiological lysosomal damage

Acid hydrolases such as cathepsins have been imaged in the nucleus of intact cells during mitosis. Although acid hydrolases function optimally at low pH, they remain stable at pH 7.2 but show different substrate preferences and activities (Boya and Kroemer, 2008; Yoon et al., 2021). Hämälistö and colleagues demonstrated the importance of cathepsin B to mitosis *in vitro* and *in vivo*: they found that perinuclear lysosomes become ‘leaky’ during mitosis, as evidenced by staining with the lysosomal damage marker Galectin-3 (Gal3). Cathepsin B was imaged outside of lysosomes and near the nucleus, where it cleaves histone H3 to promote chromosome segregation (Hamalisto et al., 2020). In another study, Cathepsin L was captured near the nucleus of NIH-3T3 cells that were in between the G1 and S phases of the cell cycle, where it regulates cell cycle progression (Goulet et al., 2004). It has been suggested that telomeres can induce lysosomal damage and leakage

during mitosis, promoting cathepsin release into the nucleus (Stahl-Meyer et al., 2021).

Acid proteases have also been detected in the cytosol, where they regulate cytoskeletal motor proteins and cell motility. In T cells, Cathepsin X co-localises with the cytoskeletal protein Talin and the adhesion molecule lymphocyte function-associated antigen 1 (LFA-1) to promote cell movement (Jevnikar et al., 2009). Additionally, redistribution of cell cytoskeleton components results from the interactions of cytosolic Cathepsin L with dynamin and synaptopodin proteins in kidney cells, altering renal filtration (Sever et al., 2007; Yaddanapudi et al., 2011). Confirmation that the source of cathepsin in these studies is from lysosomal leakage, although likely, is not yet demonstrated, and the instigator of lysosomal damage in these circumstances is unknown.

Lysosomal damage in immune cells such as macrophages is important during inflammation: low levels of lysosomal leakage mediate nucleotide-binding domain, leucine-rich repeat-containing family, pyrin domain containing 3 (NLRP3) activation (Katsnelson et al., 2016). The NLRP3 inflammasome is a cytosolic multiprotein complex that assembles upon sensing of cytosolic PAMPs. After assembly it interacts with apoptosis-associated speck-like protein containing a CARD (ASC) to form ASC specks, resulting in activation of caspase-1, release of IL-1β and initiation of pyroptosis (discussed below) (Nguyen et al., 2022). The link between NLRP3 inflammasome activation and lysosomal leakage is based on data showing cathepsin inhibition or knock-out/knock-down of genes encoding cathepsins inhibits NLRP3 activation, indicating that it is the action of cathepsins, presumably in the cytosol after leakage through the damaged lysosomal membrane, that triggers NLRP3 activation (Bruchard et al., 2013; Halle et al., 2008; Orlowski et al., 2015). Interestingly, NLRP3 activation is limited to conditions of low-level lysosomal leakage – at high levels of lysosomal damage, there is polyubiquitination of the inflammasome with reduced caspase-1 activation (Katsnelson et al., 2016). The NLRP3 inflammasome is essential for the control of bacterial, fungal, and viral infections and in producing an inflammatory response to trauma that is required for tissue repair, thus it is an important part of normal immune cell function (Menu and Vince, 2011). A summary

of the physiological processes involving lysosomal damage are summarised in **Figure** 1.12.1.

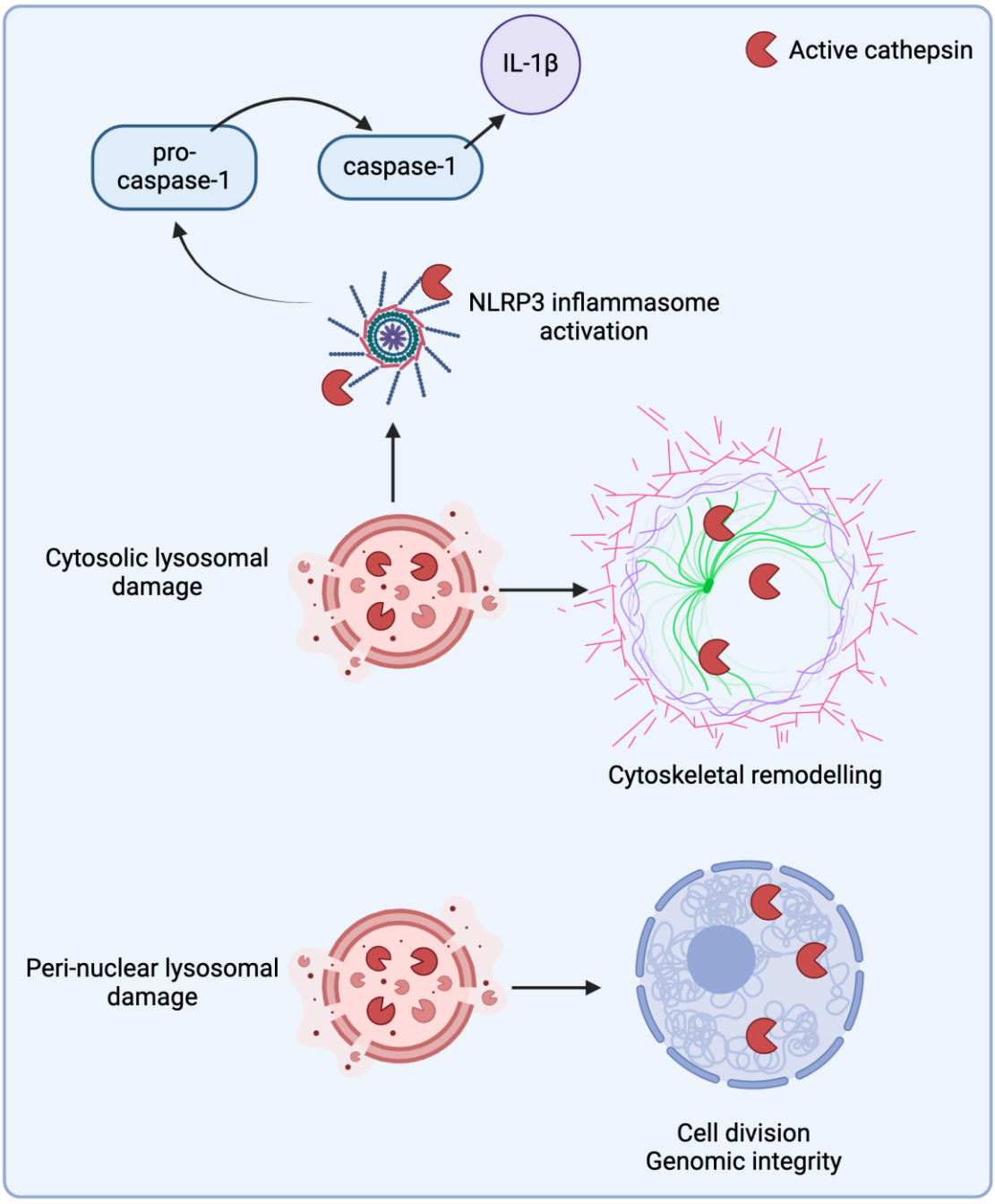

Figure 1.12.1. An overview of physiological processes that involve lysosomal damage.

Cathepsin activity has been reported in the nucleus and cytosol of intact cells. In the nucleus, cathepsins released from leaky peri-nuclear lysosomes were essential for cell cycle progression, mitosis, and maintenance of genomic integrity. In the cytoskeleton, active cathepsins interact with motor proteins to regulate cell motility.

Finally, cathepsin release from damaged lysosomes in the cytosol can trigger NLRP3 inflammasome activation, resulting in the release of pro-inflammatory mediators such as IL-1β. Image created on biorender.com.

1.12.2 Lysosomal damage in disease

In several human infections pathogens induce lysosomal damage to escape the degradative lysosomal environment, thus evading killing by the host cell. Tuberculosis infection by the pathogen Mtb triggers lysosomal damage during infection: Mtb is found in the cytosol of macrophages as early as 2 h post-infection, and by 48 h post-infection up to 50% of bacteria are present in the cytosol (Lerner et al., 2017). The ESX-1 secretion system produced by Mtb is essential for its lysosomal escape into the cytosol, and bacteria lacking ESX-1 activity are unable to replicate efficiently (Bussi and Gutierrez, 2019). Another example of a pathogen that damages the lysosomal membrane is Listeria monocytogenes. Listeria secretes the protein Listeriolysin-O (LLO), which forms pores in the lysosomal membrane through which bacteria escape into the cytosol and replicate (Ruan et al., 2016). Finally, the fungal organism Candida albicans produces the pore-forming compound Candidalysin, and this is a key virulence factor in its infection (Russell et al., 2023).

Intriguingly, lysosomal damage is also linked to α-synuclein, the main component of Lewy bodies in PD. α-synuclein fibrils cause lysosomal membrane damage *in vitro* in neuronal cell lines and THP-1 cells (Freeman et al., 2013). In post-mortem brain tissue from PD patients over 50% of Lewy bodies were surrounded by a ring of the damage marker Gal3, strongly suggestive of previous membrane damage at this region (Flavin et al., 2017). It has also been suggested that reduced cathepsin and LAMP-1 immunostaining in PD brains could also reflect loss of lysosomal membrane integrity during disease (Chu et al., 2009). Loss of lysosomal membrane integrity by α-synuclein is postulated to result from mechanical stresses imposed upon the membrane, although the precise mechanism is unknown (Freeman et al., 2013). The consequences of α-synuclein-induced lysosomal damage include cytosolic α-synuclein aggregation (Sanyal et al., 2024), release of α-synuclein-containing exocytic vesicles (Abe et al., 2024), ROS production, and inflammasome activation (Freeman et al., 2013). As discussed above, NLRP3 inflammasome activation is a

normal part of the immune response and is triggered by lysosomal membrane damage. However, prolonged activation of the inflammasome leads to deleterious, pro-inflammatory states resulting in tissue damage. Indeed, the NLRP3 inflammasome is activated in PBMCs from PD patients and the degree of activation closely correlates with motor symptom severity (Fan et al., 2020; Gordon et al., 2018).

1.12.3 Induction of lysosomal damage

There are a multitude of lysosomal damaging agents that are encountered by cells in health and disease, thus representing a persistent threat to lysosomal homeostasis. These include fatty acids, bile salts, cholesterol oxidation products, cholesterol crystals, oxidative stress, osmotic stress, neurotoxic aggregates including amyloid and tau, silica crystals, urate crystals, and alum salts, to name a few (Boya, 2012). L-leucyl-L-leucine methyl ester (LLOMe) is a drug that is commonly used to study lysosomal damage: it is rapidly taken into cells by amino acid transporters on the plasma membrane and lysosomal membrane (Katsnelson et al., 2016; Thiele and Lipsky, 1990a). LLOMe is cleaved and activated by the lysosomal enzyme dipeptidyl-peptidase I (also known as Cathepsin C) into membranolytic metabolites that destabilise the lysosomal membrane (Thiele and Lipsky, 1990a). Lysosomal damage is detected immediately upon LLOMe treatment in live cell imaging of human cancer cell lines and human fibroblasts (Eriksson et al., 2023; Eriksson et al., 2020). The damage marker Gal3 can be detected after 30 minutes of LLOMe treatment and reaches peak levels after 1-2 hours (Eriksson et al., 2020; Radulovic et al., 2018). The prompt uptake and action of LLOMe is advantageous in experimental settings as it induces a relatively synchronous form of lysosomal damage, thus reducing variability.

1.13 Cellular responses to lysosomal membrane damage

Lysosomal membrane damage can ultimately lead to cell death (Boya and Kroemer, 2008). However, cells employ several pathways to manage lysosomal damage that allow them to survive. In the next section, I will discuss pathways activated by lysosomal damage including lysosomal membrane repair, lysophagy, and lysosomal

biogenesis. I will also discuss the types of cell death that occur in response to lysosomal damage.

1.13.1 Lysosomal membrane repair

Lysosomal repair is activated early in the response to lysosomal damage (Radulovic et al., 2018). Stress granules are a type of membraneless organelle described as cytosolic condensates comprising derivates of mRNA admixed with proteins like G3BP1 and G3BP2 (Guillen-Boixet et al., 2020). Bussi and colleagues demonstrated that stress granules rapidly seal sites of lysosomal membrane damage in human iPSDM, human monocyte derived macrophages and epithelial cell lines, functioning to both stabilise the damaged membrane and facilitate repair pathways (Bussi et al., 2023). One of these pathways is the Endosomal Sorting Complexes Required for Transport (ESCRT) machinery (Radulovic et al., 2018; Skowyra et al., 2018), comprising complexes ESCRT-0, -I, -II, -III, and VPS4. Notably, the ESCRT-III complex, consisting of charged multivesicular body protein- (CHMP) -2A, -2B, -3, -4A, -4B, -4C, and -6, is downstream of all ESCRT reactions (Schmidt and Teis, 2012). Many ESCRT components, except for ESCRT-0, have been identified at sites of lysosomal damage across multiple cell types, and this recruitment is calcium-dependent (Radulovic et al., 2018; Skowyra et al., 2018). ESCRT recruitment to lysosomal damage is also dependent on Gal3, which promotes interactions between various ESCRT components (Jia et al., 2020). ESCRT recruitment is rapid, detectable after 1 minute of damaged induced by LLOMe, and transient, disappearing over time (Skowyra et al., 2018). ESCRT-mediated lysosomal repair is critical for cell survival: cells deficient in ESCRT machinery show excessive cell death in response to lysosomal damage (Radulovic et al., 2018).

In recent years, several ESCRT-independent lysosomal membrane repair pathways have come to light. Yim *et al.* describe the role of Annexins (ANX) ANXA1 and ANXA2 in lysosomal repair: after 30 minutes of LLOMe treatment, around 20-30% of lysosomes recruit these proteins (Yim et al., 2022). The recruitment of ANXA1 and ANXA2 is calcium-dependent but limited to a subset of lysosomes that do not recruit ESCRT components. Using an unbiased proteomics approach to identify proteins

enriched on damaged lysosomes, Tan *et al.* identified an ESCRT-independent repair pathway mediated by phosphatidylinositol-4-kinase 2α (PI4K2A), which mediates the recruitment of oxysterol-binding protein (OSBP)-related proteins (ORP) family proteins (Tan and Finkel, 2022). ORP family proteins action lysosomal membrane repair through delivery of cholesterol and other membrane components. Finally, Niekamp *et al*. discovered that the lysosomal membrane lipid sphingomyelin, which is normally present on the inner aspect of the lysosomal membrane, becomes exposed on the outer aspect of the lysosomal membrane during damage in a calcium-dependent manner, where it mediates lysosomal repair through its interactions with neutral Sphingomyelinase-2, an enzyme that converts sphingomyelin to ceramide (Niekamp et al., 2022).

1.13.2 Lysophagy

Lysosomal damage also results in the removal of lysosomes by the autophagy machinery, a process deemed “lysophagy”. Initiation of lysophagy is via galectins (Gal), a family of carbohydrate-binding proteins that are ordinarily diffusely disturbed throughout the cytosol in cells (Cummings and Liu, 2009). Eleven galectins are expressed in human tissue, however Gal3 and Galectin-8 (Gal8) are implicated in the response to lysosomal damage by binding to exposed sugar moieties at areas of lysosomal membrane damage (Cummings and Liu, 2009; Papadopoulos and Meyer, 2017). Gal3 and Gal8 recruitment appears to dependent on the amount of damage and the initiator of damage, and each Gal activates independent downstream effectors. Gal3 detects complete lysosomal rupture, for example following treatment by LLOMe, and lysosomes damaged by Mtb (Papadopoulos and Meyer, 2017). In addition to co-ordinating the recruitment of ESCRT membrane repair components, Gal3 recruits tripartite motif 16 (TRIM16), an E3 ligase that results in ubiquitination of damaged lysosomes and components of the autophagic machinery, resulting in engagement of autophagy receptors (Chauhan et al., 2016). Gal8 recognises damage induced by viruses and the bacterium *Salmonella typhimurium* (Thurston et al., 2012). In response, Gal8 directly interacts with autophagy receptors (Papadopoulos and Meyer, 2017). Autophagy receptor activation ultimately results in the formation of a double membrane autophagosome, characterised by the

presence of Atg8/LC3, which fuses with lysosomes to degrade luminal components (Maejima et al., 2013).

1.13.3 Lysosomal biogenesis

In the absence of lysosomal damage, the lysosomal protein kinase mTORC1 phosphorylates and inactivates transcription factor TFEB, a master regulator of lysosomal biogenesis (Napolitano and Ballabio, 2016). In response to lysosomal damage, mTORC1 is inactivated by the damage sensing protein Gal8 (Jia et al., 2019). This results in dephosphorylation of TFEB and its translocation to the nucleus, leading to the transcription of genes encoding lysosomal components. In this way, new lysosomes are synthesised, presumably to compensate for those lost by lysosomal damage during lysophagy or lysosomal exocytosis.

1.13.4 Lysosomal cell death

The above processes are crucial for cell homeostasis because the leakage of lysosomal contents into the cytosol can cause widespread damage and cell death (Wang et al., 2018a). There are to-date 27 different types of cell death which can be divided into two categories: regulated cell death and unregulated cell death (Dehghan et al., 2023). Necrosis is unregulated cell death that cannot be molecularly defined because it occurs secondary to a disordered and random deluge of events (Dehghan et al., 2023). For the other 26 types of regulated cell death, there is precise activation of defined molecular pathways, although some are cell-type specific and only present in defined contexts. In this next section, I will discuss three well-defined modes of regulated cell death that are linked to lysosomal damage and LRRK2: apoptosis, pyroptosis and necroptosis.

Apoptosis was first described in 1972 as a mechanism of “controlled cell deletion” (Kerr et al., 1972). Apoptosis shows characteristic morphological features of nuclear condensation and apoptotic body formation (Kerr et al., 1972) and a defined molecular pathway comprising caspase (cas) family proteins (Alberts, 2022). Intrinsic

apoptosis is initiated by intracellular stressors that trigger mitochondrial outer membrane permeabilisation (MOMP), leading to activation of cas-9, followed by activation of the “executioner caspases” Cas-3 and Cas-7 (Vitale et al., 2023). Extrinsic apoptosis is triggered by binding of a ligand to a cell surface death receptor – for example binding of Fas ligand (FAS) ligand to FAS death receptor. The engagement of death receptors results in activation of Cas-8, which subsequently activates the “executioner caspases” Cas-3 and Cas-7. Notably, apoptosis is often described as an “immune silent” form of cell death because there is removal of apoptotic cells by efferocytosis, preventing release of cell components into the extracellular space and triggering inflammation (Alberts, 2022). However, late stages of apoptosis do eventually result in loss of membrane integrity and release of contents into the extracellular space, a process deemed “secondary necrosis” (Silva, 2010).

Pyroptosis is a type of pro-inflammatory cell death that can be triggered by cells that express components of the inflammasome such as macrophages (Wei et al., 2022). Morphologically, pyroptotic cells become swollen and show membrane “blebs” prior to lysis. Pyroptosis activation occurs when intracellular pattern recognition receptors bind to damage associated molecular patterns (DAMPs) or PAMPs, triggering inflammasome assembly, recruitment of ASC and pro-caspase 1, followed by activation of Cas-1 and cleavage of IL-1β and Gasdermin D (GSDMD). Alternatively, endocytosed LPS components binding to intracellular cas-4 or cas-11 results in direct assembly of GSDMD. Finally, LPS binding to TLR4 receptor is also important for NF-$\kappa\beta$-mediated transcription of pyroptotic genes including pro-IL-1β. GSDMD cleavage is thus the hallmark of pyroptosis, and results in the creation of pores in the plasma membrane.

Necroptosis appears morphologically indistinguishable from necrosis but is in fact controlled by defined molecular machinery (Bertheloot et al., 2021). Necroptosis is initiated by binding of TNF-α to TNF receptor. For necroptosis to proceed, an absence of caspase-8 activity is required. In the absence of Caspase-8, RIPK1 and RIPK3 are recruited and act to phosphorylate one another, leading to the recruitment and phosphorylation of MLKL. pMLKL then induces damage at the plasma

membrane, resulting in cell lysis. A summary of the pathways implicated in apoptosis, necroptosis and pyroptosis are shown in Figure 1.13.1.

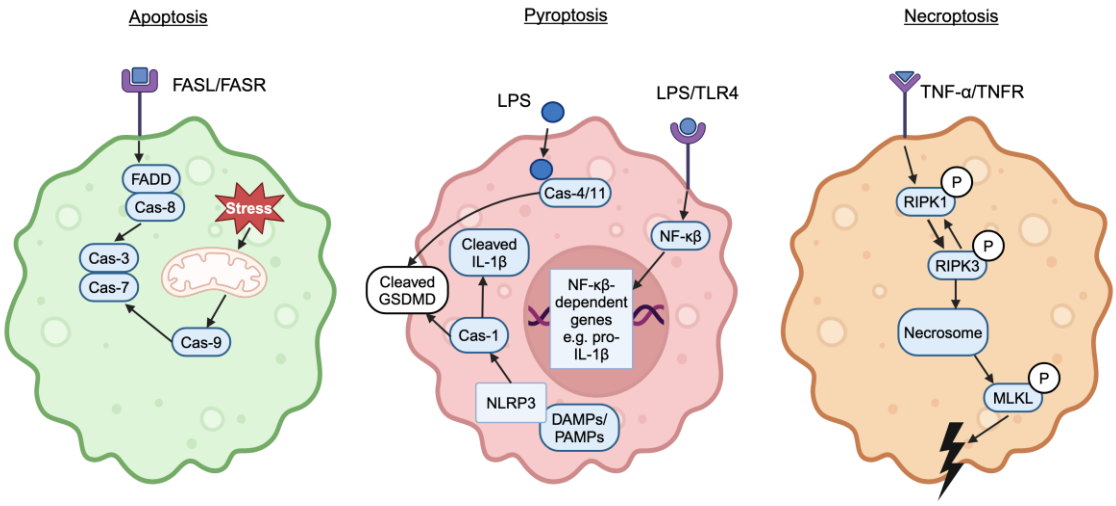

Figure 1.13.1. Summary of apoptosis, pyroptosis and necroptosis pathways.

Abbreviations: FASL – Fas ligand; FASR – FAS receptor; FASDD – FAS-associated death domain; Cas – caspase; LPS – lipopolysaccharide; TLR – toll-like receptor; NF-κβ - nuclear factor κβ; IL-1β - interleukin-1β; DAMP – damage associated molecular pattern; PAMP – pathogen associated molecular pattern; GSDMD – Gasdermin D; RIPK – receptor interacting protein kinase; MLKL – mixed lineage kinase domain like pseudokinase; TNF - tumour necrosis factor; TNFR – TNF receptor.

Lysosomal damage can induce different forms of cell death dependent upon the area of membrane damaged within an individual lysosome, overall number of lysosomes damaged within a cell, the size and subcellular location of the damaged lysosomes, and cell type (Wang et al., 2018a). In the case of acute and extensive lysosomal damage, necrosis is thought to be the primary form of cell death due to massive cathepsin release into the cytosol (Wang et al., 2018a). However, lysosomal damage and release of cathepsins into the cytosol can also trigger MOMP and the intrinsic apoptotic pathway (Aits and Jaattela, 2013; de Castro et al., 2016). Finally, as discussed above, lysosomal damage induced by some agents such as pathogens and neurotoxic aggregates can result in inflammasome activation in immune cells, thus induction of cell death by pyroptosis (Wang et al., 2018a).

1.14 LRRK2 and lysosomal damage

Lysosomal damage is a robust and reproducible activator of LRRK2 (Bonet-Ponce et al., 2020; Eguchi et al., 2018; Herbst et al., 2020; Kuwahara et al., 2020). Eguchi and colleagues first described LRRK2 activation in RAW 264.7 cells treated with chloroquine, a drug that induces lysosomal stress and the accumulation of enlarged lysosomes (Eguchi et al., 2018). In chloroquine-treated cells, LRRK2 localises to enlarged lysosomes along with its substrates Rab8A and Rab10 in a LRRK2 kinase-dependent manner. Herbst and colleagues demonstrated LRRK2 kinase-dependent phosphorylation of a group of Rab GTPases using an anti-phospho-pan-Rab antibody in RAW 264.7 cells in response to several lysosomal damaging agents including LLOMe, Mtb, Listeria and Candida (Herbst et al., 2020). LRRK2 activation by LLOMe appears to be cell type-dependent and time-dependent, peaking at around 60 minutes of treatment in RAW 264.7 cells and after 4 hours treatment mouse primary astrocytes (Bonet-Ponce et al., 2020; Herbst et al., 2020). In the next sections I will discuss the reported functions of activated LRRK2 during lysosomal damage.

1.14.1 LRRK2 co-ordinates lysosomal repair and lysophagy responses

Herbst *et al.* demonstrated in RAW 264.7 cells that LRRK2 is targeted to damaged lysosomes and, via its kinase activity, recruits the membrane damage marker Galectin-3 (Gal3) and the ESCRT-III component CHMP4B (Herbst et al., 2020) through Rab8A (Figure 1.14.1). LRRK2KO cells or cells treated with the LRRK2 kinase inhibitor GSK2578215A show reduced recruitment of CHMP4B and Gal3 to damaged lysosomes. Conversely, cells lacking in LRRK2 or treated with GSK2578215A demonstrated elevated levels of the lysophagy marker LC3B, indicating that LRRK2 kinase inactivation results in increased removal of damaged lysosomes through the autophagy pathway (Figure 1.14.1).

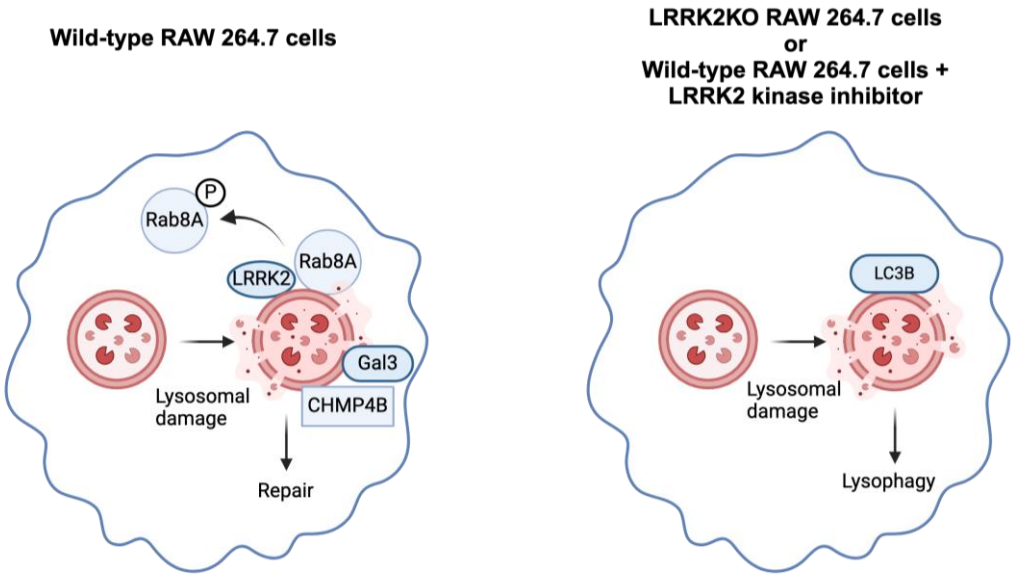

Figure 1.14.1. Summary of the role of LRRK2 in lysosomal damage and repair in RAW 264.7 cells.

Herbst *et al.* show lysosomal damage results in the recruitment of LRRK2 and Rab8A to damaged lysosomes alongside the membrane damage marker Galectin-3 (Gal3) and the ESCRT III repair component CHMP4B. In cells lacking LRRK2 (LRRK2KO) and in cells treated with a LRRK2 kinase inhibitor, damaged lysosomes accumulate the lysophagy marker LC3B. (Herbst et al., 2020).

Intriguingly, monocyte-derived macrophages from PD patients carrying LRRK2 mutations show an accumulation of Gal3-positive vesicles in the resting state (Herbst et al., 2020). Although only 3 patients were included in this study, this suggests that lysosomal damage is a feature in immune cells from LRRK2-PD patients (Herbst et al., 2020).

1.14.2 LRRK2-mediates tubulation and vesicle sorting from lysosomes

Work performed in mouse primary astrocytes and HEK293T cells revealed that LRRK2 is involved in a process named Lysosomal tubulation/sorting driven by LRRK2 (LYTL) (Bonet-Ponce et al., 2020). This study found no effect of LRRK2 kinase inhibition on the recruitment of Gal3 or induction of lysophagy, suggesting that these effects are cell type dependent. During lysosomal damage, there is LRRK2 kinase-dependent phosphorylation of Rab10 and Rab35, and co-localisation of LRRK2, Rab35, and Rab10 at sites of lysosomal damage. In this context, a downstream interactor of pRab10 is the motor protein JNK-interacting protein 4

(JIP4), which forms tubular structures at sites of lysosomal damage. These tubular structures are highly dynamic and appeared to interact with neighbouring lysosomes via generation of small vesicles. Although the exact role of these tubular structures and vesicles is unknown, the authors hypothesise that LRRK2 activation is key to sorting components of damaged lysosomes within the cell.

1.15 LRRK2 and cell death

The pathological hallmark of PD is death of dopaminergic neurons in the substantia nigra pars compacta of the midbrain, however there is neuronal cell death throughout the brain with different cell types displaying different degrees of vulnerability (Braak et al., 2004). The induction of cell death in PD is reported to involve ROS-mediated toxicity, mitochondrial dysfunction, neuroinflammation and apoptosis (Przedborski, 2005). The role of LRRK2 in activation of cell death pathways is unclear, however the kinase activity of LRRK2 is essential for its cytotoxic effects (Greggio et al., 2006). When over-expressed, wild-type LRRK2 led to apoptosis in neuronal cell lines and primary neurons exposed to the neurotoxin MPP, an effect reversed by gene silencing (Chen et al., 2018). However, wild-type LRRK2 was associated with inhibition of apoptosis in thyroid carcinoma cell lines, suggesting that it may have cell-specific mechanisms of action (Jiang et al., 2019; Zhao et al., 2019). On the other hand, LRRK2-G2019S is consistently reported to increase apoptosis when overexpressed in primary neurons (Cho et al., 2018; Yuan et al., 2011) and HEK293/SHSY5Y cell lines (Liou et al., 2008), with different signalling cascades being implicated including p38-MAPK pathway, ERK1/2 pathway and oxidative stress. Further, human LRRK2-G2019S iPSC-derived neurons (Yoon et al., 2017) and LRRK2-G2019S iPSC-derived neural stem-cells (Liu et al., 2012) show increased apoptosis via the p38-MAPK pathway after induction of proteasomal stress.

LRRK2 is implicated in immune cell death. Wild-type LRRK2 induced apoptosis via the p38-MAPK and ERK1/2 pathways in RAW 264.7 and HMC3 cell lines exposed to the neurotoxin Manganese (Kim et al., 2019). Additionally, a small clinical study reported higher rates of spontaneous apoptosis in lymphocytes isolated from the blood of *LRRK2*-PD patients compared to sporadic PD patients and healthy controls

(Usenko et al., 2012). Within the immune system, cell death is an innate immune defence triggered upon infection whereby death of the host cell results in clearance of the pathogen or activation of downstream immune responses (Ashida et al., 2011). These studies suggest that LRRK2 could contribute to immune dysfunction by interfering with cell death pathways in immune cells, though the mechanism by which this could lead to PD is unclear. Finally, these studies measured apoptotic cell death and to-date it is unknown whether LRRK2 functions in other types of cell death including pyroptosis and necrosis (Tang et al., 2019).

1.16 Thesis aims

Aim 1: Investigate the effect of mutant LRRK2 on lysosomal morphology and function in macrophages

Current literature does not show a clear lysosomal phenotype in LRRK2-mutant cells: some studies report changes in lysosomal subcellular location, lysosomal size, pH, and proteolytic activity, while others report either no effect or contradictory results. Additionally, there appear to be marked differences between cell types. I aimed to clarify the effect of LRRK2 mutations on baseline lysosomal morphology and function in a physiological macrophage model with endogenous levels of LRRK2 expression. I used two different biological systems: human iPSDM and murine primary bone marrow derived macrophages, to comprehensively classify the morphology, content, and activity of lysosomes between LRRK2-mutant and LRRK2-wild-type cells.

Aim 2: Explore the pathways initiated by lysosomal damage in LRRK2 mutant macrophages

Wild-type LRRK2 is activated by lysosomal damage and phosphorylates Rab substrates at the lysosomal membrane. In the absence of LRRK2 or in the presence of a LRRK2 kinase inhibitor, RAW 264.7 cells increase lysophagy in response to lysosomal damage and are unable to efficiently initiate lysosomal repair. However, no data on the effect of LRRK2 mutations on these pathways exists in the published literature. I aimed to explore the response of macrophages carrying a LRRK2-mutation to lysosomal damage. Given that LRRK2 mutations cause increased kinase

activity, I aimed to investigate whether this increase in kinase activity would translate into hyper-activation or dysfunction of lysosomal repair pathways and lysophagy.

Further, another consequence of lysosomal damage is initiation of cell death. Lysosomal damage has been linked to apoptosis, pyroptosis and necrosis. Given that LRRK2-G2019S is associated with an increase in apoptosis across multiple cell types, I aimed to explore the cell death pathways initiated by lysosomal damage in LRRK2-WT and LRRK2-G2019S macrophages. Moreover, the lysosomal repair and lysophagy pathways are vital for cell survival. I aimed to translate any changes in the lysosomal repair and lysophagy pathway's in LRRK2 mutant macrophages to effects on the amount or type of cell death present after lysosomal damage.

Aim 3: Define the substrates of LRRK2 in macrophages

Previous studies have defined the bona fide substrates of endogenous LRRK2 kinase in non-immune cells. LRRK2 is expressed at high levels in immune cells and is closely regulated by immune stimuli, thus its function and substrates may differ according to cell type. Utilising macrophages that express a kinase-dead form of LRRK2, I aimed to define the bona fide substrates of LRRK2 kinase in macrophages in both resting state and after lysosomal damage. Further, I aimed to compare substrates of mutant LRRK2 and wild-type LRRK2 during lysosomal damage to identify novel pathways in macrophages that are altered by LRRK2 mutations.

Chapter 2. Materials & Methods

2.1 Cell culture

2.1.1 Animals

Depending on the mouse strain, breeding pairs, embryos or sperm were purchased from Taconic Biosciences or Jackson laboratories. The strains utilised were C57BL/6NTac and C57BL/6-Lrrk2$^{tm4.1Arte}$ (Taconic Biosciences, 13940) (Matikainen-Ankney et al., 2016); C57BL/6NJ and B6(SJL)-Lrrk2$^{tm4.1Mjff/J}$ (Jackson laboratories, 021830) (Crabbe et al., 1985); C57BL/6J (6J-WT) and B6.129X1(FVB)-Lrrk2$^{tm1.1Cai/J}$ (6J-LRRK2KO) (Jackson laboratories, 012453) (Parisiadou et al., 2009). The LRRK2-G2019S mutation was present in the C57BL/6-Lrrk2$^{tm4.1Arte}$ constitutive homozygous knock-in mouse model through introduction of a single point mutation into exon 41 of the LRRK2 gene. The LRRK2-D1994A mutation was present in the B6(SJL)-Lrrk2$^{tm4.1Mjff/J}$ heterozygous knock-in mouse model through introduction of a single point mutation into exon 41 of the LRRK2 gene. The homozygous LRRK2 KO mouse model B6.129X1(FVB)-Lrrk2$^{tm1.1Cai/J}$ was created by deletion of exon 2, resulting in a premature stop codon in exon 3.

As the wild-type mouse corresponding to each of the LRRK2 mutants and LRRK2 KO was different, the following nomenclature was used to clarify this in the results chapters (Table 2.1.1).

Mouse strain	**Wild-type or mutant**	**Nomenclature**
C57BL/6NTac C57BL/6-Lrrk2$^{tm4.1Arte}$	Wild-type LRRK2-G2019S mutant	Tac-WT Tac-G2019S
C57BL/6NJ B6(SJL)-Lrrk2$^{tm4.1Mjff/J}$	Wild-type LRRK2-D1994A mutant	NJ-WT NJ-D1994A
C57BL/6J B6.129X1(FVB)-Lrrk2$^{tm1.1Cai/J}$	Wild-type LRRK2 KO	6J-WT 6J-LRRK2KO

Table 2.1.1. Nomenclature used for the wild-type and LRRK2 mutant/LRRK2 KO mice

Mice were re-derived, bred in-house and maintained under specific pathogen-free conditions at the Francis Crick Institute (UK). Animal studies and breeding were approved by the Francis Crick Institute ethical committee and performed under U.K Home Office project license (P4D8F6075). All animal studies were ethically reviewed and carried out in accordance with Animals (Scientific Procedures) Act 1986. All animal handling was carried out by Dr Angela Rodgers (Principal Laboratory Research Scientist, The Francis Crick Institute).

2.1.2 Culture of RAW 264.7 cells

The mouse macrophage cell line RAW 264.7 was maintained in RPMI 1640 medium (72400-021, Gibco) supplemented with 10% heat inactivated fetal bovine serum (FBS) (10270-106, Gibco) with the addition of 1% penicillin-streptomycin (P4333, Thermo). Cells were incubated at 37^{o}C, 5% CO_2 atmosphere and media was changed every 2-3 days.

The RAW 264.7 cell lines used in this thesis were genome edited to express LRRK2-G2019S, LRRK2-R1398H, LRRK2-N551K and LRRK2-R1398H-N551K mutations and were a gift from Professor Erwin Schurr (McGill University Health Centre, Montreal) (Dallmann-Sauer et al.).

2.1.3 Culture of murine primary bone marrow-derived macrophages

Primary bone marrow derived macrophages (BMDM) were isolated as described previously (Schnettger and Gutierrez, 2017). The femur and tibia bones were dissected from the mouse hind legs. The bone marrow cavity was accessed by removing the ends of the bones, and ice-cold PBS was flushed through the medullary cavity using a 25G needle. Bone marrow cells were differentiated in RPMI 1640 medium (72400-021, Gibco) containing 10% FBS (10270-106, Gibco), 50 ng/ml GM-CSF (576306, BioLegend) and 1% penicillin-streptomycin (P4333, Thermo) for 7 days at 37^{o}C in 5% CO_2 atmosphere with an 80% media replacement on day 4. BMDM were detached in ice-cold PBS and plated in RPMI containing 10% FCS and 1% penicillin-streptomycin for experiments.

2.1.4 Gene editing to generate isogenic human induced pluripotent stem cells

In this thesis, one isogenic control-generated iPSC line was used. This isogenic control line was generated from LRRK2-G2019S iPSC derived from a PD patient (clone ID: CDI00002173) obtained from the Michael J Fox Foundation (MJFF) Parkinson's Progression Markers Initiative (PPMI) resource. The LRRK2-G2019S CDI00002173 clone showed a normal karyotype (46 XY) and was Mycoplasma negative. The CDI00002173 clone was confirmed to show the heterozygous LRRK2-G2019S mutation by Sanger sequencing (Figure 2.1.1) using the primers detailed in Table 2.1.1.

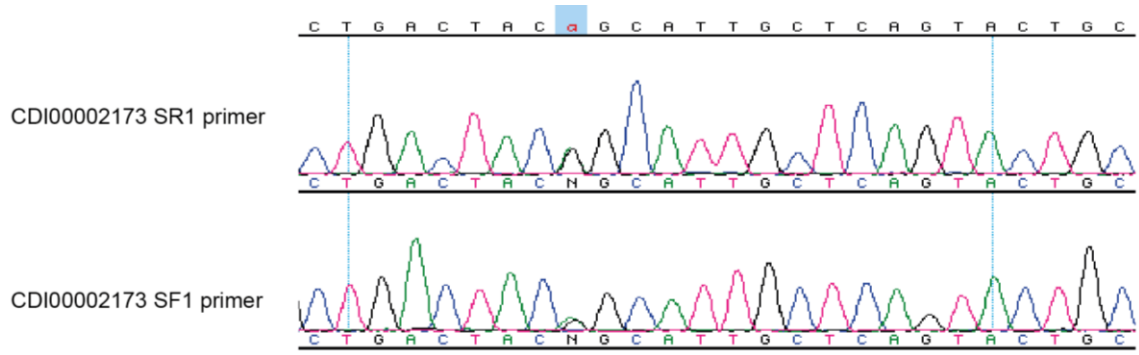

Figure 2.1.1. Sanger sequencing of LRRK2-G2019S iPSC line (CDI00002173)

Sanger sequencing of PCR products from LRRK2-G2019S iPSC line using the SR1 and SF1 primers.

Primer name	Sequence
Primers for PCR	
G2019S_GR1	5' – TAT ATC TCC TAG ACC CAC ACT TGA G – 3'
G2019S_GF1	5' – TAC CAG GCT TGA TGC TTT AGT TAT G -3'
Primers for sequencing	
G2019S_SR1	5' – GGG CAC TGA TGG TCC ACT GC -3'
G2019S_SF1	5' – TGG CAG GTA TCT CCA CTC AG -3'

Table 2.1.2. Primers used to confirm LRRK2-G2019S mutation

The isogenic control iPSC line was generated by Dr Enrica Pellegrino and Natalia Athanasiadi at the Host-Pathogen Interactions in Tuberculosis laboratory, The Francis Crick Institute. They devised the CRISPR strategy, including the selection of

sgRNAs and ssODN templates, and conducted experimental procedures such as nucleofection of iPSCs, following the protocol outlined below. Subsequently, clones were screened using PCR and sequencing methods. Confirmed corrected clones, exhibiting the reversal of the G2019S mutation, were subjected to further analyses, including testing for Mycoplasma contamination, assessment of pluripotency, and karyotyping.

To generate isogenic control iPSC, the clustered regularly interspaced palindromic repeats (CRISPR)/ CRISPR-associated protein-9 (Cas9) system was utilised. This system utilises a single guide RNA (sgRNA) to recognise a target gene and Cas9, an endonuclease which causes a double-stranded DNA breakage, allowing modifications to the genome by, for example, insertion of a single stranded oligodeoxyribonucleotide (ssODN) that introduces a nucleotide substitution into the gene. A protospacer adjacent motif (PAM) is a sequence of 3 nucleotides 'NGG' (where 'N' can be any nucleotide) within DNA that must bind to the 3' end of the sgRNA as this is where the Cas9 enzyme will induce DNA breakage.

Notably, most *LRRK2-G2019S* PD patients are heterozygous for the mutation, with only a few reported cases of PD patients homozygous for *LRRK2-G2019S* in North Africa (Bouhouche et al., 2017; Ishihara et al., 2006). In our patient donor iPSCs, the *LRRK2-G2019S* mutation is a heterozygous mutation thus there is one wild-type allele and one mutated allele. In the mutated allele there is a guanine to adenine nucleotide substitution in exon 41 (Figure 2.1.2). For correction of the LRRK2-G2019S mutation, the PAM sequence nearest the mutation was 27 nucleotides away (Figure 2.1.2). This meant that the designed sgRNA did not overlap with the mutation site (Figure 2.1.2), leading to increased risk of insertions/deletions (InDel) and decreased the likelihood of correcting the mutation during the CRISPR/Cas9 reaction. In addition, InDel were also possible in the wild-type allele.

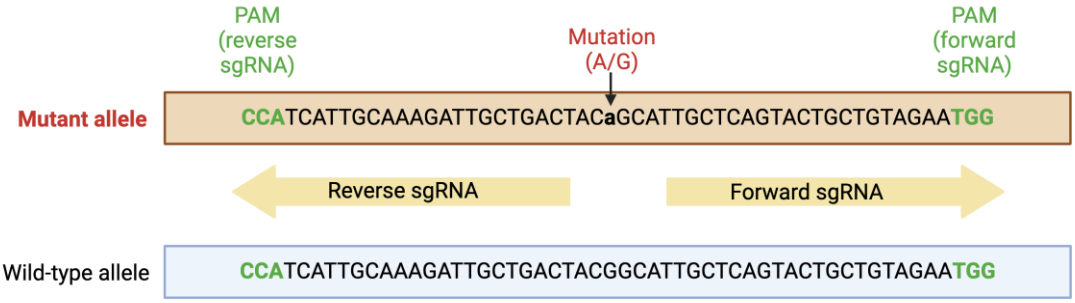

Figure 2.1.2. CRISPR/Cas9 approach number 1 to correction of LRRK2-G2019S mutation in iPSC

Nucleofection using the Amaxa 4D-Nucleofector (V4XP-3024, Lonza) was performed in the LRRK2-G2019S iPSCs (clone ID: CDI00002173). For each nucleofection, 1 × 10^6 iPSCs were resuspended in 100 µl of P3 buffer (V4XP-3024, Lonza) containing 20 µg Alt-R® S.p. Cas9 Nuclease V3 (1081059, IDT) mixed with 16 µg targeting synthetic chemically modified sgRNAs (Synthego) (Table 2.1.3**,** LRRK2-1st-step) and 200 pmol of the ssODN (harbouring the corrected nucleotide), as previously described (Skarnes et al., 2019).

Name	**Sequence 5'->3'**
LRRK2-1st-step	TGCTCAGTACTGCTGTAGAATGG
LRRK2-2nd-step	TGTAGTCAGCAATCTTTGCA
ssODN-LRRK2	GAAACCCCACAATGTGCTGCTTTTCACACT GTATCCCAATGCTGCCATCATTGCAAAGA TTGCTGACTACGGCATTGCTCAGTACTGCTGTAGAAT GGGG

Table 2.1.3. Sequence of sgRNA and ssODN used in CRISPR/Cas9 reactions to generate isogenic control iPSC.

As predicted, the mutation was not corrected in most clones using this approach (30 out of 50 tested clones) and InDel were detected in most clones. Using the ICE platform from Synthego (https://ice.synthego.com/#/), we identified an InDel in the mutant allele only in 3 of the tested clones. Utilising this difference between wild-type and mutant alleles, a new CRISPR site was formed and a new sgRNA overlapping the InDel in the mutant allele were designed (Table 2.1.3, LRRK2-2nd-step) so that

only the mutant allele would be cut in the CRISPR/Cas9 reaction (Figure 2.1.3). For this study, we picked clone D4 containing an insertion of 6 bp (GCAGCA) for use in further experiments. The new sgRNA targeting the mutant allele was used to performed nucleofection in the selected clone. 1 × 10^6 of the selected clone were resuspended in 100 µl of P3 buffer (V4XP-3024, Lonza) containing 20 µg Alt-R® S.p. Cas9 Nuclease V3 (1081059, IDT), mixed with a total of 16 µg of the sgRNAs and 200 pmol of ssODN (Table 2.1.3), as described previously (Skarnes et al., 2019).

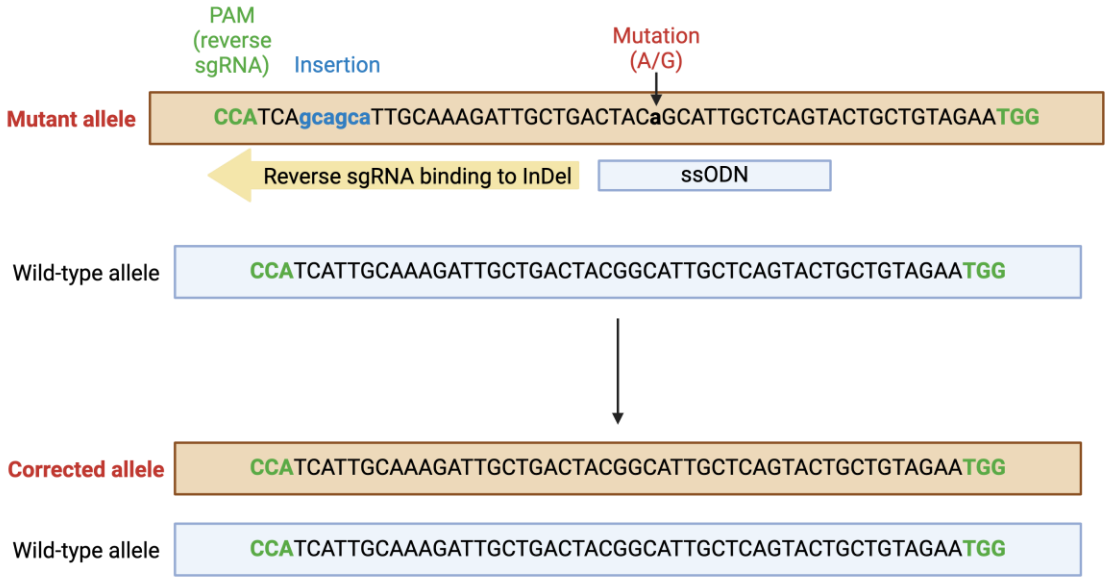

Figure 2.1.3. CRISPR/Cas9 2-step approach to correction of LRRK2-G2019S mutation in iPSC

The clones were screened by Sanger sequencing for the wild-type sequence, resulting in multiple independent wild-type clones (14 out of 48 tested). After karyotyping, pluripotency and Mycoplasma testing, the clone 0043052531 was selected for use in experiments. Sanger sequencing results are shown in Figure 2.1.4.

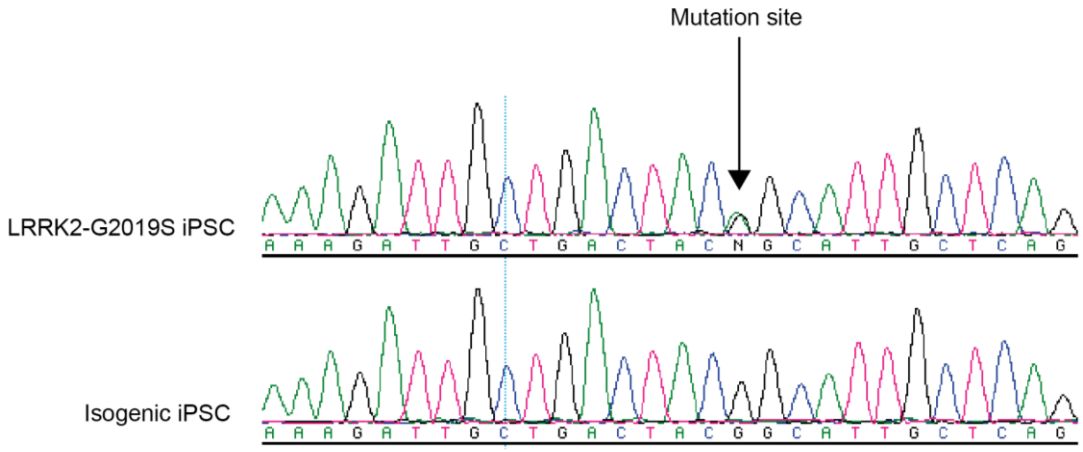

Figure 2.1.4. Sanger sequencing of LRRK2-G2019S (clone ID: CDI00002173) and isogenic control iPSC (clone ID: 0043052531).

2.1.5 Culture of induced pluripotent stem cells (iPSC)

I performed iPSC culture in collaboration with Natalia Athanasiadi (Host-Pathogen Interactions in Tuberculosis laboratory, The Francis Crick Institute). Human iPSC lines as described above (LRRK2-G2019S and isogenic control) were maintained in E8 (A1517001, Thermo) on Vitronectin XF (07180, Stem Cell Technologies) coated plates at 37ºC and 5% CO_2. Cells were passaged 1:6 at confluency using Versene (15040033, Thermo).

2.1.6 Culture of induced pluripotent stem cell-derived macrophages (iPSDM)

iPSDM differentiation was performed by Natalia Athanasiadi (Host-Pathogen Interactions in Tuberculosis laboratory, The Francis Crick Institute). I worked with the cells after collection of macrophage precursors from factories.

iPSCs were used to generate iPSDM following a previously reported protocol using embryoid bodies (EB) (Bernard et al., 2020; van Wilgenburg et al., 2013). Briefly, EBs were fed daily with two 50% media changes comprising E8 media (A1517001, Life Technologies), BMP4 50 ng/ml (120-05, Peprotech) and VEGF 50 ng/ml (100-20, Peprotech), SCF 20 ng/ml (300-07, Peprotech). On day 4, EBs were transferred to T225cm^2 flasks for macrophage differentiation using factory media consisting of

X-VIVO 15 (LZBE02-061Q, Lonza), 2 mM Glutamax (35050061, Life Technologies), 50 µM β-Mercaptoethanol (31350010, Life Technologies), 100 ng/ml M-CSF (300-25, Peprotech) and 25 ng/ml IL-3 (200-03, Peprotech). 20 ml fresh factory media was added once per week and after 4-5 weeks macrophage precursors were collected from the supernatant. These precursors were differentiated into macrophages in X-VIVO 15 (LZBE02-061Q, Lonza) containing 2 mM Glutamax (35050061, Life Technologies) and 100 ng/ml M-CSF (300-25, Peprotech) for 7 days. Macrophages were detached using Versene (15040066, Life Technologies), centrifuged at 300 x g and plated for experiments.

2.2 Cell treatments

2.2.1 Induction of lysosomal membrane damage

L-leucyl-L-leucine methyl ester (LLOMe) (4000725, Bachem) was prepared in methanol at a stock concentration of 333 mM and frozen at -20^{o}C. BMDM were treated with LLOMe at a concentration of 1 mM by dilution in RPMI. iPSDM were treated with LLOMe at a concentration of 0.5 mM by dilution in X-VIVO 15.

Stock crystalline silica (MIN-U-SIL-15, US Silica) was prepared at 30 mg/ml by dilution in sterile PBS immediately prior to use. A working solution of 300 µg/ml crystalline silica was prepared in RPMI for subsequent treatments.

2.2.2 LRRK2 kinase inhibition

Cells were pre-treated with MLi-2 (5756/10, Tocris) at 100 nM, GZD-824 (CAY21508, Cambridge Bioscience) at 0.1 µM, or GSK2578215A (ab254316, Abcam) at 0.1 µM for 1 hour and all subsequent treatments were performed in the presence of MLi-2, GZD-824 or GSK2578215A as indicated.

2.2.3 LRRK2 PROTAC treatment

The LRRK2 PROTAC XL01126 was purchased from MCE (HY-148030). 1 mM stock solution was prepared in DMSO and stored at -20 ^{o}C. For imaging, cells were pre-treated with XL01126 200 nM for 2 h and all subsequent treatments were performed in the presence of XL01126 where indicated.

2.2.4 LPS treatment

LPS (L8274, Sigma) was added to cells at a concentration of 250 ng/ml for 3 hours prior to downstream applications. Subsequent treatments were performed in the absence of LPS.

2.2.5 Positive controls for cell death

For induction of apoptosis, BMDMs were stimulated with 100 ng/ml TNF-α (300-O1A, Peprotech) and 125 nM 5Z-7-Oxozeaenol (9890, Sigma) for 7 h. For induction of necroptosis, BMDMs were stimulated with 100 ng/ml TNF-α (300-O1A, Peprotech), 125 nM 5Z-7-Oxozeaenol (9890, Sigma) and 10 μM Z-VAD-FMK (tlrl-vad, Invivogen) for 7 hours. For induction of pyroptosis, BMDMs were pre-treated with 250 ng/ml LPS (L8274, Sigma) for 3 h followed by 20 μM Nigericin for 3 h (ICT9146, Bio-Rad).

2.3 Imaging and image analysis

2.3.1 Indirect immunofluorescence

Cells were seeded in 96 well plates (6055302, Revvity) at a concentration of 50,000 cells/well. Cells were fixed in 4% PFA (15710, Electron Microscopy Sciences) for 15 minutes and then washed once with PBS. The samples were quenched with 50 mM NH_4Cl (A9434, Sigma) for 10 min at room temperature. Permeabilisation was performed with ice-cold methanol for 10 min at -20°C, 0.05% saponin, or 0.01% triton-X-100, depending on the primary antibody (Table 2.3.1). Cells were blocked in 5% FBS (10270-106, Gibco) in PBS for 1 h at room temperature. Primary antibodies (Table 2.3.1) were diluted in PBS containing 5% FBS and incubated for 1 h at room

temperature. Samples were washed three times in PBS and then secondary antibody (Table 2.3.1) was added for 1 h at room temperature. Following three washes with PBS, nuclear staining was performed using 300 nM DAPI (D3571, Life Technologies) in PBS for 10 min. After a further three washes in PBS, the samples were imaged using an automated confocal high-content imaging system (Revvity, Opera Phenix High-Content Screening System) with 63x 1.15 NA water-immersion objective and excitation lasers (405 nm, 488 nm, 561 nm, 640 nm) and preset emission filters. Channels were separated during acquisition to prevent fluorescence crosstalk. At least 800 cells per condition were imaged.

Antibody	Supplier	Catalogue	Dilution	Permeabilisation
LAMP-1	DSHB	1D4B	1:100	0.05% saponin
LAMP-2	Sigma	L0668	1:100	0.05% saponin
Galectin-3	BioLegend	125410	1:250	Methanol
CHMP4B	ProteinTech	13683	1:250	Methanol
LC3B	MBL	PM036	1:100	0.05% saponin
LRRK2*	Abcam	Ab133476	1:100	0.05% saponin Methanol 0.01% Triton-X-100
Goat anti-Rat IgG (H+L) AF-488	Thermo	A-11006	1:800	N/A
Goat anti-Rabbit IgG (H+L) AF-546	Thermo	A-11035	1:800	N/A

Table 2.3.1. Antibodies used for indirect immunofluorescence.

Permeabilisation methods used were: 0.05% saponin in PBS for 45 min at room temperature, 100% methanol for 10 min at -20^{o}C, 0.01% Triton-X-100 in PBS for 45 min at room temperature. Note – for LRRK2 antibody, multiple methods of permeabilisation were attempted.

2.3.2 Analysis of Gal3, CHMP4B and LC3B puncta in BMDM

Image analysis was performed using Harmony 4.9 image analysis software (Revvity). First, stacks were processed to create a maximum projection image. Nuclei were segmented using the “Find nuclei” building block (DAPI channel, method B, common threshold > 0.15, area > 20 μm^2, splitting coefficient 54.0, individual threshold 0.15,

contrast > 0.05). Following this, cell boundaries were segmented using the "Find cytoplasm" building block (Method A, individual threshold 0.15). The cell area was calculated in μm^2 using the "Calculate morphology properties" building block. After removing cells on the borders of the field via the "Select population, remove border objects" building block, individual puncta within a cell were segmented as follows. Using the "Find spots" building block and a set of criteria dependent on the target protein (Table 2.3.2), puncta plus some background objects were segmented. To remove the background objects, the "Select population" building block was applied using set criteria dependent on the target protein (Table 2.3.2). Next, the puncta area was calculated using the "Calculate morphology properties" building block and the total number of puncta and puncta area per cell was calculated using the "Calculate properties" building block. An example of the image analysis pipeline used to measure Galectin-3 is shown in Figure 2.3.1.

Antibody	**'Find spots' building block**	**'Select population' building block**
Gal3	Method D Cytoplasm region Detection sensitivity = 0.500 Splitting sensitivity = 0.500 Background correction = 0.500	Corrected spot intensity > 800 Spot area < 200 px^2
CHMP4B	Method A Cytoplasm region Relative spot intensity > 0.120 Splitting sensitivity = 0.711	Corrected spot intensity > 400 Spot area < 260 px^2
LC3B	Method A Cytoplasm region Relative spot intensity > 0.125 Splitting sensitivity = 0.711	Corrected spot intensity > 200

Table 2.3.2. Criteria used to segment Galectin-3, CHMP4B and LC3B puncta using Harmony 4.9 software.

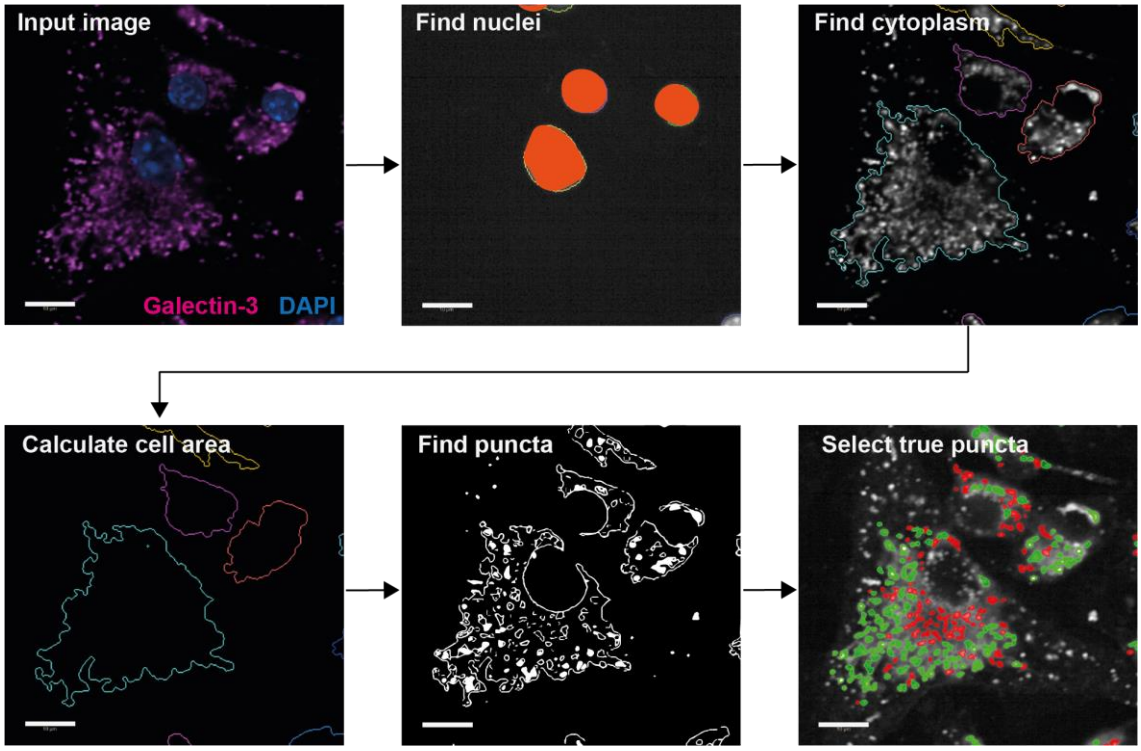

Figure 2.3.1. Example of image analysis pipeline for segmentation of Galectin-3 puncta within cells using Harmony 4.9 software.

Representative images of cell and puncta segmentation in wild-type BMDM treated with LLOMe 1mM for 30 min and stained for Galectin-3 and DAPI. Following nuclear and cytoplasm segmentation, puncta are selected in two steps: first using the "find spots" building block and then using the "selection population" building block to remove background objects. Scale bars = 10 μm.

2.3.3 Colocalisation analysis

To quantify Gal-3 and CHMP4B marker association, FIJI image analysis software (version 2.14.0) was utilised. First, a manual threshold was determined to produce a mask of Gal-3 puncta. An overlay of the Galectin-3 puncta mask was added to the CHMP4B channel using the "ROI manager" function on FIJI. Then, the "Analyse Particles" function, with pixel size 1.0-Infinity, was used to measure the mean fluorescence intensity (MFI) of CHMP4B. The MFI of manually selected CHMP4B positive and CHMP4B negative puncta was used to determine a cut-off MFI for CHMP4B+ puncta, and the percentage of CHMP4B+ association to Gal-3 puncta was calculated from this.

2.3.4 Live cell imaging with LysoTracker

Cells were seeded in 96 well plates (6055302, Revvity) and incubated with 25nM LysoTracker DND-99 (LTR) (L7528, Thermo Fisher Scientific) and NucBlue (Invitrogen, R37609) for 30 minutes at 37ºC, 5% CO_2. Next, cells were imaged using an automated confocal high-content imaging system (Revvity, Opera Phenix High-Content Screening System) with 40x 1.1 NA water-immersion objective, and excitation lasers (405 nm and 488nm) and preset emission filters. The 405 nm laser was used at 20% power with 100 ms exposure. The 488nm laser was used at 5% power with 80 ms exposure. The channels were separated during acquisition to prevent fluorescence crosstalk.

Image analysis was performed using Harmony 4.9 image analysis software (Revvity). First, stacks were processed to create a maximum projection image. Nuclei were segmented using the "Find nuclei" building block (Hoechst channel, method 'B'). Following this, cell boundaries were segmented using the "Find cytoplasm" building block (LTR channel, Method 'A'). The cell area was calculated in μm^2 using the "Calculate morphology properties" building block. Next, the LTR channel image was filtered using "Texture SER" and "SER Bright" methods (2 μm, unnormalized) to highlight the brightest portion of the LTR+ spots. Following this, LTR+ spots were segmented using the "Find image region" building block (common threshold 0.35) and the mean LTR+ cytoplasm intensity and LTR+ spot area was calculated. The LTR image analysis pipeline is demonstrated in Figure 2.3.2.

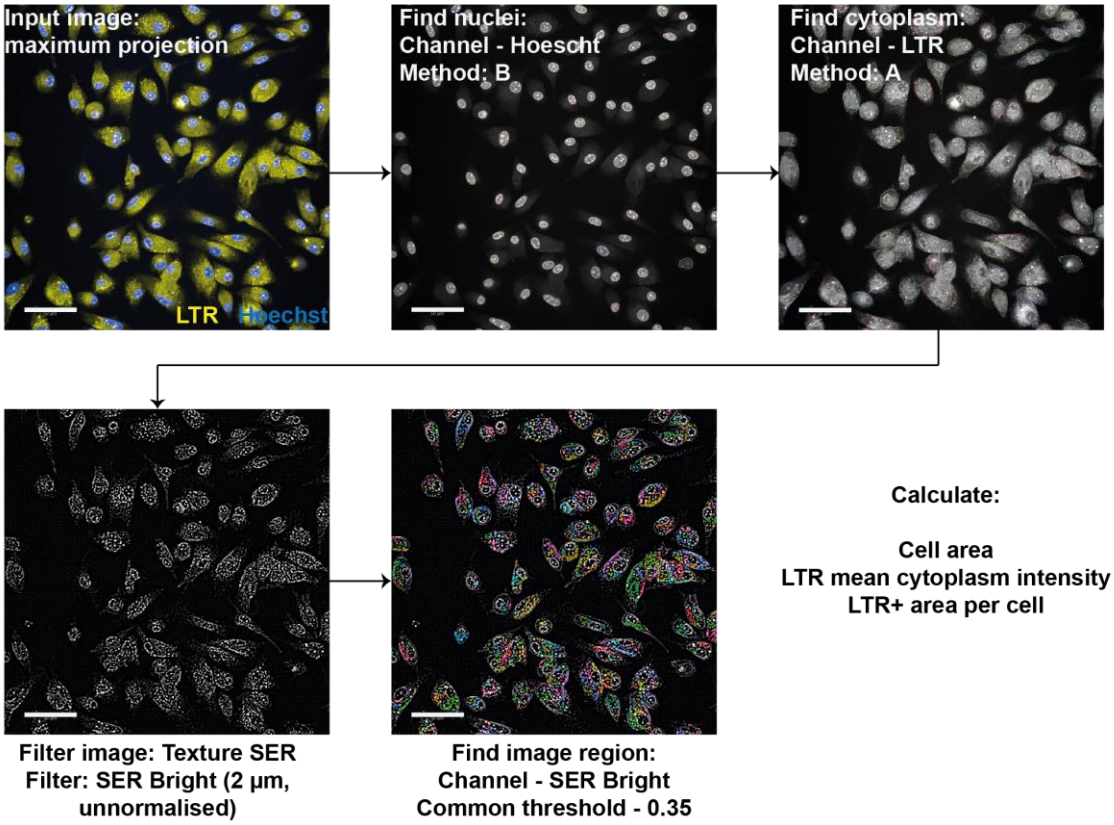

Figure 2.3.2. LTR analysis pipeline used in Harmony software.

Representative images of cell and LTR spot segmentation in wild-type BMDM. Following nuclear and cytoplasm segmentation, LTR spots are highlighted by the "Texture SER" filter and segmented by the "Find image region" building block. Scale bars = 50 µm.

2.3.5 DQ-BSA assay and live cell imaging

Cells were seeded in 96 well plates (6055302, Revvity) and incubated with 10 µg/ml DQ-BSA (Thermo, D12051) and BSA-488 (Thermo, A13100) for 4 h. The cells were then washed x3 in RPMI (BMDM) or X-VIVO 15 (iPSDM), counterstained with NucBlue and imaged at 37°C, 5% CO2 using an automated confocal high-content imaging system (Revvity, Opera Phenix High-Content Screening System) with 40x 1.1 NA water-immersion objective, and excitation lasers (405 nm and 561 nm) and preset emission filters. The 405 nm laser was used at 30% power with 100 ms exposure. The 561 nm laser was used at 20% power with 200 ms exposure.

Image analysis was performed using Harmony 4.9 image analysis software (Revvity). First, stacks were processed to create a maximum projection image. Cells were

segmented using the “Find Nuclei” (method B) and “Find Cytoplasm” (method A) building blocks. Following this, intensity of DQ-BSA and BSA-488 in the cytoplasm was calculated using the “Calculate Intensity Properties” building blocks.

2.3.6 LysoTracker leakage assay

BMDMs were seeded in 96 well plates (6055302, Revvity) and stained with 25 nM LysoTracker DND-99 (LTR) (L7528, Thermo Fisher Scientific) for 30 minutes. Following this, live cell snapshot imaging was performed at 37°C, 5% CO_2 using an automated confocal high-content imaging system (Revvity, Opera Phenix High-Content Screening System) with 40x 1.1 NA water-immersion objective, 561 nm excitation laser and 570-630 nm emission filter at a power of 30% and 100ms exposure time. Cells were imaged once prior to any treatment to establish a baseline. Then, 1 mM LLOMe in RPMI was added and the cells were imaged every minute for 5 min to track lysosomal damage. Following this, cells were washed twice in RPMI and fresh media containing 25 nM LTR was added, and the cells were imaged every minute for 10 min to track lysosomal recovery. All media changes and wash steps were performed without moving the plate so that the same cells were imaged at each snapshot.

Image analysis was performed using Harmony 4.9 image analysis software (Revvity). First, stacks were processed to create a maximum projection image. Cells were segmented using the “Find Cells” building block (method P). LTR puncta were identified using the “Find Spots” building block (method A) and LTR spot area and intensity were calculated using the “Calculate Morphology Properties” and “Calculate Intensity Properties” building blocks. The mean LTR cytoplasmic intensity at each time-point was normalised to the baseline LTR cytoplasmic intensity to correct for differences in baseline prior to analysis.

2.3.7 High-content imaging of BMDM and iPSDM during lysosomal cell death

Cells were seeded in 96 well plates (6055302, Revvity) and stained with Blue/Green ReadyProbes Cell Viability Imaging Kit (Invitrogen, R37609) according to

manufacturer's instructions. Cells were treated with LLOMe 1 mM, silica 300 μg/ml or vehicle just prior to the start of imaging. Live cell snapshot imaging was performed at 37°C, 5% CO_2 using an automated confocal high-content imaging system (Revvity, Opera Phenix High-Content Screening System) with 40x 1.1 NA water-immersion objective, and excitation lasers (405 nm and 488nm) and preset emission filters. The 405 nm laser was used at 20% power with 100 ms exposure. The 488nm laser was used at 5% power with 80 ms exposure. The channels were separated during acquisition to prevent fluorescence crosstalk. Snapshots were taken every 15 or 30 minutes depending on the length of acquisition and treatment.

Image analysis was performed using Harmony 4.9 image analysis software (Revvity). First, stacks were processed to create a maximum projection image. The total cell number was calculated using the "Find nuclei" building block in the NucBlue channel (method B). Then, intensity of NucGreen within each nucleus was calculated using the "Calculate Intensity Properties" building block. The total number of dead cells was calculated by setting a threshold for NucGreen intensity and segmenting this population using the "Select Population" building block. The percentage of dead cells was calculated by dividing the total number of NucGreen+ nuclei over the total number of NucBlue nuclei.

2.3.8 Snapshot imaging of live BMDM with NucView Caspase-3

Cells were seeded in 96 well plates (6055302, Revvity) and stained with 25 μM NucView Caspase-3 substrate (10402, Biotium), 1 μg/ml Propidium Iodide (PI) (ab14083, abcam), and NucBlue (Invitrogen, R37609). Cells were pre-treated with 250 ng/ml LPS as described above. LLOMe 1 mM or vehicle was added just prior to the start of imaging. Live cell snapshot imaging was performed at 37°C, 5% CO_2 using an automated confocal high-content imaging system (Revvity, Opera Phenix High-Content Screening System) with 40x 1.1 NA water-immersion objective, and excitation lasers (405 nm, 488nm and 561 nm) and preset emission filters. The 405 nm laser was used at 20% power with 100 ms exposure. The 488nm laser was used at 5% power with 80 ms exposure. The 561 nm laser was used at 10% power with 100 ms exposure. The channels were separated during acquisition to prevent

fluorescence crosstalk. Snapshots were taken every 30 min for the duration of the experiment as indicated.

Image analysis was performed using Harmony 4.9 image analysis software (Revvity). First, stacks were processed to create a maximum projection image. The total cell number was calculated using the “Find nuclei” building block in the NucBlue channel (method B). Then, intensity of Caspase-3 substrate and PI within each nucleus was calculated using the “Calculate Intensity Properties” building block. The total number of PI-positive, caspase-3-positive and PI-negative/caspase-3 positive cells was calculated by setting a threshold for caspase-3 and PI intensity and segmenting these populations using the “Select Population” building block.

2.4 Molecular biology

2.4.1 SDS-PAGE and Western blot analysis

Cells were washed once with PBS and lysed on ice in RIPA buffer (Millipore, 20-188) containing protease and phosphatase inhibitor (Thermo Scientific, 78440). Protein levels were normalised using the Pierce BCA protein assay kit (23227, Thermo Scientific) as per manufacturer’s instructions. Samples were boiled at 70^{o}C for 15 minutes in LDS sample buffer (Thermo Fisher Scientific, NP008) and NuPage Sample Reducing Agent (Thermo Fisher Scientific, NP009). Samples were loaded into 4–12% Bis-Tris gel (Thermo Fisher Scientific, WG1403), and electrophoresis was performed at 100 V for 120 minutes. The gels were transferred onto a PVDF membrane using an iBlot2 (Thermo Fisher Scientific, IB21001) using program P0. For detection of LRRK2 the gels were transferred onto a PVDF membrane by wet transfer (100 mA for 3 hours at 4^{o}C). Membranes were blocked in 5% skimmed milk in TBS plus 0.05% Tween20 (TBS-T) for 1 hour at room temperature, then incubated with primary antibody overnight at 4 °C. For detection of phosphorylated proteins, membranes were blocked in 5% BSA (Cell Signaling, 9998S) in TBS-T. Primary antibodies and their dilutions are shown in **Table** 2.4.1. Membranes were washed in TBS-T and incubated with horseradish peroxidase (HRP)-conjugated secondary antibodies for 1 h at room temperature. Membranes were developed with enhanced chemiluminescence reagent (Bio-Rad) and imaged on an Amersham GE Imager 680

(GE Healthcare). The molecular weight ladder was from Abcam (116028). Western blots were quantified by densitometry using FIJI software.

Antibody	Dilution	Supplier	Catalogue
Rab8A	1:1000	Cell Signaling	6975
Rab8A pT72	1:1000	Abcam	ab230260
Rab10	1:1000	Cell Signaling	8127
Rab10 pT73	1:1000	Abcam	ab230261
Rab12	1:1000	ProteinTech	18843
Rab12 pS105	1:1000	Abcam	ab256487
Cleaved caspase-3 (Asp175)	1:1000	Cell Signaling	9664T
Phospho-RIP3 (Thr231/Ser232)	1:1000	Cell Signaling	91702
Cleaved Gasdermin D (Asp275)	1:1000	Cell Signaling	10137
Cleaved PARP (Asp214)	1:1000	Cell Signaling	94885
Phospho-MLKL (Ser 345)	1:1000	Cell Signaling	37333S
Cleaved-IL-1β (Asp117)	1:1000	Cell Signaling	63124S
LAMP-1	1:2000	DSHB	1D4B
β-Actin-HRP	1:5000	Cell Signaling	12262S
LRRK2	1:1000	Abcam	Ab133474
Galectin-3	1:2000	BioLegend	125402
CHMP4B	1:2000	ProteinTech	13683
LC3B	1:1000	Sigma	L7543
Anti-rabbit HRP	1:10000	Promega	W4011
Anti-rat HRP	1:10000	Invitrogen	31470

Table 2.4.1. Antibodies used for Western blot.

2.4.2 Flow cytometry

1 x 10^6 cells were pelleted by centrifugation (350 x g for 5 min at 4^{o}C), washed with cell staining buffer (420201, BioLegend) and incubated with mouse Fc blocker TruStain fcX^{TM} (156604, BioLegend) for 20 min at 4^{o}C. Cells were resuspended in cell staining buffer with fluorochrome-conjugated antibodies for 30 min at room temperature in the dark. The antibodies used are detailed in **Table** 2.4.2. Cells were

washed in cell staining buffer and resuspended in 500 μL cell staining buffer for acquisition. Data were acquired using an BD LSRFortessa™ Cell Analyzer (BD Biosciences) and analysed using FlowJo software (FlowJo, LLC, v10.8.0). At least 10,000 events per condition were recorded.

Antibody	**Clone**	**Volume used (μl)**	**Company**	**Catalogue**
F4/80	BM8	1.25	BioLegend	123113
CD11b	M1/70	5	Biolegend	101237
MHCII	M5/114.15.2	1.25	Biolegend	107607
CD11c	N418	0.5	BioLegend	117319
TLR2	QA16A01	5	BioLegend	153009
CD80	16-10A1	0.5	BioLegend	104717
CD206	C068C2	5	BioLegend	141717
CD14	MϕP9	5	BD Biosciences	562689
CD16	3G8	5	BD Biosciences	557710
CD119	GIR-208	2	BD Biosciences	558934
CD163	GHI/61	5	BD Biosciences	563697
CD206	19.2	0.5	BD Biosciences	561763
CD169	7-239	5	BD Biosciences	565248
CD86	2331	5	BD Biosciences	562433

Table 2.4.2. Antibodies used for Flow Cytometry.

2.4.3 Cytokine measurement

LRRK2-G2019S and isogenic control iPSDM were plated in 96-well olefin-bottomed plates (6055302, Revvity) at a concentration of 60,000 cells per well. Cells were treated with LPS (250 ng/ml), PAM3CSK4 (1 μg/ml), Poly(I:C) (10 μg/ml) or IFN-γ (100 ng/ml) diluted in X-VIVO media for 24 hours (Table 2.4.3). Where stated, MLi-2 or DMSO control was also added to the media at a concentration of 100 ng/ml. All treatments were filtered through a Minisart 0.2 μm syringe filter unit (16534-K, Sartorius) before addition to cells. After 24 h treatment, 100 μl supernatant was removed and centrifuged at 1000 xg for 15 min at 4°C to remove any detached cells.

This supernatant was again centrifuged at 10000 xg for 10 min at 4°C to remove any debris. All supernatants were stored at -80°C until they were run on the Luminex plate. Cytokine levels were analysed using the magnetic Bio-Plex Pro Human Cytokine 27-plex kit (M500KCAF0Y, Bio-Rad) as per the manufacturer's instructions. Samples were analysed on a Bio-Plex 200 (BioRad).

	Concentration	**Supplier**	**Cat No.**
LPS	250 ng/mL	Bio-techne	NBP2-25295
PAM3CSK4	1 μg/mL	Bio-techne	4633/1
Poly(I:C)	10 μg/mL	Tocris	4287
IFN-γ	100 ng/mL	Thermo	PHC4031
MLi-2	100 ng/mL	abcam	ab254528
DMSO	100 ng/mL	Sigma	D2650

Table 2.4.3. List of treatments used for cytokine assay

2.5 Graph plotting and statistical analysis

All graphs were produced in GraphPad Prism V10.2.0 (GraphPad Software LLC, USA). Statistical analyses, as detailed in figure legends, were carried out in GraphPad Prism V10.2.0. Figures were compiled using Adobe Illustrator 2024 V28.4.1 (Adobe Inc. USA).

2.6 Phosphoproteomics

I conducted all differentiations of murine haematopoietic progenitor cells to BMDM, cell culture, compound treatments, cell detachment and snap freezing for proteomics and phosphoproteomics experiments.

Cell lysis, peptide/phosphopeptide enrichment, TMT-labelling, and LC-MS/MS analysis of samples for the proteomics and phosphoproteomics experiments were conducted by Simeon Mihaylov (Kinases and Brain Development Laboratory, The Francis Crick Institute) supported by Mike Skehel and Helen Flynn (Proteomics Scientific technology platform, The Francis Crick Institute).

Bioinformatics analysis was conducted by Simeon Mihaylov and Sila Ultanir (Kinases and Brain Development Laboratory, The Francis Crick Institute). Volcano plots were produced by Simeon Mihaylov. Data interpretation was performed in a collaborative manner.

2.6.1 Cell culture and treatments

For LLOMe treatment, 5 x 10^5 cells/ml were plated in three 50 mm non-treated tissue-culture dishes (122-17, Thermo Scientific). For control, 6 x 10^5 cells/ml were plated in a 90 mm petri dish (101R20, Thermo Scientific). Cells were treated with LLOMe for 30 min at a concentration of 1 mM by dilution in RPMI medium. Following treatment, cells were washed once in ice-cold PBS and then detached with ice-cold PBS containing Sigma Phosphatase Inhibitor Cocktail 3 (539134, Merck), CoMPLETE Protease Inhibitor tablets (11873580001, Merck), Pierce Phosphatase Inhibitor Mini Tablets (A32957, Thermo Fisher Scientific), 500 nM Okadaic acid (A4540, Stratech) and 1 mM EDTA (11568896, Invitrogen). A pellet was collected by centrifugation (350 xg for 5 min) and the pellet was flash-frozen using dry ice/iso-propanol. Four replicates were collected per condition.

2.6.2 Cell lysis and protein quantification

Pellets were lysed in Urea lysis buffer (8 M urea, 50 mM HEPES pH8.2, 10 mM glycerol-2-phosphate, 50 mM NaF, 5 mM sodium pyrophosphate, 1 mM EDTA, 1 mM EGTA, 1 mM sodium vanadate, 1 mM DTT, 2X cOmplete protease inhibitor cocktail (Merck), 1X phosphatase inhibitor cocktail 3 (Sigma), 500 nM okadaic acid, 1 μM microcystin-LR). After protein concentration was measured using Pierce BCA assay, equal amount (between 165-200 μg) was used of each sample for TMTpro multiplexed quantitative proteomics.

2.6.3 TMT-labelling

Each sample was reduced with 10 mM DTT for 1 h at 56°C and alkylated with 20 mM IAA for 30 min in the dark at room temperature. The reaction was quenched with 20 mM DTT then diluted to <2 M urea with 50 mM HEPES pH8.5. Each resuspended sample was digested with 3.75 µg LysC (Lysyl endopeptidase, 125-05061, FUJIFILM Wako Chemicals) and 12.5 µg Trypsin (MS grade, 90058, ThermoFisher Scientific) at 37°C shaking overnight. Each sample was cleaned-up using Nest Group BioPureSPN MACRO (Proto 300 C18; Part# HMM S18V) and vacuum-dried. Samples were then tandem mass tag (TMT) labelled for an hour at room temperature using a TMTpro 16plex Isobaric Label Reagent Set (0.8 mg per tag, A44520, ThermoFisher Scientific; LOT VE299607) and following manufacturer's instructions. A small aliquot of each sample was collected for a labelling efficiency and mixing accuracy quality checks (QCs) by liquid chromatography tandem mass spec (LC-MS/MS) using Orbitrap Eclipse Tribrid mass spectrometer and a 60 min HCD MS2 fragmentation method. The rest of the sample was stored at -80°C until QC results. Labelling efficiency of higher than 99% was obtained for each reaction and a mixing accuracy with lower than 1.5x difference between samples with lowest and highest summed intensity.

2.6.4 Mass spectrometry

Samples were defrosted, quenched with hydroxylamine for 15 min at room temperature and pooled together. Combined mixture was partially vacuum-dried and acidified to pH 2.0 followed by sample clean-up using C_{18} Sep Pak 1cc Vac, 100 mg bed volume (Waters). Final mixing check was performed by LC-MS/MS with a 240 min HCD MS2 fragmentation method. The peptide mixture was then subjected to high-select sequential enrichment of metal oxide affinity chromatography (SMOAC) to capture phospho-peptides. It was first passed through a high-select TiO_2 phospho-enrichment column (Thermo Scientific, A32993) following manufacturer protocol. Flow-through and wash fractions were combined, dried, and subsequently used for Fe-NTA phospho-enrichment (Thermo Scientific, A32992). One tenth of the combined flow-through and wash fractions from this enrichment was used for total proteome analysis. The eluates from SMOAC were freeze-dried, solubilised, and

pooled together. Both total proteome and phospho-proteome samples were subjected to high pH reversed phase fractionation (Thermo Scientific, 84868), dried and resolubilised in 0.1% TFA prior to LC-MS/MS. Total proteome was analysed on Orbitrap Eclipse Tribrid (Thermo) mass spectrometer using 180 min HCD MS2 fragmentation method and 180 min real-time search (RTS) MS3 method (Schweppe et al., 2020). The phosphoproteome was analysed using 180 min HCD MS2 and 180 min MSA SPS MS3 as described in (Jiang et al., 2017). Xcalibur software was used to control the data acquisition. The instrument was run in data dependent acquisition mode.

2.6.5 Data analysis

Raw data were processed using MaxQuant v2.1.3.0 and Uniprot mouse reference proteome from March 2021. Processed data were then analysed using an R-coding script tailored to isobaric labelling mass spectrometry. The script was generated as a hybrid using the backbone and differential gene expression analysis of ProteoViz package (Storey et al., 2020) as a general script workflow and borrowing the normalization script from Proteus package (Marek et al.). Briefly, the "proteinGroups.txt" and "Phospho (STY)Sites.txt" tables were read into matrices and filtered for "reverse" hits, "potential contaminant" and proteins "only identified by site". TMT LOT-corrected reporter intensities were then normalized using CONSTANd (Van Houtven et al., 2021), log2-transformed and differentially analysed using Linear Models for Microarray Data (limma). Volcano plots were generated using ggrepel (a ggplot2 extension) as part of the tidyverse.

Chapter 3. Results 1 Characterisation of a macrophage model to study LRRK2 mutations

3.1 Characterisation of murine RAW 264.7 cells carrying LRRK2 mutations

RAW 264.7 cells are a macrophage-like cell line developed in 1978 from an Abelson leukaemia virus induced-lymphoma in a male BALB/c mouse (Raschke et al., 1978). The cells show properties of macrophages including phagocytosis of zymosan and latex beads, secretion of lysozyme, and secretion of cytokines in response to LPS (Raschke et al., 1978; Salo et al., 1985). Due to genome alterations, RAW 264.7 cells continuously proliferate in cell culture and are widely used as an *in vitro* macrophage model.

Professor Erwin Schurr (McGill University Health Centre, Montreal) kindly gifted RAW 264.7 cells which were genome edited to express LRRK2-G2019S, LRRK2-R1398H, LRRK2-N551K and LRRK2-R1398H-N551K (Dallmann-Sauer et al.). The gain-of-function LRRK2-G2019S is the most common PD-associated mutation (Ferreira and Massano, 2017; Paisan-Ruiz et al., 2004; Williams-Gray et al., 2006), located in the kinase activation loop of LRRK2. LRRK2-G2019S is reported to increase kinase activity 1.4 to 3-fold *in vitro* (Greggio et al., 2006; Myasnikov et al., 2021; West et al., 2005). LRRK2-N551K and LRRK2-R1398H are single point mutations located in between the ARM and ANK, and in the ROC domains of LRRK2, respectively (Hui et al., 2018). These mutations are protective against the development of PD, associated with a 20% reduced risk of developing disease (Gopalai et al., 2019). A similar protective effect is reported for the LRRK2-N551K-R1398H mutation (Hui et al., 2018). As such, this *in vitro* system was chosen as the model of choice for initial experiments to study the effect of PD-associated LRRK2 mutations on macrophage function.

Upon receipt of the cells, I performed PCR and Sanger sequencing to confirm the genotypes. The following primers were used:

PCR primer name:	**Sequence**
R1398H_GR1	5’ – CAT GGG AGG ACA CAT CTT TAA ACT C -3’
R1398H_GF1	5’ – GAG AGG TCT AAA TTG CTT GGT TGG C -3’
G2019S_GR1	5’ – TAT ATC TCC TAG ACC CAC ACT TGA G – 3’
G2019S_GF1	5’ – TAC CAG GCT TGA TGC TTT AGT TAT G -3’
N551K_GR1	5’ – GGA TCA TAA AAG AAG AAC GGC CTA C -3’
N551K_GF1	5’ – CTA GTC TGA CCC AAA TTA TCC TAG C -3’
Sequencing primer name:	**Sequence**
G2019S_SR1	5’ – GGG CAC TGA TGG TCC ACT GC -3’
G2019S_SF1	5’ – TGG CAG GTA TCT CCA CTC AG -3’
R1398H_SR1	5’ – GAT CAG AAG AAA TCA CCT TG -3’
R1398H_SF1	5’ – CAT GGG AAT GAT GTC TGT TG -3’
N551K_SR1	5’ – ATG ACT TCT AAC TAT CAT AG-3’
N551K_SF1	5’ – GGA CTA TTG GAA GAA TCC AG -3’

Table 3.1.1. Primers used for PCR and sequencing in RAW 264.7 cells.

Gel electrophoresis performed on the PCR products revealed some abnormalities: no product was detected in the N551K-R1398H DNA when PCR was performed with the N551K primer (Figure 3.1.1, lane 3); and a double band PCR product was found in the LRRK2-G2019S DNA (Figure 3.1.1, lane 6).

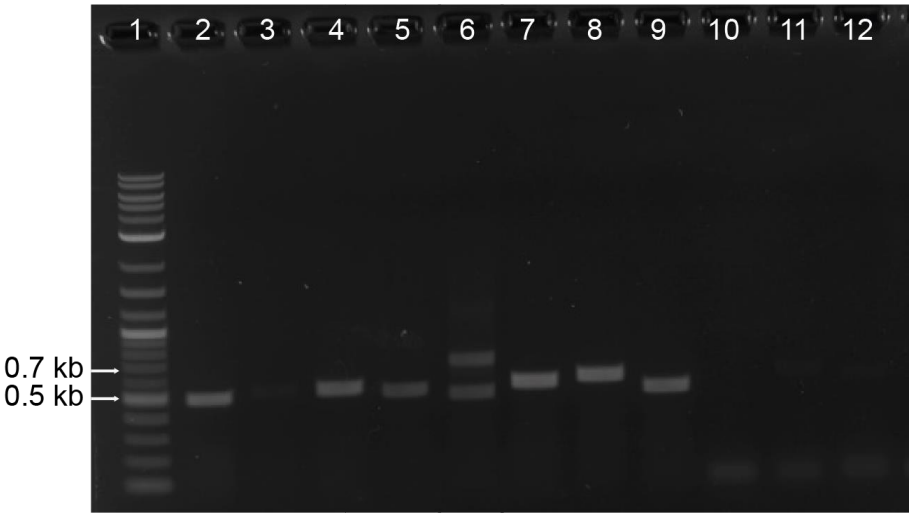

Figure 3.1.1. PCR amplification of LRRK2-mutated DNA segments in RAW 264.7 cells. Agarose gel electrophoresis after amplification of LRRK2 mutated DNA fragments using N551K, R1398H or G2019S primers by PCR. Samples were analysed by gel electrophoresis through 1% (wt/vol) agarose gel. Gels were stained with SYBR safe, and DNA was visualised under UV. Lanes: 1, 1kb plus DNA ladder (Biolabs, N3200L); 2, R1398H-N551K RAW cells (primer: R1398H); 3, R1398H-N551K RAW cells (primer: N551K); 4, N551K RAW cells (primer: N551K); 5, R1398H RAW cells (primer: R1398H); 6, G2019S RAW cells (primer: G2019S), 7, LRRK2 WT RAW cells (primer: G2019S), 8, LRRK2 WT RAW cells (primer: N551K), 9, LRRK2 WT RAW cells (primer: R1398H), 10-12 negative controls (N551K, R1398G and G2019S primers, respectively).

Sanger sequencing revealed that only the R1398H mutation was present in the R1398H and N551K-R1398H cells. The N551K mutation was not detected in the N551K or N551K-R1398H cells and the G2019S mutation was not detected in the LRRK2-G2019S cells (Figure 3.1.2). I therefore decided to discontinue experiments with these cells and instead use a different biological system.

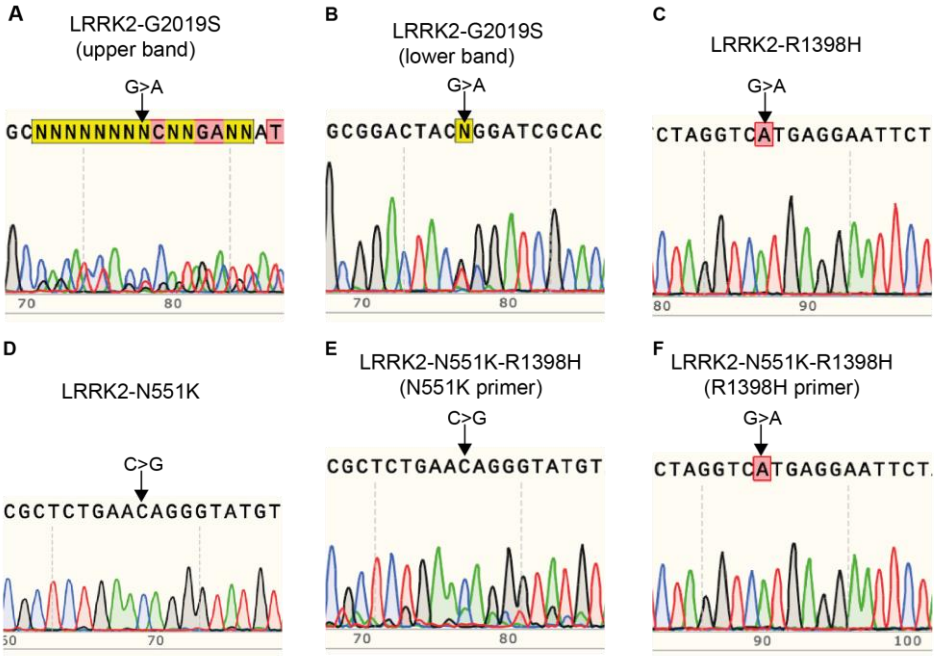

Figure 3.1.2. RAW 264.7 cells do not show the stated LRRK2 mutations. Sanger sequencing of PCR products from LRRK2 mutant RAW 264.7 cells (A) LRRK2-G2019S DNA (upper band, G2019S primer) (B) LRRK2-G2019S DNA (lower band, G2019S primer) (C) LRRK2-R1398H DNA (R1398H primer) (D) LRRK2-N551K DNA (N551K primer) (E) LRRK2-N551K-R1398H DNA (N551K primer) (F) LRRK2-N551K-R1398H DNA (R1398H primer)

3.2 Characterisation of murine bone marrow derived macrophages carrying LRRK2 mutations

As an alternative biological system for studying LRRK2 mutations in macrophages, we generated bone marrow derived macrophages (BMDM) from mice homozygous for LRRK2-G2019S (Tac-G2019S) and wild-type controls (Tac-WT) (Matikainen-Ankney et al., 2016). Murine BMDM are advantageous in that they are primary cells with a normal karyotype and are more physiologically relevant than macrophage cell lines. As a control for LRRK2 kinase activity, we generated BMDM from mice expressing a kinase-dead form of LRRK2 (NJ-D1994A) and wild-type LRRK2 (NJ-WT) (Crabbe et al., 1985). As a control for LRRK2 kinase, GTPase and non-enzymatic activities, we generated BMDM from LRRK2 KO mice (6J-LRRK2KO) and wild-type LRRK2 (6J-WT) (Parisiadou et al., 2009). Importantly, each mouse was

genotyped by ear notch sampling and sequencing (Transnetyx) prior to use in experiments.

3.2.1 LRRK2 mutations do not alter BMDM surface marker expression

Cells were first characterised by flow cytometry to confirm successful differentiation of macrophages from bone marrow precursor cells and identify possible effects of LRRK2 mutations on differentiation (Figure 3.2.1). BMDM across all genetic backgrounds showed surface expression of the macrophage markers CD11b, F4/80, MHCII, TLR2, CD80, CD206 and the dendritic cell marker CD11c, confirming previous reports that GM-CSF differentiation of bone marrow precursor cells results in a heterogeneous population mixed between macrophages and dendritic cell-like (Helft et al., 2015; Na et al., 2016). In addition, the levels of expression of all markers were similar between the LRRK2-mutant and LRRK2-wild-type macrophages, indicating that LRRK2 mutations do not alter differentiation *in vitro*.

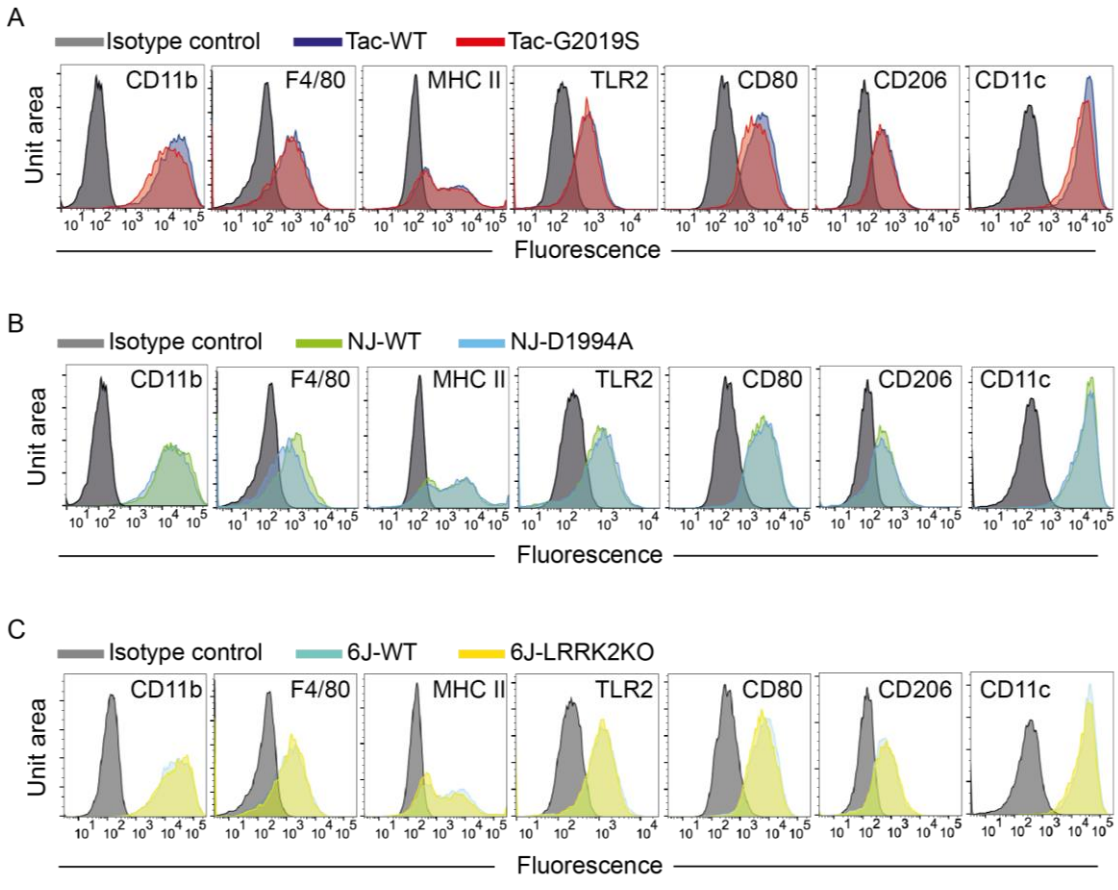

Figure 3.2.1. BMDM express markers of macrophage and dendritic cell differentiation

Flow cytometry characterisation of surface expression of macrophage markers. Data is from one representative experiment. Data are presented as histograms with compensated fluorescence of the indicated surface marker on the x-axis. (A) Tac-WT and Tac-G2019S macrophages (B) NJ-WT and NJ-D1994A macrophages (C) 6J-WT and 6J-LRRK2KO macrophages.

3.2.2 LRRK2 mutations do not alter total LRRK2 protein expression in BMDM

Western blot analysis of BMDM using LRRK2 monoclonal antibody (MJFF (c41-2), ab33474) showed that BMDM express full-length LRRK2 (molecular weight 286 kDa) except for 6J-LRRK2KO macrophages, as expected (Figure 3.2.2). There were no differences in LRRK2 expression between Tac-WT and Tac-G2019S, or NJ-WT and NJ-D1994A macrophages, respectively. LRRK2 expression levels were not significantly different between the wild-type macrophages. Interestingly, a second band on the LRRK2 membrane with a molecular weight of around 170 kDa (relative to size markers on the protein ladder) was present in wild-type, Tac-G2019S and NJ-D1994A macrophages. This band appeared to be specific for LRRK2 as it was absent in the 6J-LRRK2KO lysate. An additional LRRK2 band at a similar molecular weight has been previously described in human iPSDM and iPSC-derived microglia, although its function is unknown (Lee et al., 2020).

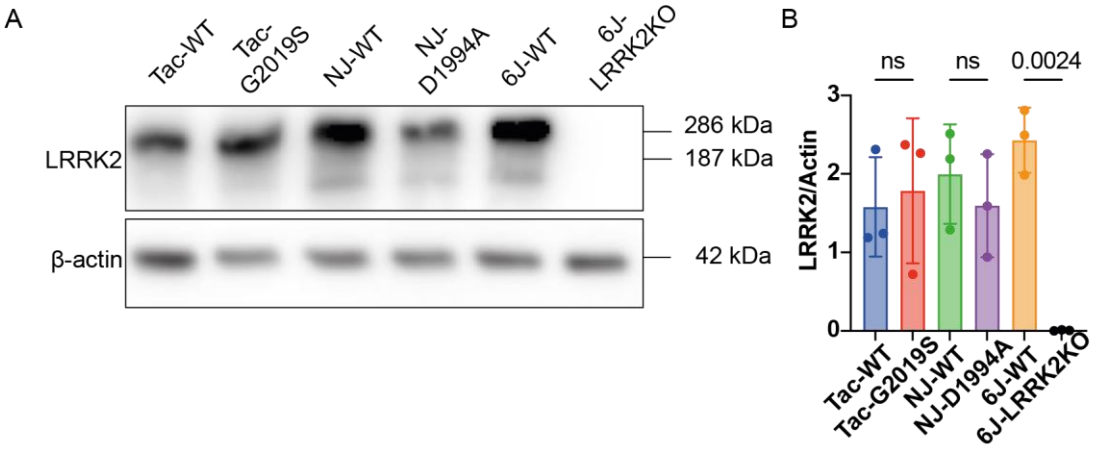

Figure 3.2.2. LRRK2 levels do not differ in LRRK2 mutant macrophages

(A) Western blot analysis of LRRK2 and β-actin from resting BMDM. One representative blot is shown. (B) LRRK2 band intensity was quantified by

densitometry and normalised to β-actin. Data are mean ± SD from 3 independent experiments. Statistical analysis by one-way ANOVA with Šidák's multiple comparisons test. ns = non-significant.

3.2.3 LRRK2 mutations do not alter LAMP-1 protein expression or localisation in BMDM

LRRK2 is implicated in lysosomal function, and there are reports that show proteolytic activity and lysosomal function is impacted by the LRRK2-G2019S mutation (Henry et al., 2015; Narayana and Shawn, 2023). I therefore investigated lysosomal content and function in the BMDM. Lysosomal-associated membrane protein-1 (LAMP-1) is an abundant lysosomal membrane glycoprotein (Chen et al., 1985). Western blot analysis for LAMP-1 showed similar levels of expression between the genotypes, indicating no differences in total lysosomal content (Figure 3.2.3).

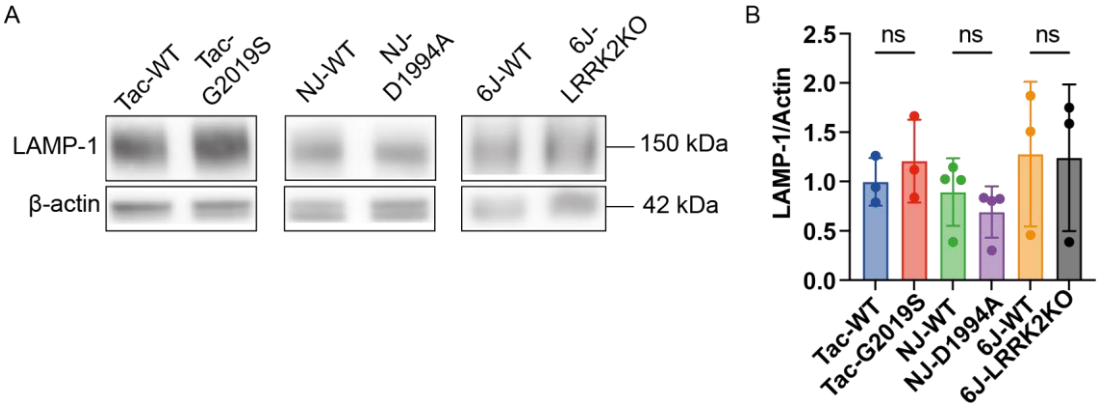

Figure 3.2.3. LAMP-1 levels do not differ in LRRK2 mutant macrophages

(A) Western blot analysis of LAMP-1 and β-actin from BMDM. One representative blot is shown. (B) LAMP-1 band intensity was quantified by densitometry and normalised to β-actin. Data are mean ± SD from 3 independent experiments. Statistical analysis by one-way ANOVA with Šidák's multiple comparisons test. ns = non-significant.

Immunofluorescence for LAMP-1 was also performed in Tac-WT and Tac-G2019S BMDM. This revealed a highly dense and compact network of LAMP-1+ lysosomes throughout the cytosol (Figure 3.2.4). The compact nature of the LAMP-1+ compartment in BMDM precluded accurate analysis of lysosomal number, diameter, and shape. However, there were no differences in total LAMP-1+ area per cell or

LAMP-1 cytoplasmic mean intensity between Tac-WT and Tac-G2019S macrophages (Figure 3.2.4).

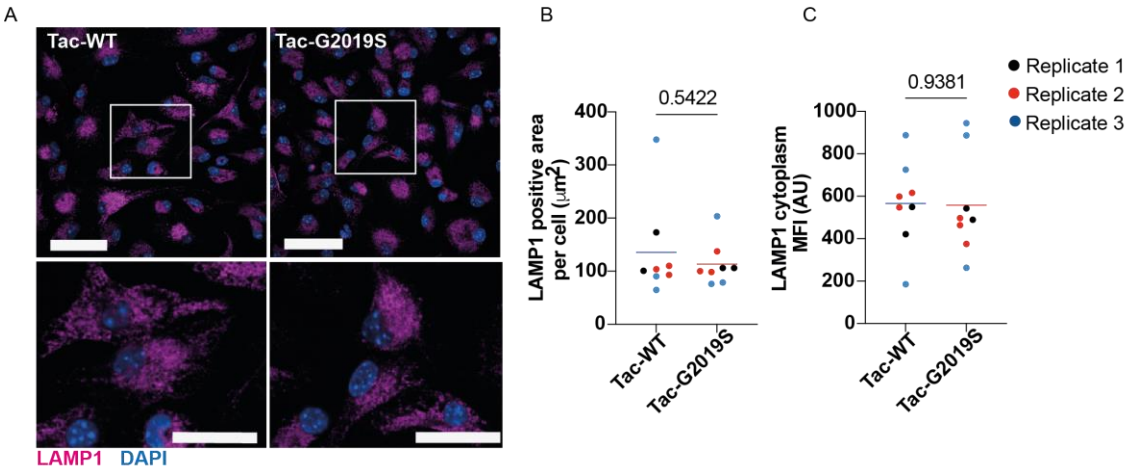

Figure 3.2.4. Tac-WT and Tac-G2019S BMDM show no differences in LAMP-1 immunofluorescence

(A) Tac-WT and Tac-G2019S BMDM were fixed and stained for LAMP-1 by immunofluorescence. Upper panel scale bars represent 20 μm; lower panel scale bars represent 10 μm. Scatterplots show quantification of (B) LAMP-1 positive area per cell and (C) cytoplasmic LAMP-1 mean fluorescence per cell from three independent experiments (each point represents the mean value from one well). Statistical analysis is by two-tailed t-test.

3.2.4 Lysosomal content, acidity and proteolytic activity are not altered by LRRK2 mutations in BMDM

Next, macrophages were stained with Lysotracker DND-99 (LTR). LTR is a hydrophobic weak base that selectively accumulates in acidic membrane-bound compartments of the cell, thus predominantly labelling lysosomes and late endosomes (Chazotte, 2011). LTR enters cells by diffusion and staining is independent of endocytosis (Chazotte, 2011). LTR may also serve as an indicator of lysosomal pH because the amount of LTR that accumulates within a lysosome is partially dependent on the acidity of the lysosome (Kazmi et al., 2013). When BMDM were stained with LTR there was a heterogeneous staining pattern: within a single field, some macrophages showed high intensity LTR staining in a punctate pattern; while other macrophages showed low intensity LTR staining in a punctate pattern or low/intermediate intensity diffuse cytosolic staining (Figure 3.2.5). Further, within a

single cell there were often heterogeneous patterns of LTR staining as described. At this resolution, it was not possible to discern single lysosomes in areas of the cytosol with diffuse-pattern staining, precluding analysis of lysosomal number, size, and shape. There were no differences in LTR mean cytoplasmic fluorescence intensity or LTR positive cell area between LRRK2 mutant and LRRK2KO BMDM and their respective wild types (Figure 3.2.5). Notably, LTR mean intensity was variable between wild-types, indicating that the genetic background of the cell influences lysosomal acidity (Figure 3.2.5).

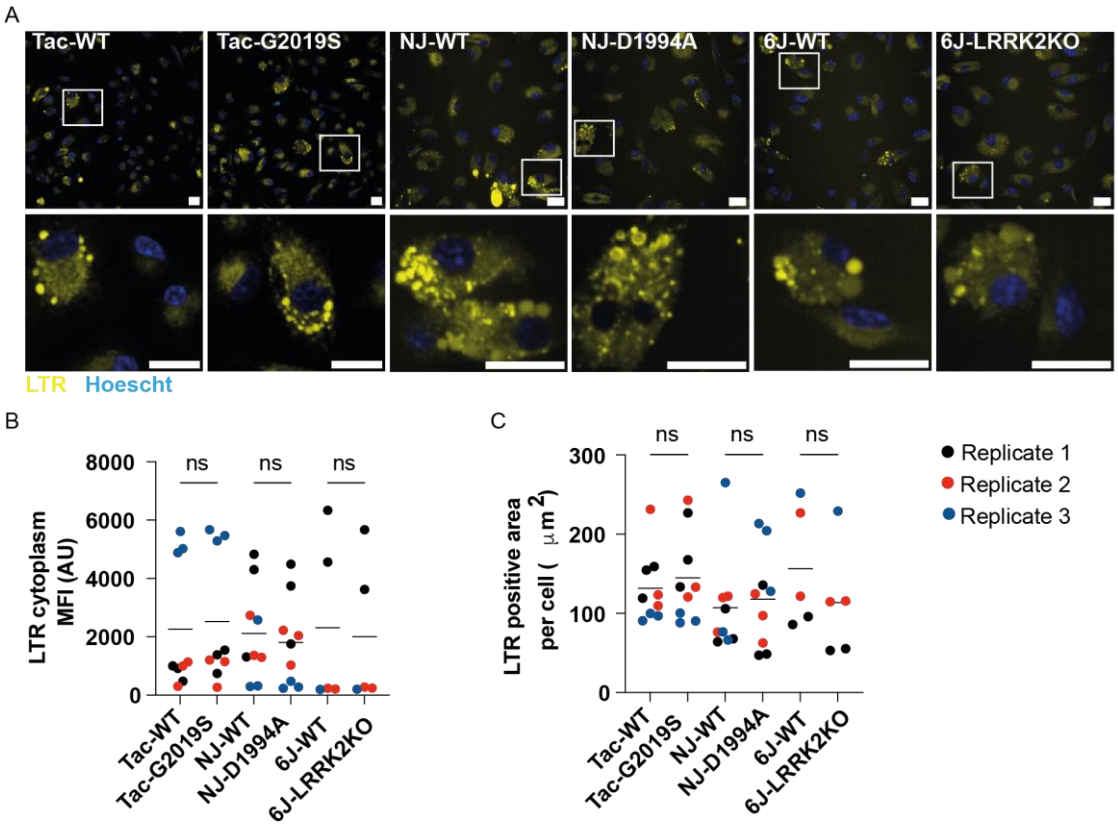

Figure 3.2.5. Lysotracker immunofluorescence does not differ in LRRK2 mutant macrophages

(A) Representative images of live BMDM stained with LTR and Hoechst dyes. Scale bars = 20μm. (B) Quantitative analysis of mean LTR fluorescence intensity (MFI) in the cytoplasm and (C) LTR positive area per cell (μm^2). Data shown is the mean ± SEM from 3 independent experiments. Statistical analysis is by two-tailed t-test.

I next analysed differences in lysosomal proteolytic activity in Tac-WT, Tac-G2019S, NJ-WT and NJ-D1994A BMDM utilising the DQ-BSA probe. DQ-BSA is a bovine serum albumin (BSA) labelled with BODIPY TR-X dye. The BODIPY TR-X

component is self-quenching and produces minimal fluorescence. However, proteolytic cleavage of DQ-BSA results in release of fragments which have λ_{ex} = 590 nm and λ_{em} = 620 nm. Thus, DQ-BSA fluorescence is a measurement of proteolytic activity in cells: higher proteolytic activity results in higher fluorescence. DQ-BSA uptake is dependent on the endocytosis pathway (Marwaha and Sharma, 2017). To control for differences in endocytic uptake, I incubated cells with BSA-488, a fluorescent dye which is also taken into the cell by endocytosis but maintains a constant level of fluorescence independent of proteolytic activity. This method has been previously used to measure the proteolytic activity of LRRK2 in macrophages (Yadavalli and Ferguson, 2023).

In contrast to previous reports (Yadavalli and Ferguson, 2023), there were no significant differences in DQ-BSA/BSA-488 fluorescence intensity ratio between LRRK2 mutant macrophages and their respective wild-type macrophages, indicating that LRRK2 mutations do not alter proteolytic activity in these cells (Figure 3.2.6).

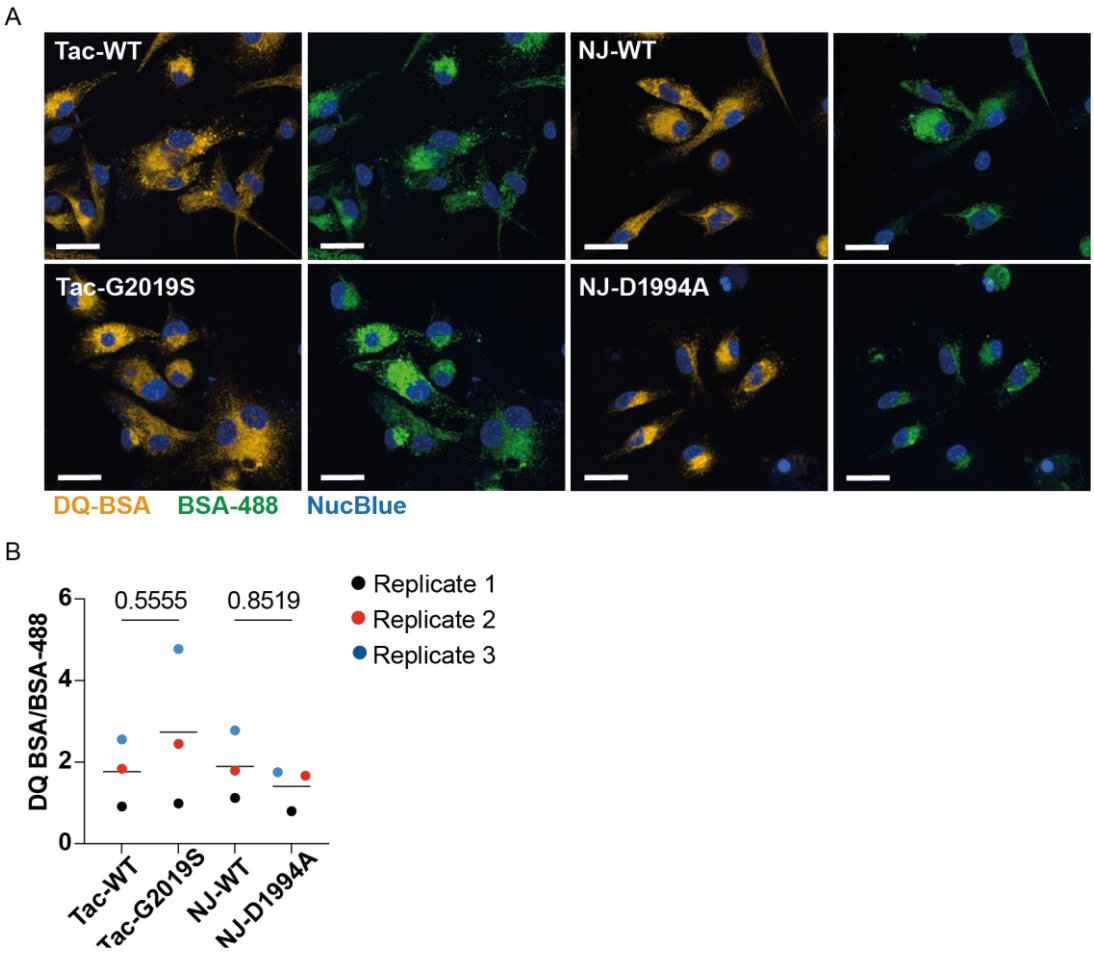

Figure 3.2.6. LRRK2 mutations do not alter proteolytic activity in BMDM

(A) Representative images of live BMDM following incubation with DQ-BSA, BSA-488 and NucBlue dyes. Scale bars = 20 μm. (B) Quantitative analysis of the mean DQ-BSA cytoplasmic intensity/mean BSA-488 cytoplasmic intensity ratio. Data shown are mean from 3 independent experiments. One-way ANOVA followed by Šidák's multiple comparisons test.

3.3 Characterisation of induced pluripotent stem cell derived macrophages from a LRRK2-G2019S Parkinson's disease patient and CRISPR/Cas9-generated isogenic control cells

3.3.1 Collaboration statement

Development of the CRISPR/Cas9 strategy for generation of isogenic control iPSC was performed by Dr Enrica Pellegrino and Natalia Athanasiadi (Host-Pathogen Interactions in Tuberculosis Laboratory, The Francis Crick Institute). Culture of iPSC, differentiation into macrophages and maintenance of macrophage factories was

performed by Natalia Athanasiadi (Host-Pathogen Interactions in Tuberculosis Laboratory, The Francis Crick Institute). Flow cytometry experiments were performed in a collaborative manner with Dr Chak Hon Luk (Host-Pathogen Interactions in Tuberculosis Laboratory, The Francis Crick Institute). I carried out cell culture of iPSDM, compound treatments and fixation, staining and imaging, and Western blot analysis. I carried out all image analysis and statistical analyses.

3.3.2 LRRK2-G2019S iPSDM show increased expression of the surface marker CD169

We obtained iPSC derived from PD patients harbouring the G2019S mutation, obtained through the Michael J Fox Foundation PPMI resource, which were gene-corrected to produce an isogenic control iPSC line using CRISPR/Cas9 genome editing (see material and methods). As a result, we obtained LRRK2-G2019S (PPMI ID clone: CDI00002173) and isogenic control cells (PPMI ID clone: 0043052321). iPSDM were differentiated following a well-established protocol (Bernard et al., 2020; van Wilgenburg et al., 2013).

Flow cytometry showed that iPSDM expressed the macrophage markers CD116, CD119, CD169 and CD86 (Figure 3.3.1). The G2019S and isogenic iPSDM expressed these markers at similar levels except for CD169, which was expressed at a higher level in G2019S iPSDM. Some macrophage markers, such as CD14, CD16, CD163, and CD206 were not expressed. Negative expression of these markers has been previously reported in iPSDM differentiated by this protocol, but macrophage functionality was maintained (Bernard et al., 2020).

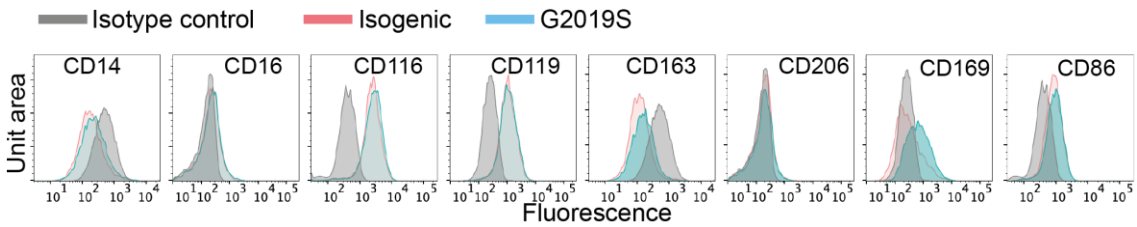

Figure 3.3.1. iPSDM derived from Parkinson's disease patient carrying LRRK2-G2019S show markers of macrophage differentiation

Flow cytometry characterisation of surface expression of macrophage markers. Data is from one representative experiment. Data is presented as histograms with compensated fluorescence of the indicated surface marker on the x-axis.

3.3.3 LRRK2-G2019S iPSDM show similar levels of LRRK2 protein expression

Western blot analysis confirmed LRRK2 expression in the iPSDM, with comparable levels of expression between G2019S and isogenic control iPSDM (Figure 3.3.2). In addition, a band around the 170 kDa, as seen in murine BMDM, was present.

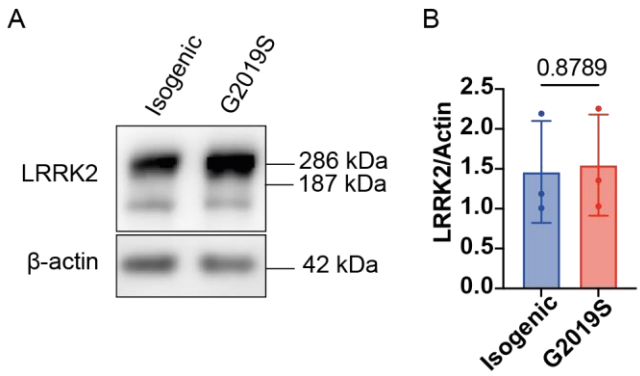

Figure 3.3.2. LRRK2 levels do not differ between G2019S and isogenic control iPSDM

(A) Western blot analysis of LRRK2 and β-actin from iPSDMs. One representative blot is shown. (B) LRRK2 band intensity was quantified by densitometry and normalised to β-actin. Data are mean ± SD from 3 independent experiments. Statistical analysis by two-tailed t-test.

3.3.4 LRRK2-G2019S macrophages show similar lysosomal content, pH and proteolytic activities

Next, lysosomal content and pH were analysed in iPSDM. LTR staining produced higher fluorescence intensity values then those seen in BMDM, indicating lower lysosomal pH in this cell type. However, like LTR imaging in BMDM, there was a heterogenous staining pattern both between and within cells. Many macrophages contained a high number of LTR positive vesicles in the cytosol which, even within a single plane, made it challenging to accurately mask individual lysosomes (Figure 3.3.3). Consistent with the data in BMDM, there were no differences in LTR mean

cytoplasmic fluorescence intensity or LTR positive cell area between G2019S and isogenic control iPSDM (Figure 3.3.3).

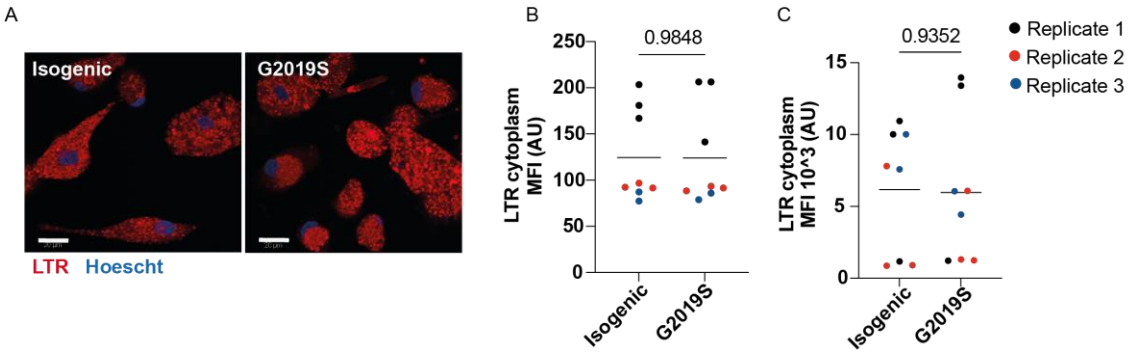

Figure 3.3.3. LTR staining does not differ in G2019S iPSDM

((A) Representative images of live iPSDM stained with LTR and NucBlue dyes. Scale bars = 20μm. Quantitative analysis of (B) mean LTR fluorescence intensity (MFI) in the cytoplasm (C) LTR positive area per cell. Data shown is the mean ± SD from 3 independent experiments. Statistical analysis is by two-tailed t-test.

Finally, iPSDM were incubated with DQ-BSA to check for differences in proteolytic activity, using the BSA-488 probe as a control for endocytic uptake as described previously. There were no differences in DQ-BSA/BSA-488 fluorescence intensity ratio between G2019S and isogenic control iPSDM, indicating that there were no differences in proteolytic activity.

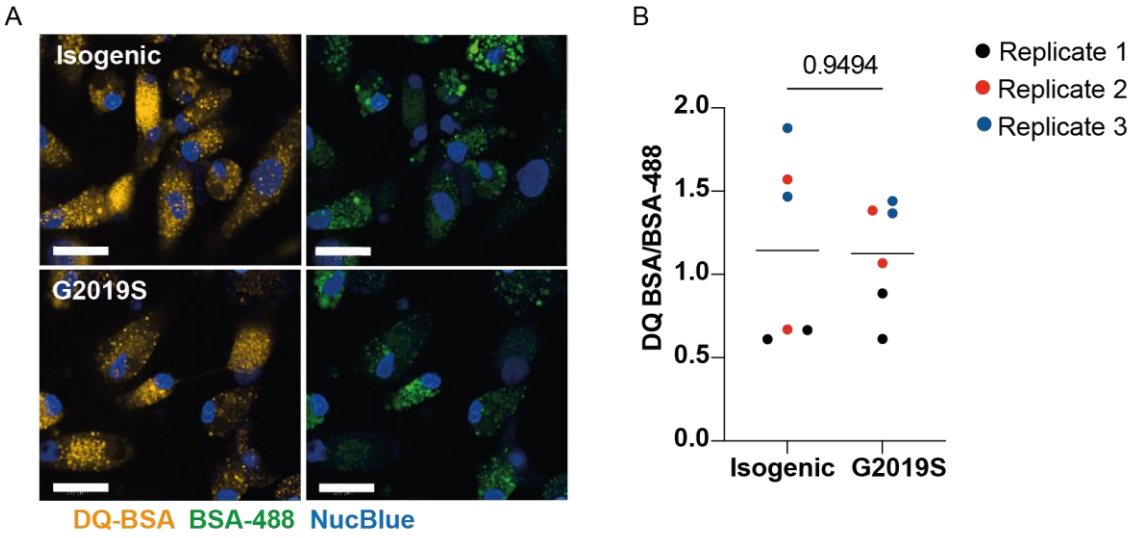

Figure 3.3.4. Proteolytic activity does not differ in G2019S iPSDM

(A) Representative images of live iPSDM incubated with DQ-BSA, BSA-488 and NucBlue dyes. Scale bars = 20 μm. (B) Quantitative analysis of the mean DQ-BSA

cytoplasmic intensity/mean BSA-488 cytoplasmic intensity ratio. Data shown are mean from 3 independent experiments. Statistical analysis is by two-tailed t-test.

3.4 Multiplex cytokine and chemokine profiling in human iPSDM

To explore whether LRRK2 kinase activity and LRRK2-G2019S alters cytokine secretion in macrophages, cell supernatants were collected from LRRK2-G2019S and isogenic control iPSDM and analysed using a Luminex multiplex array which detects a panel of 27 cytokines. As innate immune cells, macrophages express toll-like receptors (TLRs) on their cell surface which recognise and bind to specific pathogen-associated molecular patterns (PAMPs) found on bacteria, fungi, and viruses. The resulting signalling pathway and cell response is TLR receptor type-specific, so I decided to explore cytokine release following multiple different TLR agonists. In addition, IFN-γ is a cytokine that is secreted primarily by NK cells and T cells and results in macrophage activation (Ivashkiv, 2018). IFN-γ is linked to LRRK2 function in immunity as it has been shown to bind to the promoter region of the LRRK2 gene and increase LRRK2 expression in cells including macrophages (Gardet et al., 2010; Lee et al., 2020).

Macrophages were stimulated with lipopolysaccharide (LPS), Pam3CysSerLys3 (PAM3CSK4), polyinosinic:polycytidylic acid (poly(I:C)) and interferon-gamma (IFN-γ) for 24 h in X-VIVO media or in X-VIVO media containing the LRRK2 kinase inhibitor MLi-2. A summary of the target receptor, transcription factor and effectors of these treatments in immune cells are summarised in Table 3.4.1.

Name	**Produced by**	**Target**	**Transcription factors**	**Effectors/results of binding**
LPS	Gram-negative bacteria	TLR4	IRF-3 and NF-κB (MYD88)	Type 1 interferons & proinflammatory cytokines
PAM3CSK4	Fungi	TLR2/1	NF-κB (MYD88)	Type 1 interferons and IL-1β

Poly(I:C)	Viruses	TLR3	IRF-3	Type 1 interferons & proinflammatory cytokines
IFN-γ	NK cells, CD8 and TH1 T cells	IFN-γ receptor	STAT1	Macrophage reprogramming – "M1 phenotype" Increased LRRK2 expression

Table 3.4.1 Summary of target receptor, transcription factor and cytokine release following treatment with LPS, PAM3CSK4, Poly(I:D) and IFN-γ.

Data is taken from (Doan et al., 2022) and (Ivashkiv, 2018).

First, I compared cytokine secretion in MLi-2- versus DMSO-treated LRRK2-G2019S and isogenic control iPSDM. There was minimal cytokine secretion in the supernatant with only 5 cytokines detected across at least three independent experiments. 22 cytokines were below the lower limit of detection of the assay and not included in statistical analysis (Figure 3.4.1). Isogenic control and LRRK2-G2019S iPSDM showed no significant changes in any of the detected cytokines with MLi-2 treatment or in control conditions (Figure 3.4.1).

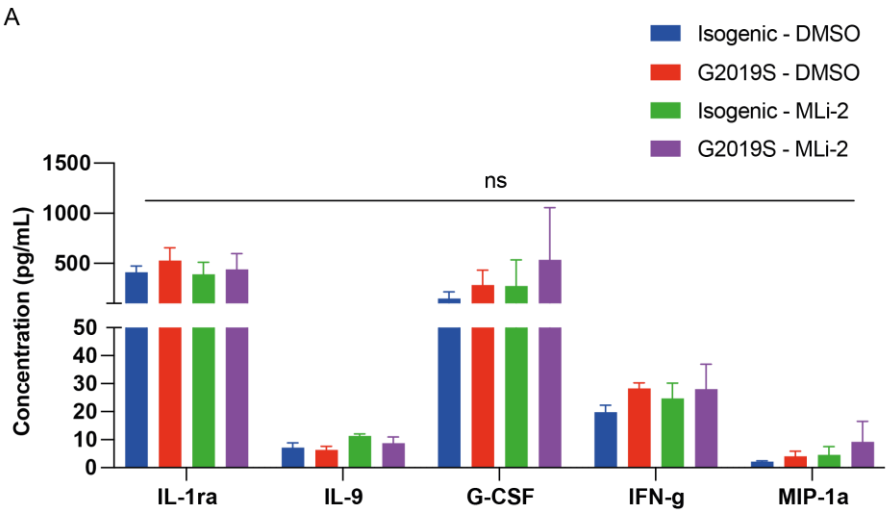

Figure 3.4.1. Cytokine secretion is not altered by MLi-2 in LRRK2-G2019S or isogenic control iPSDM

Cell supernatant was collected from LRRK2-G2019S and isogenic control iPSDM after 24 h cell culture in X-VIVO media containing MLi-2 100 nM or DMSO. Bar graphs show the mean + SEM concentration of the indicated cytokines (pg/ml) from

three independent experiments. Only cytokines which were detected in all three independent experiments are shown. Statistical significance was tested using two-way ANOVA with Bonferroni multiple comparison test. ns = not significant.

Next, LRRK2-G2019S and isogenic control iPSDM were treated with the TLR4 agonist LPS, resulting in increased secretion of all 27 cytokines. TNF-α, MIP-1β, IL-8 and MCP-1 levels increased beyond the upper detection limit of the assay. IL-13 levels showed only a marginal increase, reaching a maximum level of 1.88 pg/ml and were discounted from statistical analysis. The concentration of IL-6, IL-10 and G-CSF increased 1000-fold; IL-2, IL-5, IL-9, IL-15, IL-17, IP-10, MIP1a, PDGF-bb, RANTES and VEGF increased 100-fold; and eotaxin, IFN-γ, IL-1β, IL-1ra, IL-12, FGF-basic and GM-CSF increased 10-fold from levels detected in control macrophages (Figure 3.4.2). IL-6 concentration was significantly higher in LRRK2-G2019S iPSDM, and this increase was dependent on LRRK2 kinase activity as the effect was reversed by treatment with MLi-2 (Figure 3.4.2). There was a trend for increased secretion of IL-10 and IP-10 in LRRK2-G2019S iPSDM, however this did not reach statistical significance. In addition, there was a trend for MLi-2 to decrease RANTES production in both isogenic and LRRK2-G2019S iPSDM treated with LPS, but again this did not reach statistical significance.

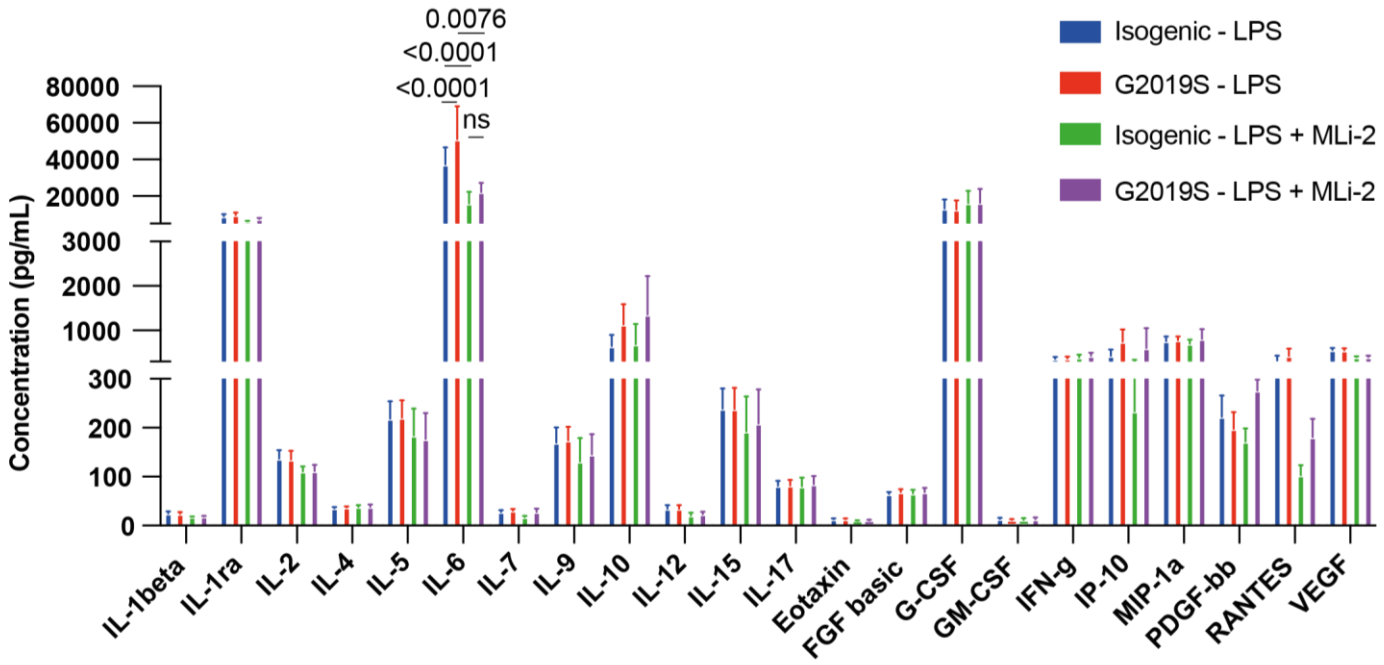

Figure 3.4.2 IL-6 secretion is increased in LRRK2-G2019S iPSDM after LPS treatment and is MLi-2 dependent.

Cell supernatant was collected from LRRK2-G2019S and isogenic control iPSDM after 24 h cell culture in X-VIVO media containing LPS or LPS + MLi-2. Bar graphs show the mean + SEM concentration of the indicated cytokines (pg/ml) from five independent experiments. Only cytokines which were detected in at least three independent experiments are shown. Statistical significance was tested using two-way ANOVA with Bonferroni multiple comparison test. Only p-values from the significantly altered cytokine are shown. ns = not significant.

Next, G2019S and isogenic control iPSDM were treated with the TLR2/1 agonist PAM3CSK4, resulting in increased secretion of all cytokines except for IL-13, which was below the lower limits of detection of the assay. TNF-α, MIP-1β, IL-8 and MCP-1 levels increased beyond the upper detection limit of the assay. The concentration of IL-1ra, IL-6, G-CSF and MIP-1a increased 1000-fold; IL-2, IL-5, IL-9, IL-10, IL-15, IL-17, IFN-G, IP-10, PDGF-bb and VEGF increased 100-fold; and IL-1beta, IL-4, IL-7, IL-12, eotaxin, FGF-basic, GM-CSF and RANTES increased 10-fold (Figure 3.4.3). There were no differences in the concentration of the measured cytokines between LRRK2-G2019S and isogenic control iPSDM in cells treated with PAM3CSK4 or PAM3CSK4 + MLi-2 (Figure 3.4.3). However, MLi-2 treatment significantly reduced the concentration of IL-6 in isogenic iPSDM (Figure 3.4.3). MLi-2 treatment did not significantly alter the concentration of any of the other measured cytokines after PAM3CSK4 treatment.

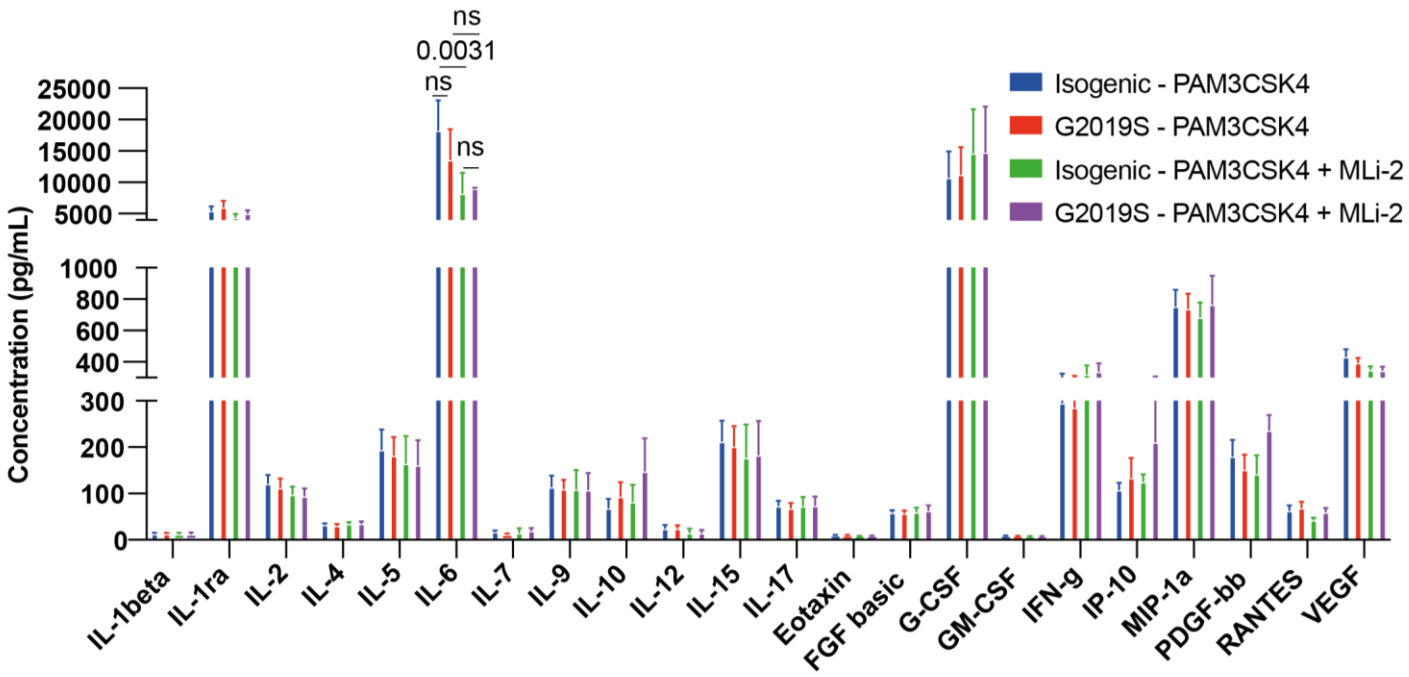

Figure 3.4.3. Cytokine secretion in LRRK2-G2019S and isogenic control iPSDM treated with PAM3CSK4 ± MLi-2

Cell supernatant was collected from LRRK2-G2019S and isogenic control iPSDM after 24 h cell culture in X-VIVO media containing PAM3CSK4 or PAM3CSK4 + MLi-2. Bar graphs show the mean + SEM concentration of the indicated cytokines (pg/ml) from five independent experiments. Only cytokines which were detected in at least three independent experiments are shown. Statistical significance was tested using two-way ANOVA with Bonferroni multiple comparison test. Only p-values from the significantly altered cytokine are shown. ns = not significant.

Poly(I:C) treatment resulted in increased supernatant concentrations of 23 cytokines, although the concentrations reached were lower than those found in cells treated with LPS or PAM3CSK4. IL-13, IL-14 and IL-15 levels were below the lower detection limit of the assay and were not included in statistical analysis. MIP-1β and IL-8 levels were above the upper detection limit of the assay and were not included in statistical analysis. TLR3 activation by poly(I:C) did not result in any significant differences between LRRK2-G2019S and isogenic control iPSDM, and cytokine secretion was not altered by MLi-2 in any of the conditions (Figure 3.4.4).

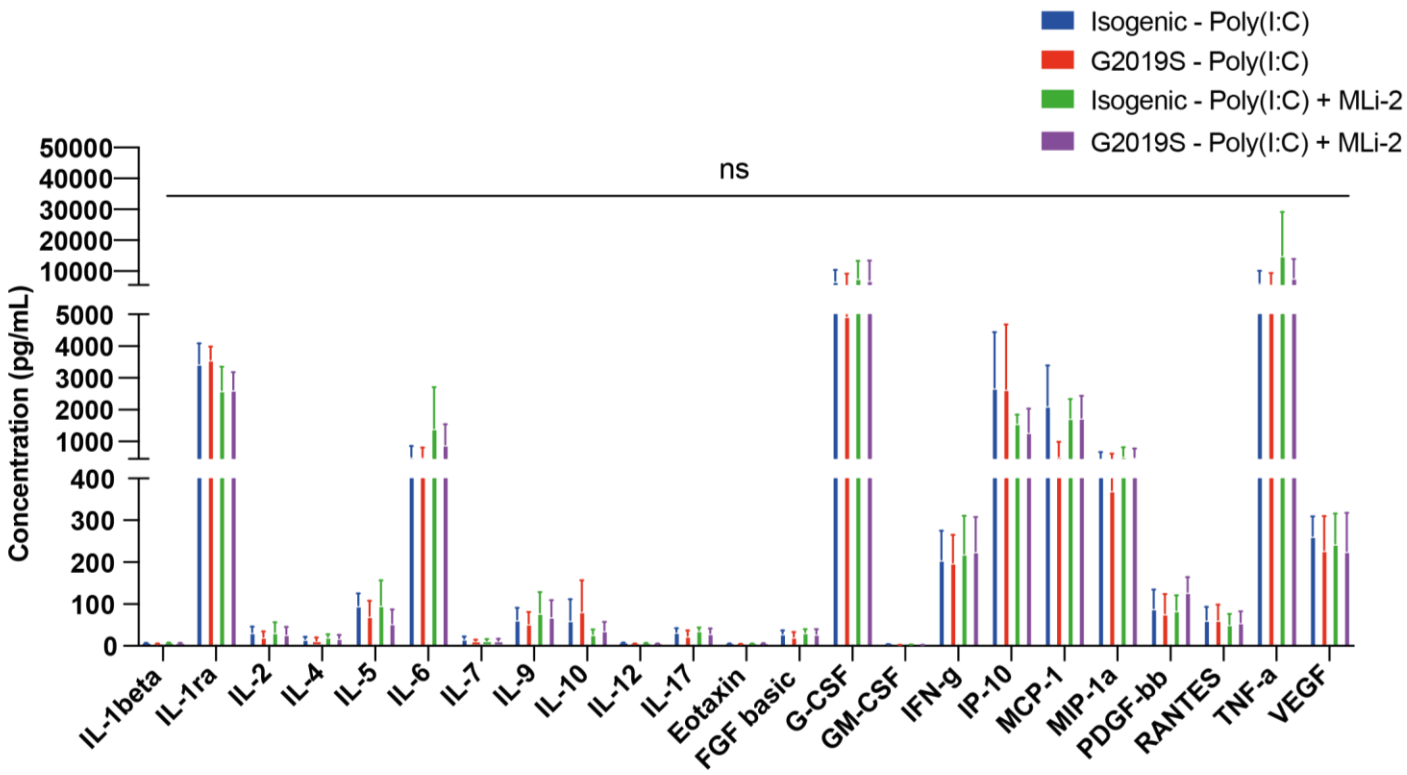

Figure 3.4.4. Cytokine secretion in LRRK2-G2019S and isogenic control iPSDM treated with Poly(I:C) ± MLi-2

Cell supernatant was collected from LRRK2-G2019S and isogenic control iPSDM after 24 h cell culture in X-VIVO media containing Poly(I:C) or Poly(I:C) + MLi-2. Bar graphs show the mean + SEM concentration of the indicated cytokines (pg/ml) from four independent experiments. Only cytokines which were detected in at least three independent experiments are shown. Statistical significance was tested using two-way ANOVA with Bonferroni multiple comparison test. ns = not significant.

When LRRK2-G2019S and isogenic control iPSDM were treated with IFN-γ, there was an increase in the production of 18 cytokines. MCP-1, IL-5, IL-13, IL-15 and PDGF-bb concentrations were outside the assay detection limits and were excluded from statistical analysis. Levels of IL-1ra, GM-CSF, RANTES did not increase beyond those seen in untreated macrophages. There was a small 1-2-fold increase in IL-2, IL-4, IL-8, IL-10, IL-12, eotaxin, FGF-basic and MIP-1b. A 10-fold increase was seen in IL-6, IL-9, IL-17, G-CSF, MIP-1a, TNF-alpha and VEGF. The concentration of IP-10 increased 1000-fold and was significantly higher in IFN-γ-treated LRRK2-G2019S iPSDM than isogenic control iPSDM (Figure 3.4.5). However, this effect was MLi-2 independent because this difference was maintained in macrophages treated with IFN-γ + MLi-2. There were no other significant changes between LRRK2-G2019S and isogenic control iPSDM and IFN-γ-mediated cytokine release was not MLi-2 dependent for any of the other tested cytokines (Figure 3.4.5). IFN-γ concentrations are included in the bar chart to show that its concentration was consistent amongst conditions when it was present in the media (Figure 3.4.5).

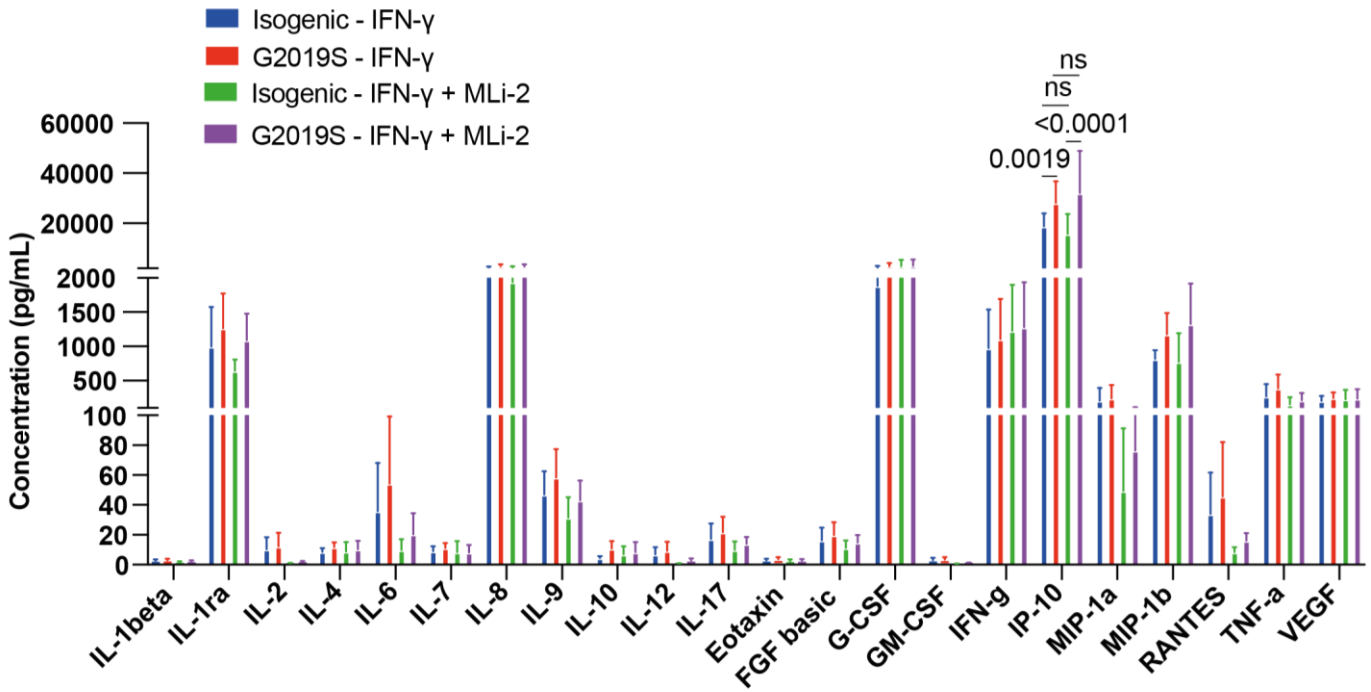

Figure 3.4.5. IFN-γ treatment results in a MLi-2 independent increase in secretion of IP-10 in LRRK2-G2019S iPSDM

Cell supernatant was collected from LRRK2-G2019S and isogenic control iPSDM after 24 h cell culture in X-VIVO media containing IFN-γ or IFN-γ + MLi-2. Bar graphs show the mean + SEM concentration of the indicated cytokines (pg/ml) from four independent experiments. Only cytokines which were detected in at least three independent experiments are shown. Statistical significance was tested using two-way ANOVA with Bonferroni multiple comparison test. Only p-values from the significantly altered cytokine are shown. ns = not significant.

A summary of the cytokine findings following the different immune agonist treatment in LRRK2-G2019S and isogenic control macrophages is shown in the table below.

	Cytokines upregulated in LRRK2-G2019S iPSDM	**MLi-2 dependent?**
MLi-2	None	N/A
LPS	IL-6	Yes
PAM3CSK4	None	N/A
Poly(I:C)	None	N/A
IFN-γ	IP-10	No

Table 3.4.2. Summary of cytokine differences in G2019S iPSDM after immune stimulation

To summarise, in this chapter I have phenotypically characterised murine BMDM and human iPSDM carrying LRRK2 mutations. My results demonstrate that LRRK2 mutations do not alter macrophage LRRK2 expression, lysosomal content, and proteolytic activity. In addition, I found that stimulation of human iPSDM carrying the G2019S mutation with LPS and IFN-γ results in increased secretion of IL-6 and IP-10, respectively.

Chapter 4. Results 2 Defining the substrates of LRRK2 kinase in macrophages

4.1 Lysosomal damage results in LRRK2 kinase dependent phosphorylation of Rab8, Rab10 and Rab12

Having demonstrated that murine BMDM and human iPSDM carrying LRRK2 mutations show no baseline deficit in lysosomal content or proteolytic activity in chapter 3, I next dissected the macrophage response to lysosomal membrane damage. To induce lysosomal damage, I used L-leucyl-L-leucine methyl ester (LLOMe), a reagent that accumulates within the acidic lysosomal compartment, condenses into membranolytic polymers, and ruptures the lysosomal membrane (Thiele and Lipsky, 1990b).

LLOMe-induced lysosomal membrane damage resulted in phosphorylation of Rab10 pT73 and Rab12 pS106 in wild-type BMDM (Figure 4.1.1). Phosphorylation was also detected using an anti-Rab8A pT72 antibody (MJF-R20, ab230260), however this antibody cross-reacts with phosphorylated Rab3A, Rab35 and Rab43 (Steger et al., 2017), thus it will be denoted as “pan-phospho-Rab” (Figure 4.1.1). Phosphorylation of Rab10 pT73, Rab12 pS106 and pan-phospho-Rab was LRRK2 kinase activity-dependent because it was inhibited by MLi-2 and was not detected in LRRK2 kinase-dead BMDM after lysosomal damage (Figure 4.1.1). Although not statistically significant, Rab12 pS106/total Rab12 increased from 0.08 at baseline to 0.3 after lysosomal damage in an MLi-2-independent manner in LRRK2 kinase-dead BMDM. Total levels of Rab8A, Rab10 and Rab12 were not significantly altered in any condition (Figure 4.1.1).

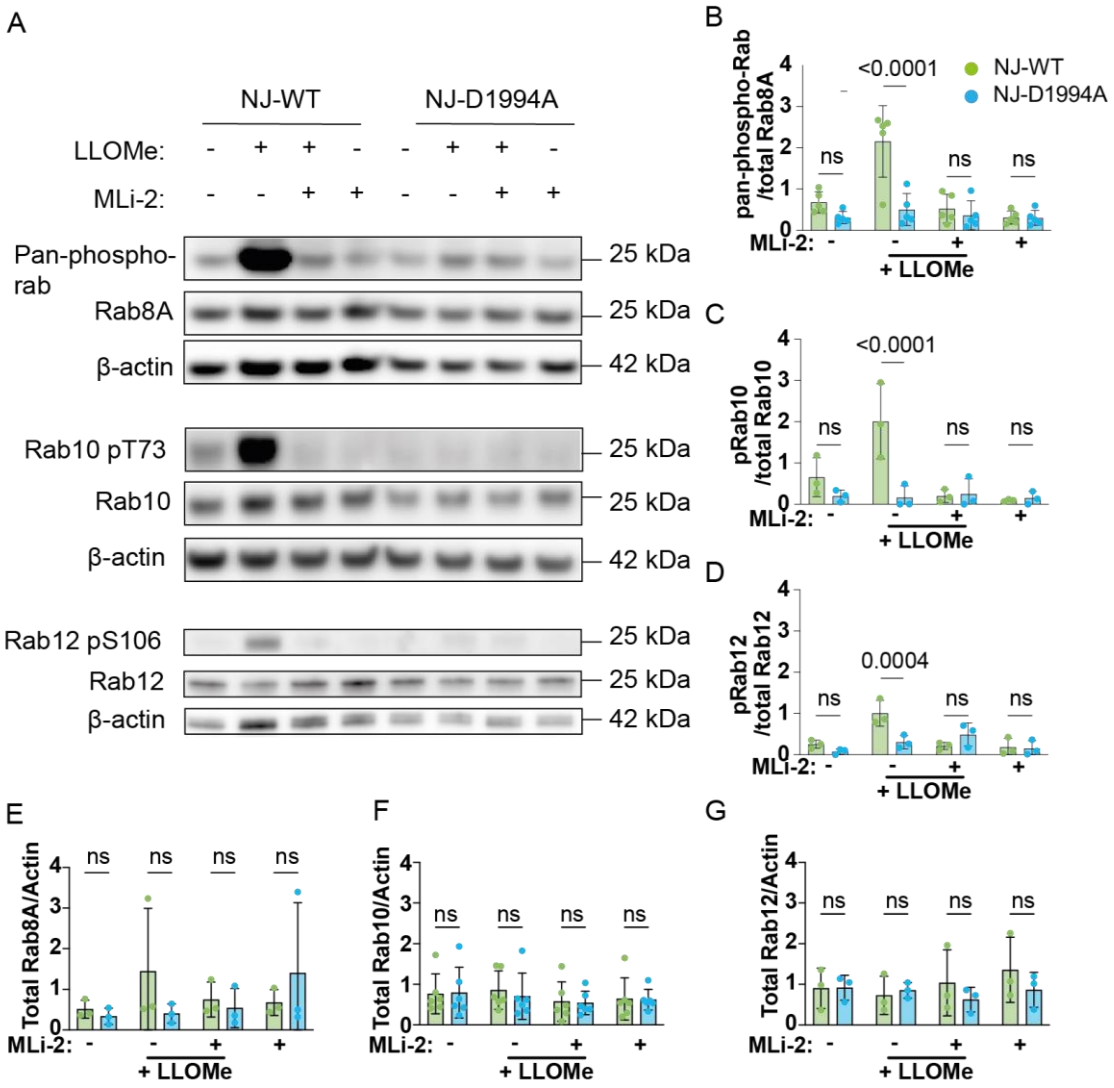

Figure 4.1.1. Phosphorylation of a subset of Rab GTPases is LRRK2 kinase dependent in NJ-WT BMDM

(A) Western blot analysis of pan-phospho-Rab, Rab8A, Rab10 pT73, Rab10, Rab12 pS106, Rab12 and β-actin in NJ-WT and NJ-D1994A macrophages in untreated, LLOMe, LLOMe + MLi-2 and MLi-2 conditions. (B to D) pan-phospho-Rab, Rab10 pT73 and Rab12 pS106 band intensities were quantified by densitometry and normalised to Rab8A, Rab10 and Rab12, respectively. (E to G) Rab8A, Rab10 and Rab12 band intensities were quantified by densitometry and normalised to β-actin. Data are mean ± SD from (B and E) 5 independent experiments and (C and D, F and G) 3 independent experiments. Two-way ANOVA followed by Tukey's multiple comparisons test.

Next, I confirmed that Rab10 pT73 and Rab12 pS106 were phosphorylated in 6J-WT BMDM after LLOMe-induced lysosomal membrane damage (Figure 4.1.2). Phosphorylation was also detected by the pan-phospho-Rab antibody in these wild-type cells. Again, this phosphorylation was LRRK2 kinase dependent because it was

inhibited by MLi-2 and was not detected in 6J-LRRK2KO BMDM after lysosomal damage (Figure 4.1.2). In addition, there was significantly reduced Rab10 pT73 in 6J-LRRK2KO compared to 6J-WT BMDM in the control condition. In 6J-LRRK2KO BMDM, Rab12 pS106/total Rab12 increased from 0.2 at baseline to 0.5 after lysosomal damage in an MLi-2-independent manner, however this small increase was not statistically significant (Figure 4.1.2). Total levels of Rab8A, Rab10 and Rab12 were not significantly altered in any condition (Figure 4.1.2).

Given that there was a trend for Rab12 pS106 levels to marginally increase with LLOMe-treatment in NJ-D1994A and 6J-LRRK2KO BMDM, a small fraction of Rab12 pS106 may be phosphorylated by kinases other than LRRK2 after lysosomal membrane damage, although a larger sample size and other kinase inhibitors would be required to test this.

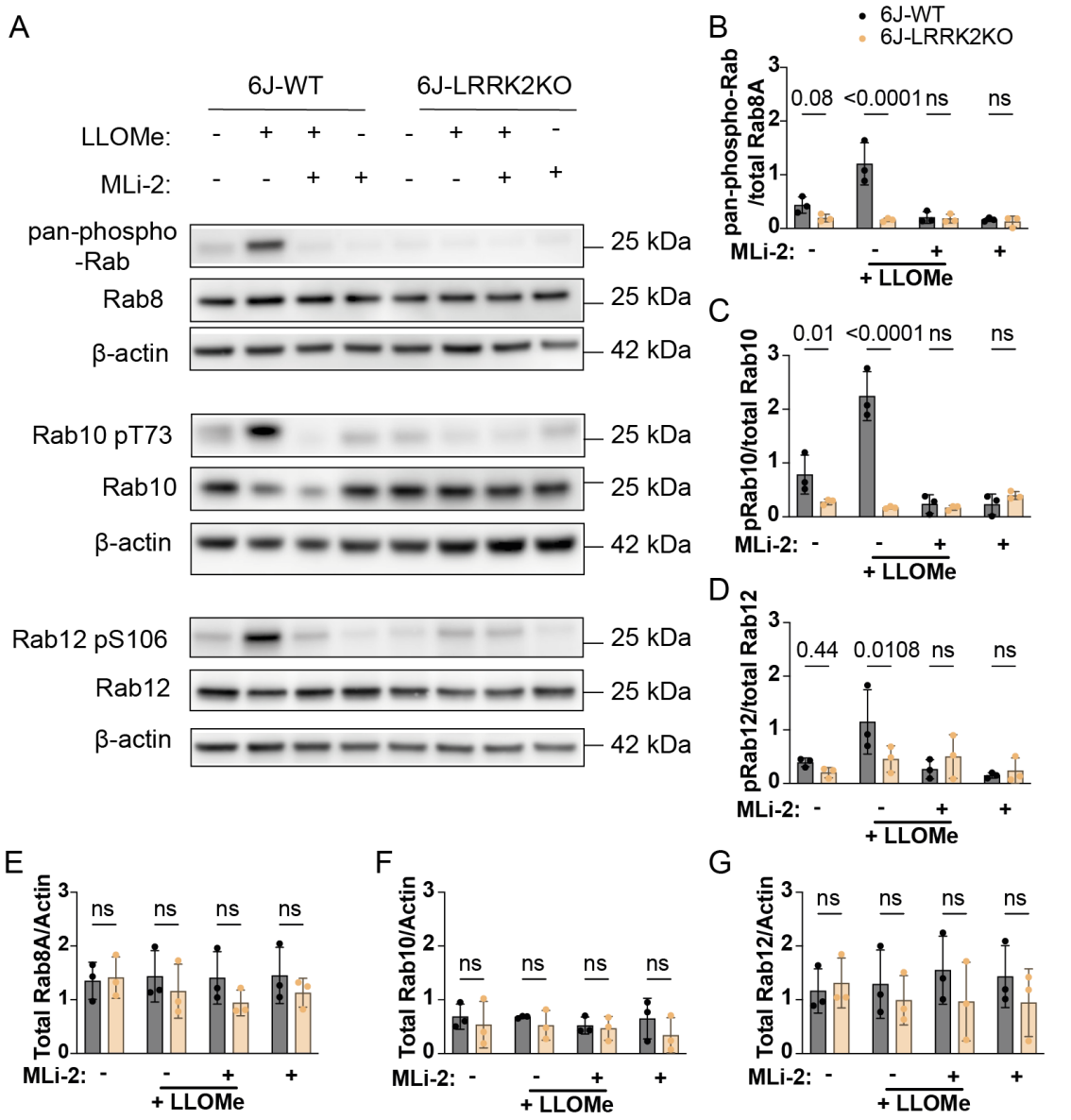

Figure 4.1.2. Phosphorylation of a subset of Rab GTPases is LRRK2 kinase dependent in 6J-WT BMDM

(A) Western blot analysis of pan-phospho-Rab, Rab8A, Rab10 pT73, Rab10, Rab12 pS106, Rab12 and β-actin in 6J-WT and 6J-LRRK2KO macrophages in untreated, LLOMe, LLOMe + MLi-2 and MLi-2 conditions. (B to D) pan-phospho-Rab, Rab10 pT73 and Rab12 pS106 band intensities were quantified by densitometry and normalised to Rab8A, Rab10 and Rab12, respectively. (E to G) Rab8A, Rab10 and Rab12 band intensities were quantified by densitometry and normalised to β-actin. Data are mean ± SD from 3 independent experiments. Two-way ANOVA followed by Tukey's multiple comparisons test.

4.2 A phosphoproteomics approach to identify substrates of LRRK2 kinase in macrophages

4.2.1 Collaboration statement

I conducted all differentiations of murine haematopoietic progenitor cells to BMDM, cell culture, compound treatments, cell detachment and snap freezing for proteomics and phosphoproteomics experiments.

Cell lysis, peptide/phosphopeptide enrichment, TMT-labelling, and LC-MS/MS analysis of samples for the proteomics and phosphoproteomics experiments were conducted by Simeon Mihaylov (Kinases and Brain Development Laboratory, The Francis Crick Institute) supported by Mike Skehel and Helen Flynn (Proteomics Scientific technology platform, The Francis Crick Institute).

Bioinformatics analysis was conducted by Simeon Mihaylov and Sila Ultanir (Kinases and Brain Development Laboratory, The Francis Crick Institute). Volcano plots were produced by Simeon Mihaylov. Data interpretation was performed in a collaborative manner.

4.2.2 Summary of experimental conditions

The Western blots in chapter 4.1 showed LRRK2 kinase activity-dependent phosphorylation of a subset of Rab GTPases after lysosomal damage in BMDM. A previous phosphoproteomics study in HEK293 cells and mouse embryonic fibroblasts reported LRRK2 kinase activity-dependent phosphorylation of 10 Rab GTPases (Rab 3A/B/C/D, Rab8A/B, Rab10, Rab12, Rab35 and Rab43) (Steger et al., 2017). I hypothesised that LRRK2 kinase phosphorylates other substrates in macrophages after lysosomal membrane damage. To test this, I collaborated with the Kinase and Brain Development Laboratory at the Francis Crick Institute to develop a non-biased phosphoproteomics approach.

Phosphoproteomics is a method to quantify a phosphoproteome (total number of phosphorylated proteins in a sample) and identify the specific amino acid residues

on proteins that are phosphorylated. Phosphoproteomics can also be used to identify bona fide substrates of a protein kinase, however this requires genetic or pharmacological manipulation to capture kinase-of-interest-specific phosphorylations. To identify LRRK2 kinase-specific phosphorylations, I utilised the NJ-D1994A macrophages as a genetic control for LRRK2 kinase activity. These cells contain endogenous levels of LRRK2 protein (see Figure 3.2.2) with a mutation in the kinase domain that results in redundant kinase activity, making this a robust control. These cells were selected over the LRRK2KO macrophages due to previous reports of compensatory LRRK1 activity in these cells (Tong et al., 2010).

The aim of these experiments was to identify bona fide LRRK2 kinase substrates in macrophages in the context of lysosomal membrane damage, during which there is Rab12-dependent recruitment of LRRK2 to lysosomes, increased LRRK2 kinase activity, and LRRK2-dependent lysosomal membrane repair and lysosomal tubulation/sorting driven by LRRK2 (LYTL) (Bonet-Ponce et al., 2020; Dhekne et al., 2023; Eguchi et al., 2018; Herbst et al., 2020; Wang et al., 2023). In contrast, in resting control conditions, LRRK2 is reported to exist as inactive cytosolic monomers with minimal kinase activity (Berger et al., 2010; Biskup et al., 2006; Schapansky et al., 2014). By utilising genetic manipulation of LRRK2 kinase in NJ-D1994A macrophages combined with pharmacological induction of LRRK2 kinase activity by LLOMe treatment, we developed a novel approach to LRRK2 phosphoproteomics which allows identification of LRRK2 kinase activity-dependent substrates in the context of lysosomal damage. Previous LRRK2 phosphoproteomics studies have looked at substrates in resting cells or cells treated with LRRK2 kinase inhibitors (Steger et al., 2017; Steger et al., 2016; Thirstrup et al., 2017).

The experimental workflow is shown in Figure 4.2.1. From four biological replicates, a total of 29,110 phosphosites were identified (Figure 4.2.1).

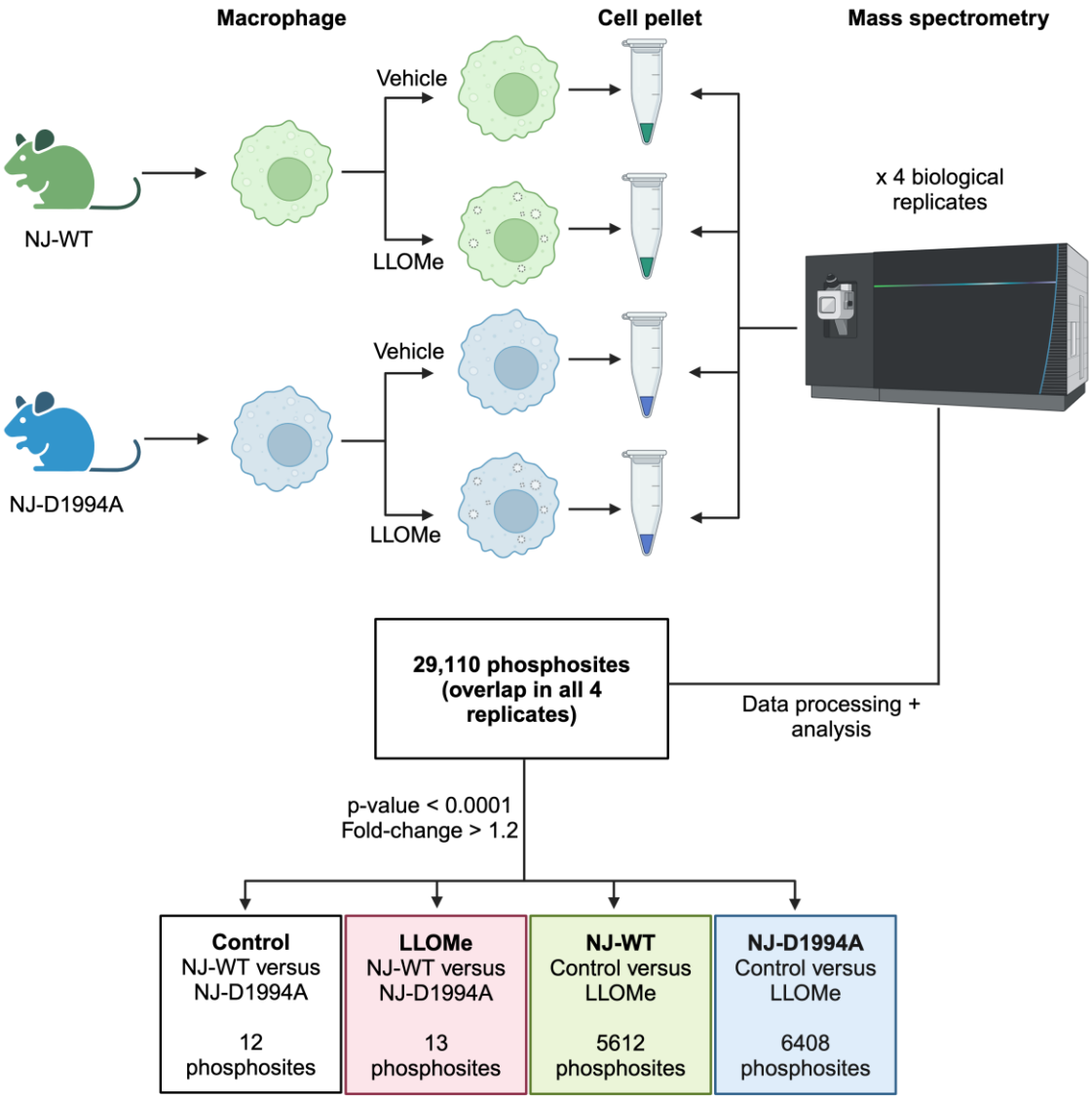

Figure 4.2.1. Phosphoproteomics experimental workflow and analysis

BMDM were differentiated from NJ-WT and NJ-D1994A mice. Following treatment with LLOMe or vehicle control, cells were collected and processed for LC-MS/MS. From four biological replicates, a total of 29,110 phosphosites were identified in all 4 experiments. Data was processed using MaxQuant (Uniprot mouse reference genome) and then analysed using R software. The TNT lot-corrected reporter intensities were normalised (CONSTANd), log-transformed and analysed using limma. The number of significantly altered phosphosites (p-value < 0.0001 and fold-change > 1.2) within each of the four indicated comparison groups are shown.

4.2.3 Altered phosphorylations between NJ-WT and NJ-D1994A macrophages

In control conditions, 12 phosphosites on 9 proteins were identified as significantly altered between NJ-WT and NJ-D1994A macrophages using selection criteria of fold-change > 1.2 and p-value < 0.0001 (Figure 4.2.2).

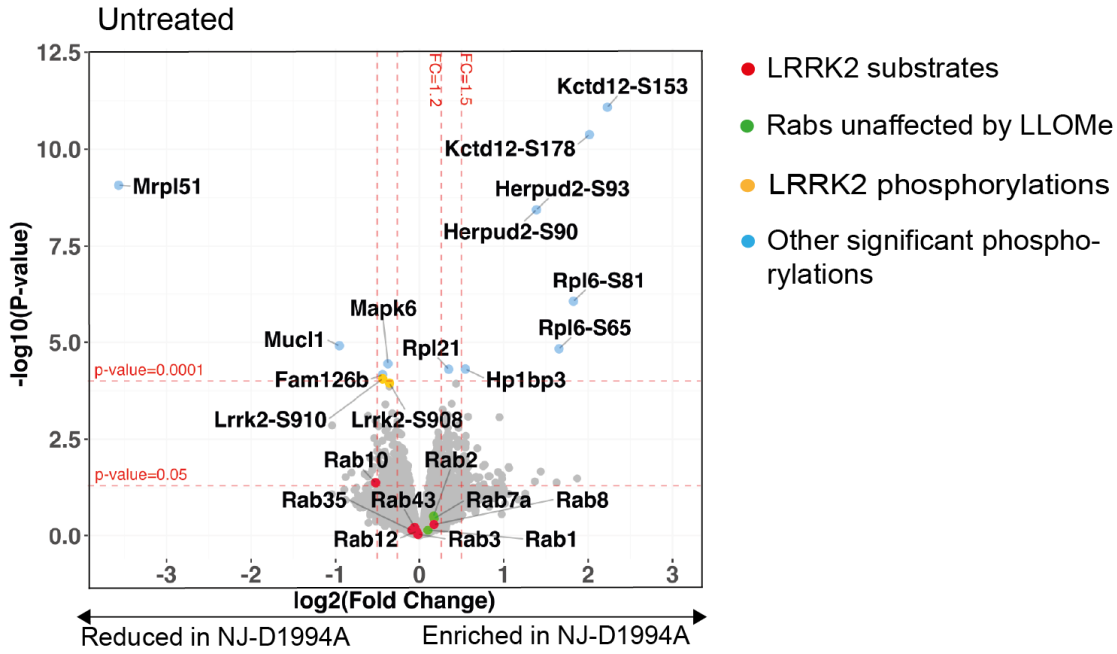

Figure 4.2.2. Phosphorylations altered in control conditions in NJ-D1994A macrophages

Vehicle control-treated NJ-WT and NJ-D1994A BMDM were analysed by mass spectrometry. Volcano plot shows the difference in phosphorylation levels between NJ-WT and NJ-D1994A BMDM. Each point represents one phosphorylation site of a protein. The x-axis shows the $\log_{10}$-transformed fold change, and the y-axis shows the significance by $-\log_{10}$-transformed P-value, obtained by linear models for microarray data. A fold-change greater than 1.2 and p value <0.0001 was deemed significant.

The significantly altered phosphorylation sites were all located on serine or threonine amino acid residues, but there were no similarities amongst the peptide sequences (Table 4.2.1).

Protein	Position (probability)	Peptide	Number of sites
Decreased in NJ-D1994A macrophages			
39S ribosomal protein L51 (Mrpl51)	S10 (1)	AGSVPWAA**S**RR	1
Mucin-like 1 (Mucl1)	S150 (0.697)	QEDNT**S**HKK	1
Mitogen-activated protein kinase 6 (Mapk6)	S189 (1)	GHL**S**EGLVTK	1
Hyccin 2 (Fam126b)	S519 (0.5)	**S**PSFNMQLISQV	1

Increased in NJ-D1994A macrophages			
Homocysteine-responsive ER-resident ubiquitin-like domain member 2 (Herpud2)	S90 (0.549) S93 (0.535)	QDEYHMVHLVCASR**S**PP**S**S PK	2
60S ribosomal protein L6 (Rpl6)	S65(1) S81(1)	GIGRY**S**R RKY**S**AAK	2
BTB/POZ domain-containing protein KCTD12 (Kctd12)	S178(0.894) S153(1)	EG**S**LGDELLPLGYAEPEPQ EGASAGAP**S**PTLELASR	2
Heterochromatin protein 1-binding protein 3 (Hp1bp3)	S475(1)	ARP**S**PSVIK	1
60S ribosomal protein L21 (Rpl21)	T124 (1)	EKG**T**WVQLK	1

Table 4.2.1. Proteins with significantly altered phosphorylations in control conditions between NJ-WT and NJ-D1994A macrophages (fold-change > 1.5, p-value < 0.0001). The phosphorylation site is marked in bold and underlined.

After LLOMe-induced lysosomal damage, 13 phosphosites on 11 proteins were significantly different between NJ-WT and NJ-D1994A macrophages using selection criteria of fold change > 1.2 and p-value < 0.0001 (Figure 4.2.3).

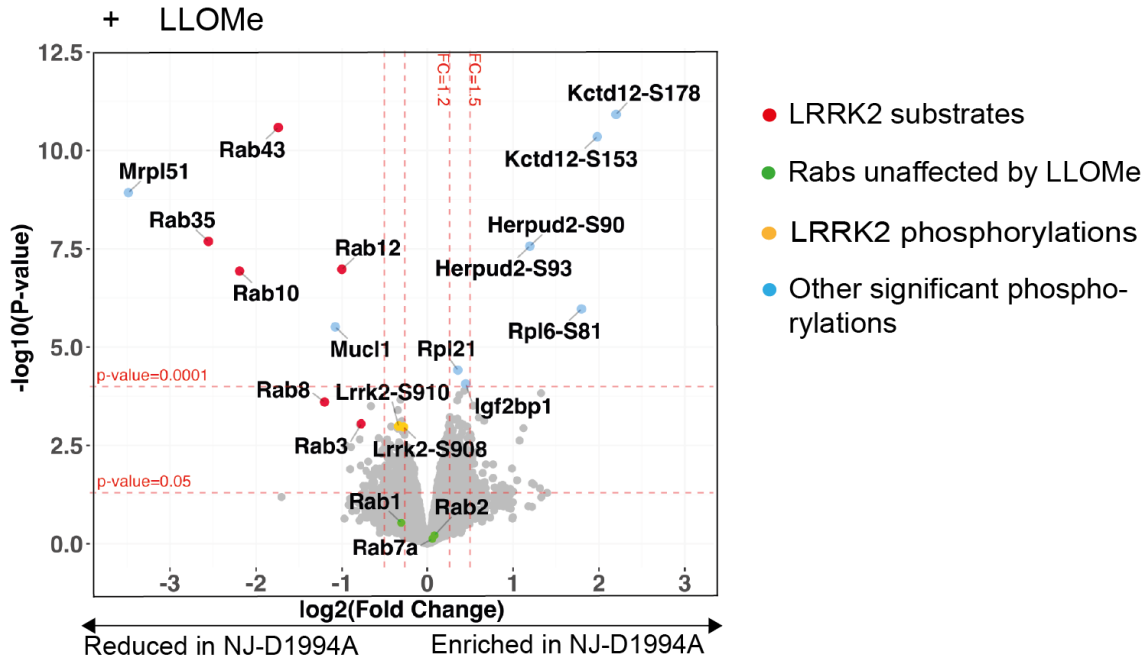

Figure 4.2.3. Phosphorylations altered by LLOMe in NJ-D1994A macrophages

LLOMe-treated NJ-WT and NJ-D1994A BMDM were analysed by mass spectrometry. Volcano plot shows the difference in phosphorylation levels between

NJ-WT and NJ-D1994A BMDM. Each point represents one phosphorylation site of a protein. The x-axis shows the log_{10}-transformed fold change, and the y-axis shows the significance by $-log_{10}$-transformed P-value, obtained by linear models for microarray data. A fold-change greater than 1.2 and p value <0.0001 was deemed significant.

Strikingly, a subset of Rab GTPases (Rab10, Rab12, Rab35, Rab43) were significantly less phosphorylated in NJ-D1994A macrophages after LLOMe. These phosphorylations were located on a serine or threonine amino acid residue within a common peptide sequence: F-X-**S/T**-I-T-X-X-Y-Y-R (where bold and underlined is the phosphorylation site, and X is a variable amino acid) (Table 4.2.2).

Protein	Position (probability)	Peptide	Number of sites
Decreased in NJ-D1994A macrophages			
Rab10	T73 (1)	FH**T**ITTSYYR	1
Rab12	S105 (1)	FN**S**ITSAYYR	1
Rab35	T72 (1)	FR**T**ITSTYYR	1
Rab43	T80 (1)	FR**T**ITQSYYR	1
39S ribosomal protein L51 (Mrpl51)	S10 (1)	AGSVPWAA**S**RR	1
Mucin-like 1 (Mucl1)	S150 (0.697)	QEDNT**S**HKK	1
Increased in NJ-D1994A macrophages			
Homocysteine-responsive endoplasmic reticulum-resident ubiquitin-like domain member 2 protein (Herpud2)	S90 (0.535) S93 (0.549)	QDEYHMVHLVCASR**S**P P**S**SPK	2
60S ribosomal protein L6 (Rpl6)	S81(1)	RKY**S**AAK	1
BTB/POZ domain-containing protein KCTD12 (Kctd12)	S153 (1) S178 (0.894)	EG**S**LGDELLPLGYAEPE PQEGASAGAP**S**PTLEL ASR	2
60S ribosomal protein L21 (Rpl21)	T124 (1)	EKG**T**WVQLK	1
Insulin-like growth factor 2 mRNA-binding protein 1(Igf2bp1)	S181 (1)	QG**S**PVAAGAPAK	1

Table 4.2.2. Proteins with significantly altered phosphorylations in LLOMe conditions between NJ-WT and NJ-D1994A macrophages (fold-change > 1.5, p-value < 0.0001). The phosphorylation site is marked in bold and underlined.

In addition to the Rab GTPases, Mrpl51 pS10 and Mucl1 pS150 were significantly less phosphorylated in NJ-D1994A macrophages (Figure 4.2.3 and Table 4.2.2). These phosphorylations were also significantly reduced in NJ-D1994A macrophages in the control condition (Figure 4.2.2 and Table 4.2.1). Importantly, these phosphorylations were not associated with lysosomal damage in NJ-WT macrophages (Figure 4.2.4), indicating that LRRK2 activation and recruitment to lysosomes does not alter phosphorylation of these proteins.

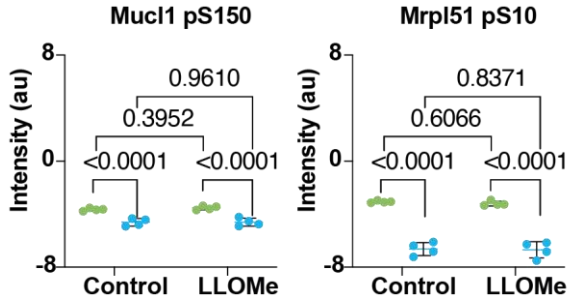

Figure 4.2.4 Phosphorylation of Mucl1 and Mrpl51 is not associated with lysosomal damage

Scatterplots showing the raw intensity data obtained by mass spectrometry and unadjusted p-values for the phosphorylation of Mucl1 pS150 and Mrpl51 pS10. Each point represents the normalised and log2 transformed TMT-corrected reporter intensity value obtained by mass spectrometry (n=4 biological replicates). P values by linear models for microarray data.

In contrast, phosphorylations of Herpud2 pS90 and pS93, Rpl6 pS81, Kctd12 pS153 and pS178, Rpl21 pT124, and Igf2bp1 pS181 were increased in NJ-D1994A macrophages (Table 4.2.2). Increased phosphorylation in a kinase-dead mutant suggests downstream effects like activation of a kinase or inhibition of a phosphatase secondary to the LRRK2-D1994A mutation. These phosphorylations were also unaffected by lysosomal damage (Figure 4.2.5).

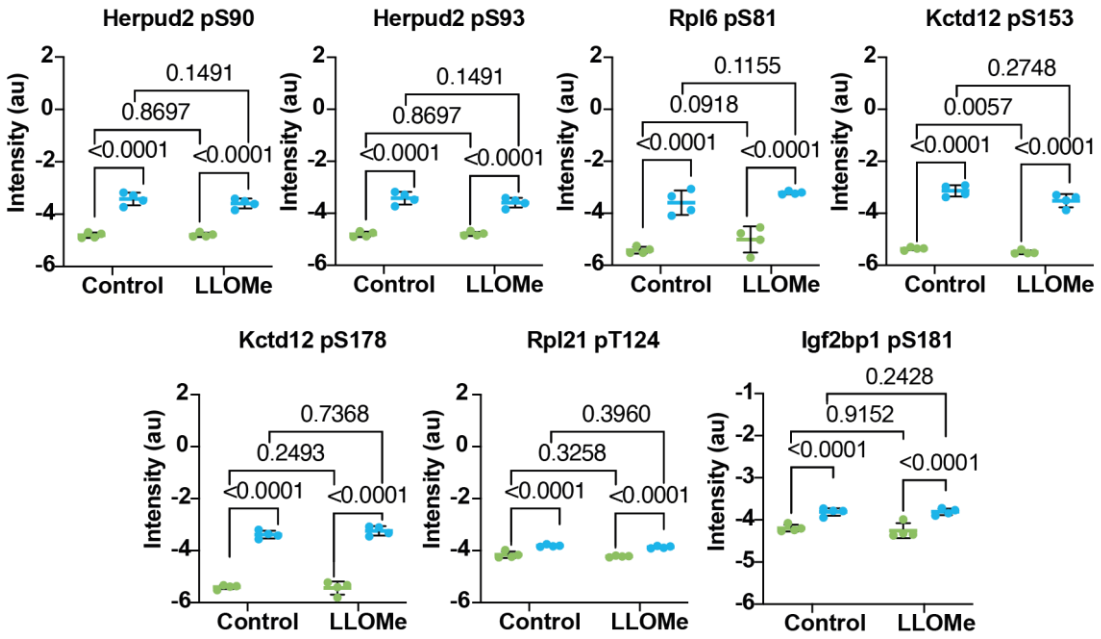

Figure 4.2.5 Phosphorylation of Herpud2, Rpl6, Kctd12, Rpl21 and Igf2bp1 is increased in NJ-D1994A macrophages

Scatterplots showing the raw intensity data obtained by mass spectrometry and unadjusted p-values for the Herpud2 pS90, Herpud2 pS93, Rpl6 pS81, Kctd12 pS153, Kctd12 pS178, Rpl21 pT124 and Igf2bp1 pS181 phosphorylation sites. Each point represents the normalised and log2 transformed TMT-corrected reporter intensity value obtained by mass spectrometry (n=4 biological replicates). P values by linear models for microarray data.

4.2.4 Further exploration of Rab GTPase phosphorylations in NJ-WT and NJ-D1994A macrophages after lysosomal damage

On further analysis of the phosphoproteomics dataset, a total of 58 phosphorylation sites on 23 Rab GTPases were identified (Figure 4.2.6). It is intriguing that LRRK2 kinase phosphorylates only a subset of Rab GTPases and this may be linked to Rab intracellular location (Kluss et al., 2020) rather than cell type-specific differences in Rab expression, or Rab domain structure. In keeping with this, Rab1A pT75, Rab2A pS70 and Rab7 pS72 are known to contain the LRRK2 phosphorylation motif in their switch II domain but have previously been excluded as bona fide targets of LRRK2 kinase (Steger et al., 2017; Steger et al., 2016). In our dataset, there were no significant differences in phosphorylation of Rab1 pT75, Rab2A pS70 or Rab7 pS72 between NJ-WT and NJ-D1994A macrophages (Figure 4.2.6).

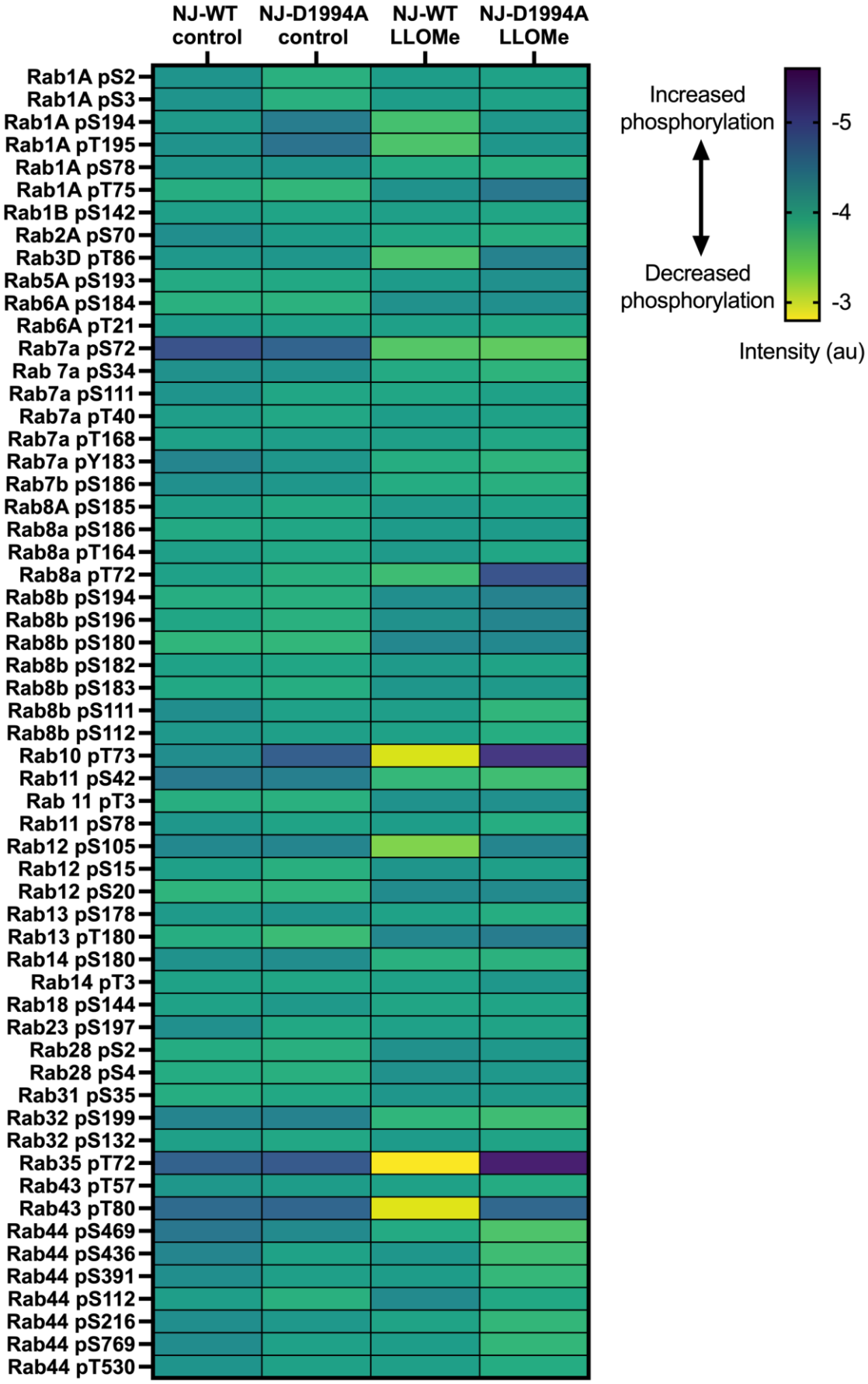
NJ-WT control
NJ-D1994A control
NJ-WT LLOMe
NJ-D1994A LLOMe
Rab1A pS2
Rab1A pS3
Rab1A pS194
Rab1A pT195
Rab1A pS78
Rab1A pT75
Rab1B pS142
Rab2A pS70
Rab3D pT86
Rab5A pS193
Rab6A pS184
Rab6A pT21
Rab7a pS72
Rab 7a pS34
Rab7a pS111
Rab7a pT40
Rab7a pT168
Rab7a pY183
Rab7b pS186
Rab8A pS185
Rab8a pS186
Rab8a pT164
Rab8a pT72
Rab8b pS194
Rab8b pS196
Rab8b pS180
Rab8b pS182
Rab8b pS183
Rab8b pS111
Rab8b pS112
Rab10 pT73
Rab11 pS42
Rab 11 pT3
Rab11 pS78
Rab12 pS105
Rab12 pS15
Rab12 pS20
Rab13 pS178
Rab13 pT180
Rab14 pS180
Rab14 pT3
Rab18 pS144
Rab23 pS197
Rab28 pS2
Rab28 pS4
Rab31 pS35
Rab32 pS199
Rab32 pS132
Rab35 pT72
Rab43 pT57
Rab43 pT80
Rab44 pS469
Rab44 pS436
Rab44 pS391
Rab44 pS112
Rab44 pS216
Rab44 pS769
Rab44 pT530
Increased phosphorylation
Decreased phosphorylation
-5
-4
-3
Intensity (au)

Figure 4.2.6 LRRK2 kinase-dependent Rab phosphorylation is limited to a small subset of Rab GTPases

Heatmap of all identified Rab phosphopeptide intensities (au) in NJ-WT and NJ-D1994A macrophages treated with vehicle control or LLOMe. The intensity values were obtained by mass spectrometry, TMT reporter corrected, normalised and log2 transformed.

Rab3 pT86 and Rab8 pT72 were phosphorylated less in NJ-D1994A macrophages than NJ-WT macrophages after LLOMe within a common peptide sequence (Table 4.2.3). However, these differences were significant only at $p < 0.05$.

Protein	Position (probability)	Peptide	Number of sites
Rab3	T86 (1)	YR**T**ITTAYYR	1
Rab8	T72 (1)	FR**T**ITTAYYR	1

Table 4.2.3. Rab3 and Rab8 phosphorylations were reduced in NJ-D1994A macrophages after LLOMe treatment (p-value < 0.001 and fold-change > 0.5 or < -0.5). The phosphorylation site is marked in bold and underlined.

4.2.5 LRRK2 phosphorylation sites in NJ-WT and NJ-D1994A macrophages

There are 207 phosphorylation sites reported on human LRRK2 (accessed 17th February 2024, www.phosphosite.org), of which around 20 are reported to be autophosphorylation sites (Marchand et al., 2020). Studies have previously used autophosphorylation sites as a surrogate marker of LRRK2 kinase activity (Kluss et al., 2018). I therefore explored LRRK2 phosphorylation sites in NJ-WT and NJ-D1994A macrophages identified in our dataset. However, only 4 sites were identified across 4 biological replicates (Table 4.2.4).

Protein	Position (probability)	Peptide	Number of sites
LRRK2	S908 (0.614)	**S**NSISVGEVYRDLALQR	1
LRRK2	S910 (1)	SN**S**ISVGEVYRDLALQR	1
LRRK2	S954 (1)	IL**S**SDESLR	1
LRRK2	S955 (0.886)	ILS**S**DESLR	1

Table 4.2.4. Sites of phosphorylation on LRRK2 in NJ-WT and NJ-D1994A macrophages.

LRRK2 pS908 and pS910 have previously been reported as sites of LRRK2 phosphorylation by casein kinase 1α (Chia et al., 2014). Another study reported LRRK2 pS910 phosphorylation by protein kinase A (PKA), which in turn promoted the binding of 14-3-3 proteins to LRRK2 (Muda et al., 2014). LLOMe-treatment was associated with a significant dephosphorylation of LRRK2 pS908, pS910 and pS954 in wild-type macrophages (Figure 4.2.7). Dephosphorylation would be in keeping with activation of a phosphatase or inhibition of kinase activity during lysosomal membrane damage. NJ-D1994A macrophages showed reduced phosphorylation of LRRK2 pS908 and pS910 compared to wild-type macrophages, however this was independent of lysosomal membrane damage (Figure 4.2.7). There were no differences in phosphorylation of LRRK2 pS954 or LRRK2 pS955 between NJ-WT and NJ-D1994A macrophages in control or LLOMe conditions in keeping with these being sites of LRRK2 phosphorylation by another kinase (Figure 4.2.7).

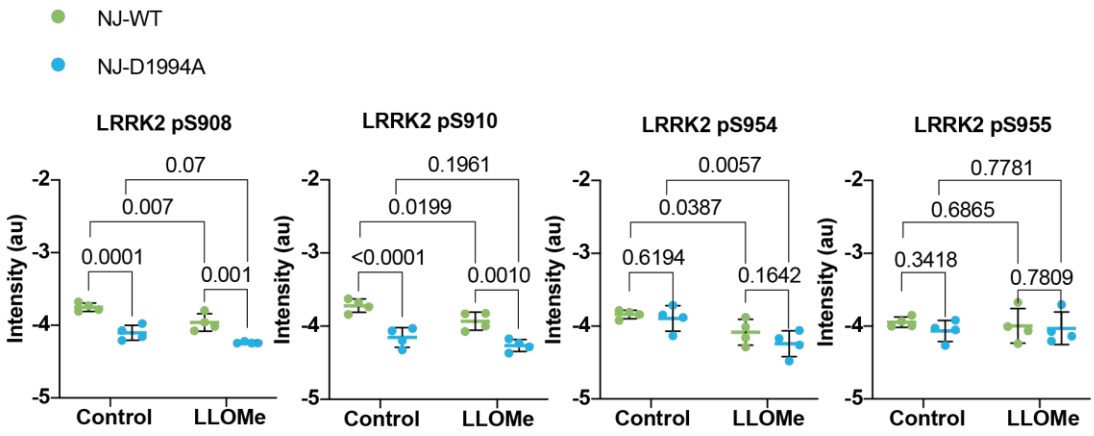

Figure 4.2.7. LRRK2 S908 and S910 phosphorylations are reduced in NJ-D1994A macrophages and are independent of LLOMe treatment

Scatterplots showing the raw intensity data obtained by mass spectrometry and p-values for the LRRK2 phosphorylation sites S908, S910, S954 and S955. Each point represents the normalised and log2 transformed TMT-corrected reporter intensity value obtained by mass spectrometry (n=4 biological replicates). P values by linear models for microarray data.

4.2.6 Proteome changes induced by LLOMe in NJ-WT and NJ-D1994A macrophages

Proteome analysis was also performed to control for phosphorylation changes secondary to an increase or decrease in the total protein level. Hp1bp3 was increased in NJ-D1994A macrophages in control conditions (Figure 4.2.8) and this could explain why Hp1bp3 pS475 phosphorylation was increased in these cells (Figure 4.2.2 and Table 4.2.1). While we did not detect a change in the phosphorylation of Rab44, its total level was increased in NJ-D1994A macrophages after LLOMe treatment (Figure 4.2.8). Importantly, none of the other proteins with significantly altered phosphorylations showed altered total proteome levels in untreated or LLOMe-treated conditions (Figure 4.2.8).

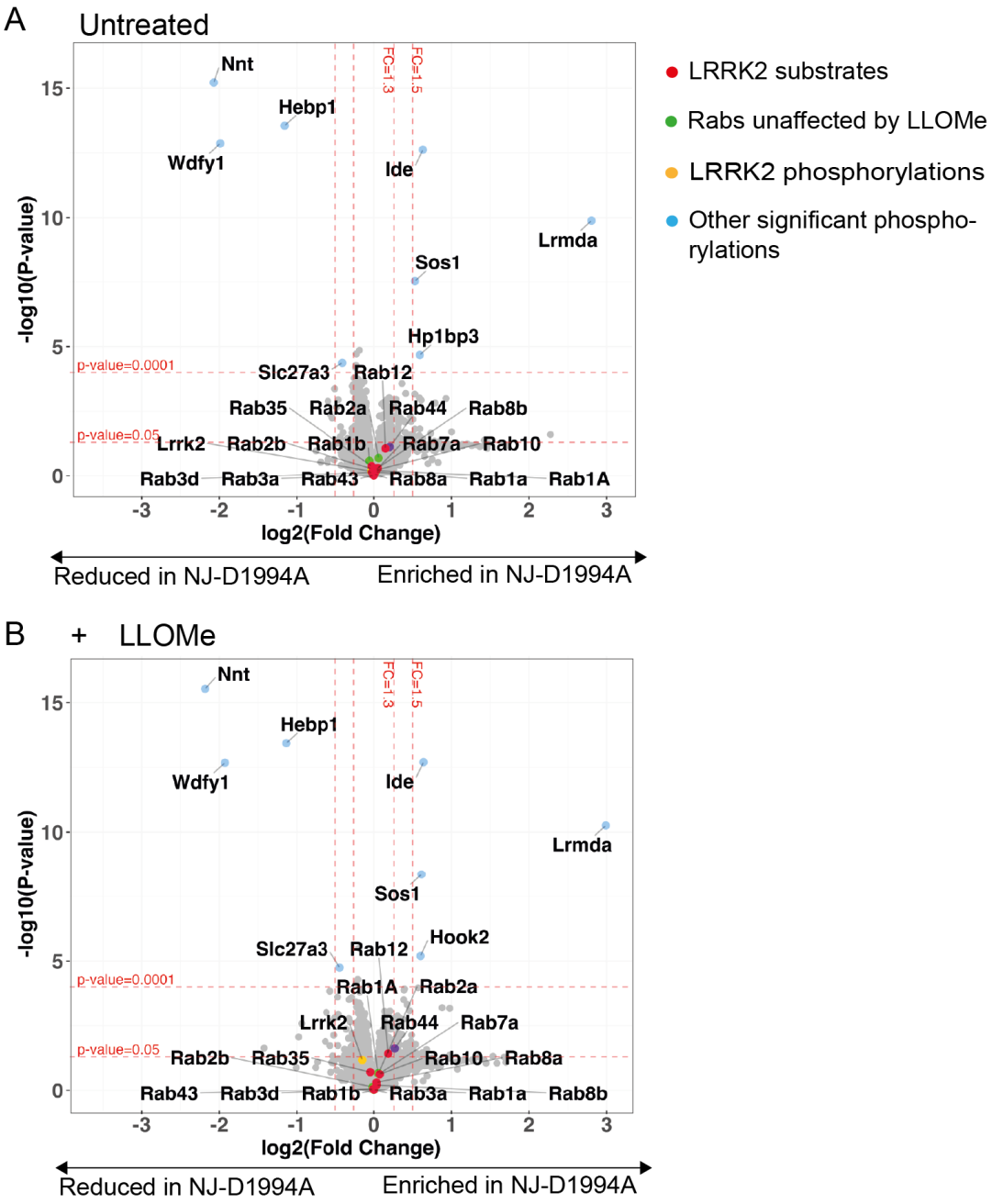

Figure 4.2.8. Proteomic analysis in NJ-WT and NJ-D1994A macrophages in untreated and LLOMe-treated conditions

Macrophages were treated with vehicle control or LLOMe 1 mM for 30 min and cells were analysed by mass spectrometry. Volcano plots in the untreated (A) and LLOMe-treated (B) conditions of the difference in total protein levels between NJ-WT and NJ-D1994A macrophages. Each point represents one protein. The x-axis shows the log_2-transformed fold-change and the y-axis shows the significance by $-log_{10}$-transformed P-value, obtained by linear models for microarray data. A fold-change greater than 1.2 and p value<0.05 was deemed significant

4.2.7 Summary of LRRK2 kinase substrates in macrophages after lysosomal damage

After accounting for the above analysis, a set of criteria were defined to identify the substrates of LRRK2 kinase after lysosomal membrane damage (Figure 4.2.9).

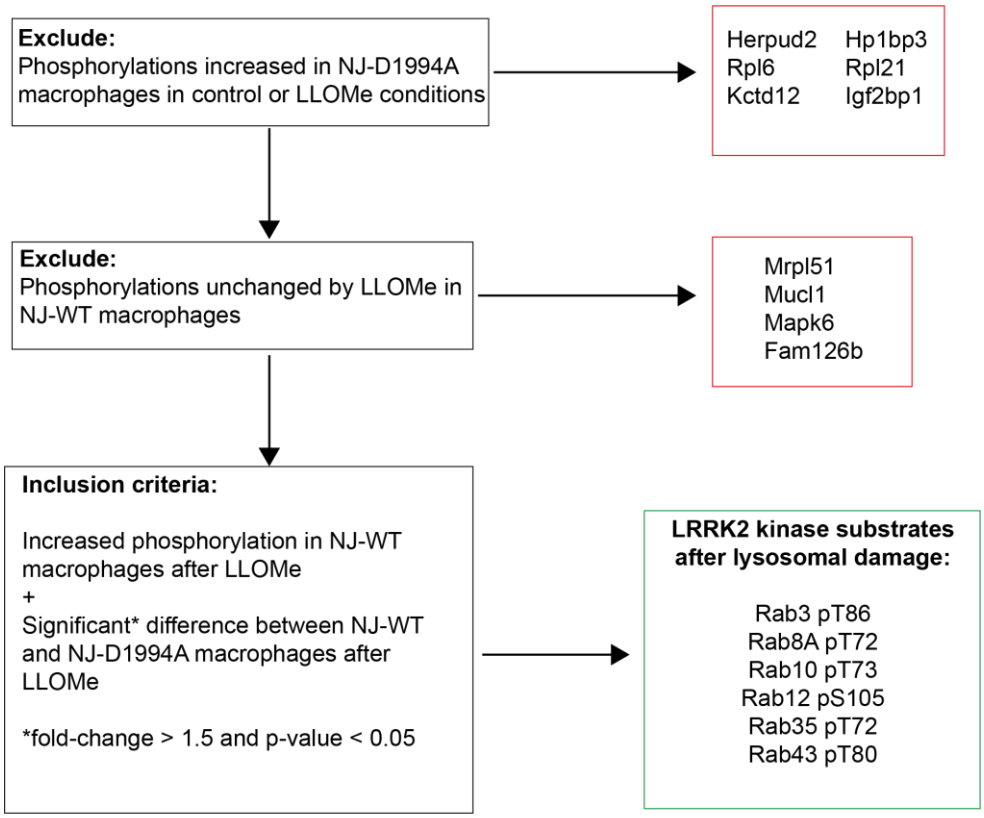

Figure 4.2.9. Selection criteria used to identify LRRK2 kinase substrates after lysosomal damage in macrophages

Rab8A pT72 was included in the list of LRRK2 kinase substrates after lysosomal damage but showed a significant dephosphorylation after LLOMe in NJ-D1994A macrophages and no significant phosphorylation after LLOMe in NJ-WT macrophages (Figure 4.2.10). In contrast, Rab3 pT86, Rab10 pT73, Rab12 pS105, Rab35 pT72 and Rab43 pT80 all showed in significant increase in phosphorylation after LLOMe in NJ-WT macrophages (Figure 4.2.10).

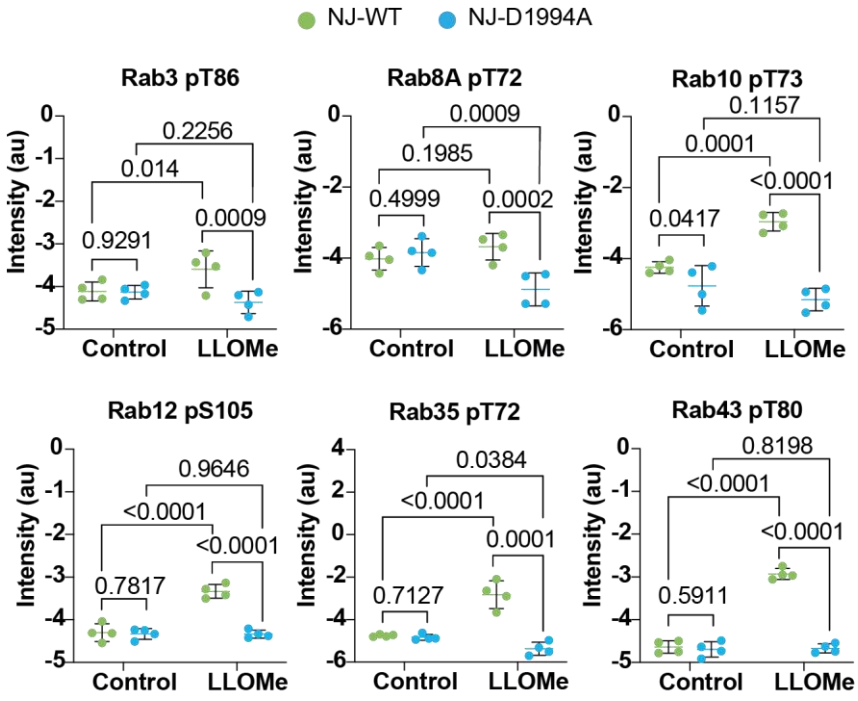

Figure 4.2.10. Rab8 is dephosphorylated after lysosomal damage in NJ-D1994A macrophages

Scatterplots showing the raw intensity data obtained by mass spectrometry and unadjusted p-values for the significantly altered Rabs. Each point represents the normalised and log2 transformed TMT-corrected reporter intensity value obtained by mass spectrometry (n=4 biological replicates). P-values by linear models for microarray data.

4.3 A phosphoproteomics approach to identify LRRK2-G2019S kinase-dependent phosphorylations in macrophages after lysosomal membrane damage

Next, I sought to explore the substrates of the gain-of-function LRRK2-G2019S after lysosomal membrane damage. Given that this mutation is associated with an increase in kinase activity, I hypothesised that LRRK2-G2019S increased phosphorylation of Rab GTPases in both vehicle control and LLOMe conditions. To test this, I employed a phosphoproteomics approach like that described in chapter 4.2, this time using Tac-WT and Tac-G2019S BMDM. A total of 32,803 phosphorylation sites were identified consistently across 4 biological replicates (Figure 4.3.1).

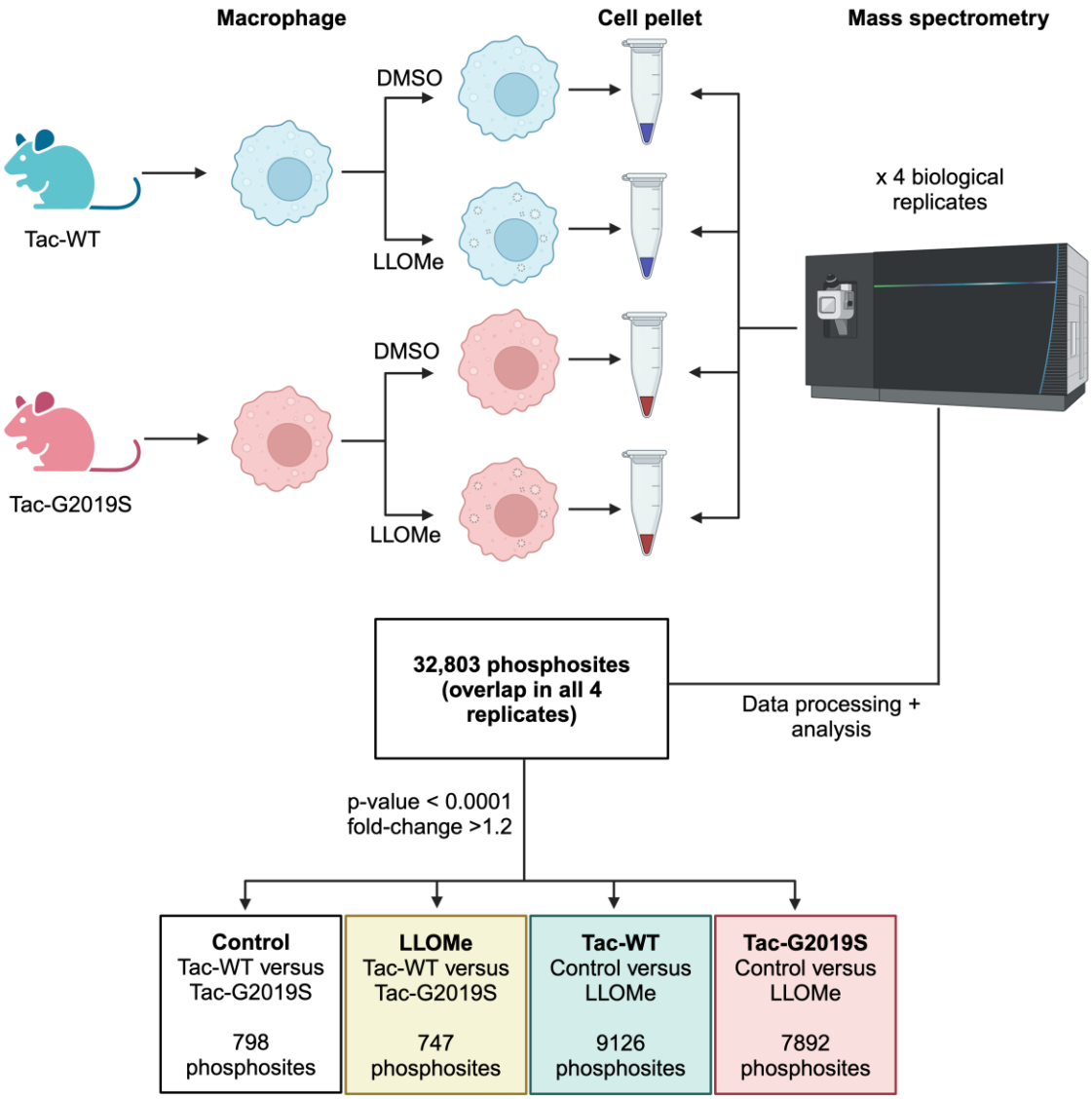

Figure 4.3.1. G2019S phosphoproteomics experimental design and workflow

BMDM were differentiated from Tac-WT and Tac-G2019S mice. Following treatment with LLOMe or vehicle control, cells were collected and processed for LC-MS/MS. From four biological replicates, a total of 32,803 phosphosites were identified in all 4 experiments. Data was processed using MaxQuant (Uniprot mouse reference genome) and then analysed using R software. The TNT lot-corrected reporter intensities were normalised (CONSTANd), log-transformed and analysed using limma. The number of significantly altered phosphosites (p-value < 0.0001 and fold-change > 1.2) within each of the four indicated comparison groups are shown.

4.3.1 Tac-G2019S BMDM show no changes in Rab phosphorylation in control conditions

In control conditions, none of the Rab GTPases identified as LRRK2 kinase substrates in chapter 4.2.7 showed altered phosphorylations between Tac-WT and Tac-G2019S macrophages (Figure 4.3.2). Rab3 pT86 was not identified in this experiment.

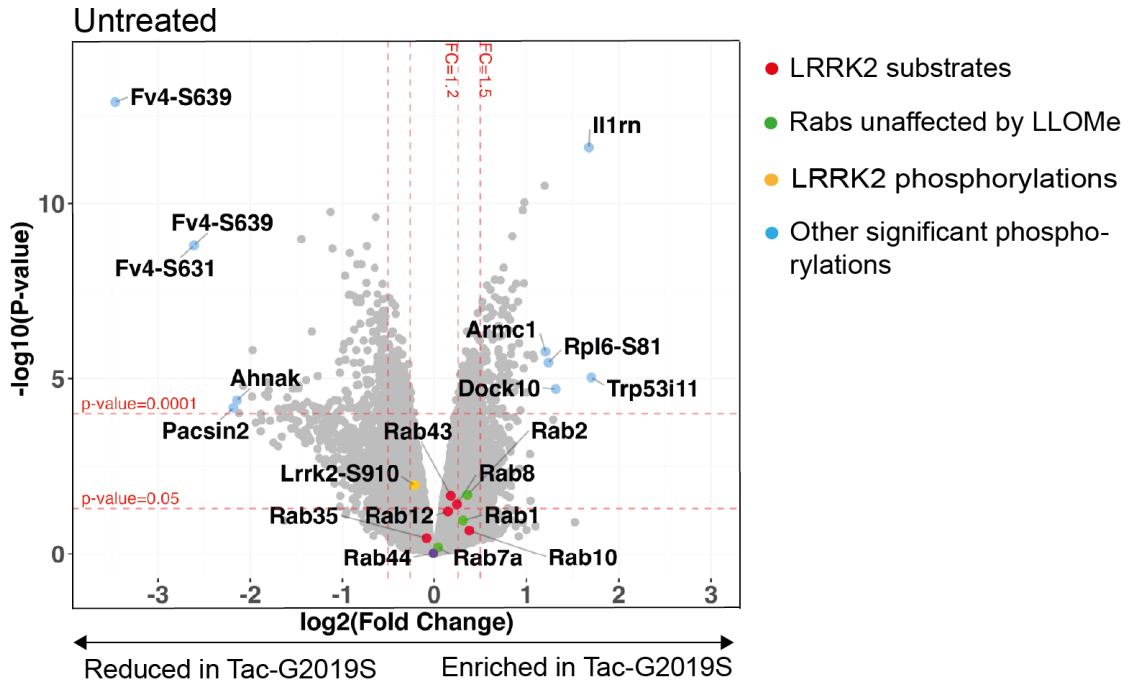

Figure 4.3.2 Phosphorylations altered in control conditions in Tac-G2019S macrophages

Vehicle control-treated Tac-WT and Tac-G2019S BMDM were analysed by mass spectrometry. Volcano plot shows the difference in phosphorylation levels between Tac-WT and Tac-G2019S BMDM. Each point represents one phosphorylation site of a protein. The x-axis shows the $\log_{10}$-transformed fold change, and the y-axis shows the significance by $-\log_{10}$-transformed P-value, obtained by linear models for microarray data. A fold-change greater than 1.2 and p value <0.05 was deemed significant.

Given that there were 798 significantly different phosphosites in control conditions between Tac-WT and Tac-G2019S, only those showing the greatest fold-change were further explored. Phosphorylations of the proteins Il1rn, Trp53i11, Rpl6, Armc1 and Dock10 were most increased, while Fv4, Ahnak and Pacsin2 were most

decreased in Tac-G2019S BMDM (Figure 4.3.2), however there were no commonalities amongst the peptide sequences (Table 4.3.1).

Protein	Position (probability)	Peptide	Number of sites
Increased in Tac-G2019S macrophages			
Interleukin-1 receptor antagonist protein (Il1rn)	S82 (1)	**S**GDDIK	1
Tumour protein p53-inducible protein 11 (Trp53i11)	S14 (1)	KH**S**QT	1
60S ribosomal protein L6 (Rpl6)	S81 (1)	RKY**S**AAK	1
Armadillo repeat containing protein-1 (Arm1)	S189 (1)	IR**S**DLK	1
Dedicator of cytokinesis protein 10	S12 (1)	**S**LLRPGQAAELR	1
Decreased in Tac-G2019S macrophages (fold-change < -1.2 and p< 0.05)			
Retrovirus-related Env polyprotein from Fv-4 locus (Fv4)	S631 S639	**S**IDPEEVE**S**RE	1 2
AHNAK nucleoprotein (Ahnak)	S5652 (0.69)	VGIQLPEVELSV**S**TKKE	1

Table 4.3.1. Selected phosphorylations increased and decreased in Tac-G2019S macrophages in control conditions.

4.3.2 Tac-G2019S BMDM show increased phosphorylation of Rab12 and reduced phosphorylation of Rab35 after lysosomal membrane damage

After LLOMe-induced lysosomal membrane damage a total of 747 phosphosites were significantly altered between Tac-WT and Tac-G2019S macrophages (Figure 4.3.3).

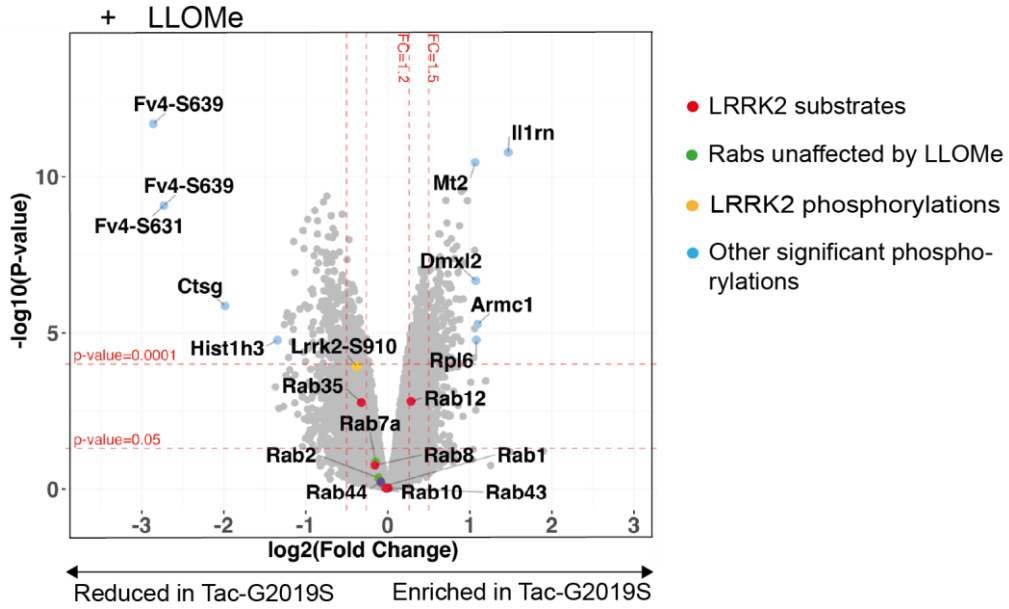

Figure 4.3.3 Phosphorylations altered by LLOMe treatment in Tac-G2019S macrophages

LLOMe-treated Tac-WT and Tac-G2019S BMDM were analysed by mass spectrometry. Volcano plot shows the difference in phosphorylation levels between Tac-WT and Tac-G2019S BMDM. Each point represents one phosphorylation site of a protein. The x-axis shows the $\log_{10}$-transformed fold change, and the y-axis shows the significance by -$\log_{10}$-transformed P-value, obtained by linear models for microarray data. A fold-change greater than 1.2 and p value <0.05 was deemed significant.

Rab10 pT73, Rab12 pS105, Rab 35 pT72 and Rab43 pT80 were phosphorylated in Tac-WT and Tac-G2019S macrophages after lysosomal membrane damage (Figure 4.3.4). Rab8A pT72 was phosphorylated in Tac-WT macrophages (p = 0.0171) but was not phosphorylated in Tac-G2019S macrophages with LLOMe treatment (p = 0.3201) (Figure 4.3.4).

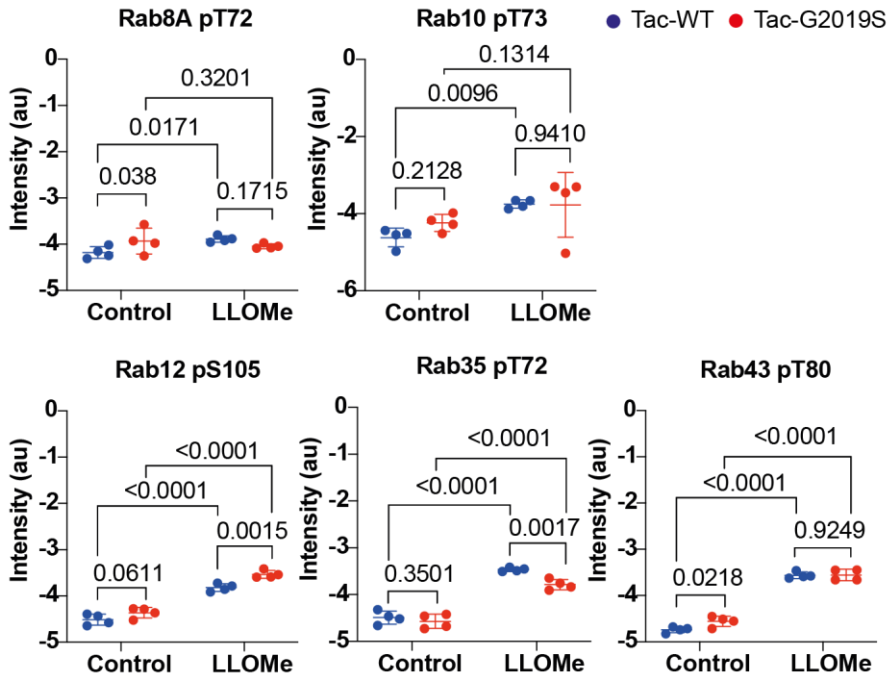

Figure 4.3.4. Phosphorylation of Rab GTPases after lysosomal damage in Tac-WT and Tac-G2019S macrophages

Scatterplots showing the raw intensity data obtained by mass spectrometry and p-values for the Rabs identified as substrates of LRRK2 kinase. Each point represents the normalised and log2 transformed TMT-corrected reporter intensity value obtained by mass spectrometry (n=4 biological replicates). P values by linear models for microarray data.

Unexpectedly, the amount of phosphorylated protein detected after lysosomal damage was similar between Tac-WT and Tac-G2019S for most of these Rab substrates (Figure 4.3.3 and Figure 4.3.4). Only Rab12 pS105 phosphorylation was increased in Tac-G2019S macrophages (fold change > 1.2, p-value < 0.05) (Figure 4.3.3). In contrast, Rab8A pT72, Rab10 pT73 and Rab43 pT80 showed no significant phosphorylation differences between Tac-WT and Tac-G2019S macrophages (Figure 4.3.3). Rab35 pT72 was decreased in Tac-G2019S macrophages (fold change < -1.2, p-value (< 0.05) (Figure 4.3.3).

The Rab phosphorylation sites in Tac-G2019S and Tac-WT macrophages were identical to those found in chapter 4.2.3 (Table 4.3.2).

Protein	Position (probability)	Peptide	Number of sites

Increased in Tac-G2019S macrophages (fold-change > 1.2 and p< 0.05)			
Rab12	S105 (1)	FN**S**ITSAYYR	1
Unchanged between Tac-WT and Tac-G2019S macrophages			
Rab8	T72 (1)	FR**T**ITTAYYR	1
Rab10	T73 (1)	FH**T**ITTSYYR	1
Rab43	T80 (1)	FR**T**ITQSYYR	1
Decreased in Tac-G2019S macrophages (fold-change < -1.2 and p< 0.05)			
Rab35	T72 (1)	FR**T**ITSTYYR	1

Table 4.3.2 Sites of Rab phosphorylation in Tac-WT and Tac-G2019S macrophages after LLOMe treatment

Phosphorylations of Il1rn, Mt2, Dmxl2, Armc1 and Rpl6 were increased, while Fv4, Ctsg, Hist1h3 phosphorylations were decreased in Tac-G2019S compared to Tac-WT macrophages after lysosomal damage (Figure 4.3.3). These phosphorylations were all located on serine amino acid residues but did not show a common peptide sequence (Table 4.3.3). Intriguingly, Cathepsin G and Hist1h3 phosphorylations significantly increased in Tac-WT macrophages treated with LLOMe but did not increase in Tac-G2019S macrophages (Figure 4.3.5). Cathepsin G enzyme is localized inside the lysosome and is not expected to be phosphorylated; its phosphorylation may indicate a cytoplasmic localization due to lysosomal damage. Phosphorylations of Il1rn and Dmxl2 increased with LLOMe treatment in Tac-WT and Tac-G2019S macrophages and were significantly higher in Tac-G2019S macrophages in both conditions (Figure 4.3.5). Phosphorylations in Mt2, Armc1, Rpl6 and Fv4 were unaffected by LLOMe treatment (Figure 4.3.5).

Protein	**Position (probability)**	**Peptide**	**Number of sites**
Increased in Tac-G2019S macrophages			
Interleukin-1 receptor antagonist protein (Il1rn)	S82 (1)	**S**GDDIK	1
Metallothionein-2 (Mt2)	S58 (1)	EASDKC**S**CCA	1
DmX-like protein 2 (Dmxl2)	S933 (0.706)	AAEGISSD**S**LLSVPGQK	1
Armadillo repeat-containing protein 1 (Armc1)	S189 (1)	IR**S**DLK	1

60S ribosomal protein L6 (Rpl6)	S65(1) S81(1)	GIGRY**S**R RKY**S**AAK	2
Decreased in Tac-G2019S macrophages			
Retrovirus-related Env polyprotein from Fv-4 locus (Fv4)	S631 (1) S639 (1)	**S**IDPEEVESRE SIDPEEVE**S**RE	1 2
Cathepsin G (Ctsg)	S121 (1)	**S**GSVKPVALPQASK	1
Histone H3 (Hist1h3)	S74	**S**APATGGVK	1

Table 4.3.3 Sites of phosphorylation on selected proteins in Tac-WT and Tac-G2019S macrophages after LLOMe treatment

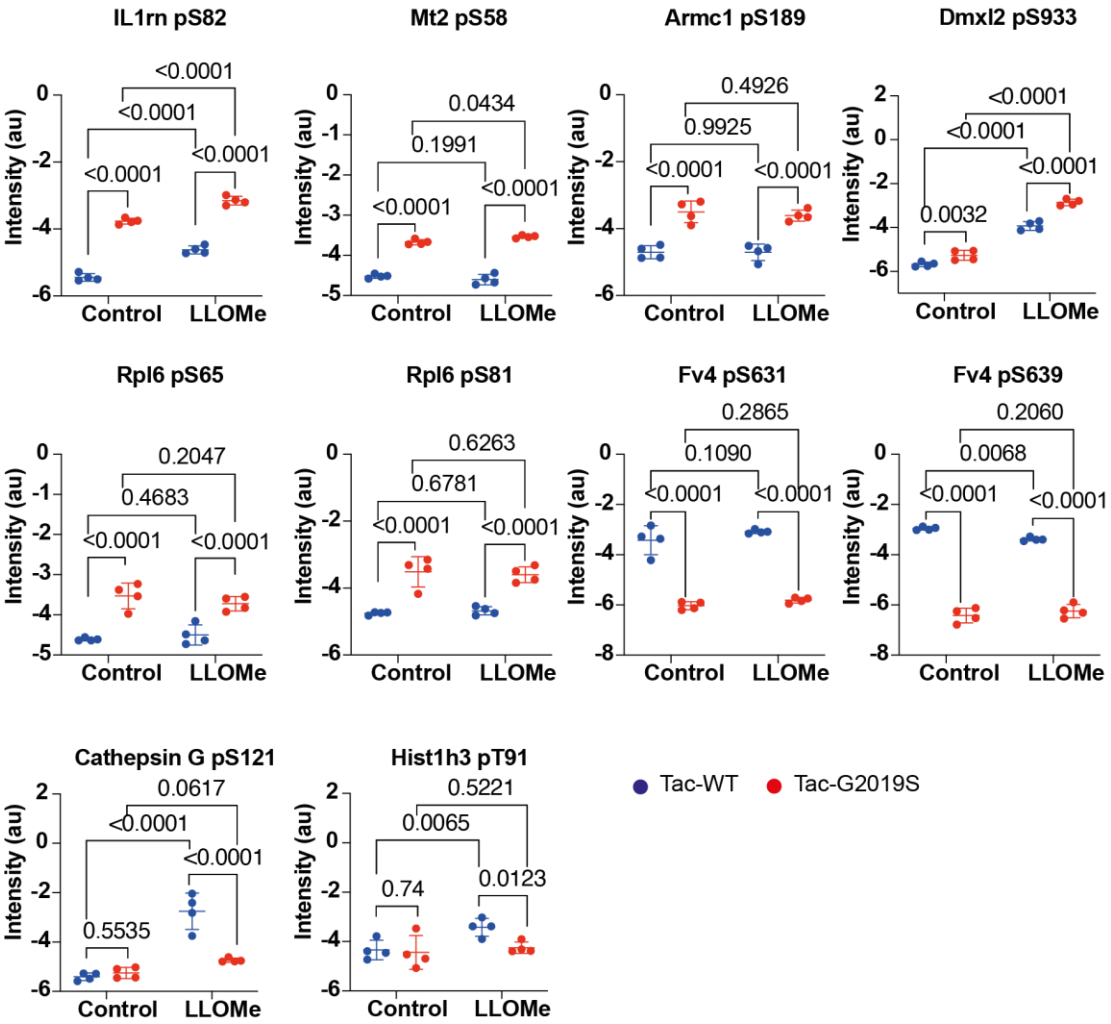

Figure 4.3.5. Significant phosphorylation changes in selected proteins in control and LLOMe conditions

Scatterplots showing the raw intensity data obtained by mass spectrometry and unadjusted p-values for other selected proteins showing greatest fold-change. Each point represents the normalised and log2 transformed TMT-corrected reporter

intensity value obtained by mass spectrometry (n=4 biological replicates). P values by linear models for microarray data.

4.3.3 Sites of LRRK2 phosphorylation in Tac-WT and Tac-G2019S macrophages

In this experiment, only LRRK2 pS910 and pS935 phosphorylations were identified (Table 4.3.4). These sites mediate interactions between LRRK2 and 14-3-3 proteins, with decreased phosphorylation associated with decreased binding to 14-3-3 proteins (Li et al., 2011; Rudenko and Cookson, 2010). LRRK2 pS935 showed no phosphorylation changes between Tac-WT and Tac-G2019S macrophages and was unaffected by LLOMe treatment (Figure 4.3.6). LRRK2 pS910 showed a significant dephosphorylation after LLOMe treatment in both Tac-WT and Tac-G2019S macrophages, with reduced levels in Tac-G2019S macrophages (Figure 4.3.6).

Protein	Position (probability)	Peptide	Number of sites
LRRK2	S910 (0.803)	SN**S**ISVGEVYRDLALQR	1
LRRK2	S935 (1)	HSN**S**LGPVFDHEDLLR	1

Table 4.3.4

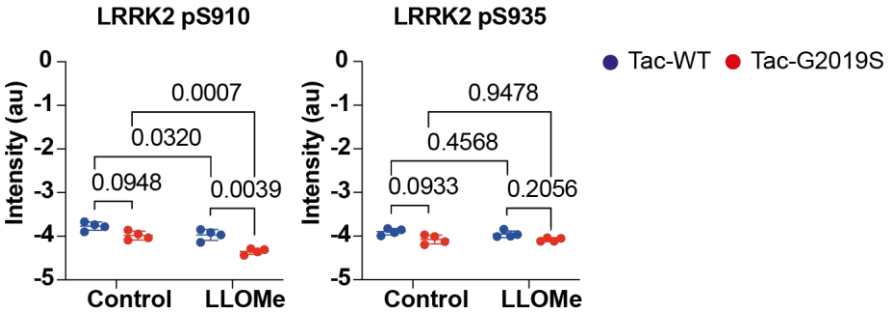

Figure 4.3.6. LRRK2 phosphorylation sites in Tac-WT and Tac-G2019S macrophages in control and LLOMe conditions

Scatterplots showing the raw intensity data obtained by mass spectrometry and p-values for detected sites of phosphorylation on LRRK2. Each point represents the normalised and log2 transformed TMT-corrected reporter intensity value obtained by mass spectrometry (n=4 biological replicates). P values by linear models for microarray data.

4.3.4 Proteome changes in Tac-WT and Tac-G2019S macrophages after lysosomal membrane damage

Finally, the total proteome was compared between Tac-WT and Tac-G2019S macrophages in the control and LLOMe-treatment conditions (Figure 4.3.7). This revealed that levels of Mt2 were in higher in Tac-G2019S macrophages in control and LLOMe treatment conditions (Figure 4.3.7). As such, the increased levels of Mt2 pS58 phosphorylation in Tac-G2019S BMDM (Figure 4.3.3 and Figure 4.3.5) are likely secondary to these proteome changes. For the LRRK2 kinase Rab substrates and the other significant phosphorylations discussed in this chapter, there were no proteome differences. Total Rab44 levels were decreased after LLOMe in the Tac-G2019S macrophages (Figure 4.3.7).

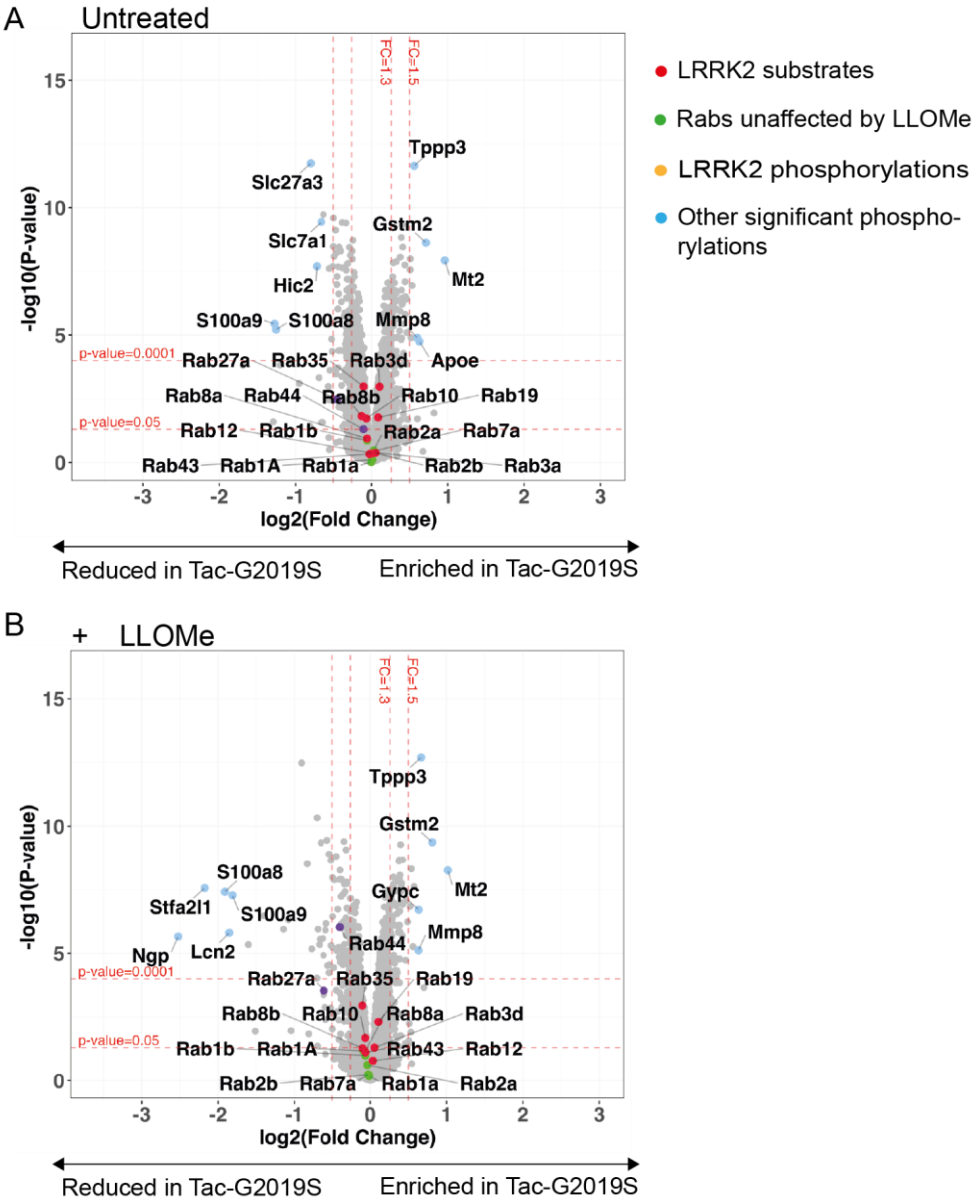

Figure 4.3.7 Proteomic analysis in Tac-WT and Tac-G2019S macrophages in untreated and LLOMe-treated conditions

Macrophages were treated with LLOMe 1 mM for 30 min and cells were analysed by mass spectrometry. Volcano plots in the untreated (A) and LLOMe-treated (B) conditions of the difference in total protein levels between Tac-WT and Tac-G2019S macrophages. Each point represents one protein. The x-axis shows the log_2-transformed fold change, and the y-axis shows the significance by $-log_{10}$-transformed P-value, obtained by linear models for microarray data. A fold-change greater than 1.2 and p value<0.05 was deemed significant

4.4 Validation of Rab phosphorylation changes after lysosomal damage in Tac-G2019S BMDM

I next sought to validate my phosphoproteomics data by Western blot, using LRRK2 kinase inhibitors to confirm that these effects are LRRK2 kinase activity-dependent in Tac-WT and Tac-G2019S BMDM. For this, BMDM were treated with the LRRK2 type 1 kinase inhibitor MLi-2 and the LRRK2 type 2 kinase inhibitor GZD-824. In keeping with the phosphoproteomics data, pan-phospho Rab and Rab10 pT73 showed no differences between Tac-WT and Tac-G2019S BMDM in control or LLOMe-treatment conditions, and these phosphorylations were LRRK2 kinase dependent because they were inhibited by MLi-2 and GZD-824 (Figure 4.4.1). Further, Rab12 pS106 was increased in Tac-G2019S BMDM after LLOMe (Figure 4.4.1). Rab12 phosphorylation was also LRRK2 kinase dependent because it was inhibited by MLi-2 and GZD-824. There were no differences in levels of total Rab8A, Rab10 or Rab12 between Tac-WT and Tac-G2019S BMDM (Figure 4.4.1).

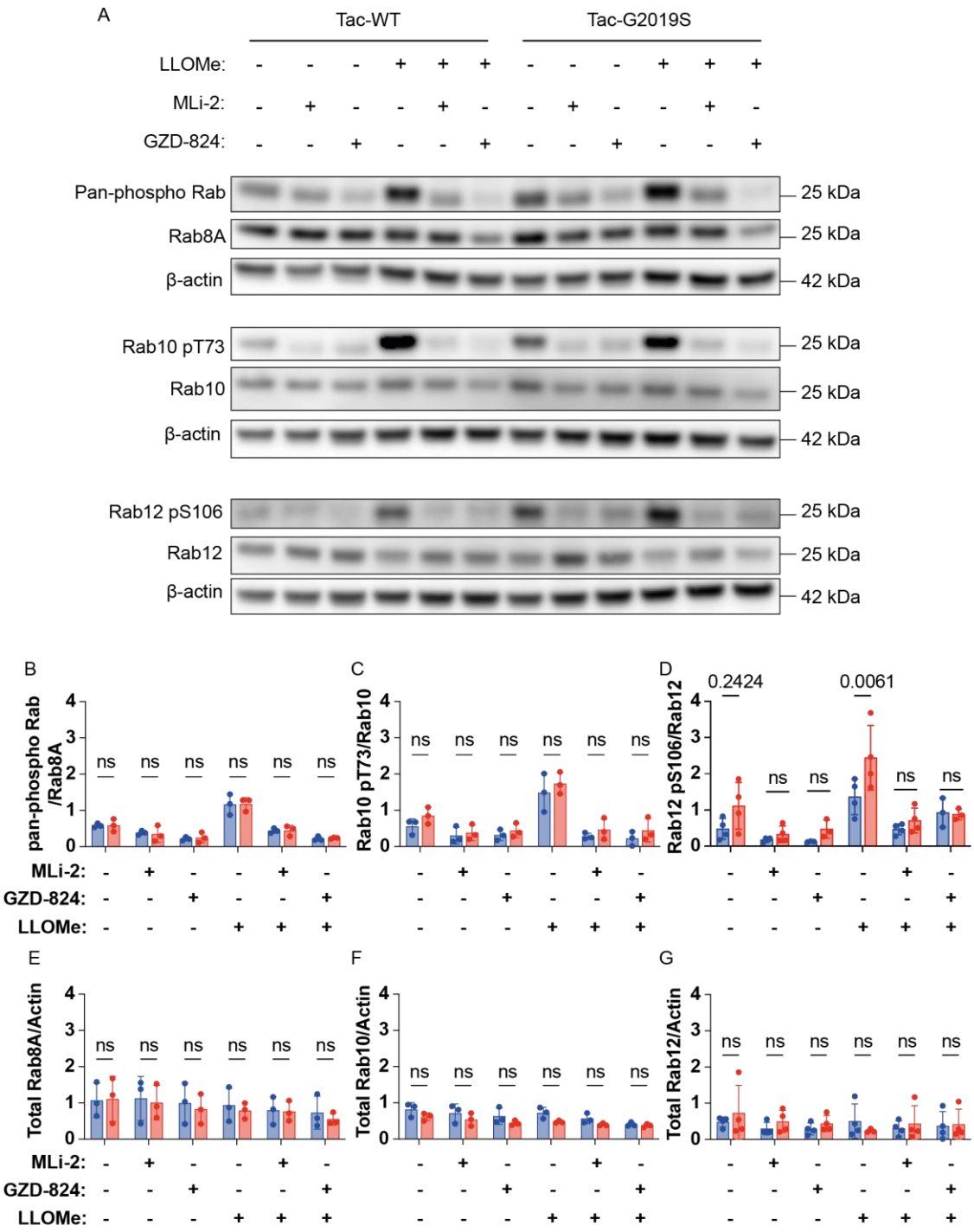

Figure 4.4.1. Tac-G2019S BMDM show increased LRRK2 kinase dependent phosphorylation of Rab12 pS106

(A) Western blot analysis of pan-phospho Rab, Rab8A, Rab10 pT73, Rab10, Rab12 pS106, Rab12 and β-actin in Tac-WT and Tac-G2019S BMDM in untreated, MLi-2, GZD-824, LLOMe, LLOMe + MLi-2 and LLOMe + GZD-824 conditions. (B to D) pan-phospho Rab, Rab10 pT73 and Rab12 pS106 band intensities were quantified by densitometry and normalised to Rab8A, Rab10 and Rab12, respectively. (E to G) Rab8A, Rab10 and Rab12 band intensities were quantified by densitometry and

normalised to β-actin. Data are mean ± SD from (A-B, E-F) 3 independent experiments (C and G) 4 independent experiments. Two-way ANOVA followed by Tukey's multiple comparisons test.

4.5 Validation of Rab phosphorylation changes after lysosomal damage in human LRRK2-G2019S iPSDM

The phosphoproteomics experiments required large numbers of cells and this meant that it was not feasible to perform in LRRK2-G2019S and isogenic control iPSDM. However, Western blot analysis confirmed phosphorylation of pan-phospho Rabs, Rab10 pT73 and Rab12 pS106 in these cells (Figure 4.5.1). While there were no significant differences between G2019S and isogenic control iPSDM, there was a small trend for increased Rab12 pS106 phosphorylation in G2019S iPSDM ($p = 0.0994$) (Figure 4.5.1). There were no significant changes in total levels of Rab8A, Rab10 and Rab12 between G2019S and isogenic control iPSDM (Figure 4.5.1).

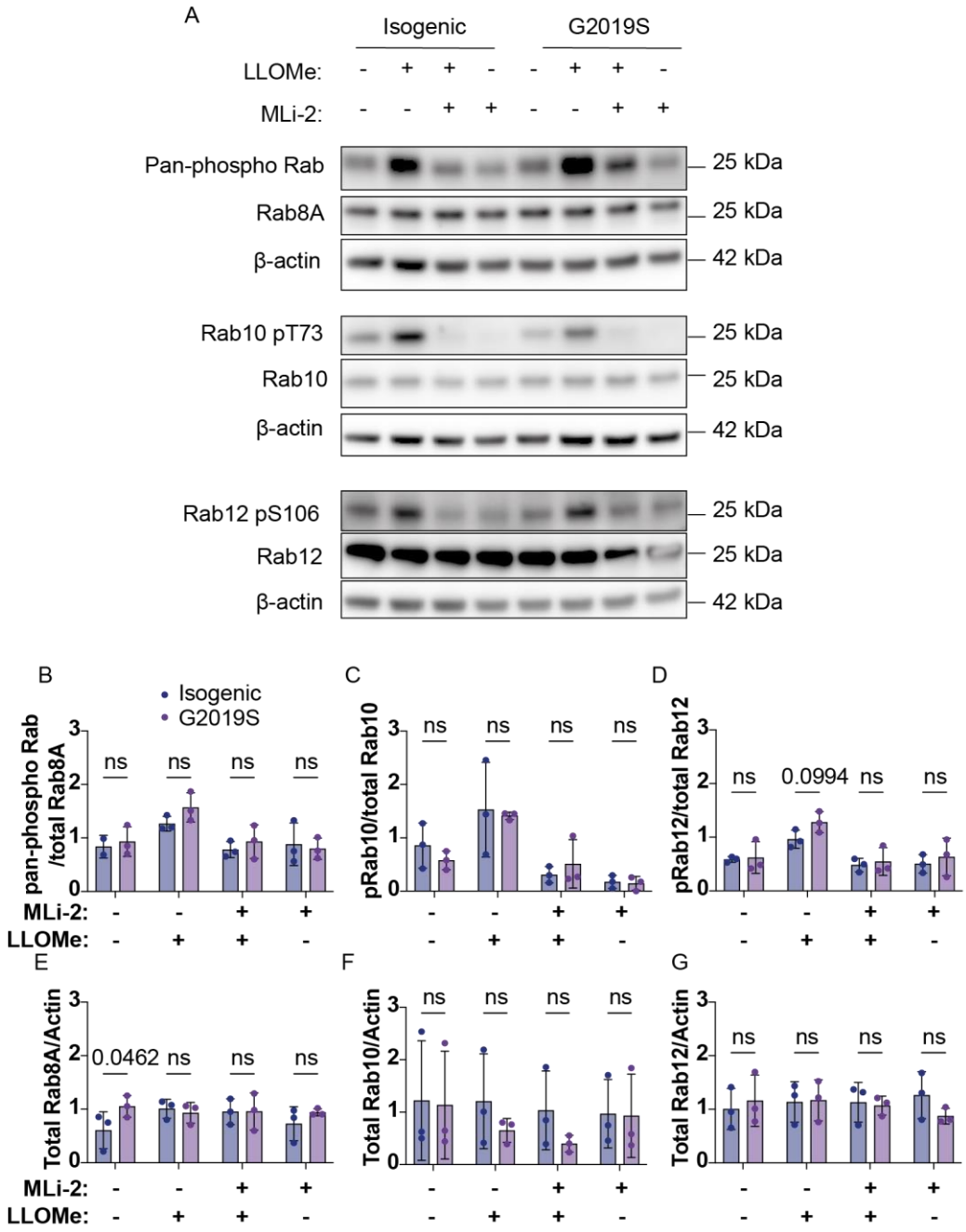

Figure 4.5.1. Patient-derived iPSDM show LRRK2 kinase dependent phosphorylation of a subset of Rab GTPases after lysosomal damage

(A) Western blot analysis of pan-phospho Rab, Rab8A, Rab10 pT73, Rab10, Rab12 pS106, Rab12 and β-actin in isogenic control and G2019S iPSDM in untreated, LLOMe, LLOMe + MLi-2 and MLi-2 conditions. (B to D) pan-phospho Rab, Rab10 pT73 and Rab12 pS106 band intensities were quantified by densitometry and normalised to Rab8A, Rab10 and Rab12, respectively. (E to G) Rab8A, Rab10 and Rab12 band intensities were quantified by densitometry and normalised to β-actin. Data are mean ± SD from 3 independent experiments. Two-way ANOVA followed by Tukey's multiple comparisons test.

To summarise, in this chapter I used an unbiased phosphoproteomics approach to define the substrates of LRRK2 kinase in macrophages that are phosphorylated after lysosomal membrane damage. Despite identification of over 29,000 phosphosites, only a subset of Rab GTPases met criteria as LRRK2 kinase activity-dependent substrates: Rab3 pT86, Rab8A pT72, Rab10 pT73, Rab12 pS105, Rab35 pT72 and Rab43 pT80. Surprisingly, although LRRK2-G2019S is associated with increased kinase activity, LRRK2-G2019S macrophages showed a similar phosphorylation profile to wild-type macrophages after lysosomal membrane damage, except for Rab12 and Rab35, showing increased and decreased phosphorylation in Tac-G2019S BMDM, respectively.

Chapter 5. Results 3 Exploring the response to lysosomal damage in LRRK2-mutant macrophages

5.1 Introduction

Having characterised the substrates of LRRK2 kinase in wild-type and LRRK2-G2019S macrophages following lysosomal membrane damage in the previous chapter, I next sought to explore the role that LRRK2 mutations have in lysosomal membrane damage and repair. Based on previous work (Herbst et al., 2020)I hypothesised that LRRK2-G2019S would result in increased recruitment of Gal3 and CHMP4B to damaged lysosomes alongside reduced LC3B-association. To study the effects of LRRK2-G2019S on this pathway, we utilised Tac-G2019S and Tac-WT macrophages and stained cells for endogenous protein by immunofluorescence followed by high-content microscopy.

5.2 Gal3, CHMP4B and LC3B recruitment is LRRK2 kinase-independent in Tac-WT and Tac-G2019S BMDM

5.2.1 Quantification of lysosomal damage in BMDM

I have previously shown that BMDM contain a highly dense and compact LAMP-1+ compartment (see chapter 3.2, Figure 3.2.4). I initially carried out co-staining of lysosomal damage and repair markers with a lysosomal marker such as LAMP-2 (Figure 5.2.1). Given that it was not possible to mask individual lysosomes, and that LAMP-2 staining was positive throughout most of the cytosol (Figure 5.2.1), I decided not to perform colocalisation of membrane damage/repair markers with a lysosomal marker.

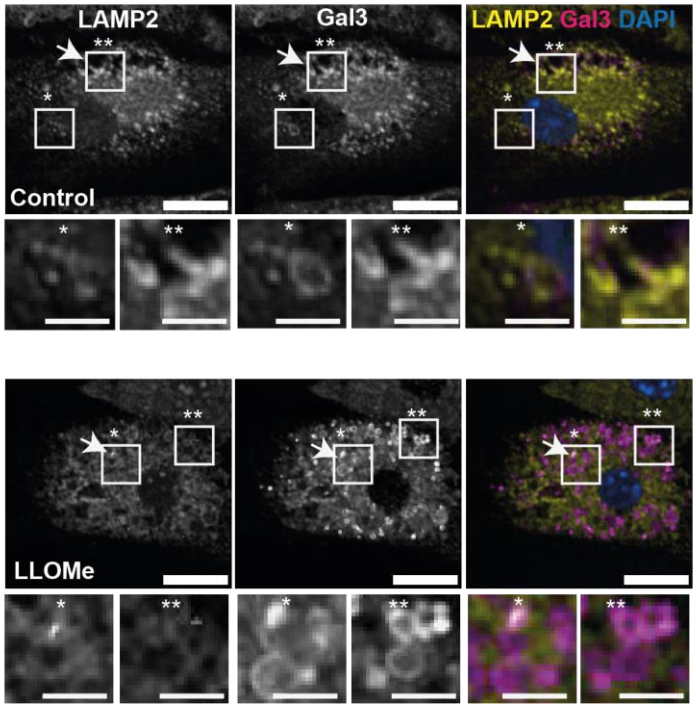

Figure 5.2.1. LAMP-2 staining is diffusely positive throughout the cytosol of BMDM.

Tac-WT BMDM were co-stained for LAMP-2/Galectin-3 (Gal3) in control and LLOMe-treatment conditions. Scale bars = 20 μm on larger images and 5 μm on insets. Arrows indicate sites of colocalisation.

5.2.2 Galectin-3 increases with LLOMe to similar levels in Tac-WT and Tac-G2019S macrophages

Gal3 is widely used as a sensitive marker of lysosomal membrane damage (Aits et al., 2015). It is reported to be diffusely present in the cytosol in the basal state and forms discrete puncta at areas of lysosomal damage due to its affinity for β-galactoside sugars within the lysosomal membrane (Paz et al., 2010). In a proportion of Tac-WT and Tac-G2019S BMDM, there were many Gal3 puncta in control conditions – around 10% of cell area was positive for Gal3 (Figure 5.2.2). Lysosomal damage induced by LLOMe resulted in a 10% increase in Gal3 positive cell area in both Tac-WT and Tac-G2019S BMDM (Figure 5.2.2). The number of Gal3 puncta reached >1000 in many cells after lysosomal damage. The type 1 LRRK2 kinase inhibitor MLi-2 did not reduce Gal3 puncta after lysosomal damage in Tac-WT or Tac-G2019S BMDM. Similarly, treatment with the type 2 LRRK2 kinase inhibitor GZD-824 did not alter Gal3 recruitment to damaged lysosomes. These results suggest that the overall number of damaged lysosomes is independent of LRRK2

kinase activity and does not differ in LRRK2-G2019S macrophages. However, this data should be interpreted with caution given the high number Gal3 positive vesicles in the basal state in these primary macrophages.

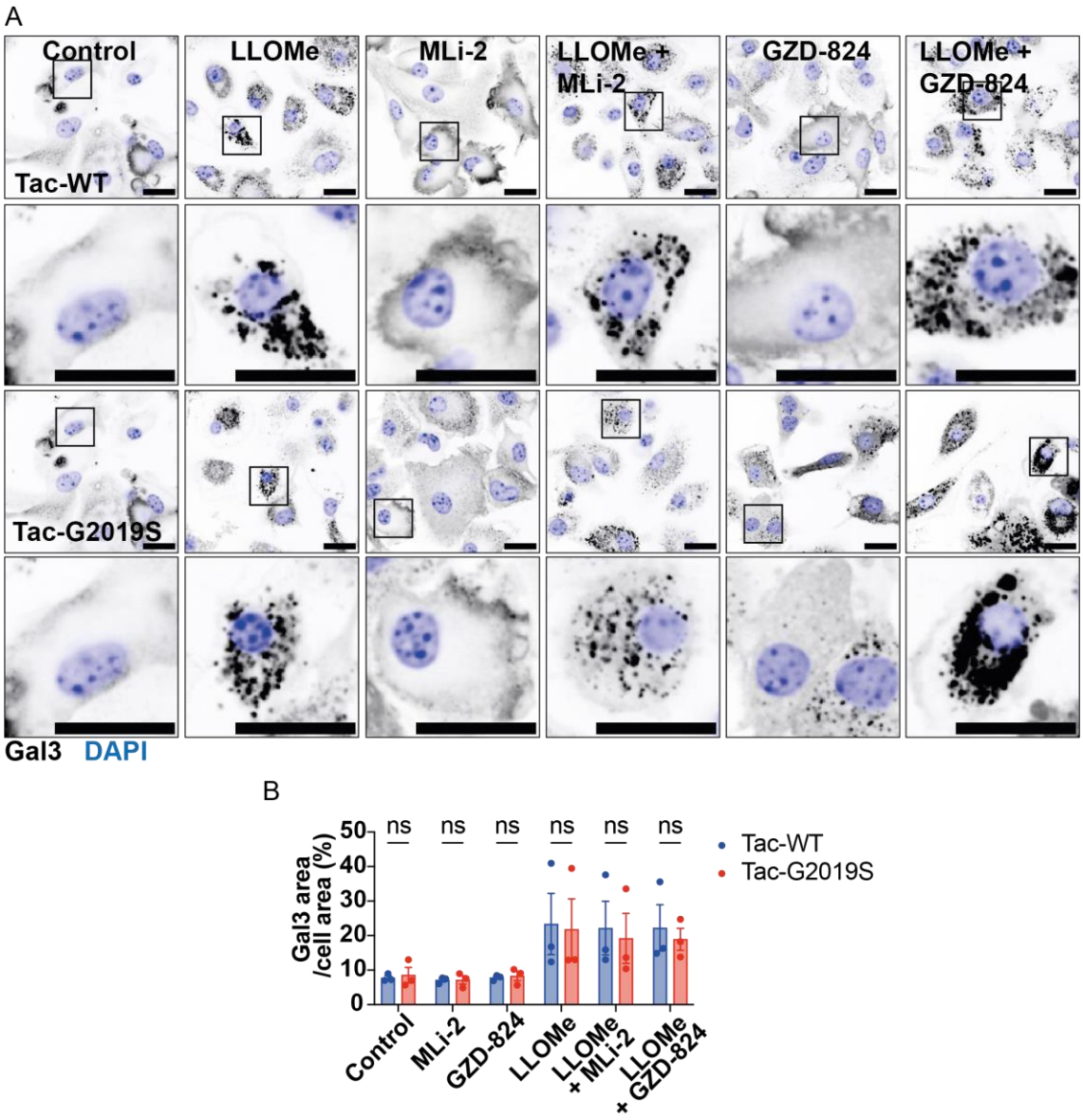

Figure 5.2.2. Gal3 puncta increase after lysosomal damage and are unaffected by LRRK2-G2019S, MLi-2 and GZD-824

BMDM were treated with LLOMe 1 mM +/- MLi-2 100 nM or GZD-824 (GZD) 0.1 μM and endogenous Galectin-3 (Gal3) positive cell area was visualised by immunofluorescence and quantified using Harmony software. Scale bars, 20 μm. Data representative of (B) 3 independent experiments. Results are shown as mean ± SEM. Two-way ANOVA followed by Šidák's multiple comparisons test.

5.2.3 CHMP4B is reduced in Tac-G2019S BMDM after lysosomal damage

Next, the recruitment of the ESCRT-III component CHMP4B was analysed to monitor lysosomal repair. In control conditions, CHMP4B signal was largely cytosolic in the majority of BMDM with low detection limit (Figure 5.2.3). Following lysosomal damage, CHMP4B puncta formation was significantly reduced in Tac-G2019S BMDM compared to Tac-WT BMDM (Figure 5.2.3). Unexpectedly, lysosomal damage in the presence of LRRK2 kinase inhibition did not significantly reduce CHMP4B recruitment in wild-type BMDM (Figure 5.2.3). Instead, MLi-2 treatment showed a trend to increase CHMP4B recruitment in Tac-G2019S BMDM (Figure 5.2.3). GZD-824 treatment increased CHMP4B recruitment to damaged lysosomes in Tac-WT BMDM and showed a trend to increase CHMP4B recruitment to damaged lysosomes in Tac-G2019S BMDM (Figure 5.2.3). As LRRK2 kinase inhibition did not reduce CHMP4B recruitment to damaged lysosomes in wild-type BMDM, it is unlikely that the differences between Tac-WT and Tac-G2019S BMDM demonstrated in these experiments are due to LRRK2 kinase activity. Nonetheless, these results suggest that there is an effect of LRRK2-G2019S, perhaps independent of kinase activity, in lysosomal repair.

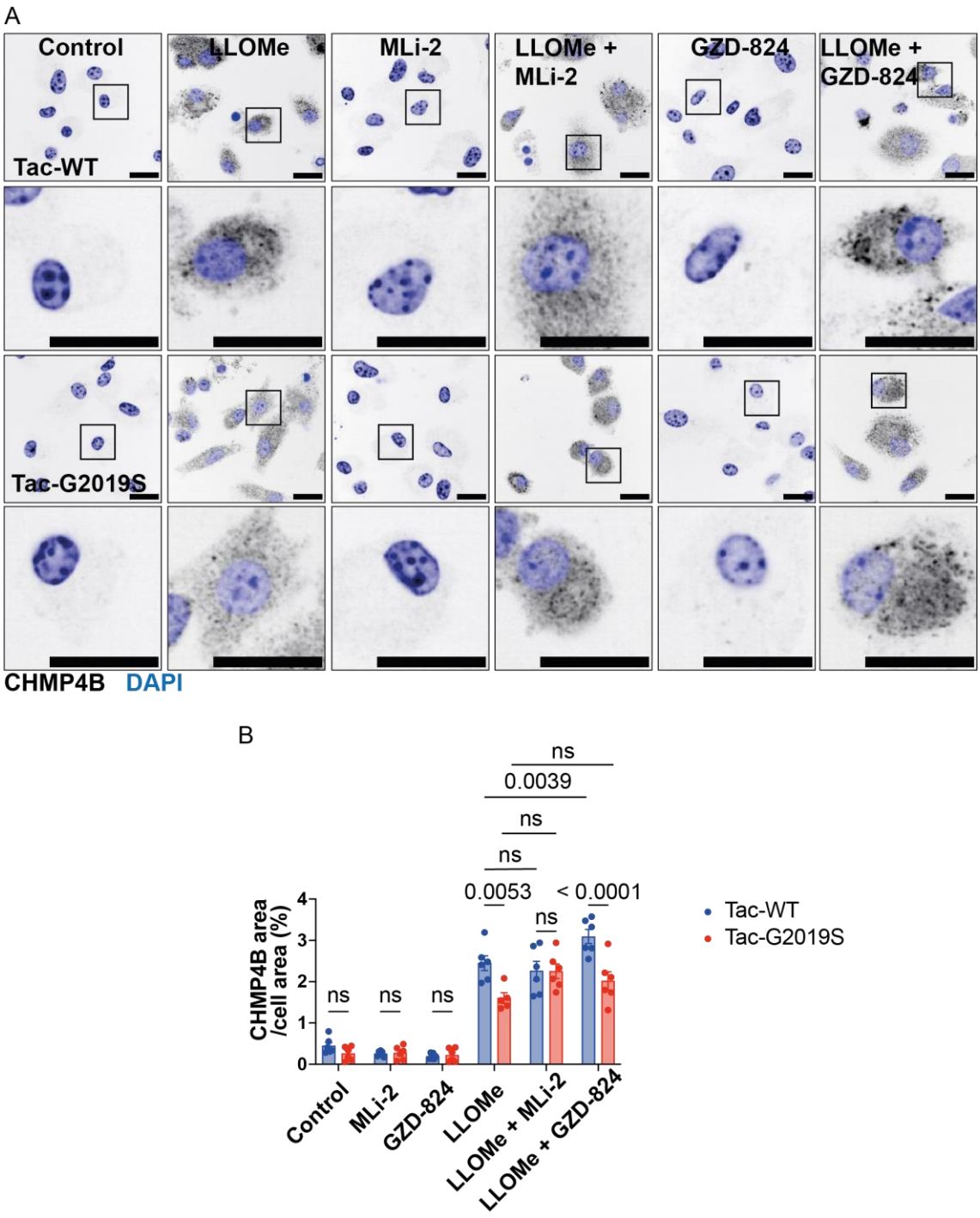

Figure 5.2.3. Tac-G2019S BMDM show reduced CHMP4B puncta formation after lysosomal damage

BMDM were treated with LLOMe 1 mM +/- MLi-2 100 nM or GZD-824 (GZD) 0.1 μM and endogenous CHMP4B positive cell area was visualised by immunofluorescence and quantified using Harmony software. Scale bars, 20 μm. Data representative of (B) 3 independent experiments (n=6 independent wells). Results are shown as mean ± SEM. Two-way ANOVA followed by Šidák's multiple comparisons test.

Previous reports have shown that Gal3 and CHMP4B highly colocalise in cell lines such as HeLa cells (Radulovic et al., 2018). In wild-type BMDM, Gal3/CHMP4B colocalisation significantly increased with LLOMe, however this was highly variable between cells with some cells showing high levels of colocalisation and others showing almost no colocalisation (Figure 5.2.4). These experiments indicated that on average only 15% of Gal3 puncta also show CHMP4B positive staining in BMDM (Figure 5.2.4).

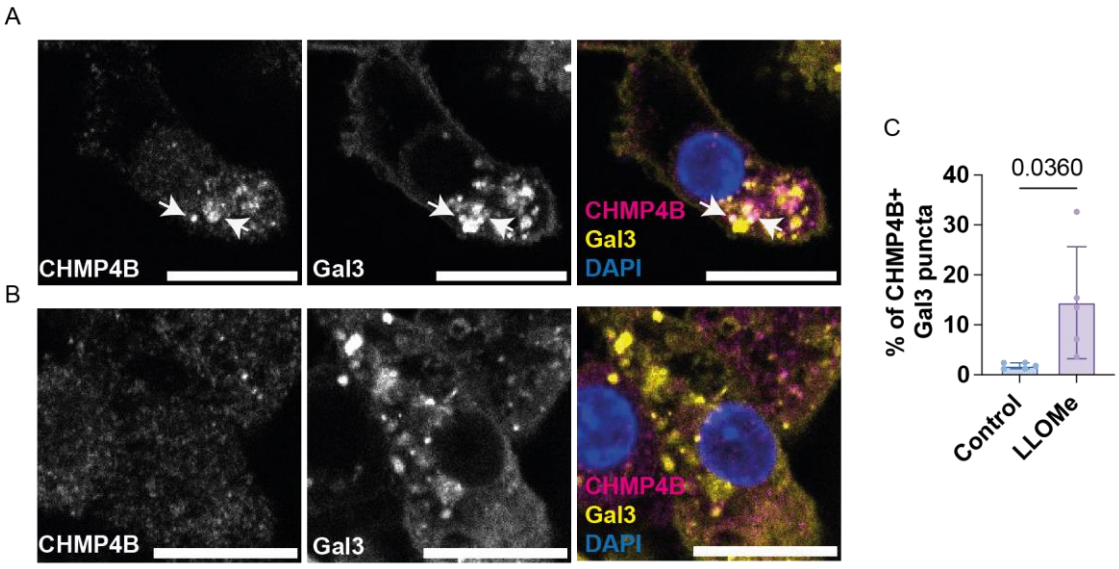

Figure 5.2.4. Gal3 and CHMP4B puncta show variable colocalisation in BMDM after lysosomal damage

Tac-WT BMDM were treated with vehicle control or LLOMe 1 mM for 30 min and co-stained for Gal3, CHMP4B and DAPI. (A) Example of LLOMe-treated cell showing high level of colocalisation. Arrows show sites of colocalisation (B) Example of LLOMe-treated cell showing low level of colocalization. (C) The percentage of Gal3 puncta showing CHMP4B+ intensity was quantified using FIJI. Data shown are the mean % from two independent experiments (n=5 individual wells).

5.2.4 Lysophagy is not increased in Tac-G2019S BMDM after lysosomal damage

Next, I analysed the autophagy marker microtubule-associated protein 1 light chain 3B (LC3B) in Tac-WT and Tac-G2019S BMDM. Extensive lysosomal damage that cannot be efficiently repaired is marked by LC3B and undergoes lysophagy (Radulovic et al., 2018), where the lysosome is degraded by autophagy (Chu et al.,

2017). There were no differences in LC3B puncta in control conditions (Figure 5.2.5). After lysosomal damage, LC3B puncta increased in both Tac-WT and Tac-G2019S BMDM with no significant differences between the genotypes, although I noted a trend for increased LC3B in Tac-G2019S BMDM (Figure 5.2.5). Lysosomal damage in the presence of kinase inhibition with the LRRK2 kinase inhibitor MLi-2 increased LC3B recruitment to damaged lysosomes in Tac-G2019S BMDM but had no effect in Tac-WT BMDM (Figure 5.2.5). GZD-824 treatment resulted in an accumulation of LC3B positive vesicles in the absence of lysosomal damage, thus its effects in LLOMe-induced lysosomal damage should be interpreted with caution (Figure 5.2.5). The finding that MLi-2 treatment did not alter LC3B recruitment to damaged lysosomes in wild-type BMDM suggests that its recruitment is not dependent on LRRK2 kinase activity. However, there were small differences present in Tac-G2019S BMDM with regards to LC3B recruitment, suggesting that this mutation may alter the lysophagy pathway after lysosomal damage in a kinase-independent manner.

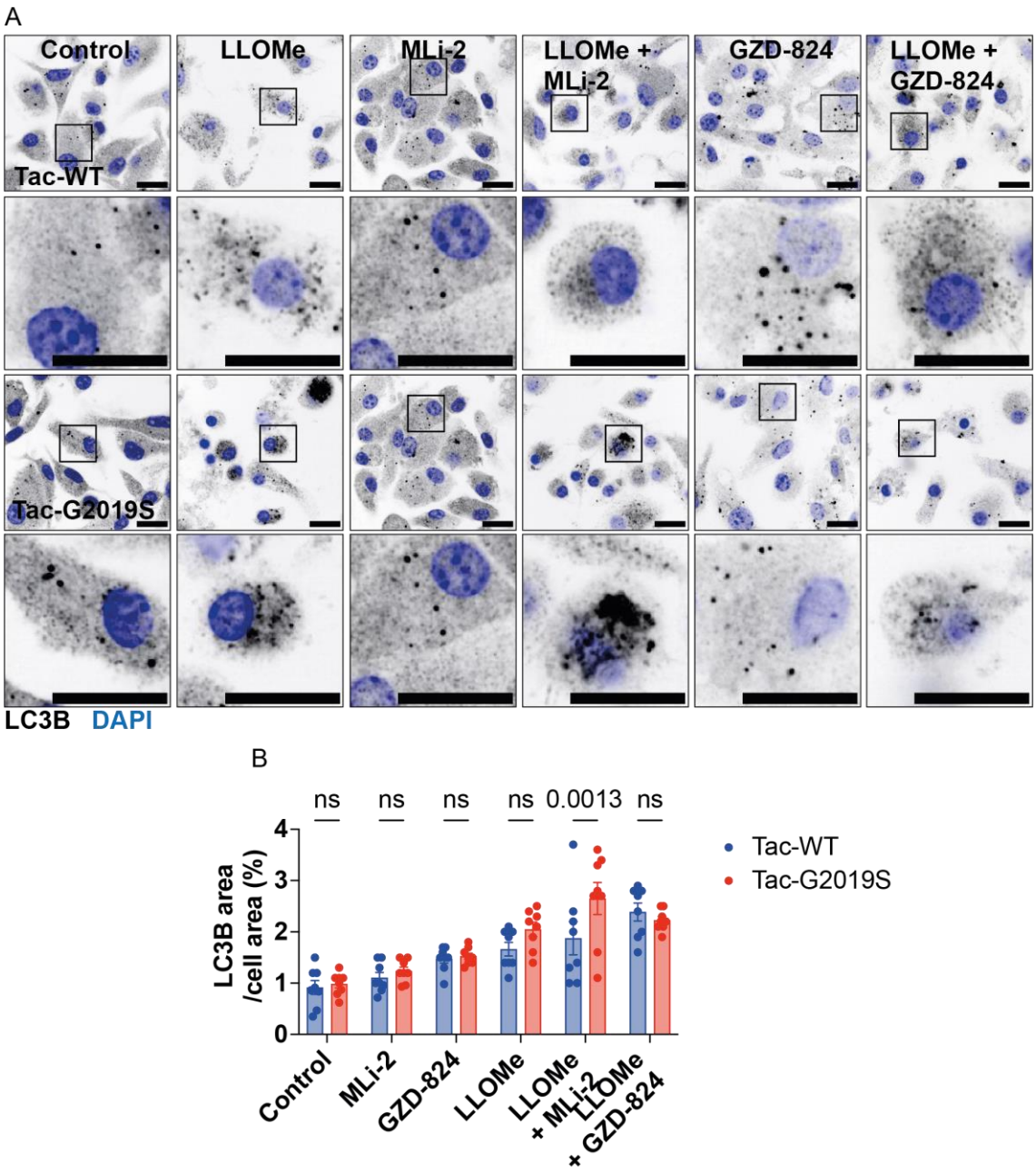

Figure 5.2.5. LC3B puncta formation is increased in both Tac-WT and Tac-G2019S BMDM after lysosomal damage

BMDM were treated with LLOMe 1 mM +/- MLi-2 100 nM or GZD-824 (GZD) 0.1 μM and endogenous LC3B positive cell area was visualised by immunofluorescence and quantified using Harmony software. Scale bars, 20 μm. Data representative of (B) 3 independent experiments (n=8 independent wells). Results are shown as mean ± SEM. Two-way ANOVA followed by Šidák's multiple comparisons test.

5.2.5 Protein expression of Gal3, CHMP4B and LC3B is not different between Tac-WT and Tac-G2019S BMDM

To control for protein expression differences in Gal3, CHMP4B and LC3B in Tac-WT and Tac-G2019S BMDM, I carried out Western blot analysis for these proteins in control, MLi-2, GZD-824 and LLOMe-treatment conditions (Figure 5.2.6). Total levels of Gal3 and CHMP4B did not differ between Tac-WT and Tac-G2019S BMDM in any condition (Figure 5.2.6). LC3B is detected as two bands by western blot – LC3B-I and LC3B-II. LC3B-I is cytosolic while LC3B-II is present on membranes and is conjugated with phosphatidylethanolamine (PE). LC3-I conversion to LC3-II by conjugation with PE occurs during autophagy – thus when autophagy increases the level of LC3-II increases, and this is quantified by measuring the ratio of LC3-II:LC3-I (Mizushima and Yoshimori, 2007). Western blot revealed an increase in LC3-II levels and a decrease in LC3-I levels after lysosomal damage in both Tac-WT and Tac-G2019S BMDM (Figure 5.2.6). However, the amount of LC3-I present on the membrane was almost undetectable, making analysis of the overall LC3-II/LC3-I ratio, used as a marker of autophagic flux, unreliable for these cells.

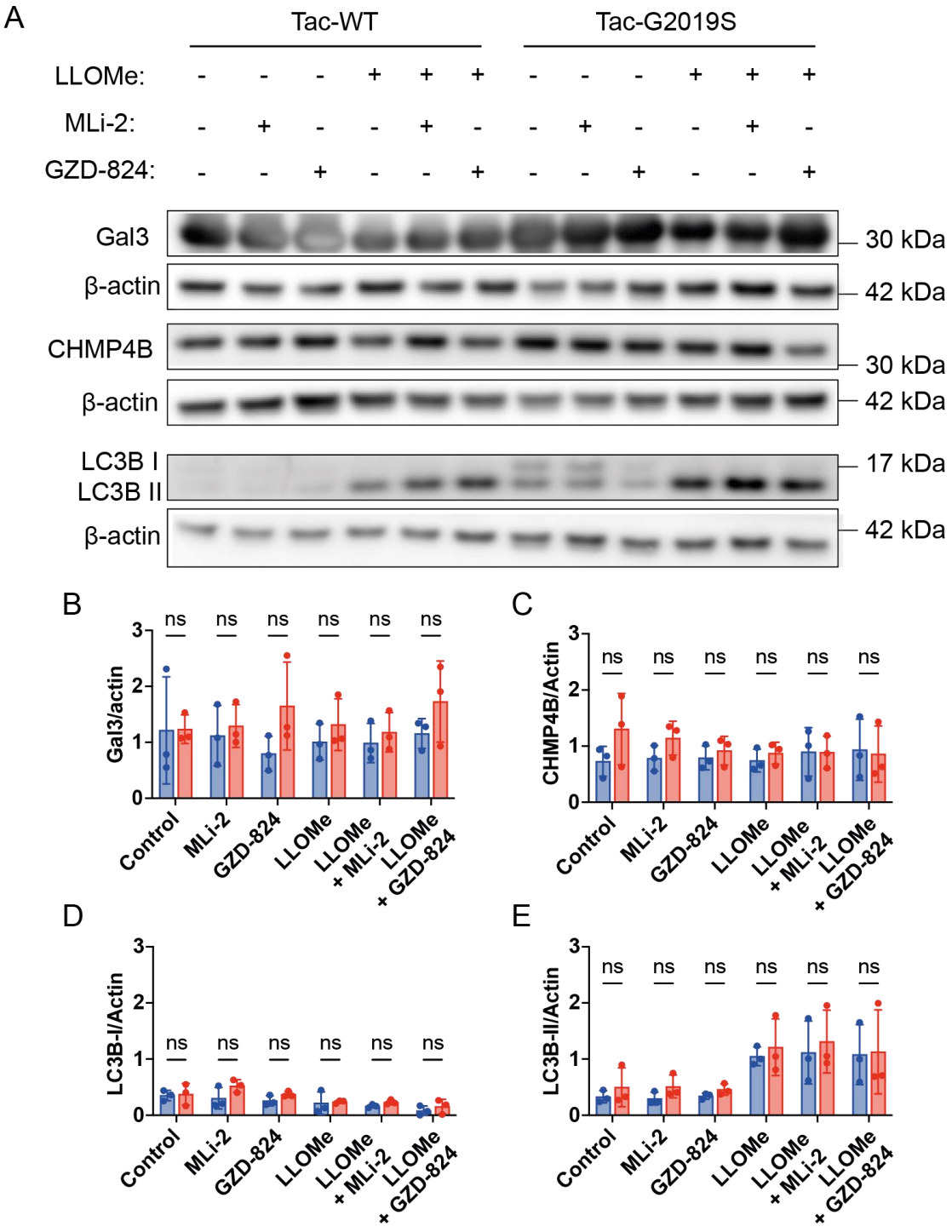

Figure 5.2.6. Expression of Gal3 and CHMP4B is unchanged by lysosomal damage

(A) Western blot analysis of Galectin-3 (Gal3), CHMP4B, LC3B-I, LC3B-II and β-actin in Tac-WT and Tac-G2019S BMDM in untreated, MLi-2, GZD-824, LLOMe, LLOMe + MLi-2 and LLOMe + GZD-824 conditions. (B to E) Gal3, CHMP4B, LC3B-I and LC3B-II band intensities were quantified by densitometry and normalised to β-actin. Data are mean ± SD from 3 independent experiments. Two-way ANOVA followed by Tukey's multiple comparisons test.

5.3 Analysis of endogenous LRRK2 in BMDM after lysosomal damage

I next attempted to stain for endogenous LRRK2 by immunofluorescence to confirm lysosomal recruitment of LRRK2 after lysosomal damage. I utilised 6J-WT and 6J-LRRK2KO BMDM to validate LRRK2 immunofluorescence in BMDM as the antibody had not previous been used in this cell type in my lab. I noted a strong signal in untreated 6J-LRRK2KO BMDM after several attempts at staining and in different conditions including differing antibody dilutions, permeabilisation reagents and primary antibody incubation periods (Figure 5.5.1). As such, the antibody was not deemed reliable for immunofluorescence studies in these cells.

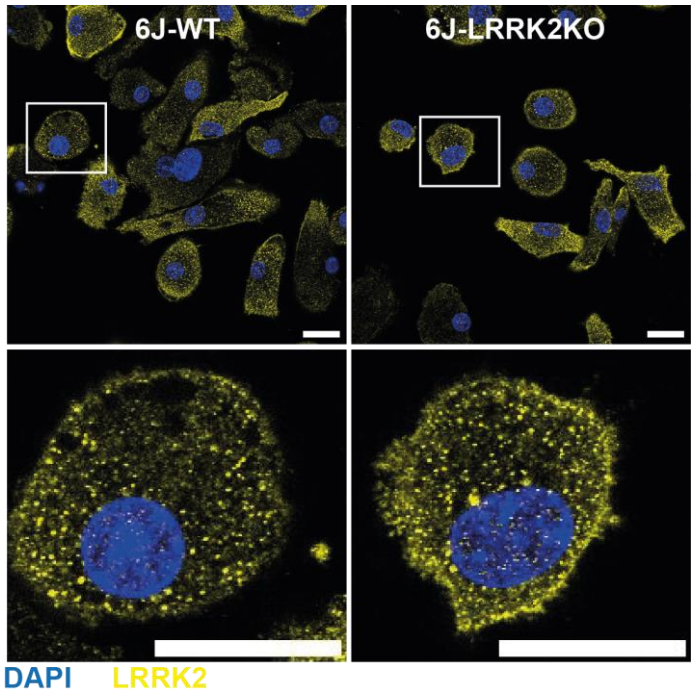

Figure 5.3.1. LRRK2 staining by immunofluorescence is unreliable in BMDM

Untreated 6J-WT and 6J-LRRK2 KO BMDM were stained for endogenous LRRK2 using a mouse monoclonal antibody (see materials and methods) and imaged by confocal microscopy. Scale bars, 20 μm. Images shown are from one representative experiment.

Although I was unable to image endogenous LRRK2 in these cells, I carried out Western blot to check for changes in LRRK2 expression after lysosomal damage (Figure 5.3.2). LRRK2 levels showed a trend to decrease in Tac-G2019S BMDM after lysosomal damage, however this was not significant at n=2 independent

experiments and would require testing with a larger sampler size. It was also notable that the 170 kDa LRRK2 band (see also Figure 3.2.2) disappeared after 30 min of lysosomal damage in both Tac-WT and Tac-G2019S BMDM (Figure 5.3.2).

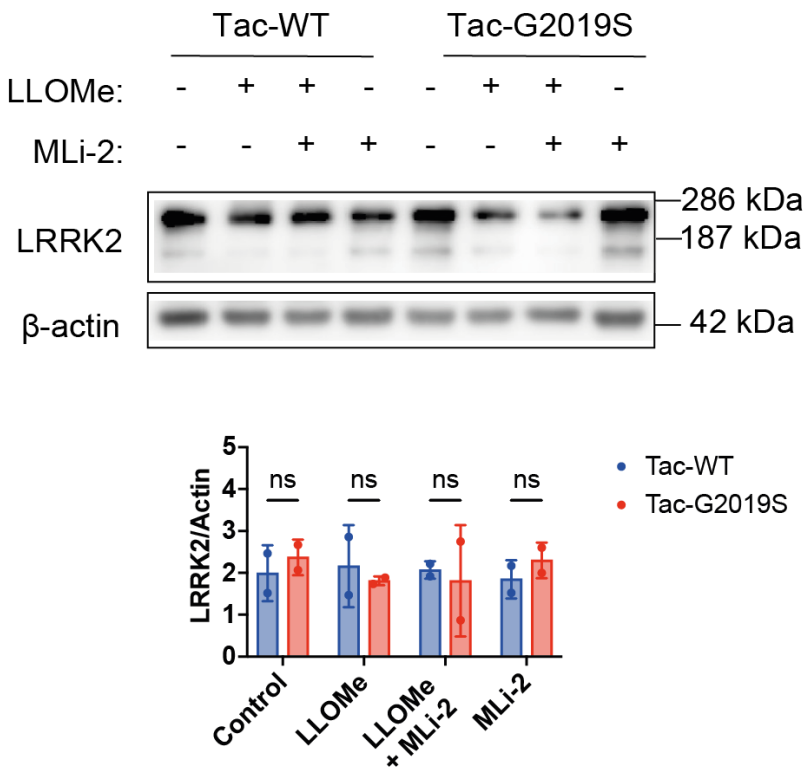

Figure 5.3.2. LRRK2 expression levels during lysosomal damage in Tac-WT and Tac-G2019S BMDM

Western blot analysis of LRRK2 and β-actin in Tac-WT and Tac-G2019S BMDM in untreated, LLOMe, LLOMe + MLi-2 and MLi-2 conditions. Full-length LRRK2 band intensity was quantified by densitometry and normalised to β-actin. Data are mean ± SD from 2 independent experiments. Two-way ANOVA followed by Tukey's multiple comparisons test.

5.4 Tac-G2019S BMDM show reduced Lysotracker recovery after LLOMe-induced lysosomal damage

The above results suggest that Tac-G2019S BMDM show no differences in the total number of damaged lysosomes or lysosomes targeted to lysophagy, but reduced recruitment of ESCRT-III machinery to damaged lysosomes. This data was acquired from fixed cells at a timepoint of 30 min LLOMe treatment and does not capture the dynamics of protein recruitment following lysosomal damage. To monitor lysosomal

integrity dynamics in BMDM, I utilised LysoTracker dye and carried out live cell snapshot imaging during LLOMe-induced lysosomal damage, followed by LLOMe-washout and snapshot imaging to monitor lysosomal repair. The experimental workflow is demonstrated in Figure 5.4.1.

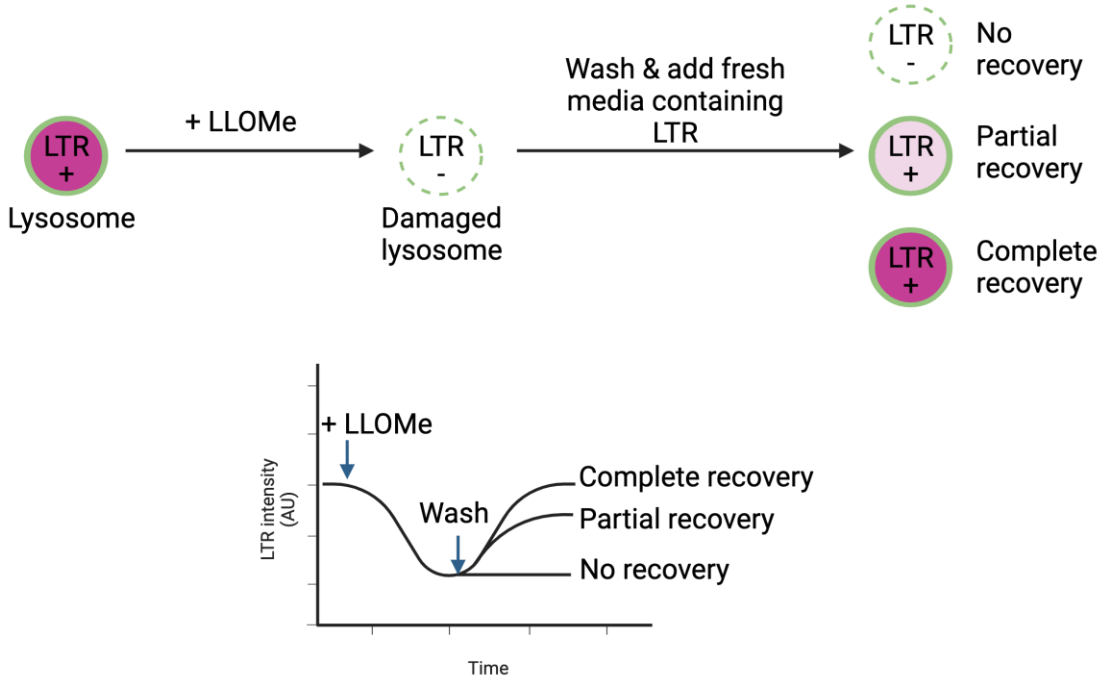

Figure 5.4.1. Workflow for LysoTracker recovery assay

The experimental workflow for the LysoTracker (LTR) recovery assay is illustrated. Following baseline LTR intensity imaging, Live BMDM are imaged every minute after the addition of LLOMe, followed by washout and replacement of media containing fresh LTR. LTR intensity increases during the recovery stage, indicative of lysosomal membrane repair.

In agreement with the Gal3 immunofluorescence data Tac-WT and Tac-G2019S macrophages leaked LysoTracker to a similar degree, suggesting similar levels of lysosomal damage. However, the recovery of the lysosomal population after removal of LLOMe was reduced in Tac-G2019S macrophages, confirming a defect in lysosomal repair (Figure 5.4.2).

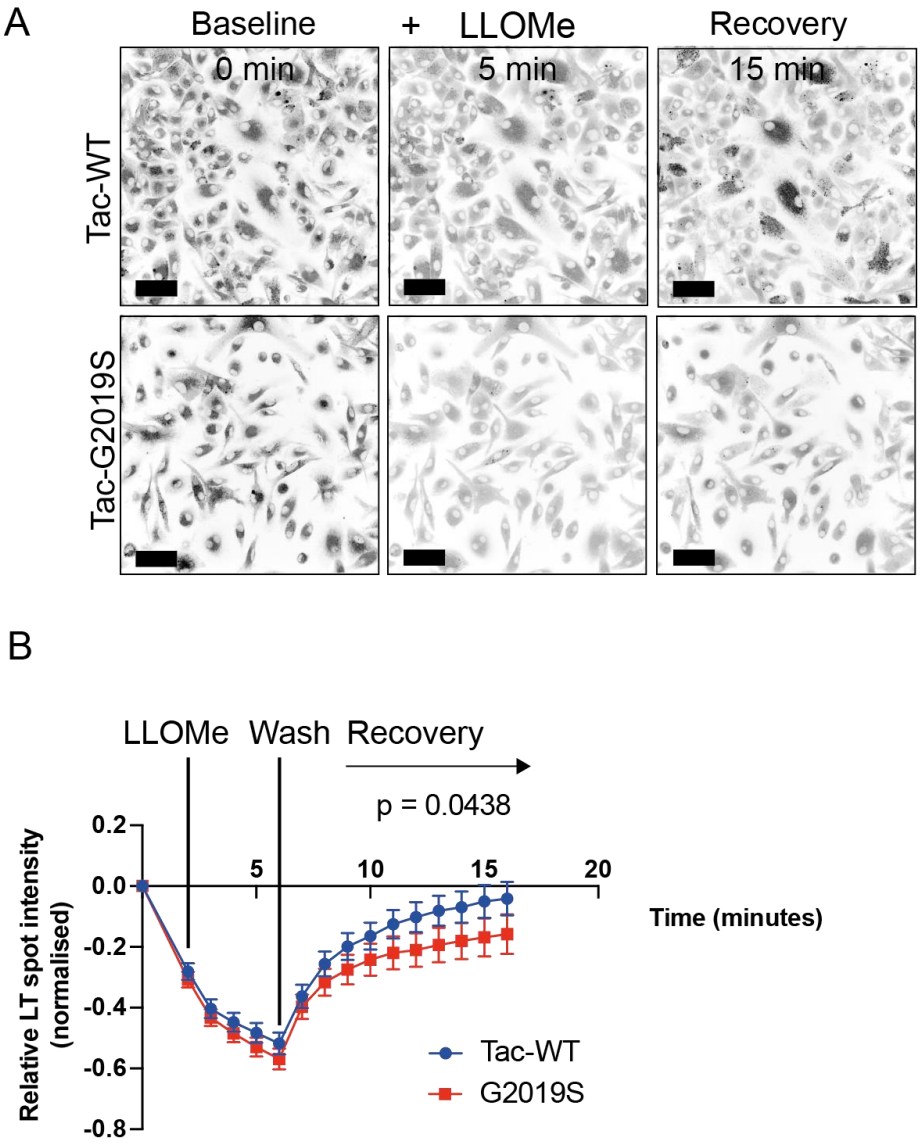

Figure 5.4.2. Tac-G2019S BMDM show reduced recovery of LysoTracker after lysosomal damage.

(A) Live cell snapshot imaging of LysoTracker positive spots in BMDM treated with LLOMe 1mM, followed by lysosomal recovery after removal of LLOMe and wash. Scale bar = 50 μm. (B) Data shown is the mean ± SD from 6 independent experiments. Differences between slopes in the recovery period (after wash) were estimated using linear regression.

5.5 LRRK2 kinase dead BMDM do not show altered response to lysosomal damage and repair

My previous data indicated that Gal3, CHMP4B and LC3B recruitment to damaged lysosomes was independent of LRRK2 kinase activity. To further explore this, I

utilised the NJ-D1994A LRRK2 kinase dead BMDM. NJ-WT and NJ-D1994A BMDM were treated with vehicle control or LLOMe ± MLi-2, followed by staining for endogenous Gal3, CHMP4B and LC3B and high content microscopy. NJ-D1994A macrophages were treated with MLi-2 to control for off-target effects.

NJ-WT and NJ-D1994A macrophages showed a similar number of Gal3 positive puncta after lysosomal damage (Figure 5.5.1), supporting that Gal3 recruitment to damaged lysosomes is LRRK2 kinase activity-independent in BMDM. Like previous experiments approximately 10% of the cell area was positive for Gal3 in control conditions (Figure 5.5.1). MLi-2 treatment did not significantly alter Gal3 in NJ-WT or NJ-D1994A BMDM (Figure 5.5.1).

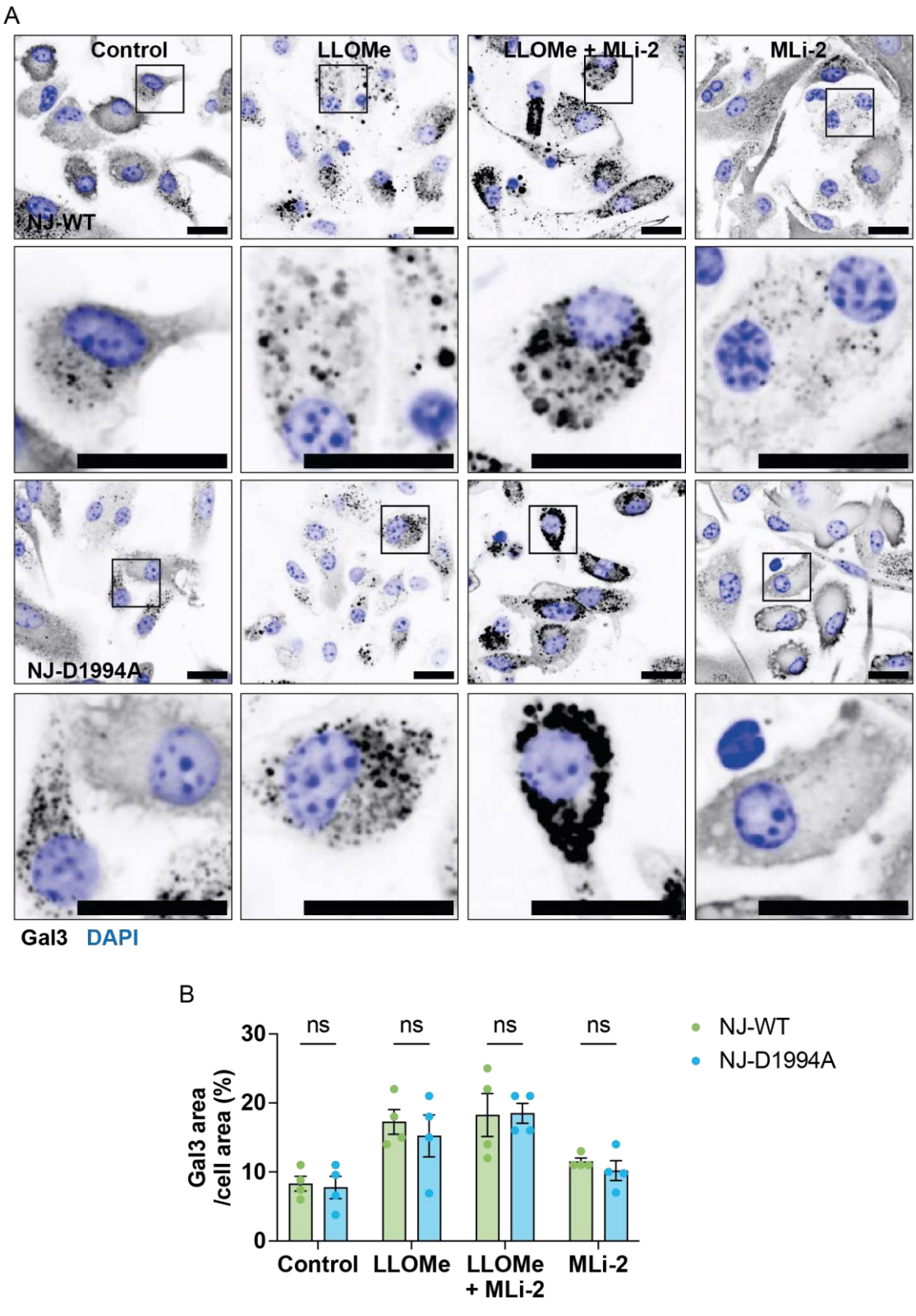

Figure 5.5.1. Gal3 levels do not differ between NJ-WT and NJ-D1994A BMDM after lysosomal damage.

BMDM were treated with LLOMe 1 mM +/- MLi-2 100 nM and endogenous Galectin-3 (Gal3) positive cell area was visualised by immunofluorescence and quantified using Harmony software. Scale bars, 20 μm. Data representative of (B) 4 independent experiments. Results are shown as mean ± SEM. Two-way ANOVA followed by Šidák's multiple comparisons test.

NJ-WT and NJ-D1994A macrophages showed a similar increase in CHMP4B puncta after lysosomal damage (Figure 5.5.2), supporting LRRK2 kinase-independent effects on CHMP4B recruitment to damaged lysosomes in BMDM. MLi-2 did not alter CHMP4B recruitment in NJ-WT and NJ-D1994A BMDM after lysosomal damage (Figure 5.5.2).

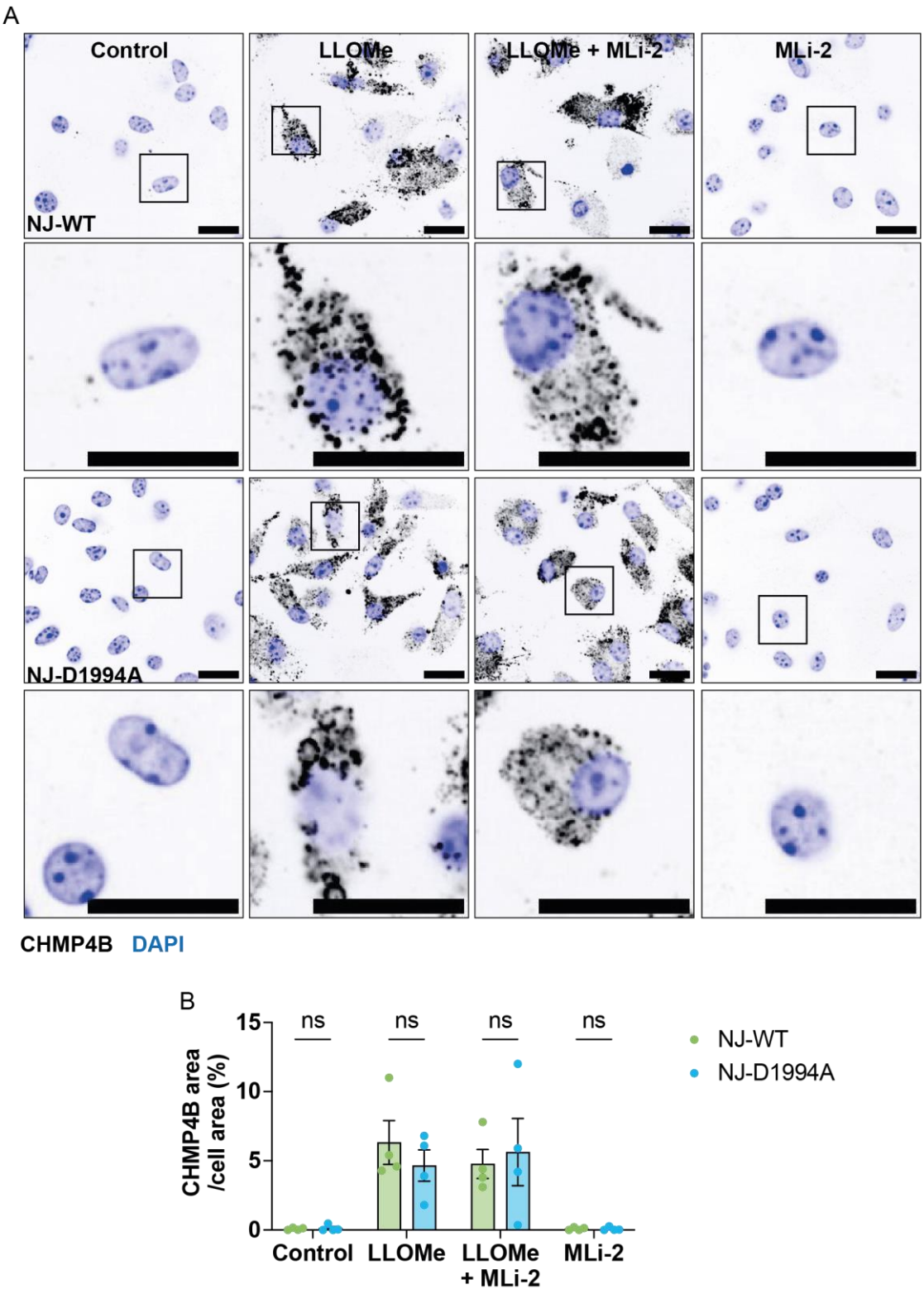

Figure 5.5.2. CHMP4B levels do not differ between NJ-WT and NJ-D1994A BMDM after lysosomal damage.

BMDM were treated with LLOMe 1 mM +/- MLi-2 100 nM for 30 min and endogenous CHMP4B positive cell area was visualised by immunofluorescence and quantified using Harmony software. Scale bars, 20 μm. Data representative of (B) 4

independent experiments. Results are shown as mean ± SEM. Two-way ANOVA followed by Šidák's multiple comparisons test.

Finally, LC3B puncta formation was monitored in NJ-WT and NJ-D1994A BMDM after lysosomal damage. There were no differences in the number of LC3B positive vesicles in control conditions (Figure 5.5.3). Following lysosomal damage, LC3B puncta formation was similar between NJ-WT and NJ-D1994A BMDM (Figure 5.5.3). Lysosomal damage in the presence of MLi-2 inhibition decreased LC3B puncta formation in NJ-WT BMDM and had no effect on NJ-D1994A BMDM (Figure 5.5.3). This data supports a LRRK2 kinase activity-independent effect on LC3B recruitment to damaged lysosomes in BMDM.

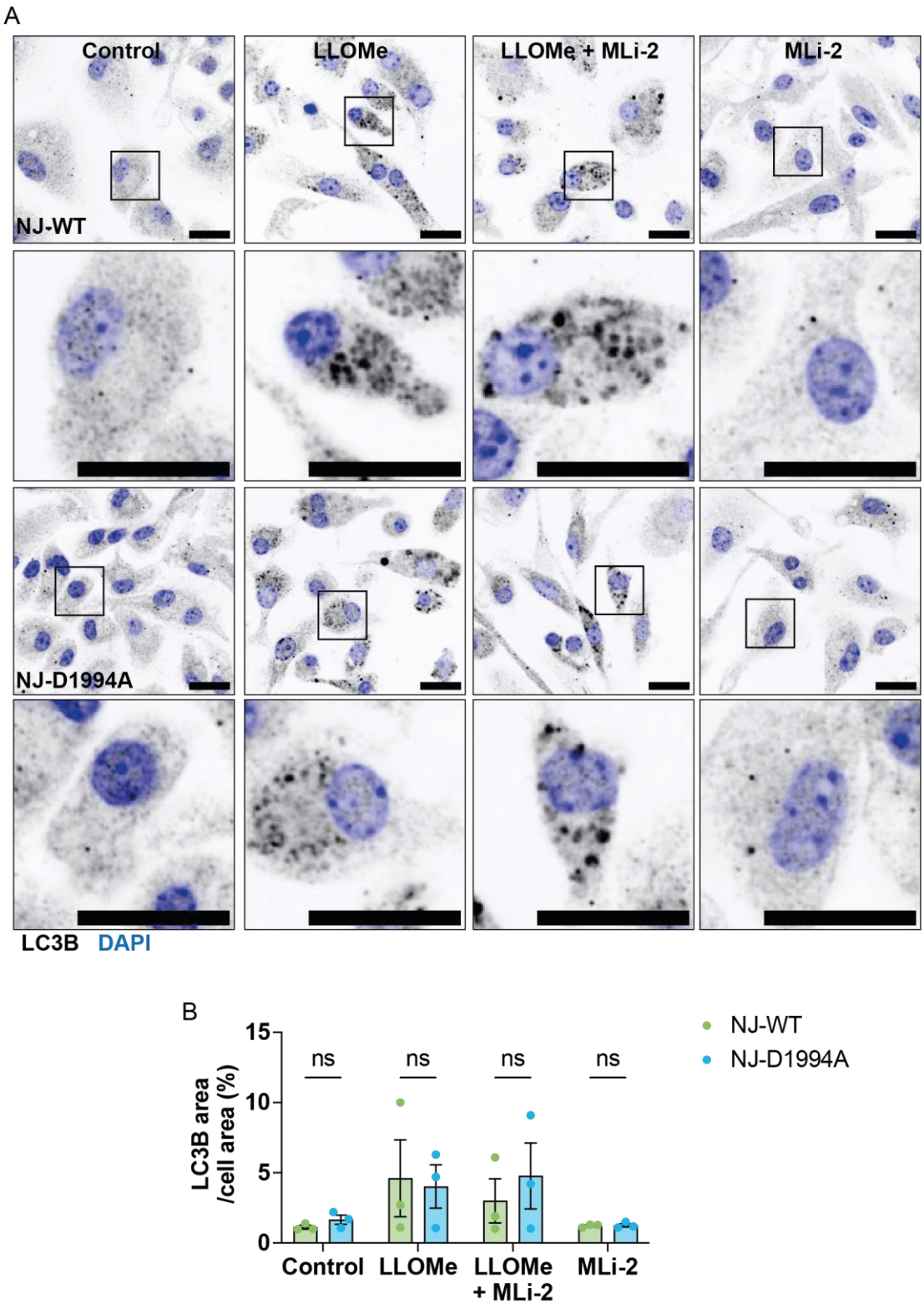

Figure 5.5.3. LC3B levels are unchanged between NJ-WT and NJ-D1994A BMDM after lysosomal damage.

BMDM were treated with LLOMe 1 mM +/- MLi-2 100 nM and endogenous LC3B positive cell area was visualised by immunofluorescence and quantified using Harmony software. Scale bars, 20 μm. Data representative of (B) 3 independent

experiments. Results are shown as mean ± SEM. Two-way ANOVA followed by Šidák's multiple comparisons test.

5.6 LRRK2 KO BMDM do not show altered response to lysosomal damage and repair

Next, I utilised the LRRK2 KO BMDM as a control for kinase, GTPase and other LRRK2 domains on Gal3, CHMP4B and LC3B recruitment after lysosomal damage in BMDM. Given that my above results were not in keeping with the previous data reported by Herbst *et al.* in wild-type RAW 264.7 cells, using the LRRK2 KO BMDM would allow me to test whether the results were like those reported in LRRK2 KO RAW cells (Figure 1.14.1) (Herbst et al., 2020). 6J-WT and 6J-LRRK2KO BMDM were treated with vehicle control or LLOMe 1 mM for 30 min, followed by staining for endogenous Gal3, CHMP4B and LC3B and high content microscopy. To control for off-target effects of kinase inhibition on BMDM, 6J-LRRK2KO BMDM were also treated with MLi-2 control.

There were high levels of Gal3 in 6J-WT and 6J-LRRK2KO BMDM in control conditions (Figure 5.6.1). 6J-WT and 6J-LRRK2KO BMDM increased Gal3 levels after LLOMe-induced lysosomal damage to similar levels with no significant differences (Figure 5.6.1). MLi-2 had no effect on Gal3 levels after lysosomal damage (Figure 5.6.1).

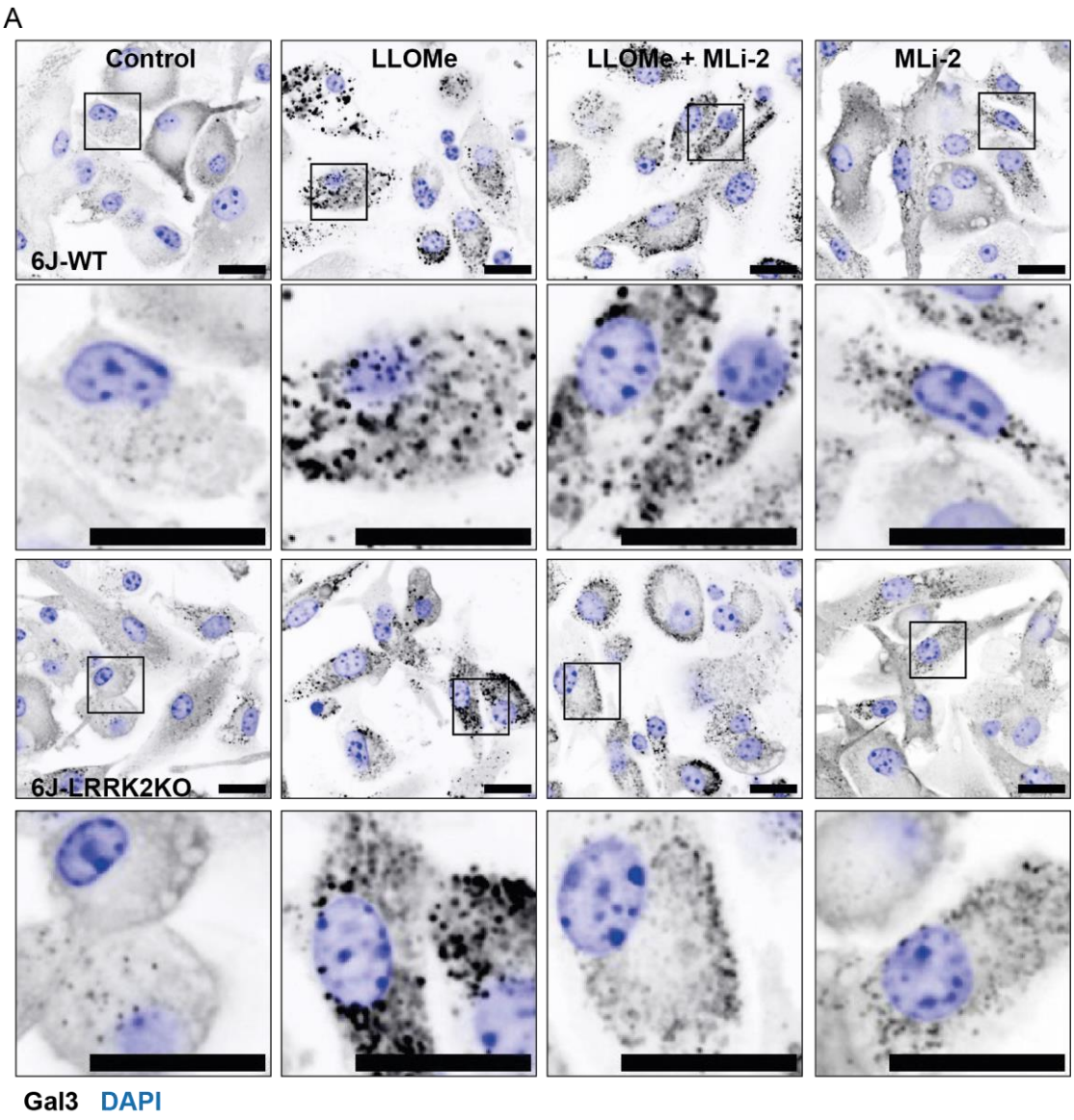

Figure 5.6.1 Gal3 levels do not differ between 6J-WT and 6J-LRRK2KO BMDM after lysosomal damage.

BMDM were treated with LLOMe 1 mM +/- MLi-2 100 nM for 30 min and endogenous Galectin-3 (Gal3) positive cell area was visualised by immunofluorescence and

quantified using Harmony software. Scale bars, 20 μm. Data representative of (B) 3 independent experiments (n=6 individual wells). Results are shown as mean ± SEM. Two-way ANOVA followed by Šidák's multiple comparisons test.

CHMP4B was largely undetectable in 6J-WT and 6J-LRRK2KO BMDM in control conditions (Figure 5.6.2). CHMP4B puncta increased after lysosomal damage in both 6J-WT and 6J-LRRK2KO BMDM, with no significant differences (Figure 5.6.2). MLi-2 had no effect on CHMP4B levels in 6J-WT or 6J-LRRK2KO BMDM (Figure 5.6.2).

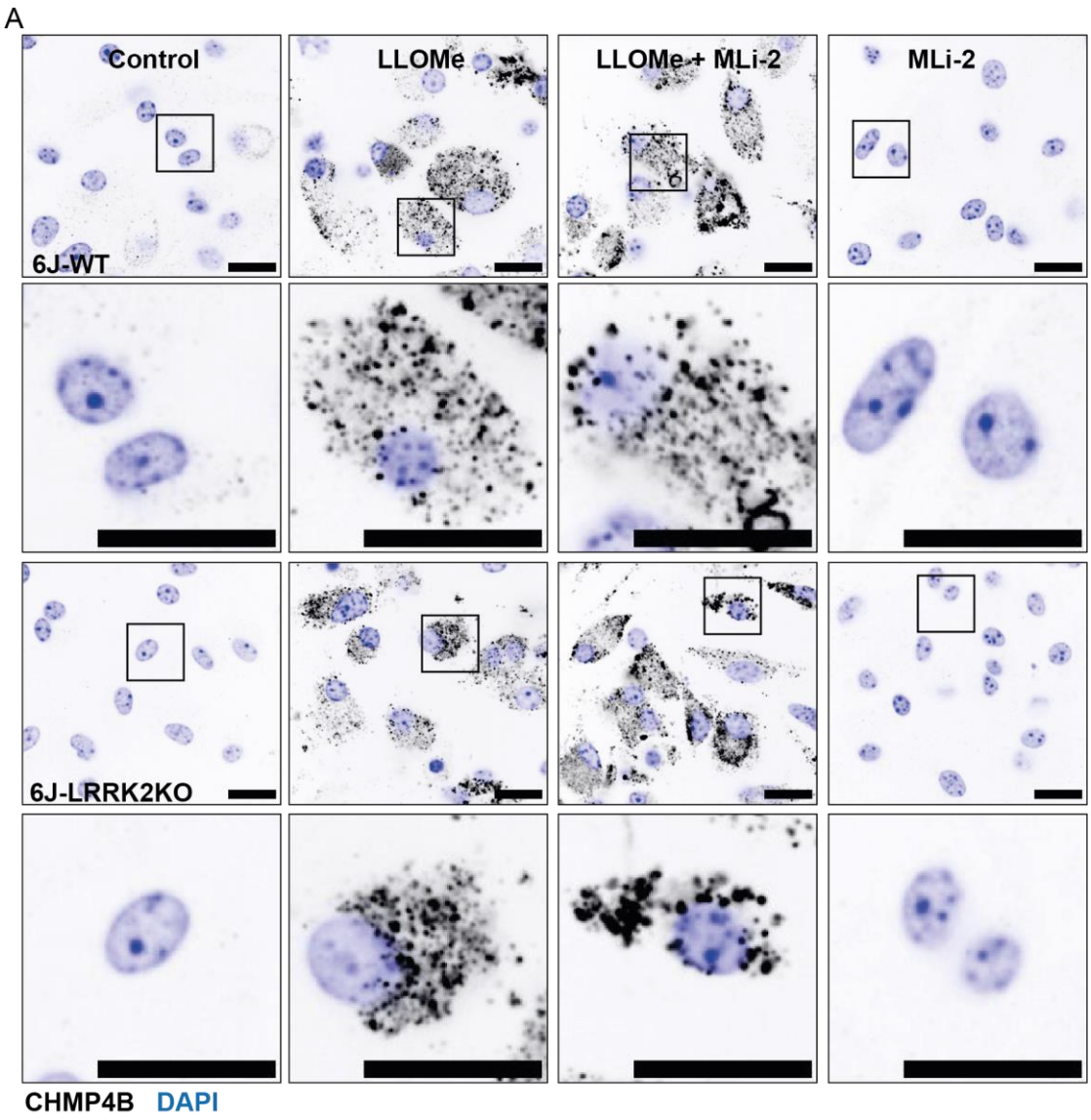

Figure 5.6.2. CHMP4B levels do not differ between 6J-WT and 6J-LRRK2KO BMDM after lysosomal damage.

BMDM were treated with LLOMe 1 mM +/- MLi-2 100 nM for 30 min and endogenous CHMP4B positive cell area was visualised by immunofluorescence and quantified

using Harmony software. Scale bars, 20 μm. Data representative of (B) 3 independent experiments (n=6 individual wells). Results are shown as mean ± SEM. Two-way ANOVA followed by Šidák's multiple comparisons test.

LC3B levels were similar between 6J-WT and 6J-LRRK2KO BMDM in control conditions (Figure 5.6.3). Following LLOMe-induced lysosomal damage, LC3B levels increased in both genotypes and there were no significant differences, although there were high levels of inter-experimental variability and a trend for increased LC3B in 6J-LRRK2KO BMDM (Figure 5.6.3). Although not statistically significant, LC3B levels trended to decrease in both 6J-WT and 6J-LRRK2KO BMDM in cells treated with LLOMe and MLi-2 (Figure 5.6.3).

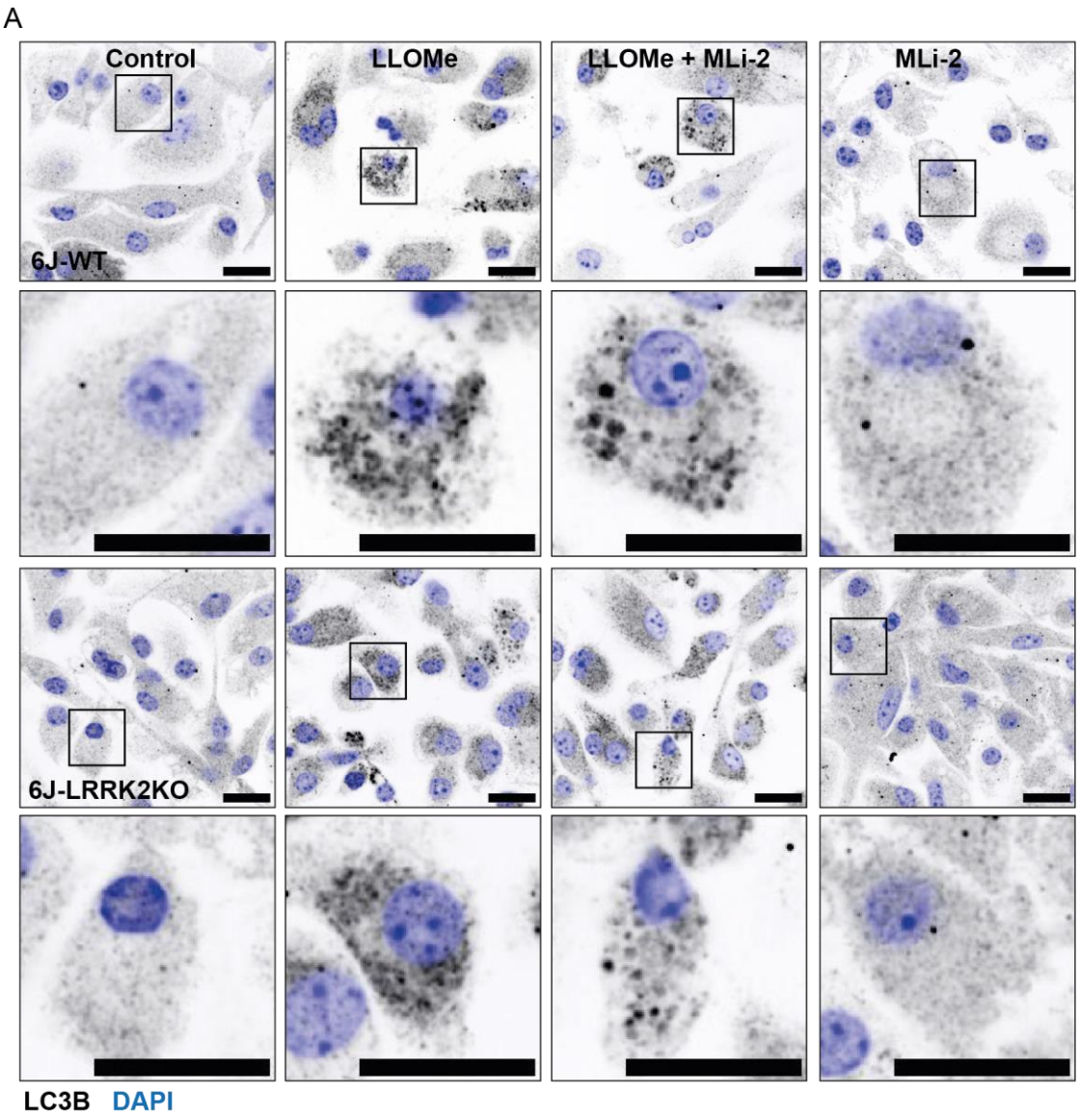

Figure 5.6.3. LC3B levels are unchanged between NJ-WT and NJ-D1994A BMDM after lysosomal damage.

BMDM were treated with LLOMe 1 mM +/- MLi-2 100 nM for 30 min and endogenous LC3B positive cell area was visualised by immunofluorescence and quantified using

Harmony software. Scale bars, 20 μm. Data representative of (B) 3 independent experiments. Results are shown as mean ± SEM. Two-way ANOVA followed by Šidák's multiple comparisons test

These results were unexpected and show quite a striking difference in lysosomal biology between BMDM and RAW cells. Given that another notable difference between these cells is the mean puncta number/cell (around 2-4 puncta/cell for cell lines; several hundred puncta/cell for BMDM), I hypothesised that BMDM were more sensitive to the effects of LLOMe than cell lines, resulting in a stressed lysosomal system in which no differences could be detected. To test this, I repeated these experiments using a lower concentration of LLOMe (0.5 mM) to check whether differences in lysosomal damage, marked by Gal3, would become apparent at this lower level of lysosomal damage. However, at 0.5 mM, no significant increase in Gal3 was noted in NJ-WT, 6J-WT and mutant cells, and so this could not explain my findings (Figure 5.6.4).

A

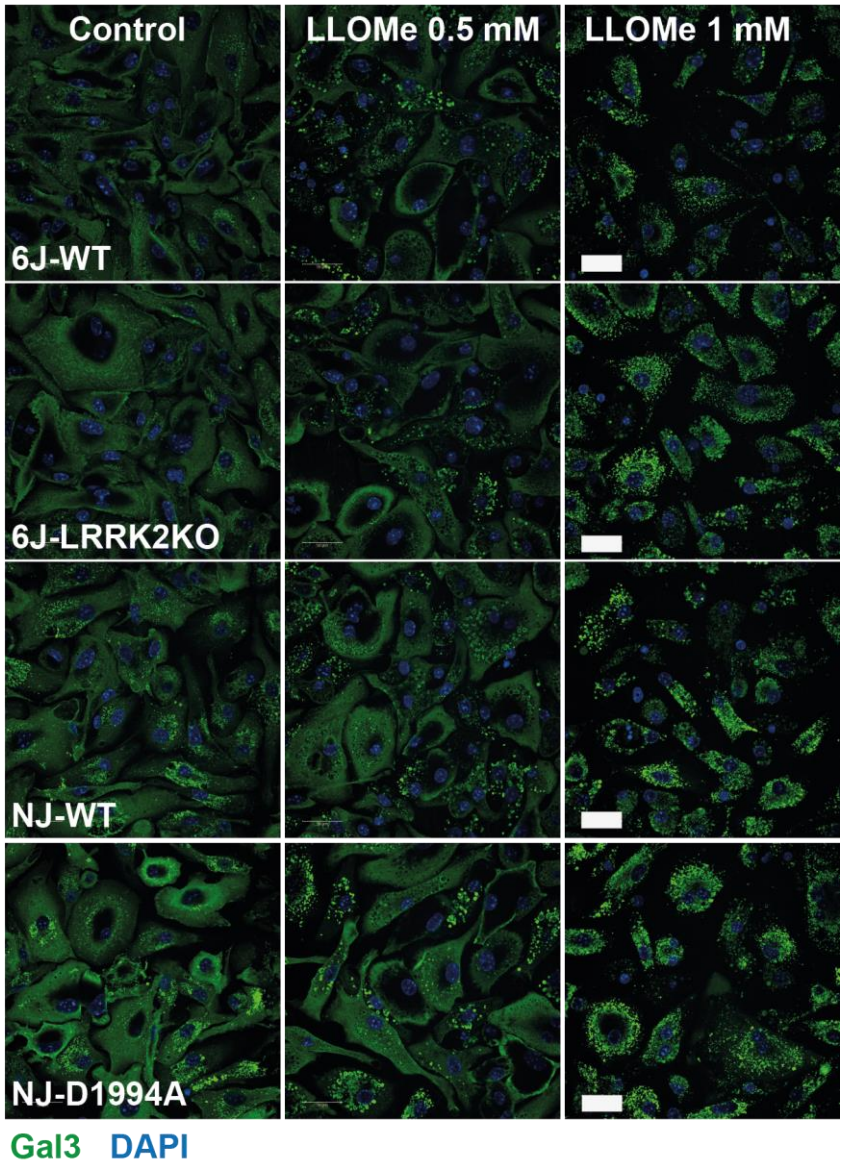
Control
LLOMe 0.5 mM
LLOMe 1 mM
6J-WT
6J-LRRK2KO
NJ-WT
NJ-D1994A
Gal3 DAPI

B

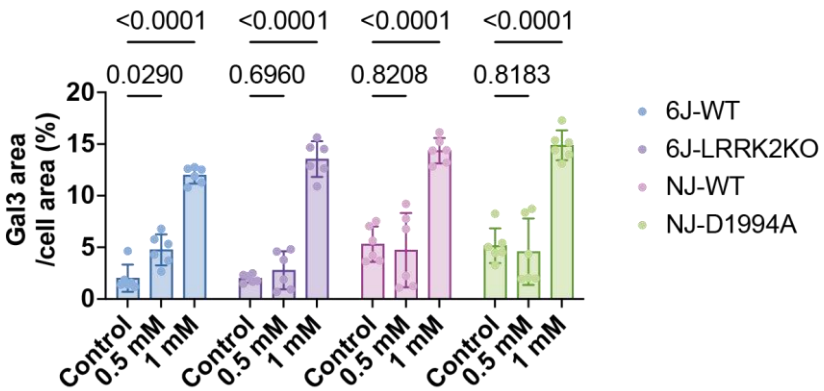
<0.0001
<0.0001
<0.0001
<0.0001
0.0290
0.6960
0.8208
0.8183
Gal3 area /cell area (%)
20
15
10
5
0
Control
0.5 mM
1 mM
6J-WT
6J-LRRK2KO
NJ-WT
NJ-D1994A

Figure 5.6.4. Gal3 levels significantly increase at 1 mM, but not 0.5 mM, LLOMe treatment in BMDM.

BMDM were treated with LLOMe 1 mM, LLOMe 0.5 mM or vehicle control for 30 min and endogenous Galectin-3 (Gal3) positive cell area was visualised by immunofluorescence and quantified using Harmony software. Scale bars, 50 μm. Data representative of (B) 2 independent experiments (n=6 individual wells). Results are shown as mean ± SD. Two-way ANOVA followed by Šidák's multiple comparisons test.

To summarise, in this chapter I found that BMDM carrying LRRK2-G2019S mutation demonstrate reduced recovery of LTR after LLOMe-induced lysosomal damage and reduced recruitment of the ESCRT-III component CHMP4B to damaged lysosomes. This suggests that LRRK2-G2019S is associated with a defect in lysosomal membrane repair. However, my data in wild-type, LRRK2 kinase dead and LRRK2 KO BMDM shows that the recruitment of Gal3, CHMP4B and LC3B is not LRRK2-dependent, because there were no differences between kinase dead and LRRK2 KO macrophages and their respective wild-types, and LRRK2 kinase inhibition did not alter Gal3, CHMP4B and LC3B puncta formation in wild-type BMDM. This data is summarised in the table below (Table 5.6.1).

	Tac-WT versus Tac-G2019S BMDM		
	Effect of LRRK2 mutation/KO	MLi-2 dependent	GZD-824-dependent
Gal3	=	No	No
CHMP4B	↓	No	No
LC3B	=	No	Levels altered in GZD control
	NJ-WT versus NJ-D1994A BMDM		
Gal3	=	No	N/A
CHMP4B	=	No	N/A
LC3B	=	No	N/A
	6J-WT versus 6J-LRRK2KO BMDM		
Gal3	=	No	N/A

CHMP4B	=	No	N/A
LC3B	=	No	N/A

Table 5.6.1. Summary of Gal3, CHMP4B and LC3B immunofluorescence results

Chapter 6. Results 4 Investigating lysosomal damage-induced cell death in LRRK2-mutant macrophages

In the previous chapter I showed that LRRK2-G2019S macrophages show a deficit in lysosomal membrane repair. This process is important for cell homeostasis because the ensuing leakage of lysosomal contents into the cytosol can cause widespread damage and cell death. It has been proposed that leakage of specific cathepsins through small membrane holes triggers apoptosis (Johansson et al., 2010), while extensive leakage results in necrotic cell death (Boya and Kroemer, 2008). Lysosomal membrane damage has also been linked to pyroptotic cell death via NLRP3 inflammasome activation (Chen et al., 2019). In this chapter I explore the consequences of lysosomal damage and repair on cell death pathways in LRRK2 mutant macrophages.

6.1 Tac-G2019S and 6J-LRRK2KO BMDM show contrasting cell death responses during LLOMe-induced lysosomal membrane damage

First, I quantified cell death during a time course of LLOMe-induced lysosomal membrane damage in Tac-WT, Tac-G2019S, NJ-WT, NJ-D1994A, 6J-WT and 6J-LRRK2KO BMDM. BMDM were stained with NucBlue, a DNA-binding dye that freely diffuses across plasma membranes thus labelling all nuclei, and NucGreen, a DNA-binding dye that cannot diffuse across the plasma membrane unless membrane integrity is compromised, thus labelling nuclei in dead cells. BMDM were imaged every 15 min using high content confocal microscopy. For each timepoint, the total number of dead cells (NucGreen positive) was calculated as a percentage of the total number of cells (NucBlue positive). After 90 min of lysosomal damage there were significantly higher levels of cell death in Tac-G2019S compared to Tac-WT BMDM (Figure 6.1.1, a and b). In contrast, NJ-WT and NJ-D1994A BMDM showed similar levels of cell death throughout 90 min of LLOMe treatment (Figure 6.1.1, c and d), while 6J-LRRK2KO BMDM showed significantly less cell death than 6J-WT BMDM

from 45 min of LLOMe treatment (Figure 6.1.1, e and f). This suggested that LRRK2-G2019S was associated with increased cell death during lysosomal membrane damage however LRRK2 kinase activity (as absent in NJ-D1994A BMDM) was not linked to cell death, while other functions of LRRK2 (as absent in LRRK2KO BMDM) were important for cell death.

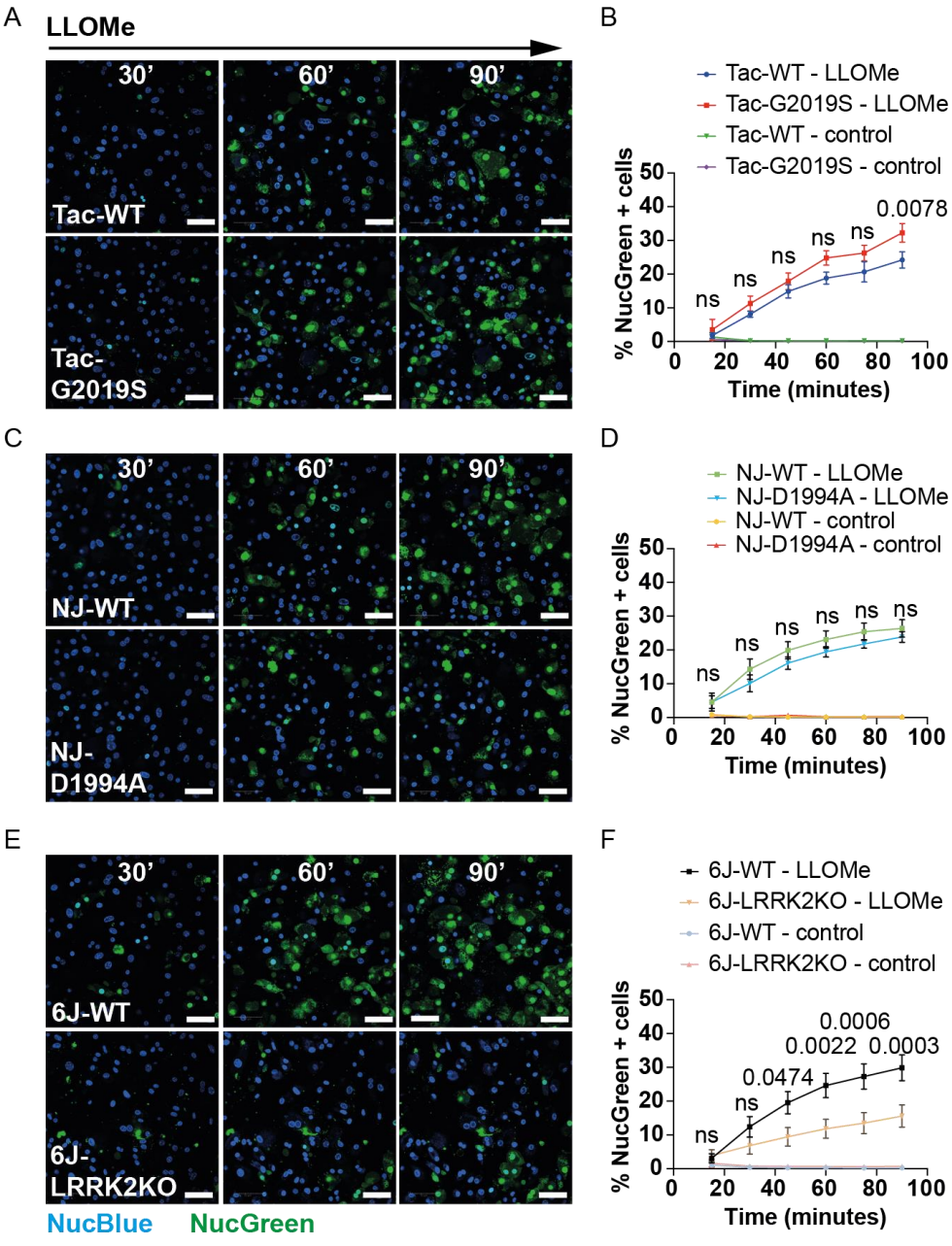

Figure 6.1.1. Tac-G2019S BMDM show increased cell death during LLOMe-induced lysosomal damage.

(A, C and E) Snapshots of BMDM treated with LLOMe at 30, 60 and 90 min. Nuclear staining (blue) and dead nuclear staining (green). Scale bars = 50μm. (B, D and F) Connecting line graphs showing the mean ± SEM percentage of dead cells at each timepoint. P-values by Two-Way ANOVA (mixed-effects model) with Bonferroni's multiple comparisons test. Data is from (B) 6 independent biological replicates (D) 5 independent replicates and (F) 5 independent biological replicates.

6.1.1 Cell death during lysosomal damage is independent of LRRK2 kinase activity

To confirm the effects of LRRK2 kinase activity in lysosomal damaged-induced cell death, Tac-WT and Tac-G2019S BMDM were treated with MLi-2 and again imaged with NucBlue and NucGreen dyes during LLOMe treatment. The overall level of cell death was not significantly altered by MLi-2 treatment in Tac-WT or Tac-G2019S BMDM (Figure 6.1.2). This is in keeping with LRRK2 kinase activity-independent effects of lysosomal damage effects on cell death.

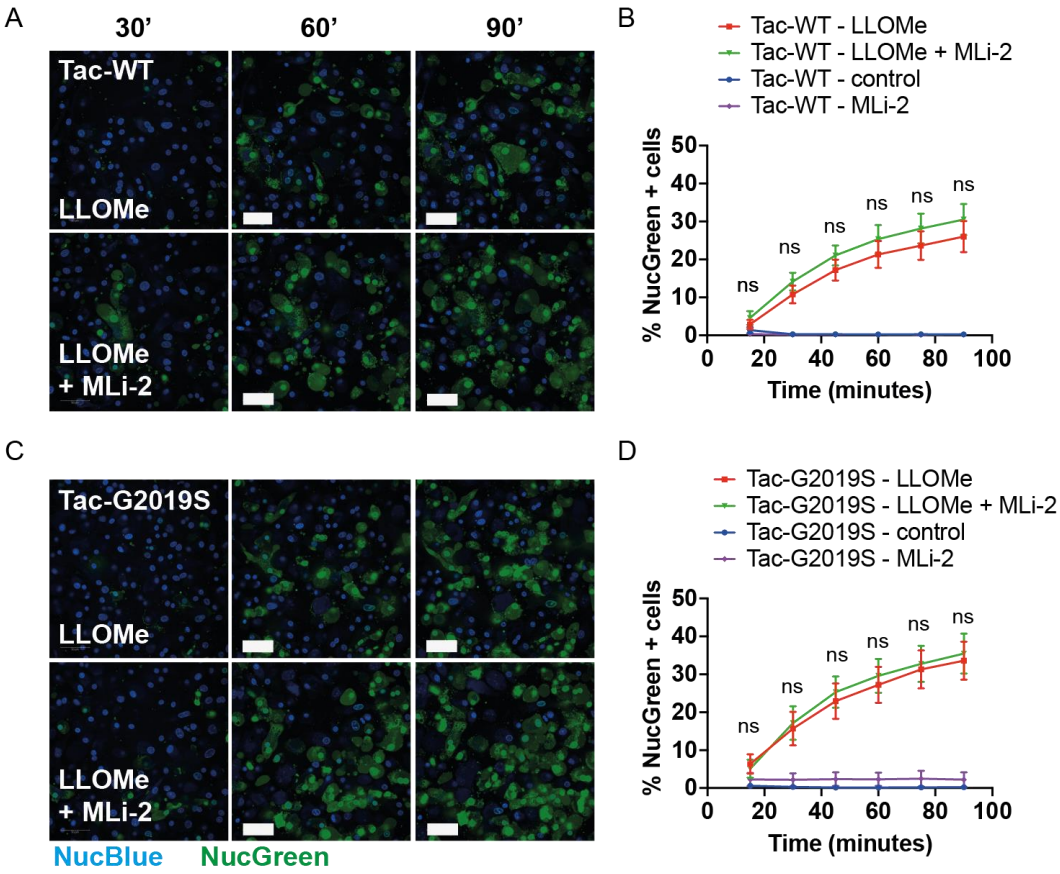

Figure 6.1.2. BMDM death after lysosomal damage is LRRK2 kinase activity-independent

(A and C) Snapshots of BMDM treated with LLOMe ± MLi-2 at 30, 60 and 90 min. Nuclear staining (blue) and dead nuclear staining (green). Scale bars = 50μm. (B and D) Connecting line graphs showing the mean ± SEM percentage of dead cells at each timepoint. P-values by Two-Way ANOVA (mixed-effects model) with Bonferroni's multiple comparisons test. Data is from 4 independent biological replicates.

6.1.2 XL01126 treatment reduces LRRK2 expression in Tac-WT and Tac-G2019S BMDM

Given that there was less cell death in 6J-LRRK2KO BMDM during lysosomal membrane damage, I next explored whether reducing LRRK2 expression could alter cell death after LLOMe-induced lysosomal damage in Tac-WT and Tac-G2019S BMDM. For this, I utilised XL01126, a LRRK2-specific Proteolysis Targeting Chimera (PROTAC) which induces degradation of LRRK2 via the proteosome (Liu et al., 2022). First, I confirmed that 1h XL01126 treatment induced LRRK2 degradation in a dose-dependent manner (Figure 6.1.3). XL01126 degraded 80% of LRRK2 at the highest tested concentration (Figure 6.1.3).

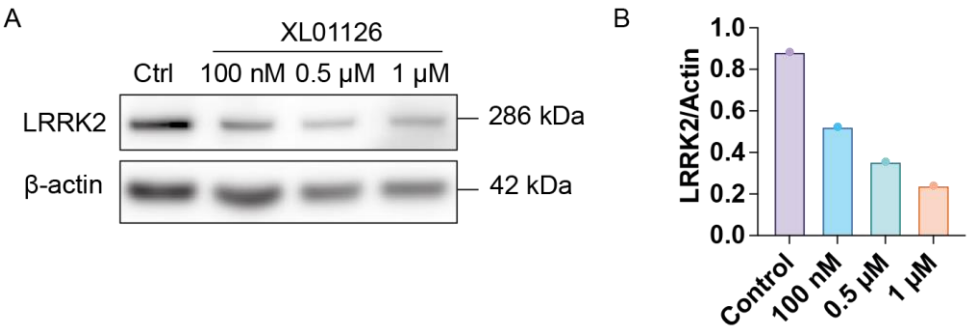

Figure 6.1.3. XL01126 PROTAC treatment results in degradation of LRRK2

(A) Western blot analysis of LRRK2 and β-actin in Tac-WT BMDM in control and 1h XL01126 LRRK2-PROTAC treatment at 100nM, 0.5 μM and 1 μM (B) LRRK2 band intensity was quantified by densitometry and normalised to β-actin. Data shown is from one experiment.

PROTACs can disrupt cell homeostasis by off-target degradation or saturation of the proteasome (Moreau et al., 2020). I therefore explored whether cytotoxic effects were present in BMDM with increasing concentrations of XL01226 by staining cells with NucBlue and NucGreen probes (Figure 6.1.4). After 90 min of XL01126 treatment, increased cell death was present at 0.5 μM, but not at the lower concentration of 100 nM (Figure 6.1.4).

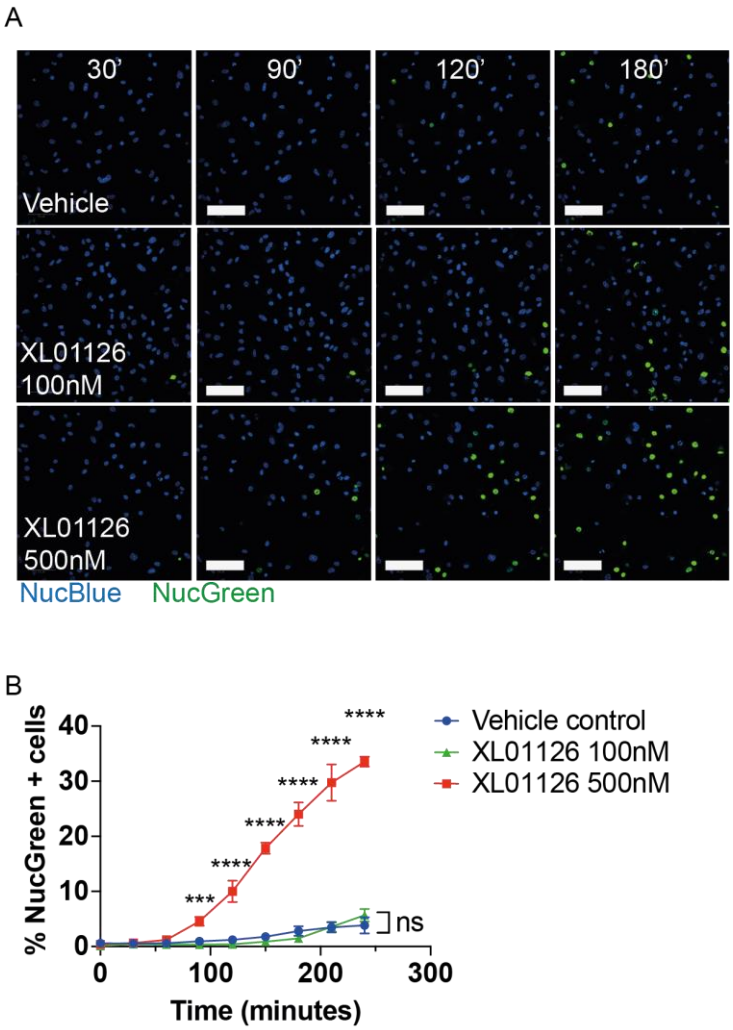

Figure 6.1.4. 500 nM XL01126 treatment is cytotoxic after 90 min in BMDM

(A) Snapshots of BMDM treated with XL01126 at 100 nM and 500 nM. Nuclear staining (blue) and dead nuclear staining (green). Scale bars = 50μm. (B) Connecting line graph showing the mean ± SEM percentage of dead cells at each timepoint. P-values by Two-Way ANOVA with Bonferroni's multiple comparisons test. Data is from 3 technical replicates within one experiment.

Given that BMDM tolerated XL01126 at a lower concentration for at least 240 min without cytotoxic effects (Figure 6.1.4), I decided to check for degradation of LRRK2 in Tac-WT and Tac-G2019S BMDM after 2h XL01126 treatment. LRRK2 expression was reduced by 40-60% in Tac-WT and Tac-G2019S BMDM after 2h XL01126 treatment at a concentration of 200 nM (Figure 6.1.5). Interestingly, I found that Tac-G2019S BMDM showed more degradation of LRRK2 than Tac-WT BMDM in response to XL01126 treatment (Figure 6.1.5).

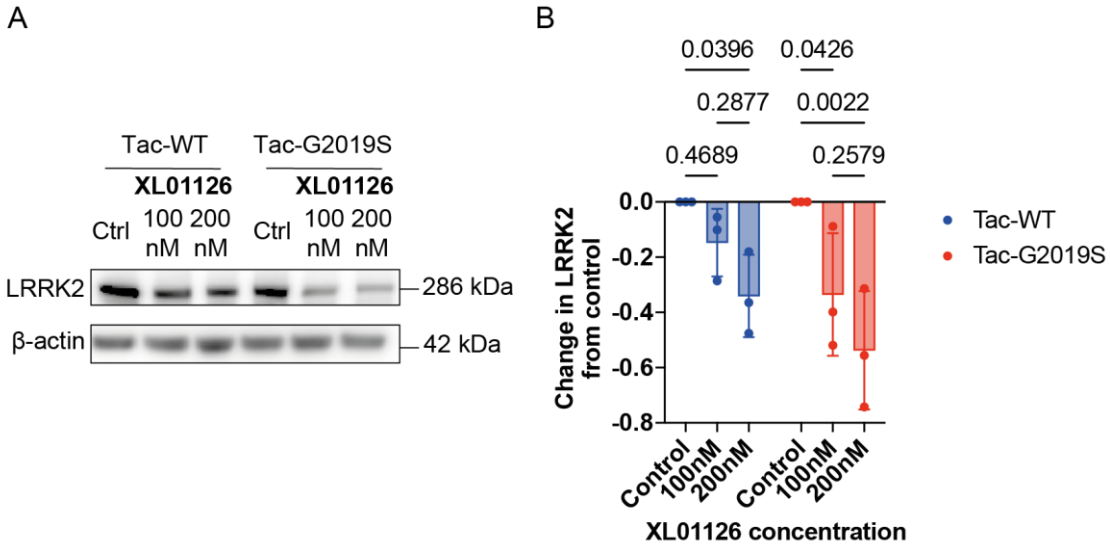

Figure 6.1.5. XL01126 PROTAC 200 nM treatment results in significant degradation of LRRK2 in Tac-WT and Tac-G2019S BMDM.

(A) Western blot analysis of LRRK2 and β-actin in Tac-WT and Tac-G2019S BMDM in control and 1h XL01126 LRRK2-PROTAC treatment at 100nM and 200nM (B) LRRK2 band intensity was quantified by densitometry and normalised to β-actin. Data shown is the mean ± SD from three independent biological replicates. P-values by P-values by Two-Way ANOVA with Bonferroni's multiple comparisons test.

I proceeded to quantify cell death in Tac-WT and Tac-G2019S BMDM during LLOMe-induced lysosomal damage after 2h pre-treatment with 200 nM XL01126. While 200 nM XL01126 pre-treatment did not result in cytotoxic effects in control conditions, XL01126 was unable to alter the amount of cell death in LLOMe-treated Tac-WT and Tac-G2019S BMDM (Figure 6.1.6). This indicated that reduction of LRRK2 expression did not change cell death during lysosomal damage. Notably, XL01126 was not able to completely degrade LRRK2 from the cell, as 40-60% of LRRK2 remained present even with XL01126 treatment (Figure 6.1.5).

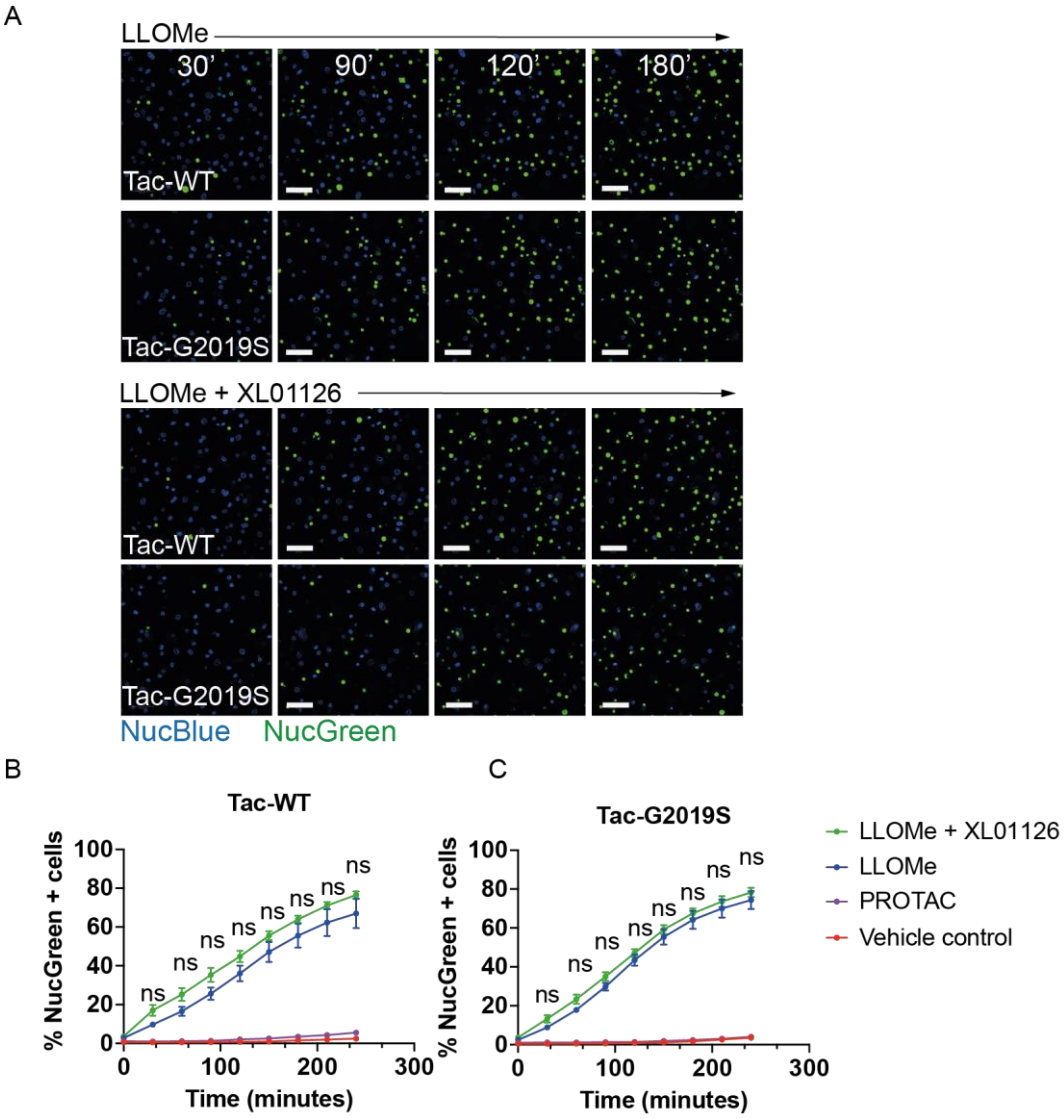

Figure 6.1.6. XL01126 LRRK2-PROTAC does not reduce BMDM cell death after lysosomal damage in Tac-WT or Tac-G2019S BMDM

(A) Snapshots of BMDM treated with LLOMe ± XL01126 at 30, 90, 120 and 180 min. Nuclear staining (blue) and dead nuclear staining (green). Scale bars = 50μm. (B) Connecting line graphs showing the mean ± SEM percentage of dead cells at each timepoint. P-values by Two-Way ANOVA with Bonferroni's multiple comparisons test. Data is from 3 independent biological replicates.

6.1.3 Tac-G2019S BMDM show increased cell death with silica crystal-induced lysosomal damage

I next investigated whether silica crystals, another lysosomal membrane damage-inducing agent, resulted in changes in cell death in Tac-G2019S BMDM. In patients, chronic inhalation of silica crystals results in a fibrotic lung disease known as silicosis

(Mossman and Churg, 1998). Silica crystals have been shown to trigger lysosomal membrane damage, NLRP3 inflammasome assembly and cell death *in vitro* (Hornung et al., 2008). The underlying mechanism of silica crystal-induced lysosomal membrane damage is not fully understood but is thought to be due to mechanical disruption of the lysosomal membrane (Hornung et al., 2008; Pavan et al., 2020). Silica crystals are taken into the cell by phagocytosis (Hornung et al., 2008), so BMDM were treated with silica-coated beads as an additional control. These silica-coated beads are taken into the cell by phagocytosis but do not cause lysosomal membrane damage (Bussi et al., 2022). Tac-G2019S BMDM showed increased cell death after 210 min of silica crystal-induced lysosomal membrane damage compared to Tac-WT BMDM (Figure 6.1.7). There were no differences in cell death between Tac-WT and Tac-G2019S BMDM in control conditions (Figure 6.1.7).

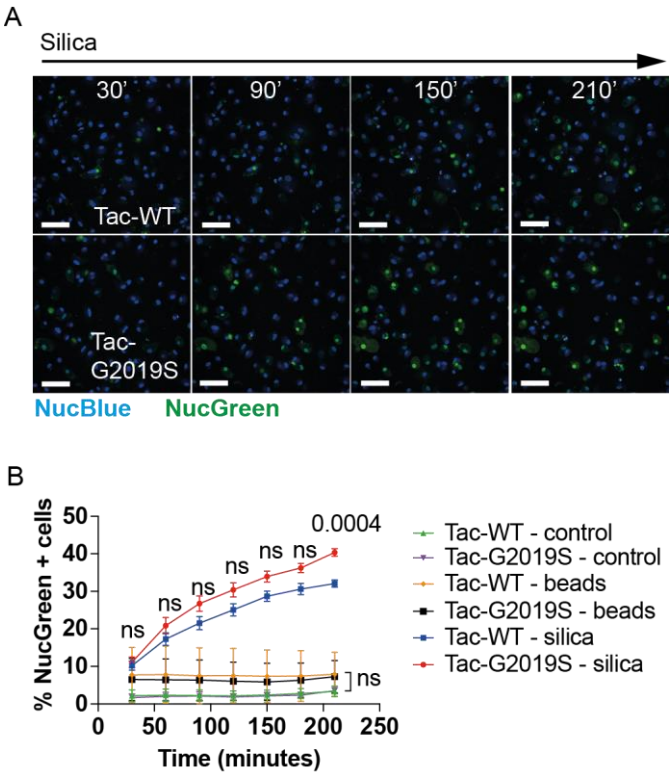

Figure 6.1.7. Silica crystal-induced lysosomal damage results in increased cell death in Tac-G2019S BMDM.

(A and C) Snapshots of BMDM treated with silica crystals at 30, 90, 150, 210, 270 and 330 min. Nuclear staining (blue) and dead nuclear staining (green). Scale bars = 50μm. (B and D) Connecting line graphs showing the mean ± SEM percentage of dead cells at each timepoint. P-values by Two-Way ANOVA (mixed-effects model)

with Bonferroni's multiple comparisons test. Data is from 3 independent biological replicates.

6.2 LRRK2-G2019S iPSDM show increased cell death after lysosomal membrane damage

I next sought to investigate whether human macrophages carrying LRRK2-G2019S mutation show changes in cell death with lysosomal membrane damage. Human iPSDM derived from a PD patient carrying LRRK2-G2019S mutation showed significantly higher levels of cell death during LLOMe-induced lysosomal membrane damage (Figure 6.2.1). There was overall around 10% more cell death in LRRK2-G2019S iPSDM and these effects were present at all time points of lysosomal damage (Figure 6.2.1). MLi-2 treatment did not significantly alter cell death in human iPSDM during lysosomal damage. However, another LRRK2 kinase inhibitor GSK2578215A did reduce death in LRRK2-G2019S iPSDM at 15 and 210 min of lysosomal damage (Figure 6.2.1), suggesting that there may be some kinase-dependent effects. However, given that this was not reproduced with MLi-2 treatment, this could also be off-target effects of the GSK2578215A inhibitor.

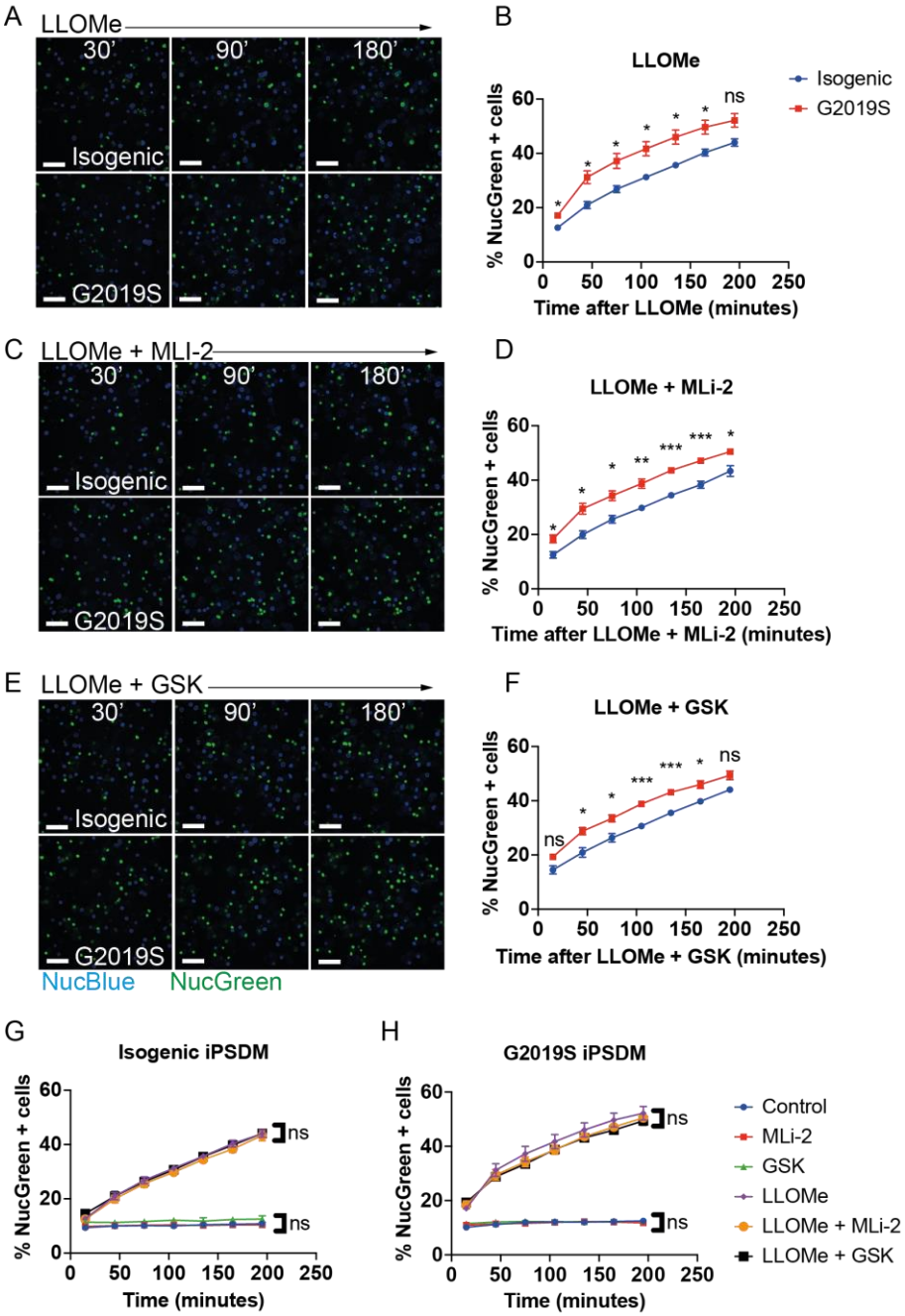

Figure 6.2.1. LRRK2-G2019S iPSDM show increased cell death after lysosomal damage that is independent of LRRK2 kinase activity.

(A, C, E) Snapshots of BMDM treated with LLOMe ± MLi-2 or GSK at 30, 90 and 180 min. Nuclear staining (blue) and dead nuclear staining (green). Scale bars = 50μm. (B, D, F-H) Connecting line graphs showing the mean ± SEM percentage of dead cells at each timepoint. P-values by Two-Way ANOVA with Bonferroni's multiple comparisons test. Data is from 3 independent biological replicates. GSK – GSK2578215A.

6.3 Validation of imaging and Western blot to explore programmed cell death in BMDM

Notably, NucBlue and NucGreen snapshot imaging does not give mechanistic insight into the mode of cell death because compromised plasma membrane integrity is present in all forms of cell death to some extent, including end-stage apoptosis (Majno and Joris, 1995; Patel et al., 2006). Next, I investigated the use of live cell snapshot imaging to differentiate and quantify cell death modes in BMDM. I utilised NucView caspase-3/7 substrate coupled to a DNA-binding Alexa-488 fluorogen (10402-T, Biotium). This compound is cleaved by activated caspase 3/7, the executioners of apoptotic pathways (Julien and Wells, 2017), to release fluorescent signal. BMDM were also incubated with NucBlue (as described previously) and propidium iodide (PI), a DNA binding dye that identifies cells with compromised plasma membrane integrity.

As a positive control for apoptosis, wild-type BMDM were treated with TNF-α and the caspase 3/7 activator, 5Z-7-Oxozeaenol (Sanjo et al., 2019). TNF-α binds to TNFR1 death receptor which triggers the extrinsic apoptotic pathway in the presence of active caspase 3/7. Necroptosis was induced in BMDM by treatment with TNF-α and the pan-caspase-inhibitor Z-VAD-FMK (Choudhury et al., 2024; Place et al., 2022). TNF-α binds to TNFR1 death receptor which triggers the necroptosis pathway in the presence of caspase inhibition. In addition, BMDM were treated with LPS followed by Nigericin to trigger pyroptosis (den Hartigh and Fink, 2018; Mariathasan et al., 2006). LPS pre-treatment primed BMDM by initiating transcription of NLRP3-associated genes, while Nigericin activated NLRP3 inflammasome and pyroptosis. Imaging with NucView caspase-3 substrate, PI and NucBlue revealed positive staining for activated caspase 3/7 in 90% of BMDM in the apoptosis positive control (Figure 6.3.1). However, almost 100% of BMDM in the pyroptosis positive control were also positive for activated caspase 3/7 (Figure 6.3.1). PI co-staining allowed some differentiation of apoptosis and pyroptosis because almost 100% of pyroptotic BMDM were positive for PI, while around 40% of apoptotic BMDM were positive for PI (Figure 6.3.1). This imaging was not able to differentiate BMDM in the necroptosis positive control (Figure 6.3.1). Thus, I concluded that identification of caspase-3/7

positive and PI-negative BMDM was indicative of apoptosis, while identification of PI-positive alone, caspase 3/7-positive alone or PI-positive and caspase 3/7-positive BMDM could not reliably differentiate between apoptosis, pyroptosis and necroptosis.

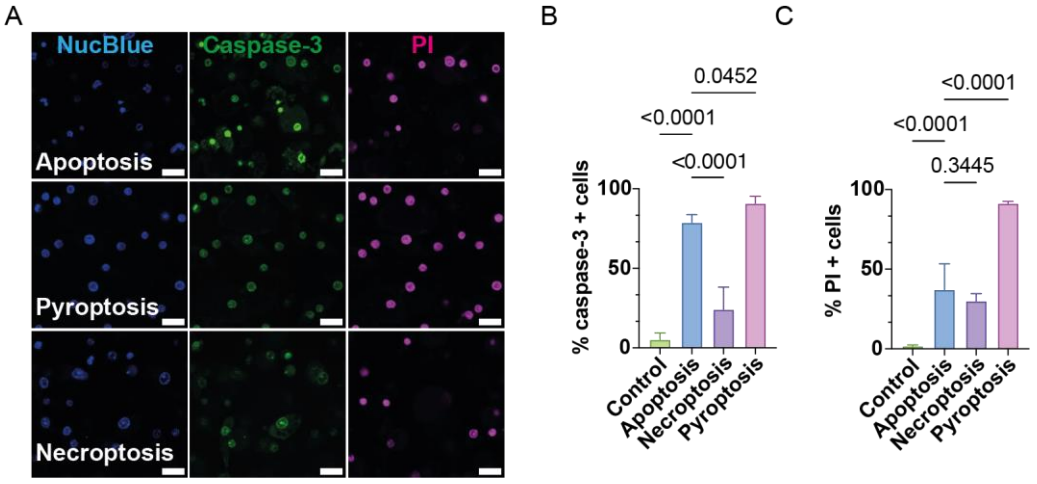

Figure 6.3.1. Caspase-3/7 and PI co-staining in BMDM can identify early apoptotic cells by imaging

(A) Tac-WT BMDM were treated with chemical inducers of apoptosis, pyroptosis and necroptosis and imaged with NucBlue, caspase-3 and PI probes. Scale bars = 20 μm. (B and C) Bar charts show the mean ± SEM from three independent biological replicates. (B) Quantification of the number of caspase-3 positive cells/total cell population (%) (C) Quantification of the number of PI positive cells/total cell population (%). P-values by One-Way ANOVA.

The finding that only 40% of BMDM showed positive PI staining in the necroptosis control (Figure 6.3.1) indicated that cells had not reached the stage of necroptosis where plasma membrane integrity is compromised. However, the necroptosis pathway could still be active at an earlier stage in these cells. To explore this, Tac-WT BMDM were induced for apoptosis, necroptosis and pyroptosis as before and cell lysates were collected for Western blot. The molecular hallmark of necroptosis is phosphorylation of the proteins RIP-3 and MLKL at S345 and T231/S232 sites, respectively. Western blot analysis confirmed that pRIP3 and pMLKL were only present in lysates from BMDM in the necroptosis positive control but not in the apoptosis or pyroptosis positive controls (Figure 6.3.2).

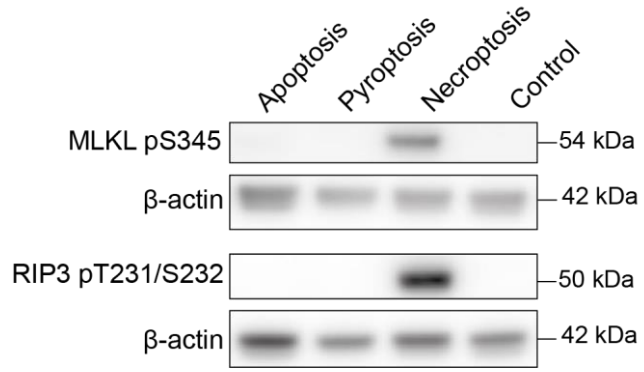

Figure 6.3.2. Detection of phosphorylated MLKL and RIP-3 in BMDM induced by necroptosis

Tac-WT BMDM were treated with positive controls for apoptosis, pyroptosis and necroptosis. Western blot for pMLKL, β-actin, pRIP3 and β-actin.

In addition, Western blot analysis of BMDM in the pyroptosis positive control showed cleavage of Gasdermin-D (GSDMD) and IL-1β, hallmarks of pyroptosis (Figure 6.3.3). Western blot analysis of BMDM in the apoptosis positive control showed cleavage of PARP and caspase-3, molecular hallmarks of apoptosis (Figure 6.3.4). I noted that there was a small amount of cleaved PARP in the pyroptosis control and a small amount of cleaved IL-1β in the apoptosis positive control, likely indicating a small amount of these other cell death modes occurring within these controls.

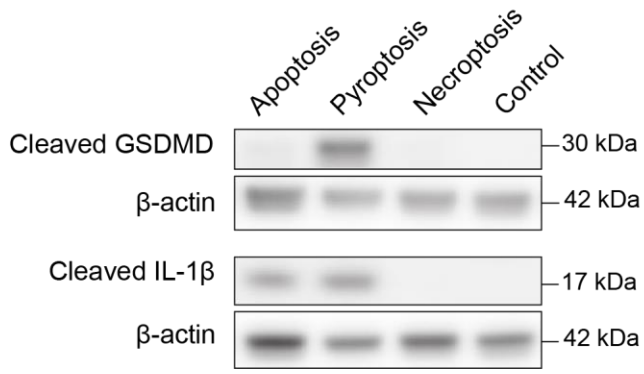

Figure 6.3.3. Detection of cleaved Gasdermin D and IL-1β in BMDM induced by pyroptosis.

Tac-WT BMDM were treated with positive controls for apoptosis, pyroptosis and necroptosis. Western blot for cleaved Gasdermin D (GSDMD), β-actin, cleaved Il-1β and β-actin.

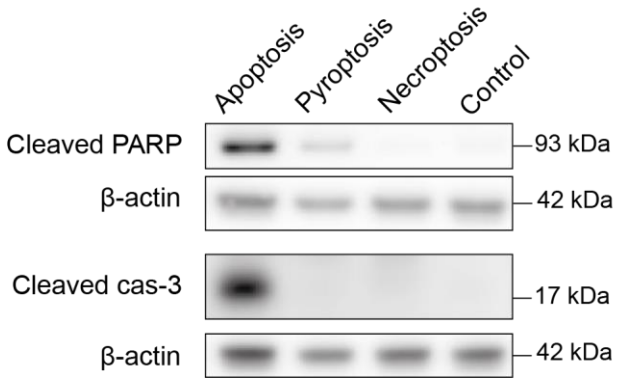

Figure 6.3.4. Detection of cleaved PARP and caspase-3 in BMDM induced by apoptosis.

Tac-WT BMDM were treated with positive controls for apoptosis, pyroptosis and necroptosis. Western blot for cleaved PARP, β-actin, cleaved caspase-3 and β-actin.

In summary, imaging with NucView caspase-3 probe, PI and NucBlue allows identification of at least a proportion of apoptotic cells. This is useful because individual cells can be monitored throughout a time course of imaging. However, imaging cannot differentiate cells in the early stages of pyroptosis or necroptosis. Western blot analysis, in contrast allows identification of apoptosis, pyroptosis and necroptosis pathways. While this is useful for quantification of overall levels of programmed cell death, single cell heterogeneity cannot be captured, and large numbers of cells are required for each experiment.

6.4 LPS-primed Tac-WT and Tac-G2019S BMDM show no differences in cell death during lysosomal damage

It is known that macrophages *in vitro* are unable to assemble the NLRP3 inflammasome, a multiprotein complex involved in inflammatory signalling and pyroptosis, unless they are primed by pre-treatment with an immune stimulus such as LPS (Bauernfeind et al., 2009; Schroder et al., 2012). *In vivo*, macrophages represent a highly heterogenous group of cells comprising a mixed population of primed and unprimed macrophages with different immune and homeostatic functions (Mosser et al., 2021). Thus, while it is biologically relevant to study unprimed macrophages experimentally, there exists important functional differences between LPS-primed and LPS-naïve macrophages that may be relevant to disease.

I next quantified cell death in LPS-primed Tac-WT and Tac-G2019S BMDM during lysosomal membrane damage in the presence or absence of the LRRK2 kinase inhibitor MLi-2. For these experiments, I utilised NucView caspase-3/7 substrate, PI and NucBlue probes to quantify the total percentage of dead cells (PI positive cells / NucBlue cells) and the total percentage of apoptotic cells (Cas 3/7-positive + PI-negative cells / NucBlue cells) at each timepoint. Surprisingly, LPS-primed Tac-G2019S and Tac-WT BMDM showed no differences in overall levels of cell death over 135 min of imaging (Figure 6.4.1). In addition, overall levels of cell death were not altered by inhibition of LRRK2 kinase activity with the inhibitor MLi-2 in Tac-WT or Tac-G2019S BMDM (Figure 6.4.1). The percentage of apoptotic cells showed a quantitative but statistically insignificant increase in Tac-G2019S BMDM after 45 min of lysosomal damage (Figure 6.4.1). Interestingly, this effect was lost when cells were treated with MLi-2 due to an increase in caspase 3/7 positive/PI-negative staining in Tac-WT BMDM in this condition (Figure 6.4.1).

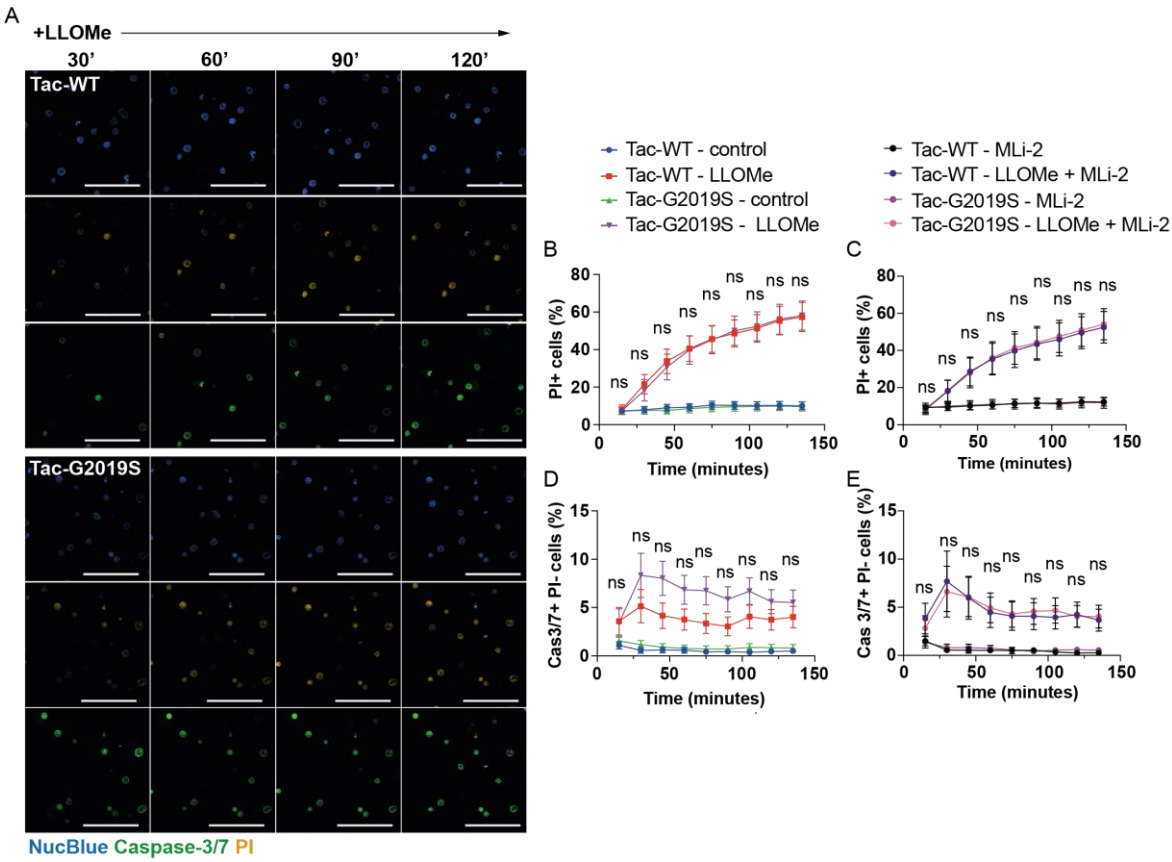

Figure 6.4.1. LPS-primed Tac-WT and Tac-G2019S BMDM show similar levels of cell death after lysosomal damage

(A) Snapshots of LPS-primed BMDM treated with LLOMe at 30, 60, 90 and 120 min. Nuclear staining (blue), PI nuclear staining (orange) and caspase-3 staining (green). Scale bars = 50μm. (B to E) Connecting line graphs showing the mean ± SEM percentage of dead cells at each timepoint. P-values by Two-Way ANOVA with Bonferroni's multiple comparisons test. Data is from 3 independent biological replicates.

6.5 G2019S BMDM show increases caspase-3 cleavage and PARP cleavage after 2 h lysosomal damage

I next investigated whether the mode of cell death in both LPS-naïve and LPS-primed BMDM was altered after lysosomal damage by Western blot analysis. These experiments required a careful balance of enough cell death induction to be able to detect protein cleavage or phosphorylation, with enough cell preservation to prevent lysis or detachment of the cells during LLOMe treatment. I initially collected cell lysates after 1 h treatment with LLOMe ± LPS but found very little detection of cell death proteins overall and no differences between Tac-WT and Tac-G2019S BMDM (Figure 6.5.1).

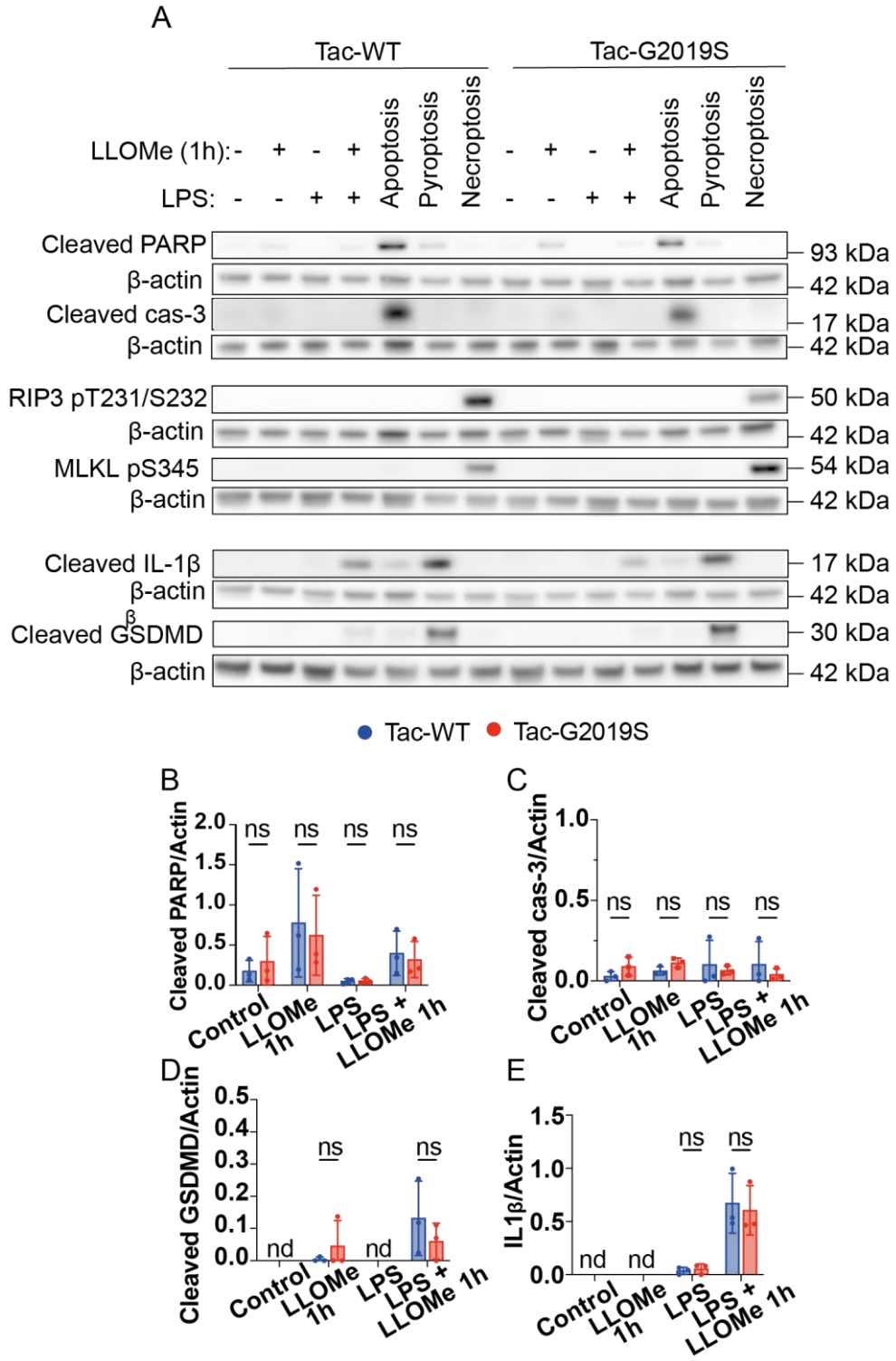

Figure 6.5.1. Detection of cell death markers is limited at 1 h LLOMe treatment in Tac-WT and Tac-G2019S BMDM

(A) Western blot analysis of cleaved PARP, cleaved caspase-3 (cas-3), RIP3 pT231/S232, MLKL pS346, cleaved IL-1β, cleaved Gasdermin D (GSDMD) and β-actin in Tac-WT and Tac-G2019S BMDM in untreated, LPS, LLOMe, and LLOMe + LPS conditions. (B to E) Cleaved PARP, cleaved cas-3, cleaved GSDMD and

cleaved IL-1β band intensities were quantified by densitometry and normalised to β-actin. Data are mean ± SD from 3 independent experiments. Two-way ANOVA followed by Tukey's multiple comparisons test.

Western blots analysis was also performed at 2 h LLOMe treatment ± LPS to be able to detect higher levels of cell death proteins. Apoptosis, as indicated by the presence of cleaved PARP and cleaved caspase-3, was observed in LPS-naïve and LPS-primed Tac-WT and Tac-G2019S BMDM after lysosomal damage (Figure 6.5.2). LPS-naïve BMDM showed higher levels of apoptosis than LPS-primed BMDM (Figure 6.5.2). In LPS-naïve cells, LRRK2-G2019S was associated with significantly higher levels of cleaved PARP and cleaved caspase-3 (Figure 6.5.2) after lysosomal damage, in keeping with increased apoptosis in these cells. While this trend for increased cleaved PARP and cleaved caspase-3 was present in LPS-primed Tac-G2019S BMDM treated with LLOMe, it did not reach statistical significance (Figure 6.5.2).

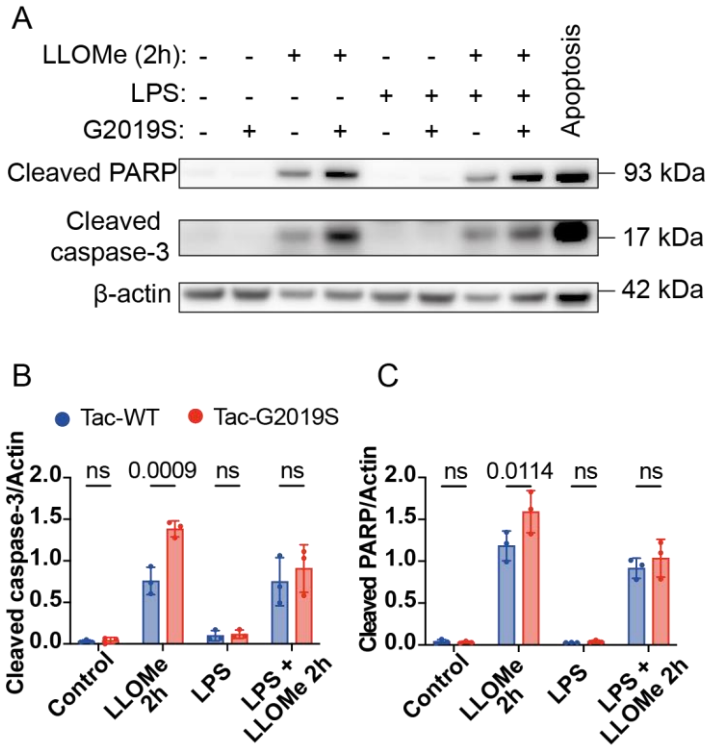

Figure 6.5.2. Apoptosis is increased in LPS-naïve Tac-G2019S BMDM after lysosomal membrane damage

(A) Western blot analysis of cleaved PARP, cleaved caspase-3 and β-actin in Tac-WT and Tac-G2019S BMDM in untreated, LLOMe, LPS and LLOMe + LPS conditions. (B and C) Cleaved caspase-3 and cleaved PARP band intensities were

quantified by densitometry and normalised to β-actin. Data are mean ± SD from 3 independent experiments. Two-way ANOVA followed by Tukey's multiple comparisons test.

Pyroptosis, as indicated by the presence of cleaved IL-1β and cleaved GSDMD was detected in LPS-primed Tac-WT and Tac-G2019S BMDM after lysosomal damage. As expected, LPS-naïve Tac-WT and Tac-G2019S BMDM did not show any evidence of pyroptosis. The levels of cleaved IL-1β and cleaved GSDMD did not differ between LPS-primed Tac-WT and Tac-G2019S BMDM, indicating that there were no differences in the level of pyroptosis induced by lysosomal damage.

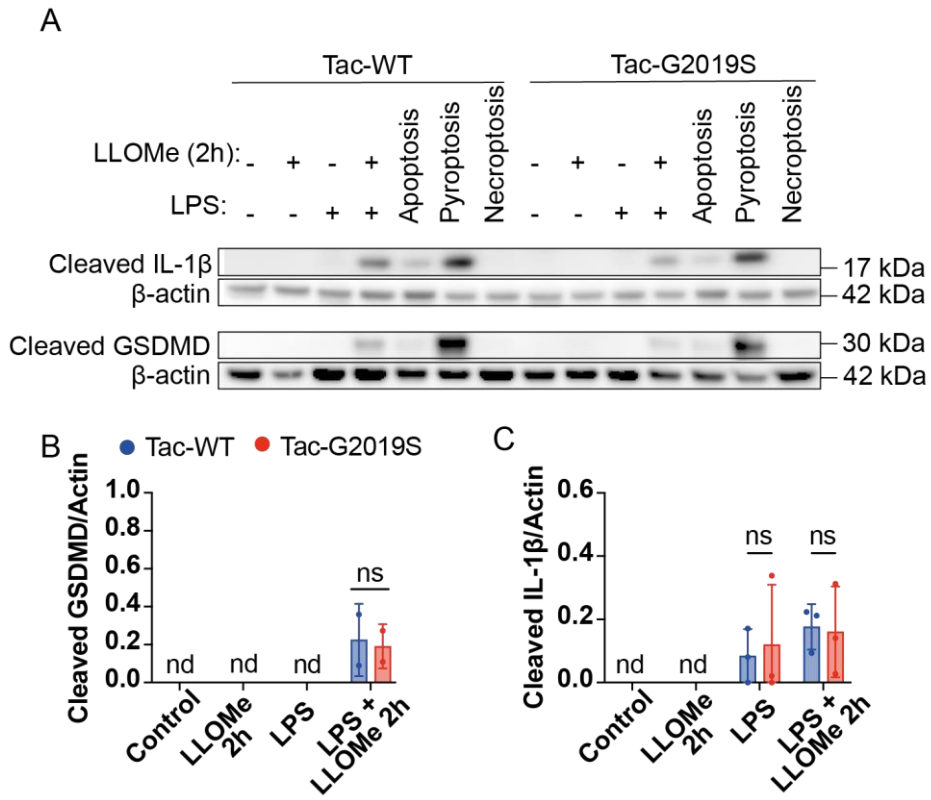

Figure 6.5.3. Pyroptosis is induced in Tac-WT and Tac-G2019S LPS-primed BMDM after lysosomal membrane damage

(A) Western blot analysis of cleaved IL-1β, cleaved Gasdermin D (GSDMD) and β-actin in Tac-WT and Tac-G2019S BMDM in untreated, LLOMe, LPS and LLOMe + LPS conditions. (B and C) Cleaved IL-1β and cleaved GSDMD band intensities were quantified by densitometry and normalised to β-actin. Data are mean ± SD from (B) 2 independent experiments and (C) 3 independent experiments. Two-way ANOVA followed by Tukey's multiple comparisons test.

Finally, necroptosis, as indicated by the presence of phosphorylated RIP-3 and phosphorylated MLKL, was not detected in LPS-naïve or LPS-primed Tac-WT or Tac-G2019S BMDM after lysosomal damage. As such, necroptosis was not considered to be a relevant mode of cell death after lysosomal damage in macrophages.

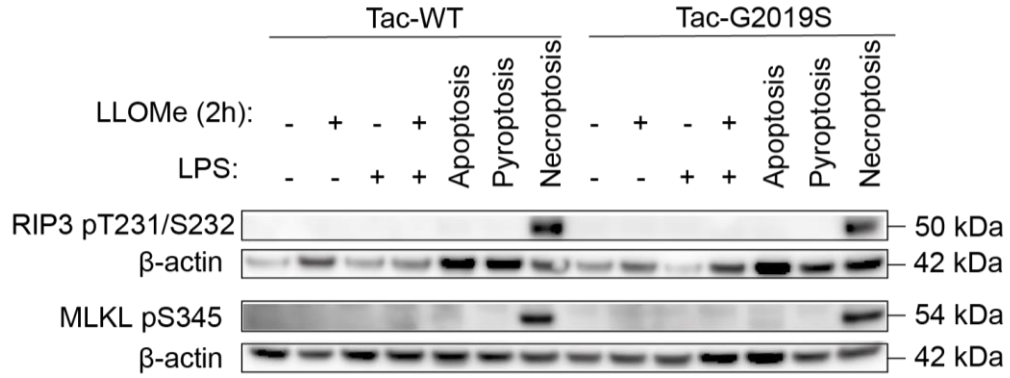

Figure 6.5.4. Necroptosis is not detected in BMDM after lysosomal damage.

Western blot analysis of RIP3 pT231/S232, MLKL pS345 and β-actin in Tac-WT and Tac-G2019S BMDM in untreated, LLOMe, LPS and LLOMe + LPS conditions. One representative Western blot is shown from three independent experiments.

6.5.1 Lysosomal damage-induced PARP and caspase-3 cleavage is MLi-2-independent

I previously found that overall levels of cell death after lysosomal damage was independent of LRRK2 kinase activity in Tac-G2019S BMDM (see Figure 6.1.2). I next investigated whether LRRK2 kinase inhibition could change the relative contribution of apoptosis to overall cell death in Tac-WT and Tac-G2019S BMDM by repeating the Western blots for cleaved PARP and cleaved caspase-3 after treatment with MLi-2. I detected cleaved PARP and cleaved caspase-3 in both Tac-WT and Tac-G2019S BMDM after LLOMe as previously, with higher levels in Tac-G2019S BMDM (Figure 6.5.5). MLi-2 treatment did not reduce the level of cleaved PARP or cleaved caspase-3 in Tac-WT and Tac-G2019S BMDM, indicating that this effect of LRRK2-G2019S is LRRK2 kinase activity-independent (Figure 6.5.5).

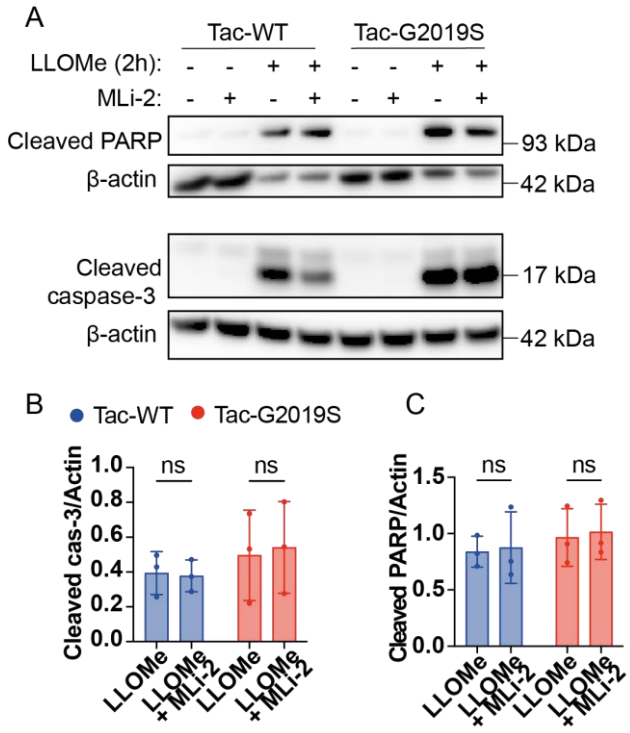

Figure 6.5.5. Lysosomal damage induced cleavage of PARP and caspase-3 is MLi-2 independent

(A) Western blot analysis of cleaved PARP, cleaved caspase-3 and β-actin in Tac-WT and Tac-G2019S BMDM in untreated, MLi-2, LLOMe, and LLOMe + MLi-2 conditions. (B and C) Cleaved caspase-3 and cleaved PARP band intensities were quantified by densitometry and normalised to β-actin. Data are mean ± SD from 3 independent experiments. Two-way ANOVA followed by Tukey's multiple comparisons test.

Additionally, there were no differences in the level of cleaved PARP and cleaved caspase-3 between LPS-naïve and LPS-primed NJ-WT and LRRK2 kinase dead NJ-D1994A BMDM, confirming that apoptosis was independent of LRRK2 kinase activity in BMDM after lysosomal damage (Figure 6.5.6).

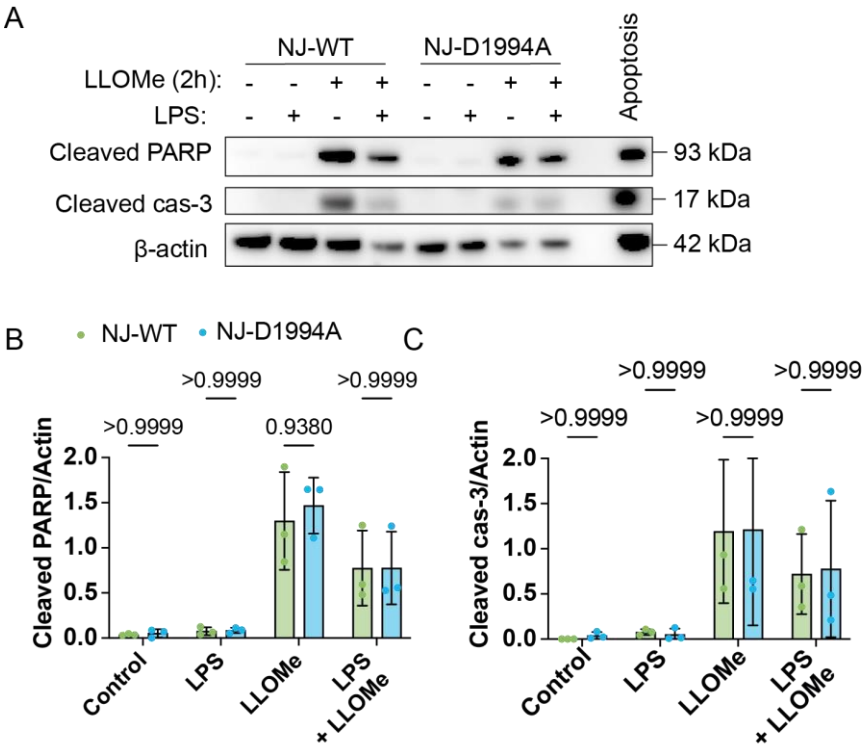

Figure 6.5.6. LRRK2 kinase dead BMDM show no differences in cleaved PARP or cleaved caspase-3 after lysosomal membrane damage.

(A) Western blot analysis of cleaved PARP, cleaved caspase-3 and β-actin in NJ-WT and NJ-D1994A BMDM in untreated, LPS, LLOMe, and LLOMe + LPS conditions. (B and C) Cleaved caspase-3 and cleaved PARP band intensities were quantified by densitometry and normalised to β-actin. Data are mean ± SD from 3 independent experiments. Two-way ANOVA followed by Tukey's multiple comparisons test.

6.5.2 Apoptosis markers do not differ in LRRK2 KO BMDM after lysosomal damage

Given that 6J-LRRK2KO BMDM showed significantly less cell death during lysosomal damage (see Figure 6.1.1), I hypothesised that a kinase activity-independent function of LRRK2 was required for apoptosis in BMDM. To test this, LPS-naïve and LPS-primed 6J-WT and 6J-LRRK2KO BMDM were treated with LLOMe for 2h and lysates were collected for Western blot. Cleaved PARP and cleaved caspase-3 was detected in LPS-naïve 6J-WT and 6J-LRRK2KO BMDM, indicating the apoptosis was induced irrespective of LRRK2 presence in the cell (Figure 6.5.7). These cells responded differently to LLOMe when LPS-primed as

cleaved PARP and cleaved caspase-3 were greatly reduced in this condition in both 6J-WT and 6J-LRRK2KO BMDM (Figure 6.5.7).

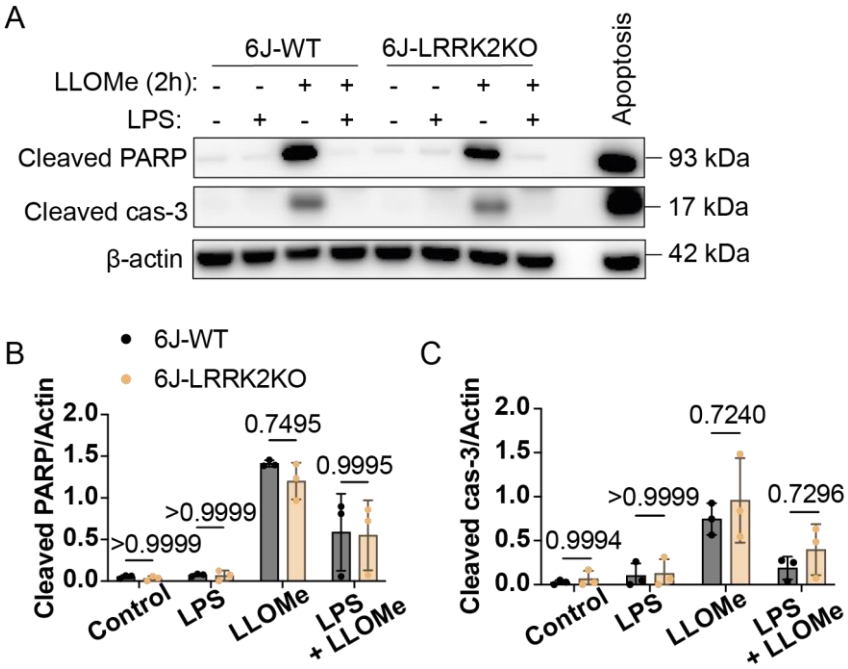

Figure 6.5.7. There are no differences in apoptosis between 6J-WT and 6J-LRRK2KO BMDM after lysosomal damage.

(A) Western blot analysis of cleaved PARP, cleaved caspase-3 and β-actin in 6J-WT and 6J-LRRK2KO BMDM in untreated, LPS, LLOMe, and LLOMe + LPS conditions. (B and C) Cleaved caspase-3 and cleaved PARP band intensities were quantified by densitometry and normalised to β-actin. Data are mean ± SD from 3 independent experiments. Two-way ANOVA followed by Tukey's multiple comparisons test.

To summarise, in this chapter I have shown that mouse and human macrophages carrying the LRRK2-G2019S mutation show increased cell death in response to lysosomal membrane damage. These effects are largely LRRK2 kinase activity-independent because they are unchanged by LRRK2 kinase inhibitor treatment and there were no differences in cell death between kinase dead BMDM and their wild-type. However, these effects are likely linked to another LRRK2 function because LRRK2KO BMDM showed significantly less cell death during lysosomal damage compared to its wild-type BMDM. I detected increased levels of the apoptotic proteins cleaved PARP and cleaved caspase-3 after lysosomal damage in Tac-G2019S BMDM, and these effects could not be reversed by LRRK2 kinase inhibition.

However, there were no differences in levels of cleaved PARP and cleaved caspase-3 between LRRK2 KO and their wild-type BMDM, indicating that the effects present in Tac-G2019S BMDM are not LRRK2-dependent. Finally, my data revealed that the activation status of the macrophage impacts the mode and amount of cell death during lysosomal membrane damage, as LPS-primed and LPS-naïve BMDM behaved differently.

Chapter 7. Discussion

7.1 Characterisation of macrophage models of LRRK2 mutations

In this thesis, I aimed to develop a LRRK2 mutant macrophage model that was physiologically relevant. As such, I avoided using LRRK2-G2019S BAC transgenic mice which overexpress LRRK2, and instead used mice which express endogenous levels of LRRK2. This is advantageous because it avoids phenotypes that are secondary to LRRK2 overexpression. I show that there are no differences in LRRK2 expression between Tac-WT and Tac-G2019S BMDM, and NJ-WT and NJ-D1994A BMDM. It is notable that the LRRK2-G2019S mice used in this project do not show any motor impairment (Crown et al., 2020) or brain pathology (Pajarillo et al., 2023). For these reasons, I decided to explore the use of human macrophages from a Parkinson's disease patient carrying the LRRK2-G2019S mutation as a more disease-relevant macrophage model. The development of the isogenic control iPSC provides a strong biological system where we can be confident that any observed effects are secondary to the mutation, as the cells are otherwise genetically identical (Pellegrino and Gutierrez, 2021).

Western blot analysis for LRRK2 revealed two bands in both BMDM and iPSDM: one around 286 kDa (in keeping with full-length LRRK2) and one additional band around 170 kDa (Figure 3.2.2 and Figure 3.3.2). These bands appeared to be specific for LRRK2 as they were absent in the LRRK2KO BMDM lysate. The LRRK2 gene has 21 reported transcripts, however this band does not correspond to any of these transcripts (Table 7.1.1). A similar sized band on a LRRK2 membrane was reported in human iPSDM derived from different donors to iPSC used in this study (Lee et al., 2020), however, in this study the additional LRRK2 band was detected at minimal levels in resting macrophages and was significantly upregulated in response to IFN-γ. The authors characterised this molecule by mass spectrometry and found a C-terminal product of LRRK2 which is cleaved at the ANK-LRR interdomain region. This is postulated to represent a natural cleavage product of LRRK2 in human

iPSDM and iPSC-derived microglia, however its function is unknown (Lee et al., 2020). There were no other LRRK2-specific bands present in the membrane.

Transcript ID	Name	bp	Protein
ENST00000298910.12	LRRK2-201	9239	2527aa
ENST00000680790.1	LRRK2-218	8875	2442aa
ENST00000343742.6	LRRK2-202	4740	1271aa
ENST00000681696.1	LRRK2-220	3828	1052aa
ENST00000636518.1	LRRK2-208	2477	454aa
ENST00000416796.5	LRRK2-203	1655	521aa
ENST00000680422.1	LRRK2-215	8598	843aa
ENST00000679360.1	LRRK2-210	7718	403aa
ENST00000430804.5	LRRK2-204	6400	207aa
ENST00000679532.1	LRRK2-211	4852	171aa
ENST00000680018.1	LRRK2-213	4523	73aa
ENST00000680453.1	LRRK2-217	4515	160aa
ENST00000680425.1	LRRK2-216	3968	43aa
ENST00000679683.1	LRRK2-212	2855	59aa
ENST00000644108.1	LRRK2-209	1151	78aa
ENST00000681136.1	LRRK2-219	4081	No protein
ENST00000680235.1	LRRK2-214	2344	No protein
ENST00000481256.1	LRRK2-207	561	No protein
ENST00000479187.5	LRRK2-206	8306	No protein
ENST00000681773.1	LRRK2-221	4718	No protein
ENST00000474202.1	LRRK2-205	556	No protein

Table 7.1.1. Transcripts of LRRK2 from Ensembl (http://www.ensembl.org, accessed 10th January 2024)

Flow cytometry revealed similar levels of macrophage surface marker expression between control and G2019S BMDM and iPSDM, except for CD169, which was expressed at higher levels in G2019S iPSDM (Figure 3.3.1). CD169 (Siglec-1) is a member of the Siglecs (sialic acid-binding Ig-like lectins) family and is expressed by macrophages, monocytes, and dendritic cells. CD169 is thought to be important for cellular interactions but is also reported to function in pathogen recognition and

immune signalling (Herzog et al., 2022). While CD169 was still positively expressed in a proportion of isogenic control iPSDM, I cannot exclude that the overall lower levels of expression led to the differences in cytokine secretion observed in G2019S iPSDM (Figure 3.4.2, Figure 3.4.3, and Figure 3.4.5). I would argue that this is unlikely to explain differences in cytokine secretion because only a select few cytokines showed significant differences in secretion between G2019S and isogenic iPSDM, and differences due to CD169 signalling would be expected to alter secretion of a larger group of cytokines. Of note, iPSDM showed overall low expression of macrophage surface markers by flow cytometry (Figure 3.3.1). This expression is similar to that of iPSDM derived from different donor iPSC and differentiated by the same protocol: despite low surface expression of macrophage markers, these iPSDM expressed macrophage-specific transcription factors and behaved as functionally relevant macrophages in terms of phagocytosis and response to immune stimuli (Bernard et al., 2020).

LAMP-1 (Figure 3.2.3) and LTR staining (Figure 3.2.5 and Figure 3.3.3) revealed that BMDM and iPSDM contain a heterogenous, compact network of lysosomes throughout the cytosol. This represents an important difference between these cells and cell lines such as RAW 264.7 cells, where the lysosomal compartment is more homogenous with overall fewer lysosomes which are larger in size (Herbst et al., 2020). It is likely that the BMDM and iPSDM lysosomal compartment is more physiological and relevant to disease than studies of the lysosomal compartment in cell lines such as RAW 264.7 cells (Bussi and Gutierrez, 2024). Previous studies have reported reduced LAMP-1/LAMP-2 expression in LRRK2-G2019S cells and increased LAMP-1/LAMP-2 expression in LRRK2KO cells (Henry et al., 2015; Yadavalli and Ferguson, 2023). In these studies, there was reduced proteolytic activity in LRRK2-G2019S cells and increased proteolytic activity in LRRK2 KO and LRRK2 kinase inhibitor-treated LRRK2 wild-type cells. In contrast, I found no differences in proteolytic activity in LRRK2-G2019S BMDM and iPSDM (Figure 3.2.6 and Figure 3.3.4). The differences between my results and these studies may be due to the different mouse models utilised, for example, Henry *et al.* studied primary astrocytes derived from transgenic mouse model with LRRK2 overexpression (Henry et al., 2015). Another important difference is that I incubated BMDM with DQ-BSA/BSA-488 probes for 4 hours prior to imaging to ensure that the probe reached

the lysosomal compartment, while Yadavalli *et al*. added probes for 1 hour before imaging, thus it could be that results reflect differences in proteolytic activity in earlier, less mature endolysosomal compartment (Yadavalli and Ferguson, 2023).

LPS treatment resulted in significantly higher levels of IL-6 secretion in G2019S iPSDM, and this increased secretion was kinase-dependent as the effects were reversed by the LRRK2 kinase inhibitor MLi-2 (Figure 3.4.2). IL-6 is a pleiotropic cytokine with both pro- and anti-inflammatory effects (Grebenciucova and VanHaerents, 2023). A recent paper using iPSC-derived monocytes reported increased levels of IL-6, alongside several other cytokines, in G2019S cells (Ahmadi Rastegar et al., 2022). Although there were trends for an increase in other cytokines such as IL-10, IP-10 and RANTES in LRRK2-G2019S iPSDM in my experiments, these did not reach statistical significance. Interestingly, IL-6 has previously been linked to PD pathogenesis by inducing iron accumulation and death of dopaminergic neurons (Li et al., 2009). Further, monocytes from PD patients show increased IL-6 secretion in response to IFN-γ stimulation compared to healthy controls (Cook et al., 2017).

Finally, IFN-γ treatment resulted in increased secretion of IP-10 in G2019S iPSDM (Figure 3.4.5). This effect was not reversed by treatment with MLi-2. IP-10 (CXCL10) is the primary cytokine secreted by macrophages in response to IFN-γ (Liu et al., 2011). IP-10 is reported to have pleiotropic effects (Liu et al., 2011) and has been linked to cognitive decline in PD (Rocha et al., 2014). IFN-γ, in addition to its effects on macrophage activation, results in a robust increase in expression of LRRK2 across multiple cell types (Cook et al., 2017; Gardet et al., 2010; Lee et al., 2020), while MLi-2 has no effect on LRRK2 expression (Fell et al., 2015; Xu et al., 2022a). It would be useful to check for differences in LRRK2 expression between isogenic control and LRRK2-G2019S iPSDM after IFN-γ to check whether these differences in IP-10 secretion are due to differences in LRRK2 expression.

7.2 Defining the substrates of LRRK2 kinase in macrophages

The finding that Rab3 pT86, Rab8A pT72, Rab10 pT73, Rab12 pS105, Rab35 pT72 and Rab43 pT80 are phosphorylated by LRRK2 kinase in macrophages after lysosomal damage strongly implicates function of these Rab GTPases in LRRK2-mediated macrophage biology (Figure 4.2.9). The Michael J Fox Foundation (MJFF) in collaboration with Abcam has developed commercially available antibodies against known LRRK2-kinase phosphorylation sites for Rab8A (pT72), Rab10 (pT73) and Rab12 (pS106) (www.michaeljfox.org/toolscatalog). However, as discussed previously, the Rab8A pT72 antibody is known to cross-react with other Rab GTPases and as such is better described as a pan-phospho Rab antibody. The antibodies against phosphorylated Rab10 and Rab12 have provided useful insight into their functions. However, there are few tools available to study Rab3 pT86, Rab35 pT72 and Rab43 pT80, and little is known about their role in lysosomal damage and repair, or their function in macrophages. Defining the role of these Rab GTPases and their phosphorylation in immune cells is an area of future research interest in the LRRK2 field. However, I cannot exclude that the Rab proteins not detected in our experiments could be expressed and modulated by LRRK2 and/or membrane damage in macrophages. Mass spectrometry may not detect all expressed proteins; therefore, I cannot reach conclusions about the Rab GTPases that have not been detected.

Except for Rab12, I found that LRRK2-G2019S kinase activity does not translate to a pronounced hyperphosphorylation effect in macrophages in both control and LLOMe-treatment conditions (Figure 4.3.2 and Figure 4.3.3). This was unexpected because LRRK2-G2019S is associated with increased kinase activity *in vitro* (Greggio et al., 2006; Jaleel et al., 2007; Myasnikov et al., 2021; West et al., 2005). LRRK2-G2019S kinase activity may behave differently *in cellulo* although increased kinase activity by LRRK2-G2019S has been reported in neutrophils (Karayel et al., 2020) and in mouse brain (Sheng et al., 2012) using LRRK2 pS1292 as a readout. Wang et al. also show increased phosphorylation of Rab10 pT73 in resting mouse primary astrocytes (Wang et al., 2021). As discussed in the introduction chapter of this thesis, each Rab GTPase shows unique cell type-dependent patterns of expression and activity, and my results suggest that mutant LRRK2 kinase activity

does not drive hyperphosphorylation of all LRRK2 kinase substrates in macrophages. This phenotype could be related to the cell type-dependent localisation of LRRK2 and its substrates. For example, phosphorylated Rab10 pT73 appears to be localised to a population of juxta-nuclear lysosomes in mouse primary astrocytes that are also positive for LRRK2 (Kluss et al., 2022a). Thus it is possible that juxta-nuclear lysosomes do not contain Rab10 in mouse primary BMDM, reflecting underlying differences in the function of Rab10 between astrocytes and macrophages.

LRRK2-G2019S has also been associated with no change or reduction in kinase activity *in vivo* (Iannotta et al., 2020). Rab10 phosphorylation did not differ between LRRK2-WT and LRRK2-G2019S mouse lung and kidney, and Rab10 phosphorylation significantly decreased with age in LRRK2-G2019S mouse brain tissue (Iannotta et al., 2020). Interestingly, LRRK2 pS1292 levels were increased in G2019S mice despite no differences or decreases in Rab10 phosphorylation.

One hypothesis for the lack of differences in Rab phosphorylation in my experiments is that there is a limit on the degree of Rab phosphorylation possible in a cell: this would be dependent on factors such as the number of LRRK2/Rab GTPase molecules, degree of phosphatase activity, and the membrane area available for binding and phosphorylation. It is possible that the amount of damage induced by LLOMe 1 mM treatment for 30 min in my experiments reached this theoretical “maximum” level of phosphorylation by LRRK2 in both wild-type and G2019S macrophages, thus any differences would only become apparent at a lower level of lysosomal damage. However, LRRK2-G2019S showed no increased phosphorylation of Rabs in control conditions.

It is notable that LRRK2-G2019S is associated with only a modest two-fold increase in kinase activity *in vitro*, and it is possible that my phosphoproteomics study was underpowered and more than 4 biological replicates would be required to detect such small differences. On the other hand, LRRK2-G2019S could be dysfunctional in cells such as macrophages: this is the first time a phosphoproteomics study has been performed in this cell type – over-activity of the kinase could eventually lead to impairment of kinase function or development of compensatory mechanisms by the cell such as increased phosphatase activity. Indeed, “exhaustion” is the name given

to a feature of lymphocytes whereby chronic activation eventually leads to exhaustion/dysfunction of the cell.

Rab12 has recently been linked to LRRK2 activation during lysosomal damage: Rab12 KO A549 and NIH-3T3 cells show reduced LRRK2 recruitment and reduced phosphorylation of Rab10 pT73 after LLOMe-induced lysosomal damage (Dhekne et al., 2023; Wang et al., 2023). However, it is important to delineate functions of total Rab12 and phosphorylated Rab12 pS105: in these studies, the phosphorylation of Rab12 pS105 did not alter its ability to activate LRRK2 during lysosomal damage: a phosphodeficient Rab12 mutant had no effect on phosphorylation of Rab10 pT73 after lysosomal damage (Wang et al., 2023). In my experiments, total levels of Rab12 did not differ between Tac-G2019S and Tac-WT BMDM in any condition; only phosphorylated Rab12 pS105 was higher in Tac-G2019S BMDM after LLOMe treatment. It is therefore possible that phosphorylated Rab12 pS105 has other roles during lysosomal damage, separate from its function in LRRK2 recruitment and activation.

While I detected reduced phosphorylations in non-Rab proteins in the LRRK2 kinase-dead macrophages (Mrpl51, Mucl1, Mapk6, Fam126b), these phosphorylations were LLOMe-independent (Figure 4.2.2 and Figure 4.2.3). It is possible that these phosphorylations are dependent on LRRK2 kinase activity in the basal state and are unaffected by LRRK2 activation/recruitment to lysosomes. Of these substrates, none showed increased phosphorylation in Tac-G2019S BMDM. Such consistent and LLOMe-independent phosphorylations could reflect genetic differences between the control and mutant mouse strains. Mutant mouse strain NJ-D1994A has the same genetic background with the control strain (NJ-WT) and has been backcrossed to the parent line two times with 98.1% homology on genetic monitoring by SNP analysis, yet it is possible that there are minor genetic differences. Large ribosomal subunit protein mL51 (Mrpl51) is a mitochondrial protein involved in mitochondrial translation, thus important for oxidative phosphorylation. Mucin-like protein 1 (Mucl1) is secreted by exocrine tissues such as salivary gland and breast cancer cells, though little else is known of its function (Miksicek et al., 2002). Mitogen-activated protein kinase 6 (Mapk6) is a kinase that is known to phosphorylate microtubule-associated protein 2 (MAP2). Mapk2 pS189, the altered site detected in our experiments, is known to

regulate the kinase activity of this protein (Schumacher et al., 2004). Hyccin-2 (Fam126b) is a phosphatidylinositol 4-kinase (PI4K) component which is important for plasma membrane integrity and growth (Baskin et al., 2016). It would be interesting to explore the effects of Hyccin-2 (Fam126b) phosphorylation in lysosomal repair given the recent identification of a PI4K-dependent repair pathway (Tan and Finkel, 2022).

There were also changes in the phosphorylation of non-Rab proteins in Tac-G2019S macrophages (Figure 4.3.2 and Figure 4.3.3). Of these, only Cathepsin G (Ctsg) and Dmxl2 phosphorylations were LLOMe-dependent. After lysosomal damage, Ctsg phosphorylation was reduced while Dmxl2 phosphorylation was increased in G2019S BMDM. Ctsg pS121 was also phosphorylated by kinase-dead macrophages after lysosomal membrane damage, indicating that it is not a LRRK2 kinase substrate. The phosphorylation of Ctsg at this site has not, to our knowledge, been previously described (site table for Cathepsin G human, phosphosite.org, accessed 16th May 2024). A working hypothesis based on these results is that lysosomal damage results in the release of Ctsg to the cytosol where it is phosphorylated by a kinase that is not LRRK2. It would be interesting to explore the effects of this phosphorylation on the function of Ctsg after lysosomal damage – phosphorylation could simply render Ctsg inactive or could affect its interactions with mediators of pathways such as cell death. Although antibodies that recognise this phosphorylation site on Ctsg have not been developed, changes in Ctsg phosphorylation during lysosomal damage could be explored using Phos-tag gels or via live cell imaging approaches following incubation with a fluorescent probe that can detect activated Ctsg. Dmxl2 (also known as Rabconnectin-3) is a large 340 kDa protein that acts as a scaffolding protein for the GAP and GEF for Rab3A, thus Dmxl2 mediates the GTP/GDP cycle of Rab3A (Kawabe et al., 2003; Nagano et al., 2002). This is intriguing, given that Rab3A is a bona fide substrate of LRRK2 kinase. Dmxl2 pS933 was not identified in the kinase dead phosphoproteomics experiment, so future experiments to determine whether this is a substrate of LRRK2 kinase in macrophages during lysosomal damage are required. Finally, I cannot exclude that the altered phosphorylations in non-Rab proteins detected in Tac-G2019S BMDM are due to genetic differences between mouse strains as discussed above. Alternatively, these may represent downstream and kinase activity-independent effects of the G2019S mutation.

Total levels of most Rab GTPases were unaltered by LLOMe treatment or LRRK2 mutations, however Rab44 levels robustly increased after LLOMe in D1994A macrophages and significantly decreased after LLOMe in G2019S macrophages (Figure 4.2.8 and Figure 4.3.7). The opposing effects of Rab44 levels in LLOMe-treated D1994A and G2019S macrophages suggests that LRRK2 kinase may have a role in regulation of its expression. Rab44 is an atypical Rab GTPase which is much larger than other Rab GTPases (molecular weight 110 kDa) containing additional domains (Yamaguchi et al., 2018). Intriguingly, Rab44 has been linked to lysosomal exocytosis, a process that may be triggered by lysosomal damage, in mast cells (Kadowaki et al., 2021). Further studies into the role of Rab44 in lysosomal damage and how LRRK2 mutations could affect expression are required.

Most studies reporting LRRK2 substrates use *in vitro* kinase assays or systems with LRRK2 overexpression. There are three previous phosphoproteomics studies of LRRK2 substrates utilising MEFs and HEK293T cells (Steger et al., 2017; Steger et al., 2016), and human PBMCs (Thirstrup et al., 2017) treated with the LRRK2 kinase inhibitor MLi-2 as a pharmacological control of LRRK2 kinase activity. These studies all identified Rab10 and Rab12 as LRRK2 substrates, while Steger *et al.* (Steger et al., 2017) additionally found Rab3B/C/D, Rab8A/B, Rab35 and Rab43 as *in cellulo* endogenous LRRK2 kinase substrates. I confirmed these substrates were phosphorylated by LRRK2 kinase in BMDM however this was only apparent in the context of lysosomal damage and there were no phosphorylation changes in kinase-dead macrophages in the control condition. While Steger *et al.* used the MLi-2-resistant LRRK2-A2016T mutant MEFs as a control for MLi-2 off-target effects (Steger et al., 2016), Thirstrup *et al*. did not have this control (Thirstrup et al., 2017). The differences between these results and my study could be down to differences in cell type or because my focus is lysosomal damage-induced LRRK2 activation, which is known to trigger dimerisation of LRRK2 and recruitment to damaged lysosomes.

An important limitation of the phosphoproteomics study is that for a phosphorylation to be included in the analysis, it had to be identified in all four biological replicates and in all genotypes. As such, if a phosphorylation was completely absent in the NJ-

D1994A macrophages, but was present in the NJ-WT macrophages, it would not be included in our dataset. In addition, the results in this chapter are specific to LRRK2 activation secondary to lysosomal damage and it may be that LRRK2 activation by other mechanisms in macrophages would result in phosphorylation of different substrates.

7.3 LRRK2-G2019S is associated with a deficit in lysosomal repair

Using phosphoproteomics and Western blot analysis in Chapter 4, I found a strong induction of LRRK2 kinase activity, as evidenced by phosphorylation of Rab GTPase substrates, in BMDM after LLOMe-induced lysosomal damage. While the Gal3, CHMP4B and LC3B pathways were clearly implicated in the LRRK2-dependent lysosomal damage response in RAW cells (Herbst et al., 2020), my data suggests that this pathway is not related to LRRK2 activation in BMDM (Figure 5.2.2, Figure 5.2.3, Figure 5.2.5, Figure 5.5.1, Figure 5.5.2, Figure 5.5.3, Figure 5.6.1, Figure 5.6.2, and Figure 5.6.3). Instead, it is possible that the reduction in CHMP4B recruitment to damaged lysosomes in Tac-G2019S BMDM (Figure 5.2.3) were due to other genetic differences between the mutant and wild-type mice. Alternatively, CHMP4B puncta formation is known to differ depending on cell subtype in dendritic cells by Gros and colleagues, and the differences in CHMP4B recruitment present in my experiments could reflect underlying differences in macrophage heterogeneity (Gros et al., 2022). Nonetheless, the LTR recovery assay in Tac-G2019S BMDM demonstrates that this mutation is associated with reduced lysosomal repair (Figure 5.4.2), possibly related to other lysosomal membrane repair pathways. It would be useful to repeat the LTR recovery assay in the presence of a LRRK2 kinase inhibitor to confirm whether these effects are LRRK2 kinase activity dependent. Further, it would be useful to repeat the LTR recovery assay in the LRRK2 kinase dead and LRRK2 KO BMDM to confirm the role of LRRK2 in lysosomal membrane repair in BMDM.

Lysosomal repair was thought to be mediated primarily by the ESCRT-mediated pathway as described previously (Papadopoulos et al., 2020; Papadopoulos and

Meyer, 2017; Radulovic et al., 2018). However, recent studies have uncovered a number of ESCRT-independent pathways of lysosomal repair including stress granules (Bussi et al., 2023), sphingomyelin (Niekamp et al., 2022), PI4K2A (Tan and Finkel, 2022) and annexins (Yim et al., 2022). It is therefore possible that LRRK2-mediated lysosomal membrane repair is implicated in one of these other pathways in BMDM and is cell type-dependent. Despite clear differences in lysosomal membrane repair in Tac-G2019S BMDM as assessed by the LTR recovery assay, CHMP4B puncta formation differed only by 1% in LRRK2-G2019S BMDM (Figure 5.2.3). Thus, it is plausible that LRRK2 is involved in repair of the population of damaged lysosomes that are CHMP4B negative, possibly by one of the other recently described lysosomal membrane repair pathways. CHMP4B formed puncta, rings, and tubules at sites of damage and while it was not possible to quantify the proportion of each of these structures in these experiments, it would be interesting to check whether this differs between Tac-WT and Tac-G2019S BMDM.

The Gal3, CHMP4B and LC3B immunofluorescence performed in BMDM revealed striking differences from previous data in RAW 264.7 cells (Herbst et al., 2020). For example, while LRRK2KO RAW cells show an increase in LC3B after lysosomal damage compared to wild-type RAW cells, no such difference was present between 6J-LRRK2KO and 6J-WT BMDM. This difference may be due to the different cell types: RAW cells are a macrophage-like cell line derived from a tumour and as such show genome alterations and altered cell and lysosomal biology; BMDM are a macrophage primary cell line and are thought to show more physiologically relevant cell and lysosomal biology. Large differences between these cell types were apparent by the immunofluorescence images: the number of Gal3 puncta found after lysosomal damage in BMDM reached > 1000 in many cells, while a mean of 4 Gal3 puncta per cell were found after lysosomal damage in LRRK2 wild-type RAW cells (Herbst et al., 2020). Such differences may be due to the underlying lysosomal biology – I previously showed that the LAMP-1 positive compartment is highly dense in BMDM (see Figure 3.2.4), while there appear to be fewer, larger lysosomes in RAW cells (Herbst et al., 2020). RAW cells and BMDM also respond differently to LLOMe-induced lysosomal damage – almost all LTR staining intensity was lost after

5 min of LLOMe treatment in BMDM (Figure 5.4.2), while 60 min of LLOMe treatment was required to see a similar effect in RAW cells (Herbst et al., 2020).

One disadvantage of using BMDM for these studies was the inherent variability associated with this cell type both within and between experiments. All experiments were performed using freshly differentiated BMDM from 6-10 weeks female mice, and it is possible that some of the inter-experimental variability was due to the use of different donor mice. However, variability was present in Gal3, CHMP4B and LC3B immunofluorescence even within a single field from one experiment with, for example, some cells showing high levels of puncta and other cells in the same well showing almost no puncta. It is unclear why this variability was present but could be due to differences in macrophage activation status or due to heterogeneity in macrophage differentiation. Previous flow cytometry characterisation of the cells (Figure 3.2.1) showed BMDM express the dendritic marker CD11c, and a previous study has shown that use of GM-CSF to differentiate haematopoietic precursor cells results in a heterogenous population of macrophages and dendritic cells (Helft et al., 2015). Further, baseline LTR staining (see Figure 3.2.5) showed that while some cells contained many strongly positive LTR+ puncta, others contained few LTR+ puncta or only weakly staining LTR puncta, indicating differences in both lysosomal content and acidity between cells. This is important because LLOMe processing is dependent on proteolytic activity (Skowyra et al., 2018) thus small differences in lysosomal activity between cells could cause this variability. It is possible that underlying differences in Gal3, CHMP4B and LC3B were masked by this heterogeneity in BMDM.

Importantly, a proportion of BMDM showed high levels of Gal3 puncta in the control condition, indicating that Gal3 puncta may not be specific for lysosomal damage in this cell type. Alongside its role in detection of lysosomal membrane damage (Aits et al., 2015), Gal3 has a functional role in the recruitment of other proteins that form part of autophagy and membrane repair pathways (Jia et al., 2020), but also has reported functions in immune signalling, exosome formation, Ras and Wnt signalling and autophagy (Johannes et al., 2018). Galectins are also secreted by cells and have extracellular functions including cell adhesion, migration, signalling, and inflammation. Thus, although Gal3 levels significantly increased in BMDM treated

with LLOMe, indicating that it was recruited to areas of lysosomal damage, it is likely that Gal3 also highlights other structures, and this effect may mask any LRRK2-dependent effects of Gal3 recruitment to lysosomes in this cell type. Herbst *et al*. found an accumulation of vesicles that are positive for Gal3 in human monocyte-derived macrophages from PD patients carrying the LRRK2-G2019S mutation compared to healthy controls in the absence of lysosomal damage. However, following LLOMe treatment there were no differences in the numbers of Gal3 positive vesicles between healthy controls and LRRK2-mutated PD patients, in keeping with my data (Herbst et al., 2020). Further, Bonet-Ponce *et al*. also report MLi-2 independent effects of Gal3 recruitment to lysosomes that are positive for overexpressed LRRK2 after lysosomal damage with LLOMe in mouse primary astrocytes (Bonet-Ponce et al., 2020). In this study, LC3 lipidation as also unchanged by MLi-2 treatment (Bonet-Ponce et al., 2020), further highlighting that these pathways are cell type-dependent.

It was technically challenging to examine the dynamics of Gal3, CHMP4B and LC3B recruitment in Tac-G2019S BMDM during this project. Instead, cells were fixed after 30 min of LLOMe treatment and as such, it cannot be ruled out that there are significant differences at earlier timepoints or differences in the dynamics of Gal3/CHMP4B/LC3B recruitment and disassociation from damaged/repaired lysosomes in Tac-G2091S BMDM. The 30-minute timepoint was chosen to allow for the detection of high numbers of damaged lysosomes but limit the amount of cell death present in the sample. My results show a significant increase in Gal3 at 30 min LLOMe treatment but not 15 min LLOMe treatment in BMDM (Figure 5.6.4). Assessment of Gal3, CHMP4B and LC3B dynamics in BMDM would be possible using lentiviral transduction systems or by nucleofection, however I was unable to optimise these experiments within the timeframe of this project.

Another possible explanation for the lack of differences in Gal3, CHMP4B and LC3B levels after lysosomal damage between NJ-D1994A and 6J-LRRK2KO BMDM and their respective wild types is that there is compensation for the lack of LRRK2 in these cells by other proteins, for example LRRK1. Indeed, these BMDM are derived from 6–10-week-old mice and as such there may be some compensation over this time. However, it is notable that there was a clear absence of Rab phosphorylation

in NJ-D1994A and 6J-LRRK2 KO BMDM after 30 min of LLOMe treatment by Western blot (see Figure 4.1.1 and Figure 4.1.2), indicating that NJ-D1994A and 6J-LRRK2 KO cells cannot compensate for LRRK2 kinase-mediated Rab phosphorylation. In addition, a recent study highlighted important sex-dependent differences in LRRK2-G2019S immune cells: male mice expressing endogenous levels of LRRK2-G2019S showed increased intestinal inflammation and aggregation of α-synuclein in gut macrophages in a chronic experimental colitis model (Fang et al., 2024), suggesting that LRRK2-mediated immune phenotypes may be stronger in male mice. As such, a limitation of this thesis is that all experiments were performed in BMDM derived from female mice and it would be useful to repeat the studies in BMDM from male mice.

7.4 LRRK2-G2019S is associated with increased, kinase-independent, cell death after lysosomal damage

An important caveat to these data is that in my cellular system, there is not yet a clear link between the deficit in lysosomal membrane repair (described in chapter 5) and the increase in cell death found in Tac-G2019S BMDM (as per chapter 6). Although the LTR recovery assay in Tac-G2019S BMDM (see Figure 5.4.2) is in keeping with a deficit in lysosomal repair, I have not shown whether this is dependent on LRRK2 kinase activity as the LTR recovery assay would need to be performed in the presence of a LRRK2 kinase inhibitor. As discussed previously, reduced CHMP4B recruitment in Tac-G2019S BMDM cannot explain the differences I see in cell death because 1) CHMP4B recruitment did not differ between LRRK2 KO and wild-type BMDM (Figure 5.6.2) while cell death was significantly different (Figure 6.1.1) and 2) MLi-2 treatment increased CHMP4B recruitment in Tac-G2019S BMDM (Figure 5.2.3) but did not change the amount of cell death (Figure 6.1.2). In addition to other lysosomal membrane repair pathways, processes activated by lysosomal damage such as lysophagy and lysosomal biogenesis could also contribute to the cell death phenotype reported here and should be further explored.

The finding that increased cell death in LRRK2-G2019S BMDM and iPSDM was not changed by treatment with MLi-2 suggests that LRRK2 G2019S may engage in other

kinase-independent functions that could be relevant to its pathogenic effects. As discussed in the introduction to this thesis, LRRK2 also contains additional protein-protein interaction domains and is hypothesised to be an important scaffolding protein within the cell, mediating a plethora of intracellular processes. It would be interesting to explore whether the scaffolding function of mutant LRRK2 is different from that of wild-type LRRK2, and whether this could interfere with cell death processes following lysosomal damage.

Although LRRK2 KO BMDM showed significantly less cell death during lysosomal damage (Figure 6.1.1), I was unable to reduce cell death in Tac-G2019S BMDM by pre-treatment with the LRRK2-specific PROTAC XL01126 (Figure 6.1.6). I showed that XL01126 pre-treatment resulted in a 40-60% reduction in LRRK2 levels (Figure 6.1.5), thus this suggests that LRRK2 needs to be degraded beyond these levels to influence cell death during lysosomal damage. Although this was not possible within the timeframe of my project, it would be useful to explore alternative modes to reduce LRRK2 expression in BMDM such as treatment with an antisense oligonucleotide or LRRK2 knock-down.

It was interesting to note that XL01126 treatment showed different efficiencies between Tac-WT and Tac-G2019S BMDM – the PROTAC was able to degrade LRRK2 more in the LRRK2-G2019S mutated cells (Figure 6.1.5). It would be interesting to explore this further: it is possible that the localisation or conformation of LRRK2-G2019S makes it more amenable to proteosome-mediated degradation. This could be tested by pre-treating cells with a type 1 LRRK2 kinase inhibitor, which promotes the closed (active) conformation of LRRK2 and its association with microtubules. Alternatively, proteosome function could be altered by LRRK2-G2019S in macrophages. Proteosome disruption has previously been reported in the midbrain of PD patients, although has not been demonstrated in immune cells (McNaught et al., 2003; Bedford et al., 2008).

In this work, I developed an imaging approach to quantify apoptosis in BMDM using a probe to detect activated caspase-3/7 alongside PI and NucBlue staining. However, using positive controls for apoptosis, pyroptosis and necroptosis, I showed that activated caspase-3/7 was almost universally positive in both the apoptosis and

pyroptosis positive controls. This can be explained by examining the pyroptotic pathway in further detail (see Figure 1.13.1): during pyroptosis, NLRP3 inflammasome activation leads to the cleavage and activation of the inflammatory Cas-1. Cas-1, alongside triggering pyroptosis through GSDMD cleavage, is also able to activate caspase 3/7. Thus, there is crosstalk between apoptotic and pyroptotic pathways. This was also clear from the Western blots performed in the positive controls for cell death: cleaved PARP was detected in the lysate from the pyroptosis control, and cleaved IL-1β was detected in the lysate from the apoptosis control (Figure 6.3.3 and Figure 6.3.4).

I showed that using PI allowed some discrimination between apoptosis and pyroptosis by imaging, as PI-positive cells were universally detected in pyroptosis, while a much smaller percentage of apoptotic cells were PI-positive. Using this imaging approach in LPS-primed BMDM, there was a trend for increased caspase-3/7+/PI- staining, indicative of apoptosis, in Tac-G2019S BMDM (Figure 6.4.1). This trend was present only at the earlier time points of lysosomal damage, presumably because apoptotic cells begin to show PI+ staining at the end-stages of apoptosis.

Western blot analysis after 2 h of LLOMe treatment revealed an increase in cleaved caspase-3 and cleaved PARP in LPS-naïve Tac-G2019S BMDM (Figure 6.5.2), indicating that there is more apoptosis in these cells. It would be useful to image LPS-naïve BMDM with the NucView caspase-3 substrate, PI and NucBlue to confirm this in live cells, however I did not include this condition in these imaging experiments as they were all performed in LPS-primed BMDM. Further, to confirm that the increase in cell death in Tac-G2019S BMDM is indeed due to increased apoptosis, imaging for total levels of cell death in the presence of LLOMe + an apoptosis inhibitor would be useful.

“Lysosomal cell death” is a term encompassing multiple forms of regulated and unregulated cell death. In this chapter I focussed on apoptosis, pyroptosis and necroptosis because these forms of cell death are well characterised and assays to identify these pathways by Western blot analysis are well established. However, I cannot exclude that there are other forms of cell death present during lysosomal damage, such as PANoptosis, parthanatos, ferroptosis and autophagic cell death, to

name a few (Aits and Jaattela, 2013; Boya and Kroemer, 2008; Samir et al., 2020; Tang et al., 2019; Wang et al., 2018a). Further, necrosis is a type of unregulated cell death that is also reported to occur in response to extensive lysosomal damage. As necrosis is unregulated it is unable to be characterised molecularly and is instead marked by its morphological findings. However, there is considerable overlap in the morphology of necrosis and other forms of programmed cell death such as secondary necrosis of apoptosis, necroptosis and pyroptosis. As such, I cannot be sure that the increase in cell death in Tac-G2019S BMDM is not simply due to an increase in necrosis or due to an increase in both necrosis and apoptosis. Use of apoptosis and necroptosis inhibitors during lysosomal membrane damage would be useful to shed further light on the mechanisms of cell death that are induced.

7.5 Conclusions

In this thesis, I characterise lysosomal function and LRRK2 activity in mouse primary macrophages and human iPSDM carrying the LRRK2-G2019S mutation. Through a combination of techniques including Western blot, live and fixed cell imaging and phosphoproteomics, I show that lysosomal function and LRRK2 activity are unchanged between LRRK2 wild-type and LRRK2-G2019S macrophages in the resting state. Utilising phosphoproteomics in a LRRK2 kinase dead mutant mouse model, I show that Rab3A, Rab8A, Rab10, Rab12, Rab35 and Rab43 are the endogenous substrates of LRRK2 kinase in macrophages after induction of lysosomal damage. This approach also revealed that only Rab12 and Rab35 show differences in phosphorylation after lysosomal damage in LRRK2-G2019S macrophages.

Using immunofluorescence and live cell imaging, I show that LRRK2-G2019S macrophages have a deficit in lysosomal membrane repair, however this does not appear to be related to the ESCRT or lysophagy pathways. Finally, I show that LRRK2-G2019S macrophages show increased cell death and increased markers of apoptosis after lysosomal damage, and that these effects are LRRK2 kinase-independent.

7.6 Future Directions

In future, there are several questions that arise from the data in this thesis including:

1. What is the function of phosphorylated Rab12 and Rab35 in macrophages during lysosomal damage?
2. What kinase-independent effects of LRRK2-G2019S are activated in macrophages during cell death and apoptosis?
3. Is LRRK2 kinase activity involved in the activation of ESCRT-independent pathways of lysosomal membrane repair?

Although there is some understanding of the effects of phosphorylation on Rab8A and Rab10 function, our understanding of the effects of phosphorylation on Rab12 and Rab35 remain limited. Given that these were the only Rabs with differences in phosphorylation in LRRK2-G2019S macrophages during lysosomal damage, it would be helpful to determine their respective roles. This could be explored by expressing phospho-mutant versions of these Rab GTPases in macrophages.

Many questions remain regarding the LRRK2 kinase-independent effects of LRRK2-G2019S in macrophages. Although many studies use over-expression of tagged LRRK2 to study its localisation, we cannot be sure that such data does not simply reflect non-physiological effects of overexpression. A key priority in LRRK2 research lies in the development of a sensitive and specific antibody that can detect endogenous LRRK2, as this would allow identification of differences in subcellular localisation of mutant LRRK2 in macrophages. It would also be helpful to use different approaches to reduce levels of mutant LRRK2 in cells such as with antisense oligonucleotides or LRRK2 knock-down.

Finally, it would be useful to explore LRRK2 activity in other ESCRT-independent pathways of lysosomal membrane repair in macrophages including stress granules, PI4K2a/ORP family, sphingomyelin and annexins. The LRRK2 kinase dead and LRRK2KO BMDM remain a useful tool for the assessment of LRRK2 kinase-dependent effects in macrophages, along with the use of LRRK2 kinase inhibitors. The development of a LRRK2 KO iPSDM model would also be helpful for identification of LRRK2 kinase dependent pathways in human macrophages.

References

Aasly, J.O., Vilarino-Guell, C., Dachsel, J.C., Webber, P.J., West, A.B., Haugarvoll, K., Johansen, K.K., Toft, M., Nutt, J.G., Payami, H.*, et al.* (2010). Novel pathogenic LRRK2 p.Asn1437His substitution in familial Parkinson's disease. Mov Disord *25*, 2156-2163.

Abdi, G., Jain, M., Patil, N., Upadhyay, B., Vyas, N., Dwivedi, M., and Kaushal, R.S. (2024). 14-3-3 proteins-a moonlight protein complex with therapeutic potential in neurological disorder: in-depth review with Alzheimer's disease. Front Mol Biosci *11*, 1286536.

Abe, T., Kuwahara, T., Suenaga, S., Sakurai, M., Takatori, S., and Iwatsubo, T. (2024). Lysosomal stress drives the release of pathogenic alpha-synuclein from macrophage lineage cells via the LRRK2-Rab10 pathway. iScience *27*, 108893.

Agalliu, I., San Luciano, M., Mirelman, A., Giladi, N., Waro, B., Aasly, J., Inzelberg, R., Hassin-Baer, S., Friedman, E., Ruiz-Martinez, J.*, et al.* (2015). Higher frequency of certain cancers in LRRK2 G2019S mutation carriers with Parkinson disease: a pooled analysis. JAMA Neurol *72*, 58-65.

Agin-Liebes, J., Hickman, R.A., Vonsattel, J.P., Faust, P.L., Flowers, X., Utkina Sosunova, I., Ntiri, J., Mayeux, R., Surface, M., Marder, K.*, et al.* (2023). Patterns of TDP-43 Deposition in Brains with LRRK2 G2019S Mutations. Mov Disord *38*, 1541-1545.

Ahamadi, M., Mehrotra, N., Hanan, N., Lai Yee, K., Gheyas, F., Anton, J., Bani, M., Boroojerdi, B., Smit, H., Weidemann, J.*, et al.* (2021). A Disease Progression Model to Quantify the Nonmotor Symptoms of Parkinson's Disease in Participants With Leucine-Rich Repeat Kinase 2 Mutation. Clin Pharmacol Ther *110*, 508-518.

Ahmadi Rastegar, D., Ho, N., Halliday, G.M., and Dzamko, N. (2019). Parkinson's progression prediction using machine learning and serum cytokines. NPJ Parkinsons Dis *5*, 14.

Ahmadi Rastegar, D., Hughes, L.P., Perera, G., Keshiya, S., Zhong, S., Gao, J., Halliday, G.M., Schule, B., and Dzamko, N. (2022). Effect of LRRK2 protein and activity on stimulated cytokines in human monocytes and macrophages. NPJ Parkinsons Dis *8*, 34.

Aits, S., and Jaattela, M. (2013). Lysosomal cell death at a glance. J Cell Sci *126*, 1905-1912.

Aits, S., Kricker, J., Liu, B., Ellegaard, A.M., Hamalisto, S., Tvingsholm, S., Corcelle-Termeau, E., Hogh, S., Farkas, T., Holm Jonassen, A.*, et al.* (2015). Sensitive detection of lysosomal membrane permeabilization by lysosomal galectin puncta assay. Autophagy *11*, 1408-1424.

Alberts, B. (2022). Molecular biology of the cell, Seventh edition. edn (New York: W. W. Norton & Company).

Allegra, R., Tunesi, S., Cilia, R., Pezzoli, G., and Goldwurm, S. (2014). LRRK2-G2019S mutation is not associated with an increased cancer risk: a kin-cohort study. Mov Disord *29*, 1325-1326.

Ashida, H., Ogawa, M., Mimuro, H., Kobayashi, T., Sanada, T., and Sasakawa, C. (2011). Shigella are versatile mucosal pathogens that circumvent the host innate immune system. Curr Opin Immunol *23*, 448-455.

Atashrazm, F., Hammond, D., Perera, G., Bolliger, M.F., Matar, E., Halliday, G.M., Schule, B., Lewis, S.J.G., Nichols, R.J., and Dzamko, N. (2019). LRRK2-mediated Rab10 phosphorylation in immune cells from Parkinson's disease patients. Mov Disord *34*, 406-415.

Bandyopadhyay, D., Cyphersmith, A., Zapata, J.A., Kim, Y.J., and Payne, C.K. (2014). Lysosome transport as a function of lysosome diameter. PLoS ONE *9*, e86847.

Baptista, M.A., Dave, K.D., Frasier, M.A., Sherer, T.B., Greeley, M., Beck, M.J., Varsho, J.S., Parker, G.A., Moore, C., Churchill, M.J.*, et al.* (2013). Loss of leucine-rich repeat kinase 2 (LRRK2) in rats leads to progressive abnormal phenotypes in peripheral organs. PLoS ONE *8*, e80705.

Baptista, M.A.S., Merchant, K., Barrett, T., Bhargava, S., Bryce, D.K., Ellis, J.M., Estrada, A.A., Fell, M.J., Fiske, B.K., Fuji, R.N.*, et al.* (2020). LRRK2 inhibitors induce reversible changes in nonhuman primate lungs without measurable pulmonary deficits. Sci Transl Med *12*.

Barrett, J.C., Hansoul, S., Nicolae, D.L., Cho, J.H., Duerr, R.H., Rioux, J.D., Brant, S.R., Silverberg, M.S., Taylor, K.D., Barmada, M.M.*, et al.* (2008). Genome-wide association defines more than 30 distinct susceptibility loci for Crohn's disease. Nat Genet *40*, 955-962.

Baskin, J.M., Wu, X., Christiano, R., Oh, M.S., Schauder, C.M., Gazzerro, E., Messa, M., Baldassari, S., Assereto, S., Biancheri, R.*, et al.* (2016). The leukodystrophy protein FAM126A (hyccin) regulates PtdIns(4)P synthesis at the plasma membrane. Nat Cell Biol *18*, 132-138.

Bauernfeind, F.G., Horvath, G., Stutz, A., Alnemri, E.S., MacDonald, K., Speert, D., Fernandes-Alnemri, T., Wu, J., Monks, B.G., Fitzgerald, K.A.*, et al.* (2009). Cutting edge: NF-kappaB activating pattern recognition and cytokine receptors license NLRP3 inflammasome activation by regulating NLRP3 expression. J Immunol *183*, 787-791.

Berger, Z., Smith, K.A., and Lavoie, M.J. (2010). Membrane localization of LRRK2 is associated with increased formation of the highly active LRRK2 dimer and changes in its phosphorylation. Biochemistry *49*, 5511-5523.

Bernard, E.M., Fearns, A., Bussi, C., Santucci, P., Peddie, C.J., Lai, R.J., Collinson, L.M., and Gutierrez, M.G. (2020). M. tuberculosis infection of human iPSC-derived macrophages reveals complex membrane dynamics during xenophagy evasion. J Cell Sci *134*.

Bertheloot, D., Latz, E., and Franklin, B.S. (2021). Necroptosis, pyroptosis and apoptosis: an intricate game of cell death. Cell Mol Immunol *18*, 1106-1121.

Bi, M., Du, X., Jiao, Q., Chen, X., and Jiang, H. (2021). Expanding the role of proteasome homeostasis in Parkinson's disease: beyond protein breakdown. Cell Death Dis *12*, 154.

Biskup, S., Moore, D.J., Celsi, F., Higashi, S., West, A.B., Andrabi, S.A., Kurkinen, K., Yu, S.W., Savitt, J.M., Waldvogel, H.J.*, et al.* (2006). Localization of LRRK2 to membranous and vesicular structures in mammalian brain. Ann Neurol *60*, 557-569.

Biskup, S., Moore, D.J., Rea, A., Lorenz-Deperieux, B., Coombes, C.E., Dawson, V.L., Dawson, T.M., and West, A.B. (2007). Dynamic and redundant regulation of LRRK2 and LRRK1 expression. BMC Neurosci *8*, 102.

Blauwendraat, C., Nalls, M.A., and Singleton, A.B. (2020). The genetic architecture of Parkinson's disease. Lancet Neurol *19*, 170-178.

Bliederhaeuser, C., Zondler, L., Grozdanov, V., Ruf, W.P., Brenner, D., Melrose, H.L., Bauer, P., Ludolph, A.C., Gillardon, F., Kassubek, J.*, et al.* (2016). LRRK2 contributes to monocyte dysregulation in Parkinson's disease. Acta Neuropathol Commun *4*, 123.

Bonet-Ponce, L., Beilina, A., Williamson, C.D., Lindberg, E., Kluss, J.H., Saez-Atienzar, S., Landeck, N., Kumaran, R., Mamais, A., Bleck, C.K.E.*, et al.* (2020). LRRK2 mediates tubulation and vesicle sorting from lysosomes. Sci Adv *6*.

Bouhouche, A., Tibar, H., Ben El Haj, R., El Bayad, K., Razine, R., Tazrout, S., Skalli, A., Bouslam, N., Elouardi, L., Benomar, A.*, et al.* (2017). LRRK2 G2019S Mutation: Prevalence and Clinical Features in Moroccans with Parkinson's Disease. Parkinsons Dis *2017*, 2412486.

Boya, P. (2012). Lysosomal function and dysfunction: mechanism and disease. Antioxid Redox Signal *17*, 766-774.

Boya, P., and Kroemer, G. (2008). Lysosomal membrane permeabilization in cell death. Oncogene *27*, 6434-6451.

Braak, H., Ghebremedhin, E., Rub, U., Bratzke, H., and Del Tredici, K. (2004). Stages in the development of Parkinson's disease-related pathology. Cell Tissue Res *318*, 121-134.

Bras, J.M., Guerreiro, R.J., Ribeiro, M.H., Januario, C., Morgadinho, A., Oliveira, C.R., Cunha, L., Hardy, J., and Singleton, A. (2005). G2019S dardarin substitution is a common cause of Parkinson's disease in a Portuguese cohort. Mov Disord *20*, 1653-1655.

Brodacki, B., Staszewski, J., Toczylowska, B., Kozlowska, E., Drela, N., Chalimoniuk, M., and Stepien, A. (2008). Serum interleukin (IL-2, IL-10, IL-6, IL-4), TNFalpha, and INFgamma concentrations are elevated in patients with atypical and idiopathic parkinsonism. Neurosci Lett *441*, 158-162.

Bruchard, M., Mignot, G., Derangere, V., Chalmin, F., Chevriaux, A., Vegran, F., Boireau, W., Simon, B., Ryffel, B., Connat, J.L.*, et al.* (2013). Chemotherapy-triggered cathepsin B release in myeloid-derived suppressor cells activates the Nlrp3 inflammasome and promotes tumor growth. Nat Med *19*, 57-64.

Bryant, N., Malpeli, N., Ziaee, J., Blauwendraat, C., Liu, Z., Consortium, A.P., and West, A.B. (2021). Identification of LRRK2 missense variants in the accelerating medicines partnership Parkinson's disease cohort. Hum Mol Genet *30*, 454-466.

Bussi, C., and Gutierrez, M.G. (2019). Mycobacterium tuberculosis infection of host cells in space and time. FEMS Microbiol Rev *43*, 341-361.

Bussi, C., and Gutierrez, M.G. (2024). One size does not fit all: Lysosomes exist in biochemically and functionally distinct states. PLoS Biol *22*, e3002576.

Bussi, C., Heunis, T., Pellegrino, E., Bernard, E.M., Bah, N., Dos Santos, M.S., Santucci, P., Aylan, B., Rodgers, A., Fearns, A.*, et al.* (2022). Lysosomal damage drives mitochondrial proteome remodelling and reprograms macrophage immunometabolism. Nat Commun *13*, 7338.

Bussi, C., Mangiarotti, A., Vanhille-Campos, C., Aylan, B., Pellegrino, E., Athanasiadi, N., Fearns, A., Rodgers, A., Franzmann, T.M., Saric, A.*, et al.* (2023). Stress granules plug and stabilize damaged endolysosomal membranes. Nature *623*, 1062-1069.

Cabezudo, D., Baekelandt, V., and Lobbestael, E. (2020). Multiple-Hit Hypothesis in Parkinson's Disease: LRRK2 and Inflammation. Front Neurosci *14*, 376.

Caesar, M., Zach, S., Carlson, C.B., Brockmann, K., Gasser, T., and Gillardon, F. (2013). Leucine-rich repeat kinase 2 functionally interacts with microtubules and kinase-dependently modulates cell migration. Neurobiol Dis *54*, 280-288.

Calakos, N., Schoch, S., Sudhof, T.C., and Malenka, R.C. (2004). Multiple roles for the active zone protein RIM1alpha in late stages of neurotransmitter release. Neuron *42*, 889-896.

Chakrabarty, P., Ceballos-Diaz, C., Lin, W.L., Beccard, A., Jansen-West, K., McFarland, N.R., Janus, C., Dickson, D., Das, P., and Golde, T.E. (2011). Interferon-gamma induces progressive nigrostriatal degeneration and basal ganglia calcification. Nat Neurosci *14*, 694-696.

Chauhan, S., Kumar, S., Jain, A., Ponpuak, M., Mudd, M.H., Kimura, T., Choi, S.W., Peters, R., Mandell, M., Bruun, J.A.*, et al.* (2016). TRIMs and Galectins Globally Cooperate and TRIM16 and Galectin-3 Co-direct Autophagy in Endomembrane Damage Homeostasis. Dev Cell *39*, 13-27.

Chazotte, B. (2011). Labeling lysosomes in live cells with LysoTracker. Cold Spring Harb Protoc *2011*, pdb prot5571.

Chen, J.W., Murphy, T.L., Willingham, M.C., Pastan, I., and August, J.T. (1985). Identification of two lysosomal membrane glycoproteins. J Cell Biol *101*, 85-95.

Chen, L., Zhang, S., Liu, Y., Hong, H., Wang, H., Zheng, Y., Zhou, H., Chen, J., Xian, W., He, Y.*, et al.* (2011). LRRK2 R1398H polymorphism is associated with decreased risk of Parkinson's disease in a Han Chinese population. Parkinsonism Relat Disord *17*, 291-292.

Chen, Q., Huang, X., and Li, R. (2018). lncRNA MALAT1/miR-205-5p axis regulates MPP(+)-induced cell apoptosis in MN9D cells by directly targeting LRRK2. Am J Transl Res *10*, 563-572.

Chia, R., Haddock, S., Beilina, A., Rudenko, I.N., Mamais, A., Kaganovich, A., Li, Y., Kumaran, R., Nalls, M.A., and Cookson, M.R. (2014). Phosphorylation of LRRK2 by casein kinase 1alpha regulates trans-Golgi clustering via differential interaction with ARHGEF7. Nat Commun *5*, 5827.

Chiu, C.C., Yeh, T.H., Lai, S.C., Weng, Y.H., Huang, Y.C., Cheng, Y.C., Chen, R.S., Huang, Y.Z., Hung, J., Chen, C.C.*, et al.* (2016). Increased Rab35 expression is a potential biomarker and implicated in the pathogenesis of Parkinson's disease. Oncotarget *7*, 54215-54227.

Cho, H.J., Liu, G., Jin, S.M., Parisiadou, L., Xie, C., Yu, J., Sun, L., Ma, B., Ding, J., Vancraenenbroeck, R.*, et al.* (2013). MicroRNA-205 regulates the expression of Parkinson's disease-related leucine-rich repeat kinase 2 protein. Hum Mol Genet *22*, 608-620.

Cho, H.J., Xie, C., and Cai, H. (2018). AGE-induced neuronal cell death is enhanced in G2019S LRRK2 mutation with increased RAGE expression. Transl Neurodegener *7*, 1.

Choudhury, S.M., Sarkar, R., Karki, R., and Kanneganti, T.D. (2024). A comparative study of apoptosis, pyroptosis, necroptosis, and PANoptosis components in mouse and human cells. PLoS ONE *19*, e0299577.

Chu, Y., Dodiya, H., Aebischer, P., Olanow, C.W., and Kordower, J.H. (2009). Alterations in lysosomal and proteasomal markers in Parkinson's disease: relationship to alpha-synuclein inclusions. Neurobiol Dis *35*, 385-398.

Chu, Y.P., Hung, Y.H., Chang, H.Y., and Yang, W.Y. (2017). Assays to Monitor Lysophagy. Methods Enzymol *588*, 231-244.

Cook, D.A., Kannarkat, G.T., Cintron, A.F., Butkovich, L.M., Fraser, K.B., Chang, J., Grigoryan, N., Factor, S.A., West, A.B., Boss, J.M.*, et al.* (2017). LRRK2 levels in immune cells are increased in Parkinson's disease. NPJ Parkinsons Dis *3*, 11.

Correia Guedes, L., Ferreira, J.J., Rosa, M.M., Coelho, M., Bonifati, V., and Sampaio, C. (2010). Worldwide frequency of G2019S LRRK2 mutation in Parkinson's disease: a systematic review. Parkinsonism Relat Disord *16*, 237-242.

Cox, J.V., Kansal, R., and Whitt, M.A. (2016). Rab43 regulates the sorting of a subset of membrane protein cargo through the medial Golgi. Mol Biol Cell *27*, 1834-1844.

Crabbe, J.C., Kosobud, A., Young, E.R., Tam, B.R., and McSwigan, J.D. (1985). Bidirectional selection for susceptibility to ethanol withdrawal seizures in Mus musculus. Behav Genet *15*, 521-536.

Crotty, G.F., Maciuca, R., Macklin, E.A., Wang, J., Montalban, M., Davis, S.S., Alkabsh, J.I., Bakshi, R., Chen, X., Ascherio, A.*, et al.* (2020). Association of caffeine and related analytes with resistance to Parkinson disease among LRRK2 mutation carriers: A metabolomic study. Neurology *95*, e3428-e3437.

Crown, L.M., Bartlett, M.J., Wiegand, J.L., Eby, A.J., Monroe, E.J., Gies, K., Wohlford, L., Fell, M.J., Falk, T., and Cowen, S.L. (2020). Sleep Spindles and Fragmented Sleep as Prodromal Markers in a Preclinical Model of LRRK2-G2019S Parkinson's Disease. Front Neurol *11*, 324.

Cummings, R.D., and Liu, F.T. (2009). Galectins. In Essentials of Glycobiology, A. Varki, R.D. Cummings, J.D. Esko, H.H. Freeze, P. Stanley, C.R. Bertozzi, G.W. Hart, and M.E. Etzler, eds. (Cold Spring Harbor (NY)).

Dallmann-Sauer, M., Xu, Y.Z., da Costa, A.L.F., Tao, S., Correa-Macedo, W., Manry, J., Abel, L., Alcaïs, A., Cobat, A., Fava, V.M.*, et al.*

Daniels, V., Vancraenenbroeck, R., Law, B.M., Greggio, E., Lobbestael, E., Gao, F., De Maeyer, M., Cookson, M.R., Harvey, K., Baekelandt, V.*, et al.* (2011). Insight into the mode of action of the LRRK2 Y1699C pathogenic mutant. J Neurochem *116*, 304-315.

de Araujo, M.E.G., Liebscher, G., Hess, M.W., and Huber, L.A. (2020). Lysosomal size matters. Traffic *21*, 60-75.

de Castro, M.A., Bunt, G., and Wouters, F.S. (2016). Cathepsin B launches an apoptotic exit effort upon cell death-associated disruption of lysosomes. Cell Death Discov *2*, 16012.

De Duve, C., Pressman, B.C., Gianetto, R., Wattiaux, R., and Appelmans, F. (1955). Tissue fractionation studies. 6. Intracellular distribution patterns of enzymes in rat-liver tissue. Biochem J *60*, 604-617.

de Rijk, M.C., Launer, L.J., Berger, K., Breteler, M.M., Dartigues, J.F., Baldereschi, M., Fratiglioni, L., Lobo, A., Martinez-Lage, J., Trenkwalder, C.*, et al.* (2000). Prevalence of Parkinson's disease in Europe: A collaborative study of population-based cohorts. Neurologic Diseases in the Elderly Research Group. Neurology *54*, S21-23.

Dehghan, S., Kheshtchin, N., Hassannezhad, S., and Soleimani, M. (2023). Cell death classification: A new insight based on molecular mechanisms. Exp Cell Res *433*, 113860.

Dejgaard, S.Y., Murshid, A., Erman, A., Kizilay, O., Verbich, D., Lodge, R., Dejgaard, K., Ly-Hartig, T.B., Pepperkok, R., Simpson, J.C.*, et al.* (2008). Rab18 and Rab43 have key roles in ER-Golgi trafficking. J Cell Sci *121*, 2768-2781.

den Hartigh, A.B., and Fink, S.L. (2018). Pyroptosis Induction and Detection. Curr Protoc Immunol *122*, e52.

Deng, C.Y., Lei, W.L., Xu, X.H., Ju, X.C., Liu, Y., and Luo, Z.G. (2014). JIP1 mediates anterograde transport of Rab10 cargos during neuronal polarization. J Neurosci *34*, 1710-1723.

Deng, J., Lewis, P.A., Greggio, E., Sluch, E., Beilina, A., and Cookson, M.R. (2008). Structure of the ROC domain from the Parkinson's disease-associated leucine-rich repeat kinase 2 reveals a dimeric GTPase. Proc Natl Acad Sci U S A *105*, 1499-1504.

Deng, X., Dzamko, N., Prescott, A., Davies, P., Liu, Q., Yang, Q., Lee, J.D., Patricelli, M.P., Nomanbhoy, T.K., Alessi, D.R.*, et al.* (2011). Characterization of a selective inhibitor of the Parkinson's disease kinase LRRK2. Nat Chem Biol *7*, 203-205.

Deniston, C.K., Salogiannis, J., Mathea, S., Snead, D.M., Lahiri, I., Matyszewski, M., Donosa, O., Watanabe, R., Bohning, J., Shiau, A.K.*, et al.* (2020). Structure of LRRK2 in Parkinson's disease and model for microtubule interaction. Nature *588*, 344-349.

Deyaert, E., Wauters, L., Guaitoli, G., Konijnenberg, A., Leemans, M., Terheyden, S., Petrovic, A., Gallardo, R., Nederveen-Schippers, L.M., Athanasopoulos, P.S.*, et al.* (2017). A homologue of the Parkinson's disease-associated protein LRRK2 undergoes a monomer-dimer transition during GTP turnover. Nat Commun *8*, 1008.

Dhekne, H.S., Tonelli, F., Yeshaw, W.M., Chiang, C.Y., Limouse, C., Jaimon, E., Purlyte, E., Alessi, D.R., and Pfeffer, S.R. (2023). Genome-wide screen reveals Rab12 GTPase as a critical activator of Parkinson's disease-linked LRRK2 kinase. Elife *12*.

Dhekne, H.S., Yanatori, I., Gomez, R.C., Tonelli, F., Diez, F., Schule, B., Steger, M., Alessi, D.R., and Pfeffer, S.R. (2018). A pathway for Parkinson's Disease LRRK2 kinase to block primary cilia and Sonic hedgehog signaling in the brain. Elife *7*.

Dhekne, H.S., Yanatori, I., Vides, E.G., Sobu, Y., Diez, F., Tonelli, F., and Pfeffer, S.R. (2021). LRRK2-phosphorylated Rab10 sequesters Myosin Va with RILPL2 during ciliogenesis blockade. Life Sci Alliance *4*.

Di Fonzo, A., Tassorelli, C., De Mari, M., Chien, H.F., Ferreira, J., Rohe, C.F., Riboldazzi, G., Antonini, A., Albani, G., Mauro, A.*, et al.* (2006). Comprehensive analysis of the LRRK2 gene in sixty families with Parkinson's disease. Eur J Hum Genet *14*, 322-331.

Di Maio, R., Hoffman, E.K., Rocha, E.M., Keeney, M.T., Sanders, L.H., De Miranda, B.R., Zharikov, A., Van Laar, A., Stepan, A.F., Lanz, T.A.*, et al.* (2018). LRRK2 activation in idiopathic Parkinson's disease. Sci Transl Med *10*.

Dihanich, S. (2012). MASL1: a neglected ROCO protein. Biochem Soc Trans *40*, 1090-1094.

Dikshit, N., Bist, P., Fenlon, S.N., Pulloor, N.K., Chua, C.E., Scidmore, M.A., Carlyon, J.A., Tang, B.L., Chen, S.L., and Sukumaran, B. (2015). Intracellular Uropathogenic E. coli Exploits Host Rab35 for Iron Acquisition and Survival within Urinary Bladder Cells. PLoS Pathog *11*, e1005083.

Doan, T., Lievano, F., Swanson-Mungerson, M., and Viselli, S. (2022). Lippincott : illustrated reviews : immunology, Third edition. edn (Philadelphia: Wolters Kluwer Health/Lippincott Williams & Wilkins).

Dzamko, N., Deak, M., Hentati, F., Reith, A.D., Prescott, A.R., Alessi, D.R., and Nichols, R.J. (2010). Inhibition of LRRK2 kinase activity leads to dephosphorylation of Ser(910)/Ser(935), disruption of 14-3-3 binding and altered cytoplasmic localization. Biochem J *430*, 405-413.

Dzamko, N., Gysbers, A.M., Bandopadhyay, R., Bolliger, M.F., Uchino, A., Zhao, Y., Takao, M., Wauters, S., van de Berg, W.D., Takahashi-Fujigasaki, J.*, et al.* (2017).

LRRK2 levels and phosphorylation in Parkinson's disease brain and cases with restricted Lewy bodies. Mov Disord *32*, 423-432.

Dzamko, N., Inesta-Vaquera, F., Zhang, J., Xie, C., Cai, H., Arthur, S., Tan, L., Choi, H., Gray, N., Cohen, P.*, et al.* (2012). The IkappaB kinase family phosphorylates the Parkinson's disease kinase LRRK2 at Ser935 and Ser910 during Toll-like receptor signaling. PLoS ONE *7*, e39132.

Dzamko, N., Rowe, D.B., and Halliday, G.M. (2016). Increased peripheral inflammation in asymptomatic leucine-rich repeat kinase 2 mutation carriers. Mov Disord *31*, 889-897.

Egami, Y., Fujii, M., Kawai, K., Ishikawa, Y., Fukuda, M., and Araki, N. (2015). Activation-Inactivation Cycling of Rab35 and ARF6 Is Required for Phagocytosis of Zymosan in RAW264 Macrophages. J Immunol Res *2015*, 429439.

Egami, Y., Fukuda, M., and Araki, N. (2011). Rab35 regulates phagosome formation through recruitment of ACAP2 in macrophages during FcgammaR-mediated phagocytosis. J Cell Sci *124*, 3557-3567.

Eguchi, T., Kuwahara, T., Sakurai, M., Komori, T., Fujimoto, T., Ito, G., Yoshimura, S.I., Harada, A., Fukuda, M., Koike, M.*, et al.* (2018). LRRK2 and its substrate Rab GTPases are sequentially targeted onto stressed lysosomes and maintain their homeostasis. Proc Natl Acad Sci U S A *115*, E9115-E9124.

Elferink, L.A., Anzai, K., and Scheller, R.H. (1992). rab15, a novel low molecular weight GTP-binding protein specifically expressed in rat brain. J Biol Chem *267*, 5768-5775.

Eriksson, I., Vainikka, L., Persson, H.L., and Ollinger, K. (2023). Real-Time Monitoring of Lysosomal Membrane Permeabilization Using Acridine Orange. Methods Protoc *6*.

Eriksson, I., Waster, P., and Ollinger, K. (2020). Restoration of lysosomal function after damage is accompanied by recycling of lysosomal membrane proteins. Cell Death Dis *11*, 370.

Fan, Y., Howden, A.J.M., Sarhan, A.R., Lis, P., Ito, G., Martinez, T.N., Brockmann, K., Gasser, T., Alessi, D.R., and Sammler, E.M. (2018). Interrogating Parkinson's disease LRRK2 kinase pathway activity by assessing Rab10 phosphorylation in human neutrophils. Biochem J *475*, 23-44.

Fan, Z., Pan, Y.T., Zhang, Z.Y., Yang, H., Yu, S.Y., Zheng, Y., Ma, J.H., and Wang, X.M. (2020). Systemic activation of NLRP3 inflammasome and plasma alpha-synuclein levels are correlated with motor severity and progression in Parkinson's disease. J Neuroinflammation *17*, 11.

Fang, P., Yu, L.W., Espey, H., Agirman, G., Kazmi, S.A., Li, K., Deng, Y., Lee, J., Hrncir, H., Romero-Lopez, A.*, et al.* (2024). Sex-dependent interactions between prodromal

intestinal inflammation and LRRK2 G2019S in mice promote endophenotypes of Parkinson's disease. Commun Biol *7*, 570.

Fell, M.J., Mirescu, C., Basu, K., Cheewatrakoolpong, B., DeMong, D.E., Ellis, J.M., Hyde, L.A., Lin, Y., Markgraf, C.G., Mei, H.*, et al.* (2015). MLi-2, a Potent, Selective, and Centrally Active Compound for Exploring the Therapeutic Potential and Safety of LRRK2 Kinase Inhibition. J Pharmacol Exp Ther *355*, 397-409.

Feng, D.D., Cai, W., and Chen, X. (2015). The associations between Parkinson's disease and cancer: the plot thickens. Transl Neurodegener *4*, 20.

Ferreira, M., and Massano, J. (2017). An updated review of Parkinson's disease genetics and clinicopathological correlations. Acta Neurol Scand *135*, 273-284.

Fischer von Mollard, G., Sudhof, T.C., and Jahn, R. (1991). A small GTP-binding protein dissociates from synaptic vesicles during exocytosis. Nature *349*, 79-81.

Flavin, W.P., Bousset, L., Green, Z.C., Chu, Y., Skarpathiotis, S., Chaney, M.J., Kordower, J.H., Melki, R., and Campbell, E.M. (2017). Endocytic vesicle rupture is a conserved mechanism of cellular invasion by amyloid proteins. Acta Neuropathol *134*, 629-653.

Forsyth, C.B., Shannon, K.M., Kordower, J.H., Voigt, R.M., Shaikh, M., Jaglin, J.A., Estes, J.D., Dodiya, H.B., and Keshavarzian, A. (2011). Increased intestinal permeability correlates with sigmoid mucosa alpha-synuclein staining and endotoxin exposure markers in early Parkinson's disease. PLoS ONE *6*, e28032.

Franke, A., McGovern, D.P., Barrett, J.C., Wang, K., Radford-Smith, G.L., Ahmad, T., Lees, C.W., Balschun, T., Lee, J., Roberts, R.*, et al.* (2010). Genome-wide meta-analysis increases to 71 the number of confirmed Crohn's disease susceptibility loci. Nat Genet *42*, 1118-1125.

Freeman, D., Cedillos, R., Choyke, S., Lukic, Z., McGuire, K., Marvin, S., Burrage, A.M., Sudholt, S., Rana, A., O'Connor, C.*, et al.* (2013). Alpha-synuclein induces lysosomal rupture and cathepsin dependent reactive oxygen species following endocytosis. PLoS ONE *8*, e62143.

Froes, L.A.R.J., Sotto, M.N., and Trindade, M.A.B. (2022). Leprosy: clinical and immunopathological characteristics. An Bras Dermatol *97*, 338-347.

Fukui, K., Sasaki, T., Imazumi, K., Matsuura, Y., Nakanishi, H., and Takai, Y. (1997). Isolation and characterization of a GTPase activating protein specific for the Rab3 subfamily of small G proteins. J Biol Chem *272*, 4655-4658.

Funayama, M., Hasegawa, K., Kowa, H., Saito, M., Tsuji, S., and Obata, F. (2002). A new locus for Parkinson's disease (PARK8) maps to chromosome 12p11.2-q13.1. Ann Neurol *51*, 296-301.

Funayama, M., Hasegawa, K., Ohta, E., Kawashima, N., Komiyama, M., Kowa, H., Tsuji, S., and Obata, F. (2005). An LRRK2 mutation as a cause for the parkinsonism in the original PARK8 family. Ann Neurol *57*, 918-921.

Funayama, M., Li, Y., Tomiyama, H., Yoshino, H., Imamichi, Y., Yamamoto, M., Murata, M., Toda, T., Mizuno, Y., and Hattori, N. (2007). Leucine-rich repeat kinase 2 G2385R variant is a risk factor for Parkinson disease in Asian population. Neuroreport *18*, 273-275.

Gardet, A., Benita, Y., Li, C., Sands, B.E., Ballester, I., Stevens, C., Korzenik, J.R., Rioux, J.D., Daly, M.J., Xavier, R.J.*, et al.* (2010). LRRK2 is involved in the IFN-gamma response and host response to pathogens. J Immunol *185*, 5577-5585.

Geppert, M., Goda, Y., Stevens, C.F., and Sudhof, T.C. (1997). The small GTP-binding protein Rab3A regulates a late step in synaptic vesicle fusion. Nature *387*, 810-814.

Gerges, N.Z., Backos, D.S., and Esteban, J.A. (2004). Local control of AMPA receptor trafficking at the postsynaptic terminal by a small GTPase of the Rab family. J Biol Chem *279*, 43870-43878.

Giasson, B.I., Covy, J.P., Bonini, N.M., Hurtig, H.I., Farrer, M.J., Trojanowski, J.Q., and Van Deerlin, V.M. (2006). Biochemical and pathological characterization of Lrrk2. Ann Neurol *59*, 315-322.

Giesert, F., Hofmann, A., Burger, A., Zerle, J., Kloos, K., Hafen, U., Ernst, L., Zhang, J., Vogt-Weisenhorn, D.M., and Wurst, W. (2013). Expression analysis of Lrrk1, Lrrk2 and Lrrk2 splice variants in mice. PLoS ONE *8*, e63778.

Giusto, E., Yacoubian, T.A., Greggio, E., and Civiero, L. (2021). Pathways to Parkinson's disease: a spotlight on 14-3-3 proteins. NPJ Parkinsons Dis *7*, 85.

Glodowski, D.R., Chen, C.C., Schaefer, H., Grant, B.D., and Rongo, C. (2007). RAB-10 regulates glutamate receptor recycling in a cholesterol-dependent endocytosis pathway. Mol Biol Cell *18*, 4387-4396.

Gopalai, A.A., Lim, J.L., Li, H.H., Zhao, Y., Lim, T.T., Eow, G.B., Puvanarajah, S., Viswanathan, S., Norlinah, M.I., Abdul Aziz, Z.*, et al.* (2019). LRRK2 N551K and R1398H variants are protective in Malays and Chinese in Malaysia: A case-control association study for Parkinson's disease. Mol Genet Genomic Med *7*, e604.

Gordon, R., Albornoz, E.A., Christie, D.C., Langley, M.R., Kumar, V., Mantovani, S., Robertson, A.A.B., Butler, M.S., Rowe, D.B., O'Neill, L.A.*, et al.* (2018). Inflammasome

inhibition prevents alpha-synuclein pathology and dopaminergic neurodegeneration in mice. Sci Transl Med *10*.

Gotthardt, K., Weyand, M., Kortholt, A., Van Haastert, P.J., and Wittinghofer, A. (2008). Structure of the Roc-COR domain tandem of C. tepidum, a prokaryotic homologue of the human LRRK2 Parkinson kinase. EMBO J *27*, 2239-2249.

Goulet, B., Baruch, A., Moon, N.S., Poirier, M., Sansregret, L.L., Erickson, A., Bogyo, M., and Nepveu, A. (2004). A cathepsin L isoform that is devoid of a signal peptide localizes to the nucleus in S phase and processes the CDP/Cux transcription factor. Mol Cell *14*, 207-219.

Grebenciucova, E., and VanHaerents, S. (2023). Interleukin 6: at the interface of human health and disease. Front Immunol *14*, 1255533.

Greggio, E., and Cookson, M.R. (2009). Leucine-rich repeat kinase 2 mutations and Parkinson's disease: three questions. ASN Neuro *1*.

Greggio, E., Jain, S., Kingsbury, A., Bandopadhyay, R., Lewis, P., Kaganovich, A., van der Brug, M.P., Beilina, A., Blackinton, J., Thomas, K.J.*, et al.* (2006). Kinase activity is required for the toxic effects of mutant LRRK2/dardarin. Neurobiol Dis *23*, 329-341.

Greggio, E., Zambrano, I., Kaganovich, A., Beilina, A., Taymans, J.M., Daniels, V., Lewis, P., Jain, S., Ding, J., Syed, A.*, et al.* (2008). The Parkinson disease-associated leucine-rich repeat kinase 2 (LRRK2) is a dimer that undergoes intramolecular autophosphorylation. J Biol Chem *283*, 16906-16914.

Gros, M., Segura, E., Rookhuizen, D.C., Baudon, B., Heurtebise-Chretien, S., Burgdorf, N., Maurin, M., Kapp, E.A., Simpson, R.J., Kozik, P.*, et al.* (2022). Endocytic membrane repair by ESCRT-III controls antigen export to the cytosol during antigen cross-presentation. Cell Rep *40*, 111205.

Grozdanov, V., Bliederhaeuser, C., Ruf, W.P., Roth, V., Fundel-Clemens, K., Zondler, L., Brenner, D., Martin-Villalba, A., Hengerer, B., Kassubek, J.*, et al.* (2014). Inflammatory dysregulation of blood monocytes in Parkinson's disease patients. Acta Neuropathol *128*, 651-663.

Guaitoli, G., Gilsbach, B.K., Raimondi, F., and Gloeckner, C.J. (2016). First model of dimeric LRRK2: the challenge of unrevealing the structure of a multidomain Parkinson's-associated protein. Biochem Soc Trans *44*, 1635-1641.

Gudimchuk, N.B., and McIntosh, J.R. (2021). Regulation of microtubule dynamics, mechanics and function through the growing tip. Nat Rev Mol Cell Biol *22*, 777-795.

Guerreiro, P.S., Huang, Y., Gysbers, A., Cheng, D., Gai, W.P., Outeiro, T.F., and Halliday, G.M. (2013). LRRK2 interactions with alpha-synuclein in Parkinson's disease brains and in cell models. J Mol Med (Berl) *91*, 513-522.

Guillen-Boixet, J., Kopach, A., Holehouse, A.S., Wittmann, S., Jahnel, M., Schlussler, R., Kim, K., Trussina, I., Wang, J., Mateju, D.*, et al.* (2020). RNA-Induced Conformational Switching and Clustering of G3BP Drive Stress Granule Assembly by Condensation. Cell *181*, 346-361 e317.

Guo, L., Gandhi, P.N., Wang, W., Petersen, R.B., Wilson-Delfosse, A.L., and Chen, S.G. (2007). The Parkinson's disease-associated protein, leucine-rich repeat kinase 2 (LRRK2), is an authentic GTPase that stimulates kinase activity. Exp Cell Res *313*, 3658-3670.

Gutierrez, M.G. (2013). Functional role(s) of phagosomal Rab GTPases. Small GTPases *4*, 148-158.

Hakimi, M., Selvanantham, T., Swinton, E., Padmore, R.F., Tong, Y., Kabbach, G., Venderova, K., Girardin, S.E., Bulman, D.E., Scherzer, C.R.*, et al.* (2011). Parkinson's disease-linked LRRK2 is expressed in circulating and tissue immune cells and upregulated following recognition of microbial structures. J Neural Transm (Vienna) *118*, 795-808.

Halle, A., Hornung, V., Petzold, G.C., Stewart, C.R., Monks, B.G., Reinheckel, T., Fitzgerald, K.A., Latz, E., Moore, K.J., and Golenbock, D.T. (2008). The NALP3 inflammasome is involved in the innate immune response to amyloid-beta. Nat Immunol *9*, 857-865.

Hamalisto, S., Stahl, J.L., Favaro, E., Yang, Q., Liu, B., Christoffersen, L., Loos, B., Guasch Boldu, C., Joyce, J.A., Reinheckel, T.*, et al.* (2020). Spatially and temporally defined lysosomal leakage facilitates mitotic chromosome segregation. Nat Commun *11*, 229.

Hartlova, A., Herbst, S., Peltier, J., Rodgers, A., Bilkei-Gorzo, O., Fearns, A., Dill, B.D., Lee, H., Flynn, R., Cowley, S.A.*, et al.* (2018). LRRK2 is a negative regulator of Mycobacterium tuberculosis phagosome maturation in macrophages. EMBO J *37*.

Hatano, T., Kubo, S., Imai, S., Maeda, M., Ishikawa, K., Mizuno, Y., and Hattori, N. (2007). Leucine-rich repeat kinase 2 associates with lipid rafts. Hum Mol Genet *16*, 678-690.

Healy, D.G., Falchi, M., O'Sullivan, S.S., Bonifati, V., Durr, A., Bressman, S., Brice, A., Aasly, J., Zabetian, C.P., Goldwurm, S.*, et al.* (2008). Phenotype, genotype, and

worldwide genetic penetrance of LRRK2-associated Parkinson's disease: a case-control study. Lancet Neurol *7*, 583-590.

Helft, J., Bottcher, J., Chakravarty, P., Zelenay, S., Huotari, J., Schraml, B.U., Goubau, D., and Reis e Sousa, C. (2015). GM-CSF Mouse Bone Marrow Cultures Comprise a Heterogeneous Population of CD11c(+)MHCII(+) Macrophages and Dendritic Cells. Immunity *42*, 1197-1211.

Henry, A.G., Aghamohammadzadeh, S., Samaroo, H., Chen, Y., Mou, K., Needle, E., and Hirst, W.D. (2015). Pathogenic LRRK2 mutations, through increased kinase activity, produce enlarged lysosomes with reduced degradative capacity and increase ATP13A2 expression. Hum Mol Genet *24*, 6013-6028.

Herbst, S., Campbell, P., Harvey, J., Bernard, E.M., Papayannopoulos, V., Wood, N.W., Morris, H.R., and Gutierrez, M.G. (2020). LRRK2 activation controls the repair of damaged endomembranes in macrophages. EMBO J *39*, e104494.

Herbst, S., and Gutierrez, M.G. (2019). LRRK2 in Infection: Friend or Foe? ACS Infect Dis *5*, 809-815.

Herzog, S., Fragkou, P.C., Arneth, B.M., Mkhlof, S., and Skevaki, C. (2022). Myeloid CD169/Siglec1: An immunoregulatory biomarker in viral disease. Front Med (Lausanne) *9*, 979373.

Hipolito, V.E.B., Diaz, J.A., Tandoc, K.V., Oertlin, C., Ristau, J., Chauhan, N., Saric, A., McLaughlan, S., Larsson, O., Topisirovic, I.*, et al.* (2019). Enhanced translation expands the endo-lysosome size and promotes antigen presentation during phagocyte activation. PLoS Biol *17*, e3000535.

Ho, D.H., Kim, H., Kim, J., Sim, H., Ahn, H., Kim, J., Seo, H., Chung, K.C., Park, B.J., Son, I.*, et al.* (2015). Leucine-Rich Repeat Kinase 2 (LRRK2) phosphorylates p53 and induces p21(WAF1/CIP1) expression. Mol Brain *8*, 54.

Ho, D.H., Seol, W., Eun, J.H., and Son, I.H. (2017). Phosphorylation of p53 by LRRK2 induces microglial tumor necrosis factor alpha-mediated neurotoxicity. Biochem Biophys Res Commun *482*, 1088-1094.

Homma, Y., and Fukuda, M. (2016). Rabin8 regulates neurite outgrowth in both GEF activity-dependent and -independent manners. Mol Biol Cell *27*, 2107-2118.

Hornung, V., Bauernfeind, F., Halle, A., Samstad, E.O., Kono, H., Rock, K.L., Fitzgerald, K.A., and Latz, E. (2008). Silica crystals and aluminum salts activate the NALP3 inflammasome through phagosomal destabilization. Nat Immunol *9*, 847-856.

Huang, X., Wu, C., Park, Y., Long, X., Hoang, Q.Q., and Liao, J. (2019). The Parkinson's disease-associated mutation N1437H impairs conformational dynamics in the G domain of LRRK2. FASEB J *33*, 4814-4823.

Hui, K.Y., Fernandez-Hernandez, H., Hu, J., Schaffner, A., Pankratz, N., Hsu, N.Y., Chuang, L.S., Carmi, S., Villaverde, N., Li, X.*, et al.* (2018). Functional variants in the LRRK2 gene confer shared effects on risk for Crohn's disease and Parkinson's disease. Sci Transl Med *10*.

Iannotta, L., Biosa, A., Kluss, J.H., Tombesi, G., Kaganovich, A., Cogo, S., Plotegher, N., Civiero, L., Lobbestael, E., Baekelandt, V.*, et al.* (2020). Divergent Effects of G2019S and R1441C LRRK2 Mutations on LRRK2 and Rab10 Phosphorylations in Mouse Tissues. Cells *9*.

Iida, H., Noda, M., Kaneko, T., Doiguchi, M., and Mori, T. (2005). Identification of rab12 as a vesicle-associated small GTPase highly expressed in Sertoli cells of rat testis. Mol Reprod Dev *71*, 178-185.

Iida, H., Wang, L., Nishii, K., Ookuma, A., and Shibata, Y. (1996). Identification of rab12 as a secretory granule-associated small GTP-binding protein in atrial myocytes. Circ Res *78*, 343-347.

Infante, J., Rodriguez, E., Combarros, O., Mateo, I., Fontalba, A., Pascual, J., Oterino, A., Polo, J.M., Leno, C., and Berciano, J. (2006). LRRK2 G2019S is a common mutation in Spanish patients with late-onset Parkinson's disease. Neurosci Lett *395*, 224-226.

Inzelberg, R., Cohen, O.S., Aharon-Peretz, J., Schlesinger, I., Gershoni-Baruch, R., Djaldetti, R., Nitsan, Z., Ephraty, L., Tunkel, O., Kozlova, E.*, et al.* (2012). The LRRK2 G2019S mutation is associated with Parkinson disease and concomitant non-skin cancers. Neurology *78*, 781-786.

Ishihara, L., Warren, L., Gibson, R., Amouri, R., Lesage, S., Durr, A., Tazir, M., Wszolek, Z.K., Uitti, R.J., Nichols, W.C.*, et al.* (2006). Clinical features of Parkinson disease patients with homozygous leucine-rich repeat kinase 2 G2019S mutations. Arch Neurol *63*, 1250-1254.

Ishikawa, H., and Marshall, W.F. (2011). Ciliogenesis: building the cell's antenna. Nat Rev Mol Cell Biol *12*, 222-234.

Ivashkiv, L.B. (2018). IFNgamma: signalling, epigenetics and roles in immunity, metabolism, disease and cancer immunotherapy. Nat Rev Immunol *18*, 545-558.

Jaleel, M., Nichols, R.J., Deak, M., Campbell, D.G., Gillardon, F., Knebel, A., and Alessi, D.R. (2007). LRRK2 phosphorylates moesin at threonine-558: characterization of how Parkinson's disease mutants affect kinase activity. Biochem J *405*, 307-317.

James, N.G., Digman, M.A., Gratton, E., Barylko, B., Ding, X., Albanesi, J.P., Goldberg, M.S., and Jameson, D.M. (2012). Number and brightness analysis of LRRK2 oligomerization in live cells. Biophys J *102*, L41-43.

Jeong, G.R., Jang, E.H., Bae, J.R., Jun, S., Kang, H.C., Park, C.H., Shin, J.H., Yamamoto, Y., Tanaka-Yamamoto, K., Dawson, V.L.*, et al.* (2018). Dysregulated phosphorylation of Rab GTPases by LRRK2 induces neurodegeneration. Mol Neurodegener *13*, 8.

Jevnikar, Z., Obermajer, N., and Kos, J. (2009). Cysteine protease-mediated cytoskeleton interactions with LFA-1 promote T-cell morphological changes. Cell Motil Cytoskeleton *66*, 1030-1040.

Jia, J., Abudu, Y.P., Claude-Taupin, A., Gu, Y., Kumar, S., Choi, S.W., Peters, R., Mudd, M.H., Allers, L., Salemi, M.*, et al.* (2019). Galectins control MTOR and AMPK in response to lysosomal damage to induce autophagy. Autophagy *15*, 169-171.

Jia, J., Claude-Taupin, A., Gu, Y., Choi, S.W., Peters, R., Bissa, B., Mudd, M.H., Allers, L., Pallikkuth, S., Lidke, K.A.*, et al.* (2020). Galectin-3 Coordinates a Cellular System for Lysosomal Repair and Removal. Dev Cell *52*, 69-87 e68.

Jiang, X., Bomgarden, R., Brown, J., Drew, D.L., Robitaille, A.M., Viner, R., and Huhmer, A.R. (2017). Sensitive and Accurate Quantitation of Phosphopeptides Using TMT Isobaric Labeling Technique. J Proteome Res *16*, 4244-4252.

Jiang, Z.C., Chen, X.J., Zhou, Q., Gong, X.H., Chen, X., and Wu, W.J. (2019). Downregulated LRRK2 gene expression inhibits proliferation and migration while promoting the apoptosis of thyroid cancer cells by inhibiting activation of the JNK signaling pathway. Int J Oncol *55*, 21-34.

Johannes, L., Jacob, R., and Leffler, H. (2018). Galectins at a glance. J Cell Sci *131*.

Johansen, K.K., White, L.R., Farrer, M.J., and Aasly, J.O. (2011). Subclinical signs in LRRK2 mutation carriers. Parkinsonism Relat Disord *17*, 528-532.

Johnson, D.E., Ostrowski, P., Jaumouille, V., and Grinstein, S. (2016). The position of lysosomes within the cell determines their luminal pH. J Cell Biol *212*, 677-692.

Jorgensen, N.D., Peng, Y., Ho, C.C., Rideout, H.J., Petrey, D., Liu, P., and Dauer, W.T. (2009). The WD40 domain is required for LRRK2 neurotoxicity. PLoS ONE *4*, e8463.

Julien, O., and Wells, J.A. (2017). Caspases and their substrates. Cell Death Differ *24*, 1380-1389.

Kadowaki, T., Yamaguchi, Y., Ogawa, K., Tokuhisa, M., Okamoto, K., and Tsukuba, T. (2021). Rab44 isoforms similarly promote lysosomal exocytosis, but exhibit differential localization in mast cells. FEBS Open Bio *11*, 1165-1185.

Kalia, L.V., Lang, A.E., Hazrati, L.N., Fujioka, S., Wszolek, Z.K., Dickson, D.W., Ross, O.A., Van Deerlin, V.M., Trojanowski, J.Q., Hurtig, H.I.*, et al.* (2015). Clinical correlations with Lewy body pathology in LRRK2-related Parkinson disease. JAMA Neurol *72*, 100-105.

Kalogeropulou, A.F., Freemantle, J.B., Lis, P., Vides, E.G., Polinski, N.K., and Alessi, D.R. (2020). Endogenous Rab29 does not impact basal or stimulated LRRK2 pathway activity. Biochem J *477*, 4397-4423.

Kalogeropulou, A.F., Purlyte, E., Tonelli, F., Lange, S.M., Wightman, M., Prescott, A.R., Padmanabhan, S., Sammler, E., and Alessi, D.R. (2022). Impact of 100 LRRK2 variants linked to Parkinson's disease on kinase activity and microtubule binding. Biochem J *479*, 1759-1783.

Karayel, O., Tonelli, F., Virreira Winter, S., Geyer, P.E., Fan, Y., Sammler, E.M., Alessi, D.R., Steger, M., and Mann, M. (2020). Accurate MS-based Rab10 Phosphorylation Stoichiometry Determination as Readout for LRRK2 Activity in Parkinson's Disease. Mol Cell Proteomics *19*, 1546-1560.

Katsnelson, M.A., Lozada-Soto, K.M., Russo, H.M., Miller, B.A., and Dubyak, G.R. (2016). NLRP3 inflammasome signaling is activated by low-level lysosome disruption but inhibited by extensive lysosome disruption: roles for K+ efflux and Ca2+ influx. Am J Physiol Cell Physiol *311*, C83-C100.

Kawabe, H., Sakisaka, T., Yasumi, M., Shingai, T., Izumi, G., Nagano, F., Deguchi-Tawarada, M., Takeuchi, M., Nakanishi, H., and Takai, Y. (2003). A novel rabconnectin-3-binding protein that directly binds a GDP/GTP exchange protein for Rab3A small G protein implicated in Ca(2+)-dependent exocytosis of neurotransmitter. Genes Cells *8*, 537-546.

Kazmi, F., Hensley, T., Pope, C., Funk, R.S., Loewen, G.J., Buckley, D.B., and Parkinson, A. (2013). Lysosomal sequestration (trapping) of lipophilic amine (cationic amphiphilic) drugs in immortalized human hepatocytes (Fa2N-4 cells). Drug Metab Dispos *41*, 897-905.

Kelly, K., Wang, S., Boddu, R., Liu, Z., Moukha-Chafiq, O., Augelli-Szafran, C., and West, A.B. (2018). The G2019S mutation in LRRK2 imparts resiliency to kinase inhibition. Exp Neurol *309*, 1-13.

Kerr, J.F., Wyllie, A.H., and Currie, A.R. (1972). Apoptosis: a basic biological phenomenon with wide-ranging implications in tissue kinetics. Br J Cancer *26*, 239-257.

Kett, L.R., Boassa, D., Ho, C.C., Rideout, H.J., Hu, J., Terada, M., Ellisman, M., and Dauer, W.T. (2012). LRRK2 Parkinson disease mutations enhance its microtubule association. Hum Mol Genet *21*, 890-899.

Khan, N.L., Jain, S., Lynch, J.M., Pavese, N., Abou-Sleiman, P., Holton, J.L., Healy, D.G., Gilks, W.P., Sweeney, M.G., Ganguly, M.*, et al.* (2005). Mutations in the gene LRRK2 encoding dardarin (PARK8) cause familial Parkinson's disease: clinical, pathological, olfactory and functional imaging and genetic data. Brain *128*, 2786-2796.

Khan, T.G., Ginsburg, D., and Emmer, B.T. (2022). The small GTPase RAB10 regulates endosomal recycling of the LDL receptor and transferrin receptor in hepatocytes. J Lipid Res *63*, 100248.

Kim, J., Pajarillo, E., Rizor, A., Son, D.S., Lee, J., Aschner, M., and Lee, E. (2019). LRRK2 kinase plays a critical role in manganese-induced inflammation and apoptosis in microglia. PLoS ONE *14*, e0210248.

Kim, K.S., Marcogliese, P.C., Yang, J., Callaghan, S.M., Resende, V., Abdel-Messih, E., Marras, C., Visanji, N.P., Huang, J., Schlossmacher, M.G.*, et al.* (2018). Regulation of myeloid cell phagocytosis by LRRK2 via WAVE2 complex stabilization is altered in Parkinson's disease. Proc Natl Acad Sci U S A *115*, E5164-E5173.

Kluss, J.H., Beilina, A., Lewis, P.A., Cookson, M.R., and Bonet-Ponce, L. (2020). Membrane targeting activates Leucine-rich repeat kinase 2 with differential effects on downstream Rab activation. bioRxiv, 2020.2012.2001.406223.

Kluss, J.H., Beilina, A., Williamson, C.D., Lewis, P.A., Cookson, M.R., and Bonet-Ponce, L. (2022a). Lysosomal positioning regulates Rab10 phosphorylation at LRRK2(+) lysosomes. Proc Natl Acad Sci U S A *119*, e2205492119.

Kluss, J.H., Bonet-Ponce, L., Lewis, P.A., and Cookson, M.R. (2022b). Directing LRRK2 to membranes of the endolysosomal pathway triggers RAB phosphorylation and JIP4 recruitment. Neurobiol Dis *170*, 105769.

Kluss, J.H., Conti, M.M., Kaganovich, A., Beilina, A., Melrose, H.L., Cookson, M.R., and Mamais, A. (2018). Detection of endogenous S1292 LRRK2 autophosphorylation in mouse tissue as a readout for kinase activity. NPJ Parkinsons Dis *4*, 13.

Ko, H.S., Bailey, R., Smith, W.W., Liu, Z., Shin, J.H., Lee, Y.I., Zhang, Y.J., Jiang, H., Ross, C.A., Moore, D.J.*, et al.* (2009). CHIP regulates leucine-rich repeat kinase-2 ubiquitination, degradation, and toxicity. Proc Natl Acad Sci U S A *106*, 2897-2902.

Kouranti, I., Sachse, M., Arouche, N., Goud, B., and Echard, A. (2006). Rab35 regulates an endocytic recycling pathway essential for the terminal steps of cytokinesis. Curr Biol *16*, 1719-1725.

Kozina, E., Byrne, M., and Smeyne, R.J. (2022). Mutant LRRK2 in lymphocytes regulates neurodegeneration via IL-6 in an inflammatory model of Parkinson's disease. NPJ Parkinsons Dis *8*, 24.

Kozina, E., Sadasivan, S., Jiao, Y., Dou, Y., Ma, Z., Tan, H., Kodali, K., Shaw, T., Peng, J., and Smeyne, R.J. (2018). Mutant LRRK2 mediates peripheral and central immune responses leading to neurodegeneration in vivo. Brain *141*, 1753-1769.

Kretzer, N.M., Theisen, D.J., Tussiwand, R., Briseno, C.G., Grajales-Reyes, G.E., Wu, X., Durai, V., Albring, J., Bagadia, P., Murphy, T.L.*, et al.* (2016). RAB43 facilitates cross-presentation of cell-associated antigens by CD8alpha+ dendritic cells. J Exp Med *213*, 2871-2883.

Kubo, M., Nagashima, R., Kurihara, M., Kawakami, F., Maekawa, T., Eshima, K., Ohta, E., Kato, H., and Obata, F. (2020). Leucine-Rich Repeat Kinase 2 Controls Inflammatory Cytokines Production through NF-kappaB Phosphorylation and Antigen Presentation in Bone Marrow-Derived Dendritic Cells. Int J Mol Sci *21*.

Kuhlmann, N., and Milnerwood, A.J. (2020). A Critical LRRK at the Synapse? The Neurobiological Function and Pathophysiological Dysfunction of LRRK2. Front Mol Neurosci *13*, 153.

Kuss, M., Adamopoulou, E., and Kahle, P.J. (2014). Interferon-gamma induces leucine-rich repeat kinase LRRK2 via extracellular signal-regulated kinase ERK5 in macrophages. J Neurochem *129*, 980-987.

Kustrimovic, N., Comi, C., Magistrelli, L., Rasini, E., Legnaro, M., Bombelli, R., Aleksic, I., Blandini, F., Minafra, B., Riboldazzi, G.*, et al.* (2018). Parkinson's disease patients have a complex phenotypic and functional Th1 bias: cross-sectional studies of CD4+ Th1/Th2/T17 and Treg in drug-naive and drug-treated patients. J Neuroinflammation *15*, 205.

Kuwahara, T., Funakawa, K., Komori, T., Sakurai, M., Yoshii, G., Eguchi, T., Fukuda, M., and Iwatsubo, T. (2020). Roles of lysosomotropic agents on LRRK2 activation and Rab10 phosphorylation. Neurobiol Dis *145*, 105081.

La Cognata, V., D'Agata, V., Cavalcanti, F., and Cavallaro, S. (2015). Splicing: is there an alternative contribution to Parkinson's disease? Neurogenetics *16*, 245-263.

Lavalley, N.J., Slone, S.R., Ding, H., West, A.B., and Yacoubian, T.A. (2016). 14-3-3 Proteins regulate mutant LRRK2 kinase activity and neurite shortening. Hum Mol Genet *25*, 109-122.

Leandrou, E., Markidi, E., Memou, A., Melachroinou, K., Greggio, E., and Rideout, H.J. (2019). Kinase activity of mutant LRRK2 manifests differently in hetero-dimeric vs. homo-dimeric complexes. Biochem J *476*, 559-579.

Lee, H., Flynn, R., Sharma, I., Haberman, E., Carling, P.J., Nicholls, F.J., Stegmann, M., Vowles, J., Haenseler, W., Wade-Martins, R.*, et al.* (2020). LRRK2 Is Recruited to Phagosomes and Co-recruits RAB8 and RAB10 in Human Pluripotent Stem Cell-Derived Macrophages. Stem Cell Reports *14*, 940-955.

Lerner, T.R., Borel, S., Greenwood, D.J., Repnik, U., Russell, M.R., Herbst, S., Jones, M.L., Collinson, L.M., Griffiths, G., and Gutierrez, M.G. (2017). Mycobacterium tuberculosis replicates within necrotic human macrophages. J Cell Biol *216*, 583-594.

Lesage, S., Ibanez, P., Lohmann, E., Pollak, P., Tison, F., Tazir, M., Leutenegger, A.L., Guimaraes, J., Bonnet, A.M., Agid, Y.*, et al.* (2005). G2019S LRRK2 mutation in French and North African families with Parkinson's disease. Ann Neurol *58*, 784-787.

Lewis, P.A. (2009). The function of ROCO proteins in health and disease. Biol Cell *101*, 183-191.

Lewis, P.A., Greggio, E., Beilina, A., Jain, S., Baker, A., and Cookson, M.R. (2007). The R1441C mutation of LRRK2 disrupts GTP hydrolysis. Biochem Biophys Res Commun *357*, 668-671.

Li, C., Wei, Z., Fan, Y., Huang, W., Su, Y., Li, H., Dong, Z., Fukuda, M., Khater, M., and Wu, G. (2017). The GTPase Rab43 Controls the Anterograde ER-Golgi Trafficking and Sorting of GPCRs. Cell Rep *21*, 1089-1101.

Li, J.Q., Tan, L., and Yu, J.T. (2014). The role of the LRRK2 gene in Parkinsonism. Mol Neurodegener *9*, 47.

Li, X., Wang, Q.J., Pan, N., Lee, S., Zhao, Y., Chait, B.T., and Yue, Z. (2011). Phosphorylation-dependent 14-3-3 binding to LRRK2 is impaired by common mutations of familial Parkinson's disease. PLoS ONE *6*, e17153.

Li, X.Z., Bai, L.M., Yang, Y.P., Luo, W.F., Hu, W.D., Chen, J.P., Mao, C.J., and Liu, C.F. (2009). Effects of IL-6 secreted from astrocytes on the survival of dopaminergic neurons in lipopolysaccharide-induced inflammation. Neurosci Res *65*, 252-258.

Li, Z., Schulze, R.J., Weller, S.G., Krueger, E.W., Schott, M.B., Zhang, X., Casey, C.A., Liu, J., Stockli, J., James, D.E.*, et al.* (2016). A novel Rab10-EHBP1-EHD2 complex essential for the autophagic engulfment of lipid droplets. Sci Adv *2*, e1601470.

Lin, D., Xu, W., Hong, P., Wu, C., Zhang, Z., Zhang, S., Xing, L., Yang, B., Zhou, W., Xiao, Q.*, et al.* (2022). Decoding the spatial chromatin organization and dynamic

epigenetic landscapes of macrophage cells during differentiation and immune activation. Nat Commun *13*, 5857.

Liou, A.K., Leak, R.K., Li, L., and Zigmond, M.J. (2008). Wild-type LRRK2 but not its mutant attenuates stress-induced cell death via ERK pathway. Neurobiol Dis *32*, 116-124.

Lis, P., Burel, S., Steger, M., Mann, M., Brown, F., Diez, F., Tonelli, F., Holton, J.L., Ho, P.W., Ho, S.L.*, et al.* (2018). Development of phospho-specific Rab protein antibodies to monitor in vivo activity of the LRRK2 Parkinson's disease kinase. Biochem J *475*, 1-22.

Liu, G.H., Qu, J., Suzuki, K., Nivet, E., Li, M., Montserrat, N., Yi, F., Xu, X., Ruiz, S., Zhang, W.*, et al.* (2012). Progressive degeneration of human neural stem cells caused by pathogenic LRRK2. Nature *491*, 603-607.

Liu, M., Guo, S., Hibbert, J.M., Jain, V., Singh, N., Wilson, N.O., and Stiles, J.K. (2011). CXCL10/IP-10 in infectious diseases pathogenesis and potential therapeutic implications. Cytokine Growth Factor Rev *22*, 121-130.

Liu, O., and Grant, B.D. (2015). Basolateral Endocytic Recycling Requires RAB-10 and AMPH-1 Mediated Recruitment of RAB-5 GAP TBC-2 to Endosomes. PLoS Genet *11*, e1005514.

Liu, X., Kalogeropulou, A.F., Domingos, S., Makukhin, N., Nirujogi, R.S., Singh, F., Shpiro, N., Saalfrank, A., Sammler, E., Ganley, I.G.*, et al.* (2022). Discovery of XL01126: A Potent, Fast, Cooperative, Selective, Orally Bioavailable, and Blood-Brain Barrier Penetrant PROTAC Degrader of Leucine-Rich Repeat Kinase 2. J Am Chem Soc *144*, 16930-16952.

Liu, Z., Bryant, N., Kumaran, R., Beilina, A., Abeliovich, A., Cookson, M.R., and West, A.B. (2018). LRRK2 phosphorylates membrane-bound Rabs and is activated by GTP-bound Rab7L1 to promote recruitment to the trans-Golgi network. Hum Mol Genet *27*, 385-395.

Liu, Z., Xu, E., Zhao, H.T., Cole, T., and West, A.B. (2020). LRRK2 and Rab10 coordinate macropinocytosis to mediate immunological responses in phagocytes. EMBO J *39*, e104862.

Luo, L., Wall, A.A., Yeo, J.C., Condon, N.D., Norwood, S.J., Schoenwaelder, S., Chen, K.W., Jackson, S., Jenkins, B.J., Hartland, E.L.*, et al.* (2014). Rab8a interacts directly with PI3Kgamma to modulate TLR4-driven PI3K and mTOR signalling. Nat Commun *5*, 4407.

Luth, T., Konig, I.R., Grunewald, A., Kasten, M., Klein, C., Hentati, F., Farrer, M., and Trinh, J. (2020). Age at Onset of LRRK2 p.Gly2019Ser Is Related to Environmental and Lifestyle Factors. Mov Disord *35*, 1854-1858.

Lv, P., Sheng, Y., Zhao, Z., Zhao, W., Gu, L., Xu, T., and Song, E. (2015). Targeted disruption of Rab10 causes early embryonic lethality. Protein Cell *6*, 463-467.

Madero-Perez, J., Fernandez, B., Lara Ordonez, A.J., Fdez, E., Lobbestael, E., Baekelandt, V., and Hilfiker, S. (2018). RAB7L1-Mediated Relocalization of LRRK2 to the Golgi Complex Causes Centrosomal Deficits via RAB8A. Front Mol Neurosci *11*, 417.

Maejima, I., Takahashi, A., Omori, H., Kimura, T., Takabatake, Y., Saitoh, T., Yamamoto, A., Hamasaki, M., Noda, T., Isaka, Y.*, et al.* (2013). Autophagy sequesters damaged lysosomes to control lysosomal biogenesis and kidney injury. EMBO J *32*, 2336-2347.

Majno, G., and Joris, I. (1995). Apoptosis, oncosis, and necrosis. An overview of cell death. Am J Pathol *146*, 3-15.

Mamais, A., Chia, R., Beilina, A., Hauser, D.N., Hall, C., Lewis, P.A., Cookson, M.R., and Bandopadhyay, R. (2014). Arsenite stress down-regulates phosphorylation and 14-3-3 binding of leucine-rich repeat kinase 2 (LRRK2), promoting self-association and cellular redistribution. J Biol Chem *289*, 21386-21400.

Mamais, A., Sanyal, A., Fajfer, A., Zykoski, C.G., Guldin, M., Riley-DiPaolo, A., Subrahmanian, N., Gibbs, W., Lin, S., and LaVoie, M.J. (2024). The LRRK2 kinase substrates RAB8a and RAB10 contribute complementary but distinct disease-relevant phenotypes in human neurons. Stem Cell Reports *19*, 163-173.

Manschwetus, J.T., Wallbott, M., Fachinger, A., Obergruber, C., Pautz, S., Bertinetti, D., Schmidt, S.H., and Herberg, F.W. (2020). Binding of the Human 14-3-3 Isoforms to Distinct Sites in the Leucine-Rich Repeat Kinase 2. Front Neurosci *14*, 302.

Mansour, H.M., Mohamed, A.F., Khattab, M.M., and El-Khatib, A.S. (2024). Heat Shock Protein 90 in Parkinson's Disease: Profile of a Serial Killer. Neuroscience *537*, 32-46.

Marchand, A., Drouyer, M., Sarchione, A., Chartier-Harlin, M.C., and Taymans, J.M. (2020). LRRK2 Phosphorylation, More Than an Epiphenomenon. Front Neurosci *14*, 527.

Marek, G., Francesco, G., Chris, C., and Geoffrey, J.B.

Mariathasan, S., Weiss, D.S., Newton, K., McBride, J., O'Rourke, K., Roose-Girma, M., Lee, W.P., Weinrauch, Y., Monack, D.M., and Dixit, V.M. (2006). Cryopyrin activates the inflammasome in response to toxins and ATP. Nature *440*, 228-232.

Marwaha, R., and Sharma, M. (2017). DQ-Red BSA Trafficking Assay in Cultured Cells to Assess Cargo Delivery to Lysosomes. Bio Protoc *7*.

Mata, I.F., Kachergus, J.M., Taylor, J.P., Lincoln, S., Aasly, J., Lynch, T., Hulihan, M.M., Cobb, S.A., Wu, R.M., Lu, C.S.*, et al.* (2005a). Lrrk2 pathogenic substitutions in Parkinson's disease. Neurogenetics *6*, 171-177.

Mata, I.F., Taylor, J.P., Kachergus, J., Hulihan, M., Huerta, C., Lahoz, C., Blazquez, M., Guisasola, L.M., Salvador, C., Ribacoba, R.*, et al.* (2005b). LRRK2 R1441G in Spanish patients with Parkinson's disease. Neurosci Lett *382*, 309-311.

Matikainen-Ankney, B.A., Kezunovic, N., Mesias, R.E., Tian, Y., Williams, F.M., Huntley, G.W., and Benson, D.L. (2016). Altered Development of Synapse Structure and Function in Striatum Caused by Parkinson's Disease-Linked LRRK2-G2019S Mutation. J Neurosci *36*, 7128-7141.

Matsui, T., and Fukuda, M. (2013). Rab12 regulates mTORC1 activity and autophagy through controlling the degradation of amino-acid transporter PAT4. EMBO Rep *14*, 450-457.

Matsui, T., Itoh, T., and Fukuda, M. (2011). Small GTPase Rab12 regulates constitutive degradation of transferrin receptor. Traffic *12*, 1432-1443.

Matsui, T., Noguchi, K., and Fukuda, M. (2014). Dennd3 functions as a guanine nucleotide exchange factor for small GTPase Rab12 in mouse embryonic fibroblasts. J Biol Chem *289*, 13986-13995.

Matsui, Y., Kikuchi, A., Kondo, J., Hishida, T., Teranishi, Y., and Takai, Y. (1988). Nucleotide and deduced amino acid sequences of a GTP-binding protein family with molecular weights of 25,000 from bovine brain. J Biol Chem *263*, 11071-11074.

Menu, P., and Vince, J.E. (2011). The NLRP3 inflammasome in health and disease: the good, the bad and the ugly. Clin Exp Immunol *166*, 1-15.

Metcalfe, R.D., Martinez Fiesco, J.A., Bonet-Ponce, L., Kluss, J.H., Cookson, M.R., and Zhang, P. (2023). Structure and regulation of full-length human leucine-rich repeat kinase 1. Nat Commun *14*, 4797.

Miksicek, R.J., Myal, Y., Watson, P.H., Walker, C., Murphy, L.C., and Leygue, E. (2002). Identification of a novel breast- and salivary gland-specific, mucin-like gene strongly expressed in normal and tumor human mammary epithelium. Cancer Res *62*, 2736-2740.

Mir, R., Tonelli, F., Lis, P., Macartney, T., Polinski, N.K., Martinez, T.N., Chou, M.Y., Howden, A.J.M., Konig, T., Hotzy, C.*, et al.* (2018). The Parkinson's disease VPS35[D620N] mutation enhances LRRK2-mediated Rab protein phosphorylation in mouse and human. Biochem J *475*, 1861-1883.

Miyazaki, I., Isooka, N., Imafuku, F., Sun, J., Kikuoka, R., Furukawa, C., and Asanuma, M. (2020). Chronic Systemic Exposure to Low-Dose Rotenone Induced Central and

Peripheral Neuropathology and Motor Deficits in Mice: Reproducible Animal Model of Parkinson's Disease. Int J Mol Sci *21*.

Mizushima, N., and Yoshimori, T. (2007). How to interpret LC3 immunoblotting. Autophagy *3*, 542-545.

Moehle, M.S., Webber, P.J., Tse, T., Sukar, N., Standaert, D.G., DeSilva, T.M., Cowell, R.M., and West, A.B. (2012). LRRK2 inhibition attenuates microglial inflammatory responses. J Neurosci *32*, 1602-1611.

Mogi, M., Kondo, T., Mizuno, Y., and Nagatsu, T. (2007). p53 protein, interferon-gamma, and NF-kappaB levels are elevated in the parkinsonian brain. Neurosci Lett *414*, 94-97.

Moreau, K., Coen, M., Zhang, A.X., Pachl, F., Castaldi, M.P., Dahl, G., Boyd, H., Scott, C., and Newham, P. (2020). Proteolysis-targeting chimeras in drug development: A safety perspective. Br J Pharmacol *177*, 1709-1718.

Mosser, D.M., Hamidzadeh, K., and Goncalves, R. (2021). Macrophages and the maintenance of homeostasis. Cell Mol Immunol *18*, 579-587.

Mossman, B.T., and Churg, A. (1998). Mechanisms in the pathogenesis of asbestosis and silicosis. Am J Respir Crit Care Med *157*, 1666-1680.

Mount, M.P., Lira, A., Grimes, D., Smith, P.D., Faucher, S., Slack, R., Anisman, H., Hayley, S., and Park, D.S. (2007). Involvement of interferon-gamma in microglial-mediated loss of dopaminergic neurons. J Neurosci *27*, 3328-3337.

Muda, K., Bertinetti, D., Gesellchen, F., Hermann, J.S., von Zweydorf, F., Geerlof, A., Jacob, A., Ueffing, M., Gloeckner, C.J., and Herberg, F.W. (2014). Parkinson-related LRRK2 mutation R1441C/G/H impairs PKA phosphorylation of LRRK2 and disrupts its interaction with 14-3-3. Proc Natl Acad Sci U S A *111*, E34-43.

Muller, M.P., and Goody, R.S. (2018). Molecular control of Rab activity by GEFs, GAPs and GDI. Small GTPases *9*, 5-21.

Myasnikov, A., Zhu, H., Hixson, P., Xie, B., Yu, K., Pitre, A., Peng, J., and Sun, J. (2021). Structural analysis of the full-length human LRRK2. Cell *184*, 3519-3527 e3510.

Na, Y.R., Jung, D., Gu, G.J., and Seok, S.H. (2016). GM-CSF Grown Bone Marrow Derived Cells Are Composed of Phenotypically Different Dendritic Cells and Macrophages. Mol Cells *39*, 734-741.

Nagano, F., Kawabe, H., Nakanishi, H., Shinohara, M., Deguchi-Tawarada, M., Takeuchi, M., Sasaki, T., and Takai, Y. (2002). Rabconnectin-3, a novel protein that binds both GDP/GTP exchange protein and GTPase-activating protein for Rab3 small G protein family. J Biol Chem *277*, 9629-9632.

Napolitano, G., and Ballabio, A. (2016). TFEB at a glance. J Cell Sci *129*, 2475-2481.

Narayan, M., Zhang, J., Braswell, K., Gibson, C., Zitnyar, A., Lee, D.C., Varghese-Gupta, S., and Jinwal, U.K. (2015). Withaferin A Regulates LRRK2 Levels by Interfering with the Hsp90- Cdc37 Chaperone Complex. Curr Aging Sci *8*, 259-265.

Narayana, Y., and Shawn, M.F. (2023). LRRK2 Suppresses Lysosome Degradative Activity in Macrophages and Microglia Through MiT-TFE Transcription Factor Inhibition. bioRxiv, 2022.2012.2017.520834.

Nguyen, L.T.N., Nguyen, H.D., Kim, Y.J., Nguyen, T.T., Lai, T.T., Lee, Y.K., Ma, H.I., and Kim, Y.E. (2022). Role of NLRP3 Inflammasome in Parkinson's Disease and Therapeutic Considerations. J Parkinsons Dis *12*, 2117-2133.

Nichols, R.J., Dzamko, N., Morrice, N.A., Campbell, D.G., Deak, M., Ordureau, A., Macartney, T., Tong, Y., Shen, J., Prescott, A.R.*, et al.* (2010). 14-3-3 binding to LRRK2 is disrupted by multiple Parkinson's disease-associated mutations and regulates cytoplasmic localization. Biochem J *430*, 393-404.

Nichols, W.C., Pankratz, N., Hernandez, D., Paisan-Ruiz, C., Jain, S., Halter, C.A., Michaels, V.E., Reed, T., Rudolph, A., Shults, C.W.*, et al.* (2005). Genetic screening for a single common LRRK2 mutation in familial Parkinson's disease. Lancet *365*, 410-412.

Niekamp, P., Scharte, F., Sokoya, T., Vittadello, L., Kim, Y., Deng, Y., Sudhoff, E., Hilderink, A., Imlau, M., Clarke, C.J.*, et al.* (2022). Ca(2+)-activated sphingomyelin scrambling and turnover mediate ESCRT-independent lysosomal repair. Nat Commun *13*, 1875.

Obergasteiger, J., Frapporti, G., Lamonaca, G., Pizzi, S., Picard, A., Lavdas, A.A., Pischedda, F., Piccoli, G., Hilfiker, S., Lobbestael, E.*, et al.* (2020). Kinase inhibition of G2019S-LRRK2 enhances autolysosome formation and function to reduce endogenous alpha-synuclein intracellular inclusions. Cell Death Discov *6*, 45.

Olkkonen, V.M., Dupree, P., Killisch, I., Lutcke, A., Zerial, M., and Simons, K. (1993). Molecular cloning and subcellular localization of three GTP-binding proteins of the rab subfamily. J Cell Sci *106 (Pt 4)*, 1249-1261.

Orlowski, G.M., Colbert, J.D., Sharma, S., Bogyo, M., Robertson, S.A., and Rock, K.L. (2015). Multiple Cathepsins Promote Pro-IL-1beta Synthesis and NLRP3-Mediated IL-1beta Activation. J Immunol *195*, 1685-1697.

Oun, A., Hoeksema, E., Soliman, A., Brouwer, F., Garcia-Reyes, F., Pots, H., Trombetta-Lima, M., Kortholt, A., and Dolga, A.M. (2023). Characterization of Lipopolysaccharide Effects on LRRK2 Signaling in RAW Macrophages. Int J Mol Sci *24*.

Ozelius, L.J., Senthil, G., Saunders-Pullman, R., Ohmann, E., Deligtisch, A., Tagliati, M., Hunt, A.L., Klein, C., Henick, B., Hailpern, S.M.*, et al.* (2006). LRRK2 G2019S as a cause of Parkinson's disease in Ashkenazi Jews. New Engl J Med *354*, 424-425.

Padmanabhan, S., Lanz, T.A., Gorman, D., Wolfe, M., Joyce, A., Cabrera, C., Lawrence-Henderson, R., Levers, N., Joshi, N., Ma, T.C.*, et al.* (2020). An Assessment of LRRK2 Serine 935 Phosphorylation in Human Peripheral Blood Mononuclear Cells in Idiopathic Parkinson's Disease and G2019S LRRK2 Cohorts. J Parkinsons Dis *10*, 623-629.

Paisan-Ruiz, C., Jain, S., Evans, E.W., Gilks, W.P., Simon, J., van der Brug, M., Lopez de Munain, A., Aparicio, S., Gil, A.M., Khan, N.*, et al.* (2004). Cloning of the gene containing mutations that cause PARK8-linked Parkinson's disease. Neuron *44*, 595-600.

Pajarillo, E., Kim, S., Digman, A., Dutton, M., Son, D.S., Aschner, M., and Lee, E. (2023). The role of microglial LRRK2 kinase in manganese-induced inflammatory neurotoxicity via NLRP3 inflammasome and RAB10-mediated autophagy dysfunction. J Biol Chem *299*, 104879.

Pal, P., Taylor, M., Lam, P.Y., Tonelli, F., Hecht, C.A., Lis, P., Nirujogi, R.S., Phung, T.K., Yeshaw, W.M., Jaimon, E.*, et al.* (2023). Parkinson's VPS35[D620N] mutation induces LRRK2-mediated lysosomal association of RILPL1 and TMEM55B. Sci Adv *9*, eadj1205.

Palmisano, N.J., Rosario, N., Wysocki, M., Hong, M., Grant, B., and Melendez, A. (2017). The recycling endosome protein RAB-10 promotes autophagic flux and localization of the transmembrane protein ATG-9. Autophagy *13*, 1742-1753.

Panagiotakopoulou, V., Ivanyuk, D., De Cicco, S., Haq, W., Arsic, A., Yu, C., Messelodi, D., Oldrati, M., Schondorf, D.C., Perez, M.J.*, et al.* (2020). Interferon-gamma signaling synergizes with LRRK2 in neurons and microglia derived from human induced pluripotent stem cells. Nat Commun *11*, 5163.

Papadopoulos, C., Kravic, B., and Meyer, H. (2020). Repair or Lysophagy: Dealing with Damaged Lysosomes. J Mol Biol *432*, 231-239.

Papadopoulos, C., and Meyer, H. (2017). Detection and Clearance of Damaged Lysosomes by the Endo-Lysosomal Damage Response and Lysophagy. Curr Biol *27*, R1330-R1341.

Parisiadou, L., Xie, C., Cho, H.J., Lin, X., Gu, X.L., Long, C.X., Lobbestael, E., Baekelandt, V., Taymans, J.M., Sun, L.*, et al.* (2009). Phosphorylation of ezrin/radixin/moesin proteins by LRRK2 promotes the rearrangement of actin cytoskeleton in neuronal morphogenesis. J Neurosci *29*, 13971-13980.

Patel, V.A., Longacre, A., Hsiao, K., Fan, H., Meng, F., Mitchell, J.E., Rauch, J., Ucker, D.S., and Levine, J.S. (2006). Apoptotic cells, at all stages of the death process, trigger

characteristic signaling events that are divergent from and dominant over those triggered by necrotic cells: Implications for the delayed clearance model of autoimmunity. J Biol Chem *281*, 4663-4670.

Patino-Lopez, G., Dong, X., Ben-Aissa, K., Bernot, K.M., Itoh, T., Fukuda, M., Kruhlak, M.J., Samelson, L.E., and Shaw, S. (2008). Rab35 and its GAP EPI64C in T cells regulate receptor recycling and immunological synapse formation. J Biol Chem *283*, 18323-18330.

Pavan, C., Santalucia, R., Leinardi, R., Fabbiani, M., Yakoub, Y., Uwambayinema, F., Ugliengo, P., Tomatis, M., Martra, G., Turci, F.*, et al.* (2020). Nearly free surface silanols are the critical molecular moieties that initiate the toxicity of silica particles. Proc Natl Acad Sci U S A *117*, 27836-27846.

Paz, I., Sachse, M., Dupont, N., Mounier, J., Cederfur, C., Enninga, J., Leffler, H., Poirier, F., Prevost, M.C., Lafont, F.*, et al.* (2010). Galectin-3, a marker for vacuole lysis by invasive pathogens. Cell Microbiol *12*, 530-544.

Pellegrino, E., and Gutierrez, M.G. (2021). Human stem cell-based models for studying host-pathogen interactions. Cell Microbiol *23*, e13335.

Peranen, J. (2011). Rab8 GTPase as a regulator of cell shape. Cytoskeleton (Hoboken) *68*, 527-539.

Pereira-Leal, J.B., Hume, A.N., and Seabra, M.C. (2001). Prenylation of Rab GTPases: molecular mechanisms and involvement in genetic disease. FEBS Lett *498*, 197-200.

Perez-Pardo, P., Dodiya, H.B., Engen, P.A., Forsyth, C.B., Huschens, A.M., Shaikh, M., Voigt, R.M., Naqib, A., Green, S.J., Kordower, J.H.*, et al.* (2019). Role of TLR4 in the gut-brain axis in Parkinson's disease: a translational study from men to mice. Gut *68*, 829-843.

Pfeffer, S.R. (2018). LRRK2 and Rab GTPases. Biochem Soc Trans *46*, 1707-1712.

Pfeffer, S.R. (2022). LRRK2 phosphorylation of Rab GTPases in Parkinson's disease. FEBS Lett.

Phaire-Washington, L., Silverstein, S.C., and Wang, E. (1980). Phorbol myristate acetate stimulates microtubule and 10-nm filament extension and lysosome redistribution in mouse macrophages. J Cell Biol *86*, 641-655.

Pischedda, F., and Piccoli, G. (2021). LRRK2 at the pre-synaptic site: A 16-years perspective. J Neurochem *157*, 297-311.

Place, D.E., Samir, P., Malireddi, R.S., and Kanneganti, T.D. (2022). Integrated stress response restricts macrophage necroptosis. Life Sci Alliance *5*.

Prashar, A., Schnettger, L., Bernard, E.M., and Gutierrez, M.G. (2017). Rab GTPases in Immunity and Inflammation. Front Cell Infect Microbiol *7*, 435.

Price, A., Manzoni, C., Cookson, M.R., and Lewis, P.A. (2018). The LRRK2 signalling system. Cell Tissue Res *373*, 39-50.

Przedborski, S. (2005). Pathogenesis of nigral cell death in Parkinson's disease. Parkinsonism Relat Disord *11 Suppl 1*, S3-7.

Purlyte, E., Dhekne, H.S., Sarhan, A.R., Gomez, R., Lis, P., Wightman, M., Martinez, T.N., Tonelli, F., Pfeffer, S.R., and Alessi, D.R. (2018). Rab29 activation of the Parkinson's disease-associated LRRK2 kinase. EMBO J *37*, 1-18.

Puschmann, A., Englund, E., Ross, O.A., Vilarino-Guell, C., Lincoln, S.J., Kachergus, J.M., Cobb, S.A., Tornqvist, A.L., Rehncrona, S., Widner, H.*, et al.* (2012). First neuropathological description of a patient with Parkinson's disease and LRRK2 p.N1437H mutation. Parkinsonism Relat Disord *18*, 332-338.

Qing, H., Wong, W., McGeer, E.G., and McGeer, P.L. (2009). Lrrk2 phosphorylates alpha synuclein at serine 129: Parkinson disease implications. Biochem Biophys Res Commun *387*, 149-152.

Quintero-Espinosa, D.A., Sanchez-Hernandez, S., Velez-Pardo, C., Martin, F., and Jimenez-Del-Rio, M. (2023). LRRK2 Knockout Confers Resistance in HEK-293 Cells to Rotenone-Induced Oxidative Stress, Mitochondrial Damage, and Apoptosis. Int J Mol Sci *24*.

Radulovic, M., Schink, K.O., Wenzel, E.M., Nahse, V., Bongiovanni, A., Lafont, F., and Stenmark, H. (2018). ESCRT-mediated lysosome repair precedes lysophagy and promotes cell survival. EMBO J *37*.

Rajput, A., Dickson, D.W., Robinson, C.A., Ross, O.A., Dachsel, J.C., Lincoln, S.J., Cobb, S.A., Rajput, M.L., and Farrer, M.J. (2006). Parkinsonism, Lrrk2 G2019S, and tau neuropathology. Neurology *67*, 1506-1508.

Raschke, W.C., Baird, S., Ralph, P., and Nakoinz, I. (1978). Functional macrophage cell lines transformed by Abelson leukemia virus. Cell *15*, 261-267.

Reinheckel, T., and Tholen, M. (2022). Low-level lysosomal membrane permeabilization for limited release and sublethal functions of cathepsin proteases in the cytosol and nucleus. FEBS Open Bio *12*, 694-707.

Ren, X., Pan, X., Zhang, Z., Wang, D., Lu, X., Li, Y., Wen, D., Long, H., Luo, J., Feng, Y.*, et al.* (2013). Identification of GZD824 as an orally bioavailable inhibitor that targets phosphorylated and nonphosphorylated breakpoint cluster region-Abelson (Bcr-Abl)

kinase and overcomes clinically acquired mutation-induced resistance against imatinib. J Med Chem *56*, 879-894.

Rentzos, M., Nikolaou, C., Andreadou, E., Paraskevas, G.P., Rombos, A., Zoga, M., Tsoutsou, A., Boufidou, F., Kapaki, E., and Vassilopoulos, D. (2007). Circulating interleukin-15 and RANTES chemokine in Parkinson's disease. Acta Neurol Scand *116*, 374-379.

Rideout, H.J., and Re, D.B. (2017). LRRK2 and the "LRRKtosome" at the Crossroads of Programmed Cell Death: Clues from RIP Kinase Relatives. Adv Neurobiol *14*, 193-208.

Rizo, J., and Xu, J. (2015). The Synaptic Vesicle Release Machinery. Annu Rev Biophys *44*, 339-367.

Rocha, E.M., De Miranda, B.R., Castro, S., Drolet, R., Hatcher, N.G., Yao, L., Smith, S.M., Keeney, M.T., Di Maio, R., Kofler, J.*, et al.* (2020). LRRK2 inhibition prevents endolysosomal deficits seen in human Parkinson's disease. Neurobiol Dis *134*, 104626.

Rocha, N.P., Scalzo, P.L., Barbosa, I.G., Souza, M.S., Morato, I.B., Vieira, E.L., Christo, P.P., Teixeira, A.L., and Reis, H.J. (2014). Cognitive Status Correlates with CXCL10/IP-10 Levels in Parkinson's Disease. Parkinsons Dis *2014*, 903796.

Roda, G., Chien Ng, S., Kotze, P.G., Argollo, M., Panaccione, R., Spinelli, A., Kaser, A., Peyrin-Biroulet, L., and Danese, S. (2020). Crohn's disease. Nat Rev Dis Primers *6*, 22.

Ross, O.A., Soto-Ortolaza, A.I., Heckman, M.G., Aasly, J.O., Abahuni, N., Annesi, G., Bacon, J.A., Bardien, S., Bozi, M., Brice, A.*, et al.* (2011). Association of LRRK2 exonic variants with susceptibility to Parkinson's disease: a case-control study. Lancet Neurol *10*, 898-908.

Ross, O.A., Toft, M., Whittle, A.J., Johnson, J.L., Papapetropoulos, S., Mash, D.C., Litvan, I., Gordon, M.F., Wszolek, Z.K., Farrer, M.J.*, et al.* (2006). Lrrk2 and Lewy body disease. Ann Neurol *59*, 388-393.

Rousseau, A., and Bertolotti, A. (2018). Regulation of proteasome assembly and activity in health and disease. Nat Rev Mol Cell Biol *19*, 697-712.

Ruan, Y., Rezelj, S., Bedina Zavec, A., Anderluh, G., and Scheuring, S. (2016). Listeriolysin O Membrane Damaging Activity Involves Arc Formation and Lineaction -- Implication for Listeria monocytogenes Escape from Phagocytic Vacuole. PLoS Pathog *12*, e1005597.

Rudenko, I.N., Chia, R., and Cookson, M.R. (2012). Is inhibition of kinase activity the only therapeutic strategy for LRRK2-associated Parkinson's disease? BMC Med *10*, 20.

Rudenko, I.N., and Cookson, M.R. (2010). 14-3-3 proteins are promising LRRK2 interactors. Biochem J *430*, e5-6.

Rudnik, S., and Damme, M. (2021). The lysosomal membrane-export of metabolites and beyond. FEBS J *288*, 4168-4182.

Ruiz-Martinez, J., de la Riva, P., Rodriguez-Oroz, M.C., Mondragon Rezola, E., Bergareche, A., Gorostidi, A., Gago, B., Estanga, A., Larranaga, N., Sarasqueta, C.*, et al.* (2014). Prevalence of cancer in Parkinson's disease related to R1441G and G2019S mutations in LRRK2. Mov Disord *29*, 750-755.

Russell, C.M., Rybak, J.A., Miao, J., Peters, B.M., and Barrera, F.N. (2023). Candidalysin: Connecting the pore forming mechanism of this virulence factor to its immunostimulatory properties. J Biol Chem *299*, 102829.

Rydell, G.E., Renard, H.F., Garcia-Castillo, M.D., Dingli, F., Loew, D., Lamaze, C., Romer, W., and Johannes, L. (2014). Rab12 localizes to Shiga toxin-induced plasma membrane invaginations and controls toxin transport. Traffic *15*, 772-787.

Salo, R.J., Bleam, D.K., Greer, V.L., and Ortega, A.P. (1985). Interferon production in murine macrophage-like cell lines. J Leukoc Biol *37*, 395-406.

Samir, P., Malireddi, R.K.S., and Kanneganti, T.D. (2020). The PANoptosome: A Deadly Protein Complex Driving Pyroptosis, Apoptosis, and Necroptosis (PANoptosis). Front Cell Infect Microbiol *10*, 238.

Sanjo, H., Nakayama, J., Yoshizawa, T., Fehling, H.J., Akira, S., and Taki, S. (2019). Cutting Edge: TAK1 Safeguards Macrophages against Proinflammatory Cell Death. J Immunol *203*, 783-788.

Sanyal, A., Scanavachi, G., Somerville, E., Saminathan, A., Nair, A., Oikonomou, A., Hatzakis, N.S., and Kirchhausen, T. (2024). Constitutive Endolysosomal Perforation in Neurons allows Induction of alpha-Synuclein Aggregation by Internalized Pre-Formed Fibrils. bioRxiv.

Sanz Murillo, M., Villagran Suarez, A., Dederer, V., Chatterjee, D., Alegrio Louro, J., Knapp, S., Mathea, S., and Leschziner, A.E. (2023). Inhibition of Parkinson's disease-related LRRK2 by type I and type II kinase inhibitors: Activity and structures. Sci Adv *9*, eadk6191.

Sardiello, M., Palmieri, M., di Ronza, A., Medina, D.L., Valenza, M., Gennarino, V.A., Di Malta, C., Donaudy, F., Embrione, V., Polishchuk, R.S.*, et al.* (2009). A gene network regulating lysosomal biogenesis and function. Science *325*, 473-477.

Saric, A., Hipolito, V.E., Kay, J.G., Canton, J., Antonescu, C.N., and Botelho, R.J. (2016). mTOR controls lysosome tubulation and antigen presentation in macrophages and dendritic cells. Mol Biol Cell *27*, 321-333.

Saunders-Pullman, R., Barrett, M.J., Stanley, K.M., Luciano, M.S., Shanker, V., Severt, L., Hunt, A., Raymond, D., Ozelius, L.J., and Bressman, S.B. (2010). LRRK2 G2019S mutations are associated with an increased cancer risk in Parkinson disease. Mov Disord *25*, 2536-2541.

Saunders-Pullman, R., Mirelman, A., Alcalay, R.N., Wang, C., Ortega, R.A., Raymond, D., Mejia-Santana, H., Orbe-Reilly, M., Johannes, B.A., Thaler, A.*, et al.* (2018). Progression in the LRRK2-Asssociated Parkinson Disease Population. JAMA Neurol *75*, 312-319.

Saunders-Pullman, R., Ortega, R.A., Wang, C., Raymond, D., Elango, S., Leaver, K., Urval, N., Katsnelson, V., Gerber, R., Swan, M.*, et al.* (2022). Association of Olfactory Performance With Motor Decline and Age at Onset in People With Parkinson Disease and the LRRK2 G2019S Variant. Neurology *99*, e814-e823.

Schapansky, J., Khasnavis, S., DeAndrade, M.P., Nardozzi, J.D., Falkson, S.R., Boyd, J.D., Sanderson, J.B., Bartels, T., Melrose, H.L., and LaVoie, M.J. (2018). Familial knockin mutation of LRRK2 causes lysosomal dysfunction and accumulation of endogenous insoluble alpha-synuclein in neurons. Neurobiol Dis *111*, 26-35.

Schapansky, J., Nardozzi, J.D., Felizia, F., and LaVoie, M.J. (2014). Membrane recruitment of endogenous LRRK2 precedes its potent regulation of autophagy. Hum Mol Genet *23*, 4201-4214.

Schluter, O.M., Khvotchev, M., Jahn, R., and Sudhof, T.C. (2002). Localization versus function of Rab3 proteins. Evidence for a common regulatory role in controlling fusion. J Biol Chem *277*, 40919-40929.

Schluter, O.M., Schmitz, F., Jahn, R., Rosenmund, C., and Sudhof, T.C. (2004). A complete genetic analysis of neuronal Rab3 function. J Neurosci *24*, 6629-6637.

Schluter, O.M., Schnell, E., Verhage, M., Tzonopoulos, T., Nicoll, R.A., Janz, R., Malenka, R.C., Geppert, M., and Sudhof, T.C. (1999). Rabphilin knock-out mice reveal that rabphilin is not required for rab3 function in regulating neurotransmitter release. J Neurosci *19*, 5834-5846.

Schmidt, O., and Teis, D. (2012). The ESCRT machinery. Curr Biol *22*, R116-120.

Schmidt, S.H., Knape, M.J., Boassa, D., Mumdey, N., Kornev, A.P., Ellisman, M.H., Taylor, S.S., and Herberg, F.W. (2019). The dynamic switch mechanism that leads to activation of LRRK2 is embedded in the DFGpsi motif in the kinase domain. Proc Natl Acad Sci U S A *116*, 14979-14988.

Schmidt, S.H., Weng, J.H., Aoto, P.C., Boassa, D., Mathea, S., Silletti, S., Hu, J., Wallbott, M., Komives, E.A., Knapp, S.*, et al.* (2021). Conformation and dynamics of the

kinase domain drive subcellular location and activation of LRRK2. Proc Natl Acad Sci U S A *118*.

Schnettger, L., and Gutierrez, M.G. (2017). Quantitative Spatiotemporal Analysis of Phagosome Maturation in Live Cells. Methods Mol Biol *1519*, 169-184.

Schroder, J.B., Pawlowski, M., Meyer Zu Horste, G., Gross, C.C., Wiendl, H., Meuth, S.G., Ruck, T., and Warnecke, T. (2018). Immune Cell Activation in the Cerebrospinal Fluid of Patients With Parkinson's Disease. Front Neurol *9*, 1081.

Schroder, K., Hertzog, P.J., Ravasi, T., and Hume, D.A. (2004). Interferon-gamma: an overview of signals, mechanisms and functions. J Leukoc Biol *75*, 163-189.

Schroder, K., Sagulenko, V., Zamoshnikova, A., Richards, A.A., Cridland, J.A., Irvine, K.M., Stacey, K.J., and Sweet, M.J. (2012). Acute lipopolysaccharide priming boosts inflammasome activation independently of inflammasome sensor induction. Immunobiology *217*, 1325-1329.

Schumacher, S., Laass, K., Kant, S., Shi, Y., Visel, A., Gruber, A.D., Kotlyarov, A., and Gaestel, M. (2004). Scaffolding by ERK3 regulates MK5 in development. EMBO J *23*, 4770-4779.

Schweppe, D.K., Eng, J.K., Yu, Q., Bailey, D., Rad, R., Navarrete-Perea, J., Huttlin, E.L., Erickson, B.K., Paulo, J.A., and Gygi, S.P. (2020). Full-Featured, Real-Time Database Searching Platform Enables Fast and Accurate Multiplexed Quantitative Proteomics. J Proteome Res *19*, 2026-2034.

Sen, S., Webber, P.J., and West, A.B. (2009). Dependence of leucine-rich repeat kinase 2 (LRRK2) kinase activity on dimerization. J Biol Chem *284*, 36346-36356.

Seto, S., Tsujimura, K., and Koide, Y. (2011). Rab GTPases regulating phagosome maturation are differentially recruited to mycobacterial phagosomes. Traffic *12*, 407-420.

Settembre, C., Di Malta, C., Polito, V.A., Garcia Arencibia, M., Vetrini, F., Erdin, S., Erdin, S.U., Huynh, T., Medina, D., Colella, P.*, et al.* (2011). TFEB links autophagy to lysosomal biogenesis. Science *332*, 1429-1433.

Sever, S., Altintas, M.M., Nankoe, S.R., Moller, C.C., Ko, D., Wei, C., Henderson, J., del Re, E.C., Hsing, L., Erickson, A.*, et al.* (2007). Proteolytic processing of dynamin by cytoplasmic cathepsin L is a mechanism for proteinuric kidney disease. J Clin Invest *117*, 2095-2104.

Shen, C.H., Chou, C.H., Liu, F.C., Lin, T.Y., Huang, W.Y., Wang, Y.C., and Kao, C.H. (2016). Association Between Tuberculosis and Parkinson Disease: A Nationwide, Population-Based Cohort Study. Medicine (Baltimore) *95*, e2883.

Sheng, Z., Zhang, S., Bustos, D., Kleinheinz, T., Le Pichon, C.E., Dominguez, S.L., Solanoy, H.O., Drummond, J., Zhang, X., Ding, X., *et al.* (2012). Ser1292 autophosphorylation is an indicator of LRRK2 kinase activity and contributes to the cellular effects of PD mutations. Sci Transl Med *4*, 164ra161.

Shinde, S.R., and Maddika, S. (2018). Post translational modifications of Rab GTPases. Small GTPases *9*, 49-56.

Silva, M.T. (2010). Secondary necrosis: the natural outcome of the complete apoptotic program. FEBS Lett *584*, 4491-4499.

Singh, V., Menard, M.A., Serrano, G.E., Beach, T.G., Zhao, H.T., Riley-DiPaolo, A., Subrahmanian, N., LaVoie, M.J., and Volpicelli-Daley, L.A. (2023). Cellular and subcellular localization of Rab10 and phospho-T73 Rab10 in the mouse and human brain. Acta Neuropathol Commun *11*, 201.

Sirohi, K., Chalasani, M.L., Sudhakar, C., Kumari, A., Radha, V., and Swarup, G. (2013). M98K-OPTN induces transferrin receptor degradation and RAB12-mediated autophagic death in retinal ganglion cells. Autophagy *9*, 510-527.

Skarnes, W.C., Pellegrino, E., and McDonough, J.A. (2019). Improving homology-directed repair efficiency in human stem cells. Methods *164-165*, 18-28.

Skowyra, M.L., Schlesinger, P.H., Naismith, T.V., and Hanson, P.I. (2018). Triggered recruitment of ESCRT machinery promotes endolysosomal repair. Science *360*.

Smith, W.W., Pei, Z., Jiang, H., Dawson, V.L., Dawson, T.M., and Ross, C.A. (2006). Kinase activity of mutant LRRK2 mediates neuronal toxicity. Nat Neurosci *9*, 1231-1233.

Snead, D.M., Matyszewski, M., Dickey, A.M., Lin, Y.X., Leschziner, A.E., and Reck-Peterson, S.L. (2022). Structural basis for Parkinson's disease-linked LRRK2's binding to microtubules. Nat Struct Mol Biol *29*, 1196-1207.

Spillantini, M.G., Schmidt, M.L., Lee, V.M., Trojanowski, J.Q., Jakes, R., and Goedert, M. (1997). Alpha-synuclein in Lewy bodies. Nature *388*, 839-840.

Stahl-Meyer, J., Stahl-Meyer, K., and Jaattela, M. (2021). Control of mitosis, inflammation, and cell motility by limited leakage of lysosomes. Curr Opin Cell Biol *71*, 29-37.

Steger, M., Diez, F., Dhekne, H.S., Lis, P., Nirujogi, R.S., Karayel, O., Tonelli, F., Martinez, T.N., Lorentzen, E., Pfeffer, S.R., *et al.* (2017). Systematic proteomic analysis of LRRK2-mediated Rab GTPase phosphorylation establishes a connection to ciliogenesis. Elife *6*.

Steger, M., Tonelli, F., Ito, G., Davies, P., Trost, M., Vetter, M., Wachter, S., Lorentzen, E., Duddy, G., Wilson, S.*, et al.* (2016). Phosphoproteomics reveals that Parkinson's disease kinase LRRK2 regulates a subset of Rab GTPases. Elife *5*.

Storey, A.J., Naceanceno, K.S., Lan, R.S., Washam, C.L., Orr, L.M., Mackintosh, S.G., Tackett, A.J., Edmondson, R.D., Wang, Z., Li, H.Y.*, et al.* (2020). ProteoViz: a tool for the analysis and interactive visualization of phosphoproteomics data. Mol Omics *16*, 316-326.

Streubel-Gallasch, L., Giusti, V., Sandre, M., Tessari, I., Plotegher, N., Giusto, E., Masato, A., Iovino, L., Battisti, I., Arrigoni, G.*, et al.* (2021). Parkinson's Disease-Associated LRRK2 Interferes with Astrocyte-Mediated Alpha-Synuclein Clearance. Mol Neurobiol *58*, 3119-3140.

Suresh, B., Saminathan, A., Chakraborty, K., Zajac, M., Cui, C., Becker, L., and Krishnan, Y. (2021). Tubular lysosomes harbor active ion gradients and poise macrophages for phagocytosis. Proc Natl Acad Sci U S A *118*.

Tan, E.K., Peng, R., Teo, Y.Y., Tan, L.C., Angeles, D., Ho, P., Chen, M.L., Lin, C.H., Mao, X.Y., Chang, X.L.*, et al.* (2010). Multiple LRRK2 variants modulate risk of Parkinson disease: a Chinese multicenter study. Hum Mutat *31*, 561-568.

Tan, J.X., and Finkel, T. (2022). A phosphoinositide signalling pathway mediates rapid lysosomal repair. Nature *609*, 815-821.

Tang, D., Kang, R., Berghe, T.V., Vandenabeele, P., and Kroemer, G. (2019). The molecular machinery of regulated cell death. Cell Res *29*, 347-364.

Tansey, M.G., Wallings, R.L., Houser, M.C., Herrick, M.K., Keating, C.E., and Joers, V. (2022). Inflammation and immune dysfunction in Parkinson disease. Nat Rev Immunol *22*, 657-673.

Tasegian, A., Singh, F., Ganley, I.G., Reith, A.D., and Alessi, D.R. (2021). Impact of Type II LRRK2 inhibitors on signalling and mitophagy. Biochem J.

Thiele, D.L., and Lipsky, P.E. (1990a). The action of leucyl-leucine methyl ester on cytotoxic lymphocytes requires uptake by a novel dipeptide-specific facilitated transport system and dipeptidyl peptidase I-mediated conversion to membranolytic products. J Exp Med *172*, 183-194.

Thiele, D.L., and Lipsky, P.E. (1990b). Mechanism of L-leucyl-L-leucine methyl ester-mediated killing of cytotoxic lymphocytes: dependence on a lysosomal thiol protease, dipeptidyl peptidase I, that is enriched in these cells. Proc Natl Acad Sci U S A *87*, 83-87.

Thirstrup, K., Dachsel, J.C., Oppermann, F.S., Williamson, D.S., Smith, G.P., Fog, K., and Christensen, K.V. (2017). Selective LRRK2 kinase inhibition reduces phosphorylation of endogenous Rab10 and Rab12 in human peripheral mononuclear blood cells. Sci Rep *7*, 10300.

Thome, A.D., Atassi, F., Wang, J., Faridar, A., Zhao, W., Thonhoff, J.R., Beers, D.R., Lai, E.C., and Appel, S.H. (2021). Ex vivo expansion of dysfunctional regulatory T lymphocytes restores suppressive function in Parkinson's disease. NPJ Parkinsons Dis *7*, 41.

Thurston, T.L., Wandel, M.P., von Muhlinen, N., Foeglein, A., and Randow, F. (2012). Galectin 8 targets damaged vesicles for autophagy to defend cells against bacterial invasion. Nature *482*, 414-418.

Tomiyama, H., Li, Y., Funayama, M., Hasegawa, K., Yoshino, H., Kubo, S., Sato, K., Hattori, T., Lu, C.S., Inzelberg, R.*, et al.* (2006). Clinicogenetic study of mutations in LRRK2 exon 41 in Parkinson's disease patients from 18 countries. Mov Disord *21*, 1102-1108.

Tong, Y., Yamaguchi, H., Giaime, E., Boyle, S., Kopan, R., Kelleher, R.J., 3rd, and Shen, J. (2010). Loss of leucine-rich repeat kinase 2 causes impairment of protein degradation pathways, accumulation of alpha-synuclein, and apoptotic cell death in aged mice. Proc Natl Acad Sci U S A *107*, 9879-9884.

Touchot, N., Chardin, P., and Tavitian, A. (1987). Four additional members of the ras gene superfamily isolated by an oligonucleotide strategy: molecular cloning of YPT-related cDNAs from a rat brain library. Proc Natl Acad Sci U S A *84*, 8210-8214.

Trabzuni, D., Ryten, M., Emmett, W., Ramasamy, A., Lackner, K.J., Zeller, T., Walker, R., Smith, C., Lewis, P.A., Mamais, A.*, et al.* (2013). Fine-mapping, gene expression and splicing analysis of the disease associated LRRK2 locus. PLoS ONE *8*, e70724.

Trilling, C.R., Weng, J.H., Sharma, P.K., Nolte, V., Wu, J., Ma, W., Boassa, D., Taylor, S.S., and Herberg, F.W. (2024). RedOx regulation of LRRK2 kinase activity by active site cysteines. NPJ Parkinsons Dis *10*, 75.

Trost, M., English, L., Lemieux, S., Courcelles, M., Desjardins, M., and Thibault, P. (2009). The phagosomal proteome in interferon-gamma-activated macrophages. Immunity *30*, 143-154.

Ujiie, S., Hatano, T., Kubo, S., Imai, S., Sato, S., Uchihara, T., Yagishita, S., Hasegawa, K., Kowa, H., Sakai, F.*, et al.* (2012). LRRK2 I2020T mutation is associated with tau pathology. Parkinsonism Relat Disord *18*, 819-823.

UniProt, C. (2023). UniProt: the Universal Protein Knowledgebase in 2023. Nucleic Acids Res *51*, D523-D531.

Usenko, T.S., Emel'ianov, A.K., Iakimovskii, A.F., Bogan'kova, N.A., Vavilova, T.V., Shvartsman, A.L., and Pchelina, S.N. (2012). Apoptosis of peripheral blood lymphocytes in patients with LRRK2-assoctated Parkinson's disease. Tsitologiia *54*, 44-48.

Van Houtven, J., Hooyberghs, J., Laukens, K., and Valkenborg, D. (2021). CONSTANd: An Efficient Normalization Method for Relative Quantification in Small- and Large-Scale Omics Experiments in R BioConductor and Python. J Proteome Res *20*, 2151-2156.

van Wilgenburg, B., Browne, C., Vowles, J., and Cowley, S.A. (2013). Efficient, long term production of monocyte-derived macrophages from human pluripotent stem cells under partly-defined and fully-defined conditions. PLoS ONE *8*, e71098.

Vieira, O.V. (2018). Rab3a and Rab10 are regulators of lysosome exocytosis and plasma membrane repair. Small GTPases *9*, 349-351.

Vijay, K. (2018). Toll-like receptors in immunity and inflammatory diseases: Past, present, and future. Int Immunopharmacol *59*, 391-412.

Vitale, I., Pietrocola, F., Guilbaud, E., Aaronson, S.A., Abrams, J.M., Adam, D., Agostini, M., Agostinis, P., Alnemri, E.S., Altucci, L.*, et al.* (2023). Apoptotic cell death in disease-Current understanding of the NCCD 2023. Cell Death Differ *30*, 1097-1154.

Wallings, R.L., Herrick, M.K., and Tansey, M.G. (2020). LRRK2 at the Interface Between Peripheral and Central Immune Function in Parkinson's. Front Neurosci *14*, 443.

Wallings, R.L., and Tansey, M.G. (2019). LRRK2 regulation of immune-pathways and inflammatory disease. Biochem Soc Trans *47*, 1581-1595.

Walseng, E., Bakke, O., and Roche, P.A. (2008). Major histocompatibility complex class II-peptide complexes internalize using a clathrin- and dynamin-independent endocytosis pathway. J Biol Chem *283*, 14717-14727.

Wang, D., Lou, J., Ouyang, C., Chen, W., Liu, Y., Liu, X., Cao, X., Wang, J., and Lu, L. (2010). Ras-related protein Rab10 facilitates TLR4 signaling by promoting replenishment of TLR4 onto the plasma membrane. Proc Natl Acad Sci U S A *107*, 13806-13811.

Wang, D., Xu, L., Lv, L., Su, L.Y., Fan, Y., Zhang, D.F., Bi, R., Yu, D., Zhang, W., Li, X.A.*, et al.* (2015). Association of the LRRK2 genetic polymorphisms with leprosy in Han Chinese from Southwest China. Genes Immun *16*, 112-119.

Wang, F., Gomez-Sintes, R., and Boya, P. (2018a). Lysosomal membrane permeabilization and cell death. Traffic *19*, 918-931.

Wang, L., Xie, C., Greggio, E., Parisiadou, L., Shim, H., Sun, L., Chandran, J., Lin, X., Lai, C., Yang, W.J.*, et al.* (2008). The chaperone activity of heat shock protein 90 is

critical for maintaining the stability of leucine-rich repeat kinase 2. J Neurosci *28*, 3384-3391.

Wang, S., Liu, Z., Ye, T., Mabrouk, O.S., Maltbie, T., Aasly, J., and West, A.B. (2017). Elevated LRRK2 autophosphorylation in brain-derived and peripheral exosomes in LRRK2 mutation carriers. Acta Neuropathol Commun *5*, 86.

Wang, X., Bondar, V.V., Davis, O.B., Maloney, M.T., Agam, M., Chin, M.Y., Cheuk-Nga Ho, A., Ghosh, R., Leto, D.E., Joy, D.*, et al.* (2023). Rab12 is a regulator of LRRK2 and its activation by damaged lysosomes. Elife *12*.

Wang, X., Negrou, E., Maloney, M.T., Bondar, V.V., Andrews, S.V., Montalban, M., Llapashtica, C., Maciuca, R., Nguyen, H., Solanoy, H.*, et al.* (2021). Understanding LRRK2 kinase activity in preclinical models and human subjects through quantitative analysis of LRRK2 and pT73 Rab10. Sci Rep *11*, 12900.

Wang, X., Zhang, X., Xue, L., and Xie, A. (2016). The association between the LRRK2 R1628P variant and the risk of Parkinson's disease in Asian: a meta-analysis. Neurosci Lett *623*, 22-27.

Wang, Z., Arat, S., Magid-Slav, M., and Brown, J.R. (2018b). Meta-analysis of human gene expression in response to Mycobacterium tuberculosis infection reveals potential therapeutic targets. BMC Syst Biol *12*, 3.

Waschbusch, D., Purlyte, E., Pal, P., McGrath, E., Alessi, D.R., and Khan, A.R. (2020). Structural Basis for Rab8a Recruitment of RILPL2 via LRRK2 Phosphorylation of Switch 2. Structure *28*, 406-417 e406.

Watanabe, R., Buschauer, R., Bohning, J., Audagnotto, M., Lasker, K., Lu, T.W., Boassa, D., Taylor, S., and Villa, E. (2020). The In Situ Structure of Parkinson's Disease-Linked LRRK2. Cell *182*, 1508-1518 e1516.

Wei, S., Feng, M., and Zhang, S. (2022). Molecular Characteristics of Cell Pyroptosis and Its Inhibitors: A Review of Activation, Regulation, and Inhibitors. Int J Mol Sci *23*.

West, A.B., Moore, D.J., Biskup, S., Bugayenko, A., Smith, W.W., Ross, C.A., Dawson, V.L., and Dawson, T.M. (2005). Parkinson's disease-associated mutations in leucine-rich repeat kinase 2 augment kinase activity. Proc Natl Acad Sci U S A *102*, 16842-16847.

West, A.B., Moore, D.J., Choi, C., Andrabi, S.A., Li, X., Dikeman, D., Biskup, S., Zhang, Z., Lim, K.L., Dawson, V.L.*, et al.* (2007). Parkinson's disease-associated mutations in LRRK2 link enhanced GTP-binding and kinase activities to neuronal toxicity. Hum Mol Genet *16*, 223-232.

Wider, C., Dickson, D.W., and Wszolek, Z.K. (2010). Leucine-rich repeat kinase 2 gene-associated disease: redefining genotype-phenotype correlation. Neurodegener Dis *7*, 175-179.

Wijeyekoon, R.S., Kronenberg-Versteeg, D., Scott, K.M., Hayat, S., Kuan, W.L., Evans, J.R., Breen, D.P., Cummins, G., Jones, J.L., Clatworthy, M.R.*, et al.* (2020). Peripheral innate immune and bacterial signals relate to clinical heterogeneity in Parkinson's disease. Brain Behav Immun *87*, 473-488.

Williams, E.T., Chen, X., and Moore, D.J. (2017). VPS35, the Retromer Complex and Parkinson's Disease. J Parkinsons Dis *7*, 219-233.

Williams-Gray, C.H., Goris, A., Foltynie, T., Brown, J., Maranian, M., Walton, A., Compston, D.A., Sawcer, S.J., and Barker, R.A. (2006). Prevalence of the LRRK2 G2019S mutation in a UK community based idiopathic Parkinson's disease cohort. J Neurol Neurosurg Psychiatr *77*, 665-667.

Xie, L., Chao, X., Teng, T., Li, Q., and Xie, J. (2020). Identification of Potential Biomarkers and Related Transcription Factors in Peripheral Blood of Tuberculosis Patients. Int J Environ Res Public Health *17*.

Xiong, Y., Coombes, C.E., Kilaru, A., Li, X., Gitler, A.D., Bowers, W.J., Dawson, V.L., Dawson, T.M., and Moore, D.J. (2010). GTPase activity plays a key role in the pathobiology of LRRK2. PLoS Genet *6*, e1000902.

Xu, E., Boddu, R., Abdelmotilib, H.A., Sokratian, A., Kelly, K., Liu, Z., Bryant, N., Chandra, S., Carlisle, S.M., Lefkowitz, E.J.*, et al.* (2022a). Pathological alpha-synuclein recruits LRRK2 expressing pro-inflammatory monocytes to the brain. Mol Neurodegener *17*, 7.

Xu, J., Fotouhi, M., and McPherson, P.S. (2015). Phosphorylation of the exchange factor DENND3 by ULK in response to starvation activates Rab12 and induces autophagy. EMBO Rep *16*, 709-718.

Xu, J., He, X., Xu, Y., Chen, X., Li, M., Zhang, L., Fu, X., Pan, M., Wang, Q., and Hu, X. (2022b). Characteristics of systemic inflammation and brain iron deposition in Parkinson's disease patients. Ann Clin Transl Neurol *9*, 276-285.

Xu, J., and McPherson, P.S. (2017). Regulation of DENND3, the exchange factor for the small GTPase Rab12 through an intramolecular interaction. J Biol Chem *292*, 7274-7282.

Xu, X.H., Deng, C.Y., Liu, Y., He, M., Peng, J., Wang, T., Yuan, L., Zheng, Z.S., Blackshear, P.J., and Luo, Z.G. (2014). MARCKS regulates membrane targeting of Rab10 vesicles to promote axon development. Cell Res *24*, 576-594.

Yadavalli, N., and Ferguson, S.M. (2023). LRRK2 suppresses lysosome degradative activity in macrophages and microglia through MiT-TFE transcription factor inhibition. Proc Natl Acad Sci U S A *120*, e2303789120.

Yaddanapudi, S., Altintas, M.M., Kistler, A.D., Fernandez, I., Moller, C.C., Wei, C., Peev, V., Flesche, J.B., Forst, A.L., Li, J.*, et al.* (2011). CD2AP in mouse and human podocytes controls a proteolytic program that regulates cytoskeletal structure and cellular survival. J Clin Invest *121*, 3965-3980.

Yamaguchi, K., Tanaka, M., Mizoguchi, A., Hirata, Y., Ishizaki, H., Kaneko, K., Miyoshi, J., and Takai, Y. (2002). A GDP/GTP exchange protein for the Rab3 small G protein family up-regulates a postdocking step of synaptic exocytosis in central synapses. Proc Natl Acad Sci U S A *99*, 14536-14541.

Yamaguchi, Y., Sakai, E., Okamoto, K., Kajiya, H., Okabe, K., Naito, M., Kadowaki, T., and Tsukuba, T. (2018). Rab44, a novel large Rab GTPase, negatively regulates osteoclast differentiation by modulating intracellular calcium levels followed by NFATc1 activation. Cell Mol Life Sci *75*, 33-48.

Yang, C., Pang, J., Xu, J., Pan, H., Li, Y., Zhang, H., Liu, H., and Xiao, S.Y. (2021). LRRK2 is a candidate prognostic biomarker for clear cell renal cell carcinoma. Cancer Cell Int *21*, 343.

Yim, W.W., Yamamoto, H., and Mizushima, N. (2022). Annexins A1 and A2 are recruited to larger lysosomal injuries independently of ESCRTs to promote repair. FEBS Lett *596*, 991-1003.

Yoon, J.H., Mo, J.S., Kim, M.Y., Ann, E.J., Ahn, J.S., Jo, E.H., Lee, H.J., Lee, Y.C., Seol, W., Yarmoluk, S.M.*, et al.* (2017). LRRK2 functions as a scaffolding kinase of ASK1-mediated neuronal cell death. Biochim Biophys Acta Mol Cell Res *1864*, 2356-2368.

Yoon, M.C., Solania, A., Jiang, Z., Christy, M.P., Podvin, S., Mosier, C., Lietz, C.B., Ito, G., Gerwick, W.H., Wolan, D.W.*, et al.* (2021). Selective Neutral pH Inhibitor of Cathepsin B Designed Based on Cleavage Preferences at Cytosolic and Lysosomal pH Conditions. ACS Chem Biol *16*, 1628-1643.

Yoshimura, S., Egerer, J., Fuchs, E., Haas, A.K., and Barr, F.A. (2007). Functional dissection of Rab GTPases involved in primary cilium formation. J Cell Biol *178*, 363-369.

Yoshimura, S., Gerondopoulos, A., Linford, A., Rigden, D.J., and Barr, F.A. (2010). Family-wide characterization of the DENN domain Rab GDP-GTP exchange factors. J Cell Biol *191*, 367-381.

Yuan, Y., Cao, P., Smith, M.A., Kramp, K., Huang, Y., Hisamoto, N., Matsumoto, K., Hatzoglou, M., Jin, H., and Feng, Z. (2011). Dysregulated LRRK2 signaling in response to endoplasmic reticulum stress leads to dopaminergic neuron degeneration in C. elegans. PLoS ONE *6*, e22354.

Zabetian, C.P., Hutter, C.M., Yearout, D., Lopez, A.N., Factor, S.A., Griffith, A., Leis, B.C., Bird, T.D., Nutt, J.G., Higgins, D.S.*, et al.* (2006). LRRK2 G2019S in families with Parkinson disease who originated from Europe and the Middle East: evidence of two distinct founding events beginning two millennia ago. Am J Hum Genet *79*, 752-758.

Zabetian, C.P., Samii, A., Mosley, A.D., Roberts, J.W., Leis, B.C., Yearout, D., Raskind, W.H., and Griffith, A. (2005). A clinic-based study of the LRRK2 gene in Parkinson disease yields new mutations. Neurology *65*, 741-744.

Zabetian, C.P., Yamamoto, M., Lopez, A.N., Ujike, H., Mata, I.F., Izumi, Y., Kaji, R., Maruyama, H., Morino, H., Oda, M.*, et al.* (2009). LRRK2 mutations and risk variants in Japanese patients with Parkinson's disease. Mov Disord *24*, 1034-1041.

Zahraoui, A., Touchot, N., Chardin, P., and Tavitian, A. (1989). The human Rab genes encode a family of GTP-binding proteins related to yeast YPT1 and SEC4 products involved in secretion. J Biol Chem *264*, 12394-12401.

Zhang, F.R., Huang, W., Chen, S.M., Sun, L.D., Liu, H., Li, Y., Cui, Y., Yan, X.X., Yang, H.T., Yang, R.D.*, et al.* (2009). Genomewide association study of leprosy. New Engl J Med *361*, 2609-2618.

Zhang, X., and Kortholt, A. (2023). LRRK2 Structure-Based Activation Mechanism and Pathogenesis. Biomolecules *13*.

Zhao, L., Zhao, J., Zhong, K., Tong, A., and Jia, D. (2022). Targeted protein degradation: mechanisms, strategies and application. Signal Transduct Target Ther *7*, 113.

Zhao, Y., Perera, G., Takahashi-Fujigasaki, J., Mash, D.C., Vonsattel, J.P.G., Uchino, A., Hasegawa, K., Jeremy Nichols, R., Holton, J.L., Murayama, S.*, et al.* (2018). Reduced LRRK2 in association with retromer dysfunction in post-mortem brain tissue from LRRK2 mutation carriers. Brain *141*, 486-495.

Zhao, Y., Vavouraki, N., Lovering, R.C., Escott-Price, V., Harvey, K., Lewis, P.A., and Manzoni, C. (2023). Tissue specific LRRK2 interactomes reveal a distinct striatal functional unit. PLoS Comput Biol *19*, e1010847.

Zhao, Y., Zhao, L., Li, J., and Zhong, L. (2019). Silencing of long noncoding RNA RP11-476D10.1 enhances apoptosis and autophagy while inhibiting proliferation of papillary thyroid carcinoma cells via microRNA-138-5p-dependent inhibition of LRRK2. J Cell Physiol *234*, 20980-20991.

Zhao, Z., Wu, H., Wang, L., Liu, Y., Knapp, S., Liu, Q., and Gray, N.S. (2014). Exploration of type II binding mode: A privileged approach for kinase inhibitor focused drug discovery? ACS Chem Biol *9*, 1230-1241.

Zhu, A.X., Zhao, Y., and Flier, J.S. (1994). Molecular cloning of two small GTP-binding proteins from human skeletal muscle. Biochem Biophys Res Commun *205*, 1875-1882.

Zhu, H., Tonelli, F., Turk, M., Prescott, A., Alessi, D.R., and Sun, J. (2023). Rab29-dependent asymmetrical activation of leucine-rich repeat kinase 2. Science *382*, 1404-1411.

Zimprich, A., Biskup, S., Leitner, P., Lichtner, P., Farrer, M., Lincoln, S., Kachergus, J., Hulihan, M., Uitti, R.J., Calne, D.B.*, et al.* (2004). Mutations in LRRK2 cause autosomal-dominant parkinsonism with pleomorphic pathology. Neuron *44*, 601-607.

Zou, L., Zhou, J., Zhang, J., Li, J., Liu, N., Chai, L., Li, N., Liu, T., Li, L., Xie, Z.*, et al.* (2009). The GTPase Rab3b/3c-positive recycling vesicles are involved in cross-presentation in dendritic cells. Proc Natl Acad Sci U S A *106*, 15801-15806.